Optical Developments for Microscale Measurement and Control of Temperature in Optogenetics

Chang Liu

Sorbonne Université

Ecole doctorale 564 : « Physique en Île-de-France »

Institut de la Vision (IVISION), UMR 7210

Optical Developments for Microscale Measurement and Control of Temperature in Optogenetics

Par Chang F. Liu

Thèse de doctorat de Physique

Dirigée par Gilles Tessier, Valentina Emiliani et Pascal Berto

Présentée et soutenue publiquement le 15 Avril 2021

Devant un jury composé de :

Dr. Leveque-Fort Sandrine	Directrice de recherche au CNRS	Rapportrice
Dr. Charlot Benoit	Directeur de recherche au CNRS	Rapporteur
Dr. Fragola Alexandra	Maître de conférences	Examinatrice
Dr. Quidant Romain	Professeur des universités	Examinateur
Dr. Waters Jack	Associate Investigator	Examinateur
Dr. Tessier Gilles	Professeur des universités	Directeur de thèse
Dr. Emiliani Valentina	Directrice de recherche au CNRS	Co-directrice de thèse
Dr. Berto Pascal	Maître de conférences	Encadrant de thèse

Développements Optiques pour la Mesure et le Contrôle Micrométrique de la Température en Optogénétique.

La combinaison de la microscopie optique et de la génétique moléculaire - l'optogénétique - a récemment bouleversé le domaine des neurosciences. L'utilisation d'opsines et d'indicateurs fluorescents codés génétiquement permet désormais de contrôler et suivre optiquement l'activité neuronale de manière peu invasive. La stimulation à 2 photons permet d'adresser individuellement plusieurs centaines de neurones en profondeur dans le cerveau, mais la puissance laser nécessaire entraîne des effets thermiques photo-induits qu'il est nécessaire d'évaluer précisément, puisqu'ils sont susceptibles d'altérer potentiellement certaines fonctions neuronales.
Dans ce manuscrit, nous décrivons le développement d'une sonde thermométrique basée sur la luminescence, permettant de mesurer *in vivo* la température à l'extrémité d'une fibre optique lors d'une stimulation optogénétique à 2 photons. Cette sonde offre une sensibilité en température de 0,05 K, une résolution temporelle de 2 ms et une résolution spatiale comparable à la taille d'un neurone (~15µm). Elle permet ainsi d'estimer l'élévation de température induite par diverses conditions d'illumination optogénétique. Pour évaluer l'altération de l'activité neuronale lors de telles variations thermiques, nous avons développé une plateforme qui offre un contrôle spatial précis de la température à l'échelle du micron. Nous démontrons que des profils de température de forme arbitraire et rapidement reconfigurables peuvent être générés en projetant un motif d'illumination sur un ensemble homogène de nanoparticules plasmoniques absorbantes. Enfin, nous avons utilisé ce concept de contrôle thermique à l'échelle micrométrique pour développer des dispositifs de contrôle du front d'onde basés sur des résistances induisant des effets thermo-optiques. Nous avons montré que des matrices de micro-lentilles électro-thermo-optiques permettent l'imagerie calcique de l'activité de neurones à différentes profondeurs simultanément.

Mots clés : Thermométrie par luminescence, optogénétique à deux photons, diffusion de la chaleur, thermoplasmonique, nanoparticules, détection du front d'onde, effets thermo-optiques, imagerie multiplan.

Optical Developments for Microscale Measurement and Control of Temperature in Optogenetics

The combination of optical microscopy and molecular genetics - optogenetics - is revolutionizing the field of neurosciences. Genetically-encoded fluorescent indicators and opsins now allow the optical monitoring and control of neuronal activities with minimal invasiveness. While 2-photon stimulation can now address individually hundreds of neurons, deep inside the brain, the associated increase in laser power leads to photo-induced thermal effects which require a careful evaluation as they can potentially alter neural functions.

In this manuscript, we describe the development of a luminescence-based thermometric probe, that provides in vivo temperature measurements at the end of a single optical fibre during 2-photon optogenetic stimulation. The method provides 0.05 K temperature sensitivity, 2 ms temporal resolution, and single-neuron-size-range spatial resolution (~15µm). This allowed us to precisely evaluate the temperature rise induced by various optogenetic illumination conditions, deep inside tissues. To evaluate the alteration of neural activity induced by such thermal variations, we developped a platform that provides precise spatial control of the temperature at the microscale. Fast, accurate, and reconfigurable temperature patterns are demonstrated over arbitrarily shaped regions by tailoring an optical pattern projected on a homogeneous array of absorbing plasmonic nanoparticles. Finally, we utilized this concept of microscale temperature control to develop wavefront-shaping devices based on tailored resistors inducing thermo-optical effects. We demonstrate that tunable electro-thermo-optical micro-lenses arrays allow the simultaneous Ca^{2+} imaging of neuron activities at different depths.

Keywords: Luminescence thermometry, two-photon optogenetics, heat diffusion, thermoplasmonics, gold nanoparticles, wavefront sensing, thermo-optical effects, multiplane imaging

Summary

Introduction

Advancements in optical microscopy have been pushing the frontier of understanding living tissues for centuries. Since Antoni van Leeuwenhoek (1632-1723) discovered micro-organism using his hand-made high magnification microscope based on a simple lens, microscopy has become one of the most popular tools for exploring biological structure. Today, with much more sophisticated optical instrumentations and advanced bioengineering techniques, microscopes enable a broad range of studies in living tissues. For example, in one of the fascinating research areas – brain study, genetically encoded proteins allow to optically record and control the activity of neuronal circuits with more and more spatiotemporal precisions and penetration depths.

During the 200 years which followed Leeuwenhoek's innovation, developments in optical microscopy mainly focused on technological improvements such as the correction of chromatic and geometrical aberrations to enhance spatial resolution. During the late 19th and early 20th centuries, as electric lamps became available as light sources, breakthroughs in the illumination techniques brought the wide-field imaging quality of classical optical microscopy close to today's levels. In particular, August Köhler developed the illumination method that bears his name in 1893. It allows the homogeneous illumination of the specimen, which highly improves the imaging quality. Most importantly, the Köhler illuminator allowed the development of the phase-contrast microscope decades later. In the 1930', Frits Zernike invented the phase-contrast microscope (Nobel Prize in Physics in 1953) that measures light interferences. Instead of relying on the intensity of light absorption or reflection, his development gave access to an entirely new type of contrast: sensitivity to the refractive index allowed much-improved imaging of transparent samples, like living mammalian cells.

Later in the 20th century, the development of fluorescence microscopy brought imaging performances to yet another level. Fluorescence provides a unique specificity by labelling targeted biological molecules with fluorophores such as fluorescent stains, fluorescent-labelled antibody or genetically encoded fluorescent proteins. However, it is mostly after the invention of confocal microscopy (patented by Marvin Minsky in 1957) that fluorescence microscopy reached its full potential. Confocal microscopy uses a scanned point-source to illuminate fluorophores and a pinhole at the conjugated plane to remove out-of-focus signals, providing spatial resolution and optical sectioning that was never accessible using traditional wide-field approaches. High-resolution 3D maps of biological samples then became accessible.

At the end of the last century, two-photon microscopy (or 2PM, pioneered by Winfried Denk and James Stricker in 1990) brought 3D imaging deeper into tissues. Two-photon scanning microscopy is intrinsically confocal but can provide optical sectioning in even thicker samples than the confocal approach. It is based on the two-photon excitation process, as theoretically proposed by Maria Goeppert-Mayer in 1931. It is a nonlinear excitation of fluorescence after absorbing two photons with ~half the energy of the emission light. The excitation probabilities depend quadratically on the light intensity; thus, the process demands high spatial and temporal energy concentration of light, which can be efficiently performed using femtosecond pulsed infrared laser. As a result, 2PM provides high spatial confinement in 3D, and the use of infrared light allows better penetration depths into biological tissues.

2PM is one of the most promising methods for optical brain investigations because it is a minimally invasive manner to achieve *in vivo* three-dimensional imaging with good penetration depth and spatial resolution. In most cases, 2PM can reach imaging depths of around 500 µm within the brain, which is enough to allow the imaging of, e.g. the superficial cortical layers of mice. The depth has been extended to more than 1mm to image the whole cortical layer through many approaches, such as adaptive optics, higher excitation pulse energy, longer excitation wavelengths, three-photon microscopy (3PM) or developing brighter fluorophores.[1]

In the meantime, a revolutionary method called '*Optogenetics'* emerged in neurosciences at the beginning of this century. It uses light to control neurons that are genetically modified to express light-sensitive ion channels or pumps. Those ion channels or pumps are transmembrane proteins called opsins, which can permit flux of specific ions across the membrane upon illumination at suitable wavelengths to induce electrical potential changes on the local membrane. These potential changes can induce activation or inhibition of neurons. Through optogenetics, one can optically control individual neurons in living tissue or even freely moving animals. In a broader sense, optogenetics also includes techniques that optically monitors neurons activities by the use of genetically encoded activity indicators that change their fluorescence properties when a neuron is activated. All in all, the combination of optogenetics reporters and actuators with advanced optical approaches enables both imaging and manipulation of neuronal circuits, which is also today often referred to as the all-optical recording of neuronal circuits.

Like fluorescence microscopy, optogenetic effects can be obtained through single-photon (1P) or two-photon (2P) absorption approaches. 1P optogenetics undergoes similar constraints as 1P microscopy: the reduced penetration depth and lack of optical sectioning, which can be solved, as done for imaging, by performing 2P optogenetics. More specifically,

the optical sectioning of 2P in combination with 3D laser beam scanning or holographic light shaping techniques, enables in-depth single or multi-neuron activation with single-cell or sub-cell resolution opening the way to a precise optical manipulation of neuronal circuits.

However, as we will see, the need to reach a high number of neurons for in-depth activation requires amplified powerful lasers. This brings forward a major concern related to possible photodamage effects. For optical configurations using parallel illumination which, as we will see, deliver low excitation density light on large surfaces, the main sources of photodamages are photoinduced thermal effects.

In this thesis, I will therefore specifically focus on the theoretical and experimental investigation of the temperature rise associated with 2P optogenetic stimulation.

In Chapter 1, I will introduce the technique of 2P optogenetics and the mathematical models to predict the temperature rise induced during a 2P optogenetic experiment. The model is based on the Fourier's heat diffusion equation solved using the Green's functions formalism.

In Chapter 2, I will present a fibre-based luminescence thermometry technique, that I developed to measure *in vivo* the temperature rises induced during 2P optogenetic experiments and to validate the prediction of the model. I will present several experimental results *in vitro* and in living mice and compare them to the simulations.

In Chapter 3, I will introduce a reconfigurable temperature control technique as a possible tool to help control temperature rises and study their influences. The method is based on the plasmonic thermal effect of gold nanoparticle assemblies and realised by light shaping illumination. The temperature shaping ability is validated by wavefront thermal sensing. Through proof-of-principle experiments, we show the potential of the technique for the study of living cell thermal responses. During the work of Chapter 3, I studied microscale thermal control and thermo-optical effects, which brought me to another - related- horizon: thermally tunable optics.

In Chapter 4, I will demonstrate a micro-device that can modify optical wavefronts through electrically generated heat in a thermo-optical medium. Using one of the functions of this device, a new 3D imaging method is developed. The thermally controlled tunable lens array is used to focus on different planes during a single wide-field image acquisition. Preliminary experiments of simultaneous multiplane imaging of neuron activities were carried out in zebrafish larvae combined with calcium imaging.

Chapter 1

Two-Photon Optogenetics and Thermal Effects

Summary

The brain is one of our body's most fascinating organs. For decades, more and more advances technologies have been applied to investigate it. Nowadays, to better understand its complex mechanisms, research increasingly focuses on the cellular, even subcellular level– neurons, synapses, and the networks they compose. Photonic methods have brought important new perspectives to this subject, and light is increasingly used for manipulating and observing brain circuits.

1.1. Photostimulation of neurons

1.1.1. Electrical activities in neurons

The mammalian brain is composed of billions of neurons interconnected into circuits by trillions of synapses[2,3]. Neurons include various cell types responsible for different functions like reception, processing, and transmission of signals[4]. They communicate through electrical or chemical signals and form complex neural systems. To decode neuronal networks, one should answer system-level questions, like the role of neurons in a neural circuit or behaviour, as well as molecular- and cellular-level questions, like how membrane proteins like ion channels and other molecules give each neuron its physiological characteristics. Perturbing one element in a neural circuit is a strategy often used in the domain of neuroscience, e.g. for describing the neural system anatomically or for functional dissection of individual cell types and their synaptic connections. This is usually realised by manipulation of neural electrical activity, such as to activate (or inhibit) certain neurons for a "gain of function" (or "loss of function") experiment while using electrophysiology tools to listen to the changes in electrical signals[3,5].

To manipulate neural electrical activity (activate or inhibit), it is essential to understand a key phenomenon: the **action potentials** (AP). AP is the sudden transient potential change on the plasma membrane that propagates along the axon to the synapse, transmitting signals downstream to directly connected neurons[6]. In all animal cells, a difference in electrical charge between the intracellular and extracellular sides of the plasma membrane creates an electrical potential. A neuron membrane at **resting potential** is about –70 mV (more negative inside than outside). By opening and closing specific membrane ion-channel proteins (who are permeable to specific ions), neurons undergo controlled changes in their membrane potentials. While the inside potential becomes more positive than the resting potential, we call it the **depolarisation** process; while it becomes more negative than the resting potential, we call it **hyperpolarisation**. The action potential is a cycle of membrane depolarisation, hyperpolarisation and returning to the resting state.

- When a neuron is at the resting state, the resting potential (inside negative) across the plasma membrane is maintained by an electro-chemical equilibrium of several ions, mainly K^+, Na^+ and Cl^-, each of different permeability through the membrane. For each ion, its equilibrium is determined by the differences in ion concentrations and electrical potentials between the inside and outside of the membrane. K^+ is the most permeable as there are many open resting

K^+ channels at the resting state. Let us take K^+ as an example to explain the process: **resting K^+ channels** are always open and allow only K^+ to pass, shown in Figure 1.1(a). The concentration of K^+ is much higher inside animal cells than in extracellular fluid; due to this concentration gradient, K^+ ions flow out of the cell through the resting K^+ channels and leave an excess negative charge on the cytosolic face. Meanwhile, this negative charge balance the K^+ efflux. Such an equilibrium and negative potential are maintained because of Na^+/K^+ active pumping (by an enzyme called Na^+/K^+-ATPase, taking K^+ in and Na^+ out) to keep the ions concentration.

- When a region of the plasma membrane is depolarised slightly, **voltage-gated Na^+ channels** open for a short period (~1ms) and allow the influx of Na^+ ions (see Figure 1.1(b)). This influx results from two forces driving in the same direction: the concentration gradient of Na^+ ions (lower in the cell) and the resting membrane potential (negative in the cytosol side). The influx causes further depolarisation of the region, which spreads along the membrane surface and continue to depolarise adjacent regions of the membrane, opening even more voltage-gated Na^+ channels. As a result, explosive entry of Na^+ ions is completed within a fraction of a millisecond, causing sudden and transient depolarisation, the action potential. The voltage-gated Na^+ channels close after this short period, entering a **refractory period** and cannot be reopened as long as the membrane stays depolarised.

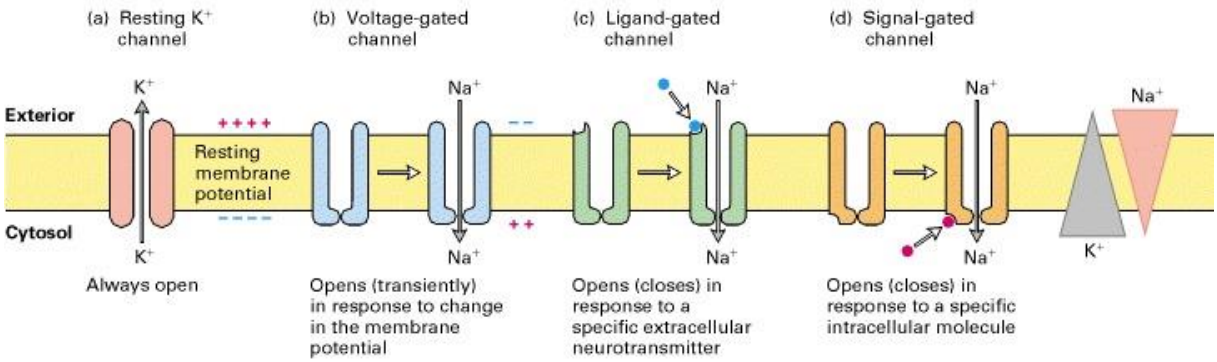

Figure 1.1 Ion channels in neuronal plasma membranes. Each type of channel protein has a specific function in the electrical activity of neurons. (a) Resting K+ channels are responsible for generating the resting potential across the membrane. (b) Voltage-gated channels are responsible for propagating action potentials along the axonal membrane. (c, d) Two types of ion channels in dendrites and cell bodies are responsible for generating electric signals in postsynaptic cells. (Two triangles on the right stand for the concentration gradient of Na+ and K+). (Adapted from ref [7])

- Following the opening and closing of voltage-gated Na^+ channels, voltage-gated K^+ channels open (with a millisecond or so delay after the initial depolarisation), which causes an increased efflux of K^+ from the cytosol. It repolarises the membrane to its resting potential. Actually, before returning to resting value, the membrane experience a brief instant of hyperpolarisation, when the potential is more negative than the resting potential. The voltage-gated K+ channels remain open until the membrane potential returns an inside negative value.
- Eventually, the voltage-gated Na^+ and K^+ channels are all closed, and the membrane returns to the resting state. This cycle lasts 1 – 2 ms and can happen hundreds of times a second. Around the peak of an action potential, the membrane depolarisation can depolarise downstream segments of the membrane to re-initiate the cycle, thus ensuring the propagation of action potential without diminution.[7]

Naturally, the initial trigger that evokes an action potential in the postsynaptic neuron can be neurotransmitters or electrical current at the synapse. For example, in the case of chemical synapses, in Figure 1.1(c,d), the ligand-gated ion channel opens while binding a specific extracellular neurotransmitter; the signal-gated channel opens in response to intracellular signals induced by binding of the neurotransmitter to a separate receptor protein (not shown). Both of them are responsible for generating an electrical signal in the postsynaptic neuron. In another case, in electrical synapses, electrical current from a presynaptic neuron can evoke depolarisations directly on the postsynaptic one. However, initial depolarisation does not always result in action potential; it can result in subthreshold depolarisations when the action potential threshold is not reached[8,9]. For simplicity, inhibition in neuron synaptic connections is not discussed here.

To artificially generate action potential *in vivo*, the most used method is electrical stimulation: an electrode is placed near neurons of interest (extracellular stimulation) or inside a neuron of interest (intracellular stimulation), and an electrical current is applied at fixed frequency and time. It elicits action potential by changing the extracellular environments or intracellular potential such that voltage-gated Na^+ channels open. Although electrical stimulation protocols have been developed and refined in the last century to produce reliable activation and minimise neural tissue damage, it still has some main limitations. As shown in Figure 1.2(a), extracellular electrical stimulation non-specifically affects all cell types near the electrode, inducing side effect on adjacent neurons and resulting in a large population of neurons excited without cellular resolution or cell specificity. Intracellular stimulation provides single-cell specificity, but only very few electrodes can be inserted in the sample and targeting

a large population is not possible. Also, most of the time, the electrode stimulation approach is not reproducible. When an experiment requires several days of operation, it is hard to go back to the same cell or group of neurons once taking out the electrodes.

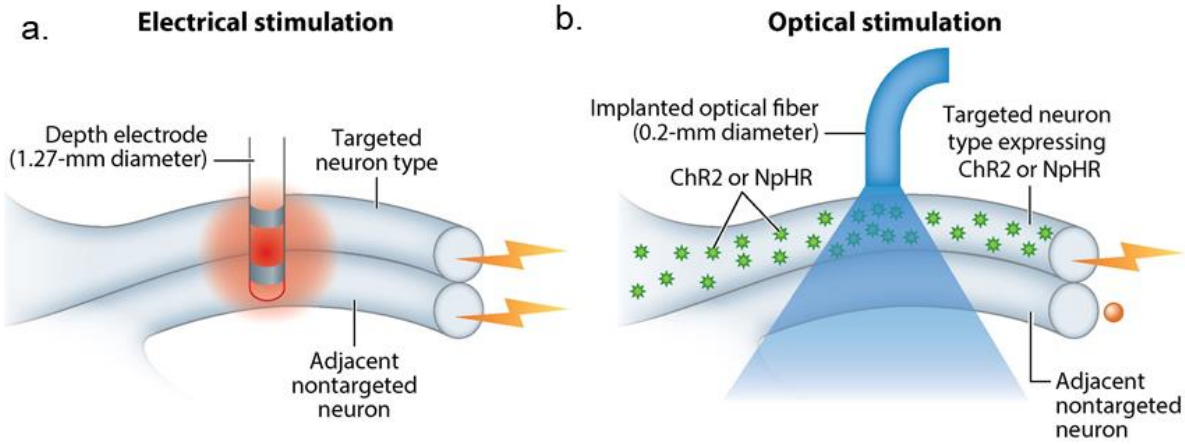

Figure 1.2 (a) Electrical stimulation non-specifically affects all cell types near the electrode, causing side effects on adjacent neuron; (b) Genetically targetable optogenetic constructs enable more precise stimulation of specified neural subtypes intermingled with nontargeted neurons. (Adapted from ref [10]*)*

In the last decade, a new method called optogenetic stimulation has emerged, as shown in Figure 1.2(b), allowing the use of light to stimulate and probe neuron functions without inserting a stimulation electrode, with high specificity and reproducibility, which has provided abundant advantages over traditional electrode-based methods.

1.1.2. Optogenetic stimulations

Optogenetics is based on the optical stimulation of photosensitive membrane-bound ion channels and pumps that are genetically encoded in activable neurons. Its mechanism was first discovered in microbial organisms in which bacteriorhodopsin acts as a light-activated ion pump [11]. Further research on this mechanism and its variants found similar membrane-bound proteins that permit ions flux across the membrane upon stimulation at a suitable wavelength, known as channelrhodopsins[12,13] and halorhodopsins[14]. Two variations of channelrhodopsins were subsequently selected for their ease of expression, conductance and photosensitivity: Channelrhodopsin-1 and Channelrhodopsin-2 (ChR2). In 2005, for the first time, the genetic code for ChR2 was introduced and expressed in mammalian neurons, allowing to reliably and

precisely control action potentials generation[15]. Since then, this method has drawn increasing interest in neuroscience research.

As shown in Figure 1.3, under illumination at around 470 nm, ChR2 opsins on the neural membrane open and allow the passive entry of cations into the cell (mostly Na^+ and very low levels of Ca^{2+})[16]. This results in the depolarisation of the local membrane, where they are expressed and activated. Sufficiently high depolarisation could further open voltage-gated Na^+ channels and possibly trigger the generation of an action potential. Other types of opsins can cause inhibition, like halorhodopsin (NpHR), which hyperpolarises membranes by actively pumping Cl^- ions into cells in response to yellow light with peak absorption at 570 nm. In the last years, the palette of optogenetics actuators that work with different wavelengths or provide different functions has significantly expanded[3].

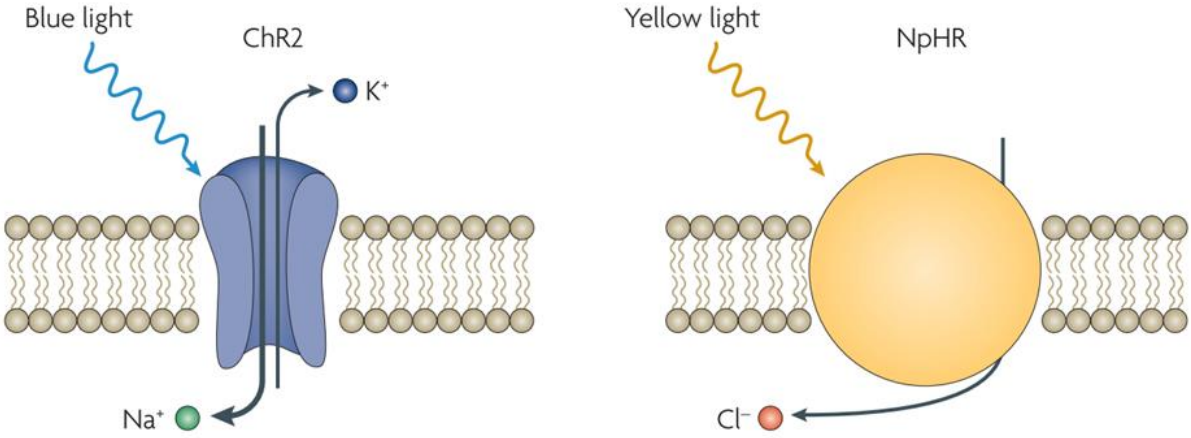

Figure 1.3 Schematic of channelrhodopsin-2 (ChR2) and the halorhodopsin (NpHR) pump. Illuminated with blue light (activation maximum ~470 nm), ChR2 allows the entry of cations (mostly Na^+ and very low levels of Ca^{2+}) into the cell. NpHR is activated by yellow light (activation maximum ~580 nm, and allows the entry of Cl^- anions. (Adapted from ref [16])

Compared to the classical electrical stimulation method, the main advantages of optogenetics are that: it can be non-invasive; it enables exciting only a specific cell type and subcellular domain using genetically encoded and targetable probes[2].

Combined with single-photon (1P), wide-field illumination (as shown in Figure 1.4(a)) or fibre induced illumination, optogenetic neuronal targeting has already shown enormous potential in neuroscience. It has enabled the optical control of entire neuronal networks[15,17–19] and disentangled their role in controlling specific behaviours[20–22]. In these studies, cellular specificity relied exclusively on genetic targeting strategies that enable the expression of opsins in specific cell types. This, however, offers a limited understanding of brain function since

neurons belonging to the same cell type and brain region may present diverse response patterning[23–25]. In order to understand the fine-scale organisation of the brain, e.g. the number of neurons required to trigger a certain behaviour or the importance of a certain node in neural circuits over others, the spatial range of light-based investigation needs to be scaled-down from genetically targeted neuronal population to individual neurons. This has encouraged researchers to develop a variety of light-targeting strategies[26,27] that enables arbitrarily controlling the spatial distribution of light into the sample and selectively target defined neurons, subsets of neurons, within the opsin-positive population, as shown in Figure 1.4(b). Light-targeting is typically achieved following two classes of approaches: either by scanning micro-scale Gaussian spots to serially activate targets, or by modulating light intensity and/or phase to obtain arbitrarily defined patterns of illumination to parallelly activate targets; sometimes, a combination of both approaches is used[28].

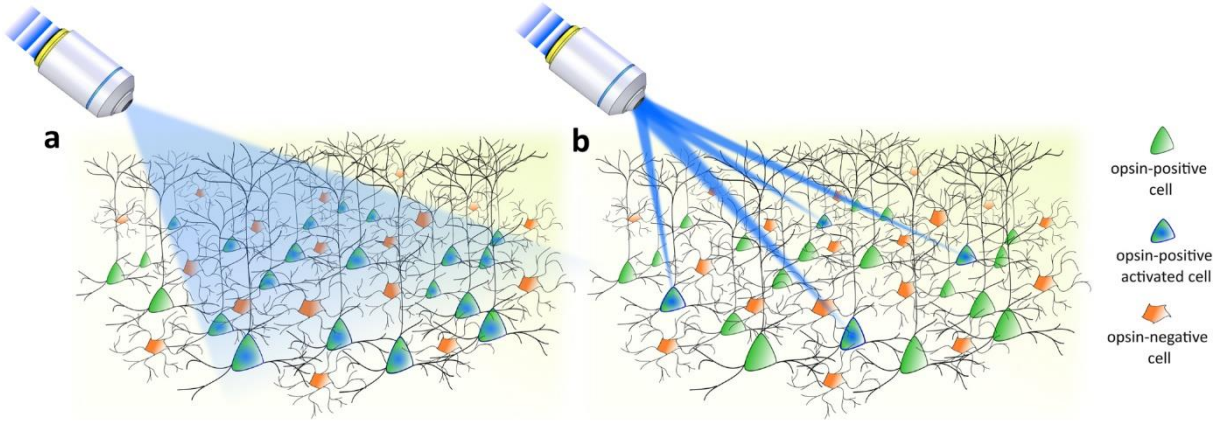

Figure 1.4 Single-photon optical approaches for optogenetic stimulation. (a) The genetically targeted, opsin-expressing neurons are activated via wide-field illumination. (b) Targeted investigations by selective activation of a specific pool of neurons via specific optical targeting. (Adapted from ref [28])

A critical challenge of using light to stimulate neurons is that it requires to overcome tissue scattering to access neurons deep in the brain. A further challenge is related to the necessity to highly confine the illumination and reach a high 3D spatial resolution, which is essential to mimic natural and realistic neural activity patterns accurately[28]. Replacing single-photon (1P) excitation with two-photon (2P) excitation is currently one of the most promising approaches[29] to solve these issues.

1.1.3. 2P excitation and 2P optogenetics

Single-photon excitation is based on a linear photon absorption process. An atom or a molecule is excited by the absorption of one photon. As shown in Figure 1.5 (one-photon), a photon excites a ground-state electron to a higher energy level. The 1P excitation probability depends linearly on light intensity. It follows that, as shown in Figure 1.6(a), for a focused beam, 1P absorption also occurs out of focus.

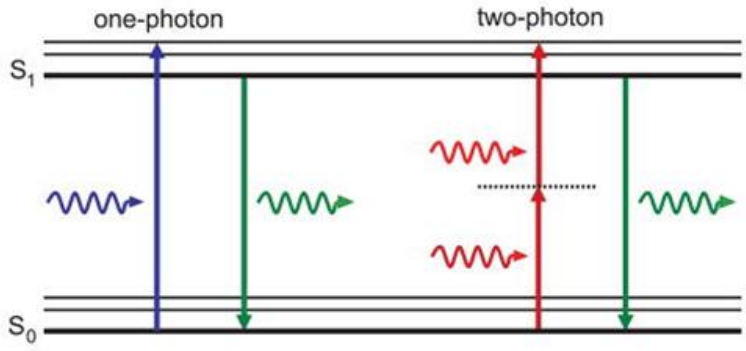

Figure 1.5 Energy-level diagram of one-photon and two-photon excitations. (Adapted from ref [30])

In 2-photon absorption processes, two photons with half the energy of those used in 1P processes must reach the molecule within an ultrashort time window limited by the intermediate virtual state (~1fs, as shown by a dashed line in Figure 1.5) [31,32] in order to promote the electron to the excited state. Such events have reasonable probabilities of occurring only if the photon density is high enough, both in space (focusing) and time (high-intensity beams and/or short and intense pulses). Therefore, 2P excitation is typically provided via focused, high-energy lasers with short pulse duration, which provide a high density of photons in the excitation area. During the 2P process, the absorption probability is quadratically dependent on the light intensity[33–35]. As illustrated in Figure 1.6 (adapted from ref[35]), this quadratic dependency intrinsically provides high spatial confinement in the z-direction (and, more marginally, in the x and y directions) compared to 1P process[33].

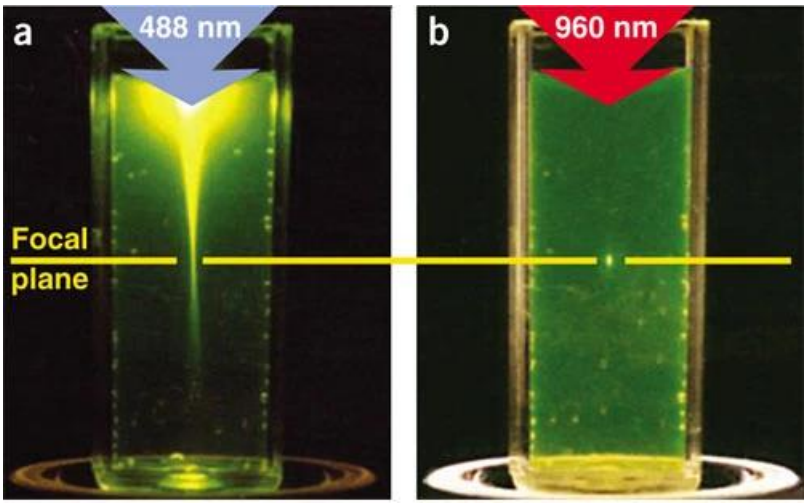

Figure 1.6 Localisation of single-photon and two-photon excitation. (a) Single-photon excitation of fluorescein by focused 488nm wavelength light (NA = 0.16). (b) Two-photon excitation with focused femtosecond pulses of 960nm light (NA = 0.16). (Adapted from ref [35])

Besides, 2P excitation has the important advantage of using longer-wavelength photons, usually in the infrared, which are much less scattered than shorter-wavelength blue photons, as the scattering coefficient decreases with the wavelength (see Figure 1.8(b)). 2P excitation is, therefore, able to address neurons at a greater depth than 1P excitation.

With higher spatial resolution and penetration depth, 2P excitation provides optogenetics with potentials of single-neuron precision, selective multi-neuron targeting, and in-depth neuron circuit investigation. However, considering the low conductance of some opsin (for ChR2: ~80 femtosiemens)[36], in order to guarantee reliable neuron activation and elicit action potentials, which require strong depolarisation, a large number of photoactivated ion channels are necessary[37]. A tightly 2P focused beam is not able, in most of the cases, to open a sufficient number of channels within its two-photon focal volume (~2-5 μm^3); increasing excitation density would not help either, as saturation of excited ChR2 channels is quickly reached owing to the high two-photon absorption cross-section of ChR2 (~260 Goeppert-Mayer units at 920 nm) and the long lifetime of the conducting excited states (~10 ms)[37]. An elegant solution that consists of illuminating the entire cell body rather than a single point using computer-generated holography (CGH), was first proposed in 2008 in 1P and in 2P (see ref[38,39]). As shown in Figure 1.7, an adapted pattern is projected into the sample using a spatial light modulator (SLM). This pattern illuminates the entire cell bodies of selected neurons and maximises the fraction of the cell membrane stimulated. All opsins in the cell are thus simultaneously opened, and depolarisation can reach the voltage threshold to action potential

generation. In order to improve illumination axial resolution (<6 µm) and propagation through scattering tissue, CGH can be combined with temporal focusing[37,40]. That is achieved by using a dispersive optical setup to modulate the temporal profile of the pulse, such that the pulse is stretched away from the objective focal plane, compressed as it travels toward it and stretched again beyond it. Temporally focused CGH illumination has allowed generating action potentials with millisecond temporal resolution[37,41] and sub-millisecond temporal onset precision[42,43]. The principal alternative to this parallel illumination method is the scanning method, in which a focused beam is scanned sequentially over the entire soma of one or several neurons in order to increase the number of accessible channels and integrate over time the current generated in different locations of the cell[28].

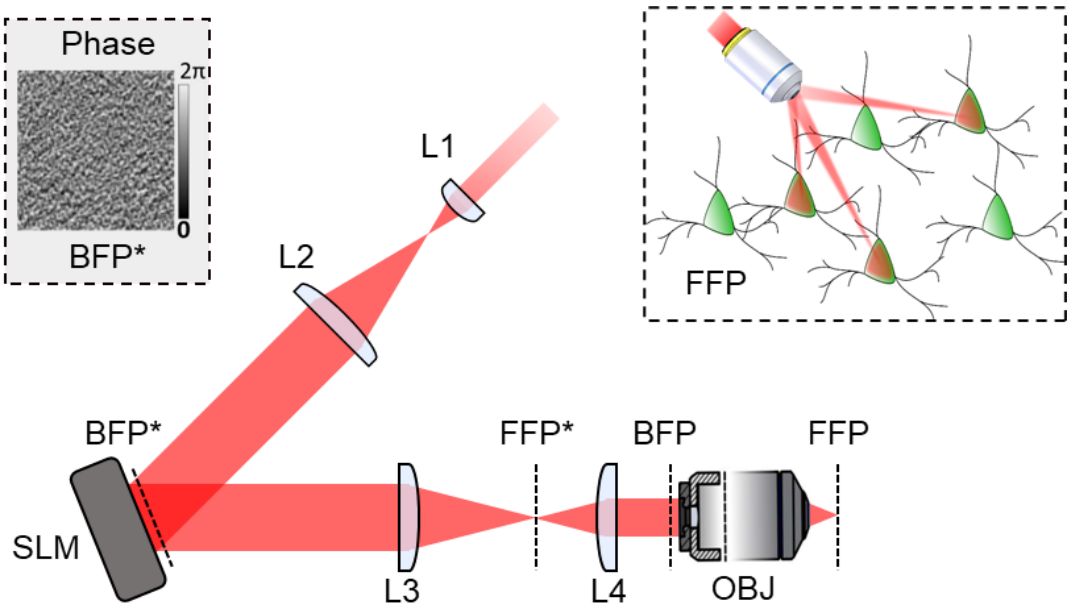

Figure 1.7 CGH setup. Principle of 2P parallel illumination of several neurons simultaneously (at the same plane). An illumination intensity pattern in FFP is here applied using a phase-only liquid crystal spatial light modulator (LC-SLM) placed in a conjugated plane (BFP) of the BFP, based on the shape and location of neurons of interest. The whole cell bodies are photoactivated at the same time, recruiting as many opsins as possible. (BFP: back focal plane; FFP: front focal plane; BFP/FFP* conjugated back/front focal plane). (Adapted from ref [28,44])*

By combining the above strategies with high-energy amplified lasers (with up to 10W output) and highly sensitive opsins, it is now possible to target hundreds of cells within mm^3-size illumination volume simultaneously. In the next paragraphs, we will discuss the possible sources of photodamage induced using 2P parallel illumination.

1.1.4. Photoinduced thermal effects in the brain

1.1.4.1. Light absorption processes

In the brain, several components are responsible for light absorption. Water is the most absorbing element, followed by blood components, while absorption by proteins (including opsins or fluorescent proteins) usually remains negligible. The absorption spectrum specific to each of these components is shown in Figure 1.8(a). To reduce thermal effects, the excitation wavelength should then clearly be chosen to minimise absorption. In living tissues, the attenuation of light as it propagates is caused by absorption and also by scattering. The "optical window" usually refers to the 600 – 1200 nm wavelength range, where this attenuation caused by both absorption and scattering is minimal.

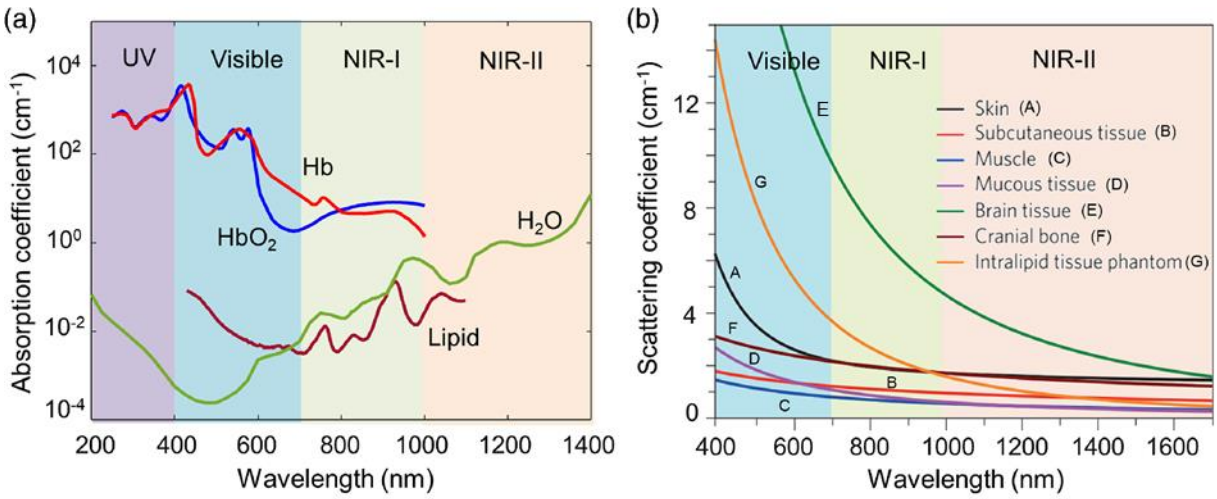

Figure 1.8 (a) Light absorption spectra of several important compounds in biological tissues. HbO2 for oxygenated and Hb for deoxygenated haemoglobin. (b) Reduced scattering coefficients of different biological tissues. Wavelengths cover the UV, visible, NIR-I and NIR-II windows (violet, blue, green and red shaded regions, respectively). (Adapted from ref [45])

Different photodamages can appear depending on the medium, and the characteristics of the illumination source, as shown in Figure 1.9. Those damages are distinguished by different pathways of absorption and dissipation. It should be clarified that the absorption process that we are discussing here is not the 1P or 2P absorption of optogenetic or fluorescent actuators, but of the biological tissue itself. For low irradiance (below 10^6 W/cm^2)[46], and long illuminations (millisecond scale), after excitation, the molecules can go back to their ground state in a non-radiative manner, transferring this absorbed energy in the form of local heating,

resulting primarily in a local temperature rise. At longer illumination times, other mechanisms can cause local chemical perturbations, as is the case for de-excitations that involve dissociation, changes in the redox state of the absorbing molecules, or transfer of energy to a dioxygen molecule to form reactive oxygen species. For higher irradiance, above the 10^6 W/cm^2 thresholds, more severe effects appear, even within a short illumination time (femtoseconds to nanoseconds). When the irradiance is high enough, the ionisation of molecules occurs as additional photons are absorbed. Released electrons can also absorb photons and collide with other molecules, generating even more free electrons. This phenomenon is known as the inverse bremsstrahlung avalanche effect[47]. This avalanche effect can lead to a low-density plasma which can cause photochemical damage. Even higher irradiances can induce mechanical damages as cells receive supersonic shock waves caused by the formation of bubbles followed by their explosion, breaking the tissue structure and killing the cell.

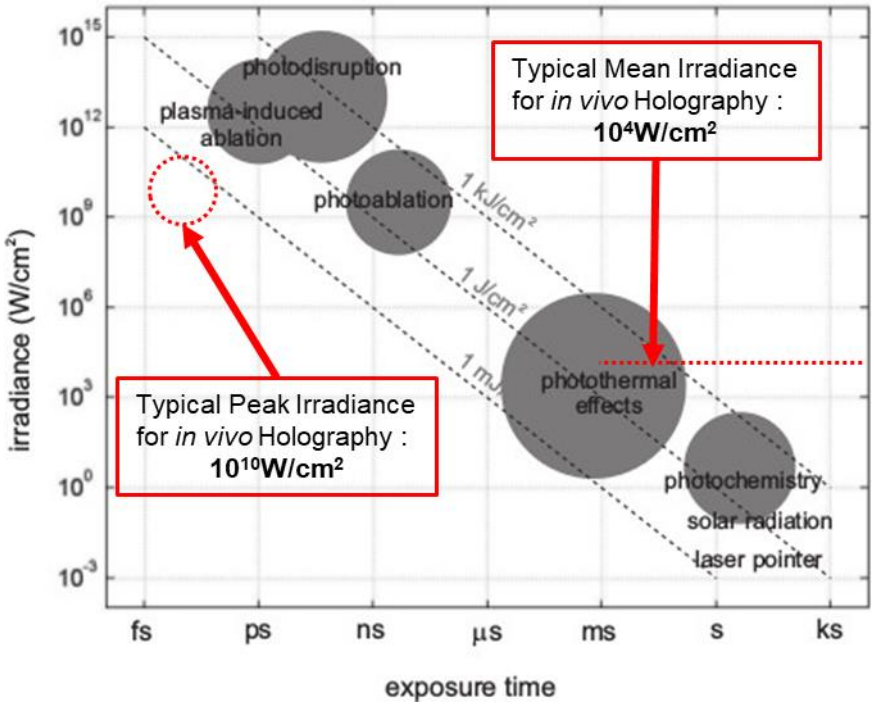

Figure 1.9 Photodamages in biological tissues depending on the irradiance and exposure time of illumination. (Adapted from ref [44,46]*)*

In a typical 2P optogenetics experiment using parallel illumination, the conditions used to elicit an AP typically involve: 3-20 ms illumination pulses with 10-40 mW mean power over around 100µm² cell surface, corresponding to a mean irradiance of ~10^4 W/cm^2. Typical laser sources provide 250 fs pulses with a 500 kHz repetition rate. Thus, the peak irradiance reaches ~10^{10} W/cm^2. As indicated in Figure 1.9, these values correspond to a range dominated by

photothermal effects and, therefore, by a linear dependence on the average power density of the laser.

1.1.4.2. Brain sensitivity to thermal perturbations

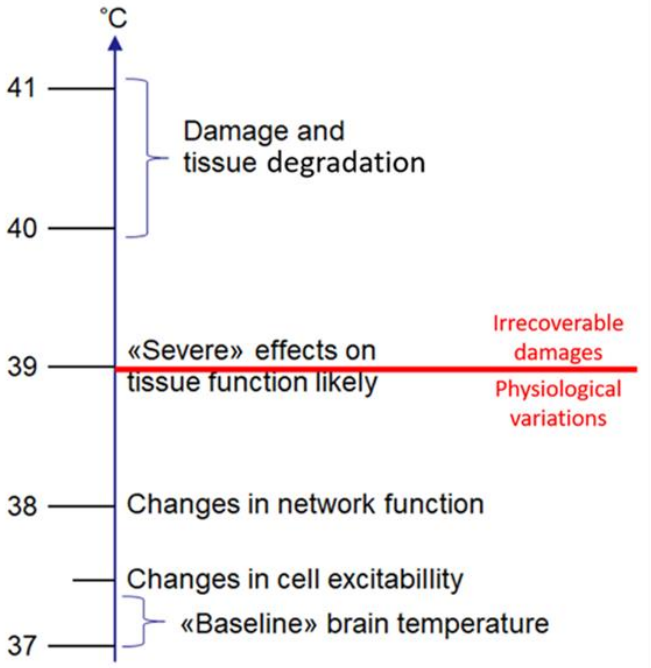

Figure 1.10 Brain tissue responses to temperature increases. (Adapted from ref [44,48])

Different levels of temperature rise in the brain could result in different kind of perturbations, as shown in Figure 1.10. Relatively small temperature rises (less than 2K) induce modulation in neuron behaviours such as the form of action potentials[49], the firing rate[50,51], and the channel conductance[52–54] or fluctuation of synaptic responses[55,56]. Higher temperature rise (3-4K) can cause severe damages such as proteins denaturation, cell structure changes and eventually cell apoptosis[57,58]. Even higher temperature rise will damage the tissue through swelling, coagulation and inflammatory responses[59,60].

These considerations lead us to conclude that the main sources of possible photodamage in 2P optogenetics experiments are damages related to local temperature rise. It highlights the importance for a theoretical model able to predict these effects, as discussed in the next paragraph.

1.2. Thermal phenomena

In this section, we introduce a model able to describe photon-induced thermal effects in the brain. Photon-induced temperature rises in tissues are the consequences of i) light absorption and conversion into heat followed by ii) heat diffusion in the surrounding media.

Using Fourier's equation for heat diffusion, we calculate the temperature distribution using a Green's function-based strategy.

1.2.1. Fourier equation of heat diffusion

The Fourier equation describes heat diffusion in a homogeneous media as[61]:

$$\frac{\partial T(\vec{r},t)}{\partial t} - D\nabla^2 T(\vec{r},t) = \frac{Q(\vec{r},t)}{\rho C} \qquad \textit{Equation 1.1}$$

Here $T(\vec{r},t)$ is the induced temperature rise due to the absorption of $Q(\vec{r},t)$, $\vec{r}$ the spatial coordinate in 3D, *t* the time, Q the absorbed power in each unit of volume [W.m^{-3}]; the medium is characterised by its thermal diffusivity D [m^{2}s^{-1}], its mass density ρ [kg.m^{-3}] and its thermal capacity C [J.kg^{-1}.K^{-1}].

In living tissue, metabolic processes can contribute as a positive (heating due to metabolic process) q_m or negative (cooling due to blood perfusion) q_p term to the temperature, in processes often described using the Pennes bio-heat equation[62]. Adding these to the Fourier equation (Equation 1.1), we have:

$$\frac{\partial T(\vec{r},t)}{\partial t} - D\nabla^2 T(\vec{r},t) = \frac{Q(\vec{r},t)}{\rho C} + \frac{q_m - q_p}{\rho C} \qquad \textit{Equation 1.2}$$

The sink term q_p can be expressed as $q_p = \rho_b C_b w_b\big((T_0 + T(\vec{r},t)) - T_b\big)$ with T_0 the initial temperature of the tissue, $T(\vec{r},t)$ the induced temperature rise, and where ρ_b, C_b, w_b and T_b respectively stand for the mass density, the thermal conductivity, the flow and the temperature of the blood. In physiological condition and while $T(\vec{r},t) = 0$, q_m and q_p are equal, maintaining the tissue temperature at a constant value. Using typical values[48,51] of ρ_b, C_b and w_b, and considering a tissue temperature rise of 1 K, the term $\frac{q_m - q_p}{\rho C}$ is estimated to be roughly[63] -9.10^{-3} K.s^{-1}. Under typical 2P photostimulation conditions, $\frac{Q(\vec{r},t)}{\rho C}$ is of the order of 2.10^{3}K.s^{-1} (for an illumination spot of 12µm diameter, 10mW illumination power inside the spot and

absorption coefficient of tissue α = 0.06 mm^{-1}, the absorbed power is $Q(\vec{r},t)$ ~ 6.10^{-6} mW/µm^3). While it could be crucial in some cases, the metabolic contribution $\frac{q_m - q_p}{\rho C}$ to local temperature changes can clearly be neglected compared to 2-photon-stimulation-induced heating, as discussed in a previously published article[63].

Thus, heat source and sink contributions from metabolic and blood perfusion are omitted in our analysis. The tissue is considered as a homogeneous medium with a fixed optical absorption coefficient (α=0.06 mm^{-1} for brain grey matter (Yaroslavsky et al. 2002)) and thermal properties (very similar to those of water). Equation 1.1 will now be solved in the case of either a transient or steady-state heat source.

1.2.2. Green's function and thermal point-spread function

To solve the Fourier Equation 1.1, we use a Green's function-based approach. Green's function is obtained for a unit source term $\delta(\vec{r} - \vec{r}_0)\delta(t - t_0)$:

$$\frac{\partial T(\vec{r},t)}{\partial t} - D\nabla^2 T(\vec{r},t) = \delta(\vec{r} - \vec{r}_0)\delta(t - t_0) \qquad \textit{Equation 1.3}$$

The solution gives the form[64]:

$$G(\vec{r},\vec{r}_0,t,t_0) = \frac{1}{(4\pi D(t - t_0))^{3/2}} exp\left(-\frac{(\vec{r} - \vec{r}_0)^2}{4D(t - t_0)}\right) \qquad \textit{Equation 1.4}$$

and the temperature $T(\vec{r},t)$ is obtained by the convolution of the Green's function and the actual spatiotemporal distributed source term $\frac{Q(\vec{r},t)}{\rho C}$:

$$T(\vec{r},t) = G(\vec{r},t) * \frac{Q(\vec{r},t)}{\rho C} \qquad \textit{Equation 1.5}$$

For a unit source term at $\vec{r}_0 = 0$ and t_0 =0:

$$T(\vec{r},t) = \frac{1}{(4\pi Dt)^{3/2}} exp\left(-\frac{r^2}{4Dt}\right) \qquad \textit{Equation 1.6}$$

We can plot it in Figure 1.11 at various multiples of an arbitrary duration τ against the normalised radial distance to the point source.

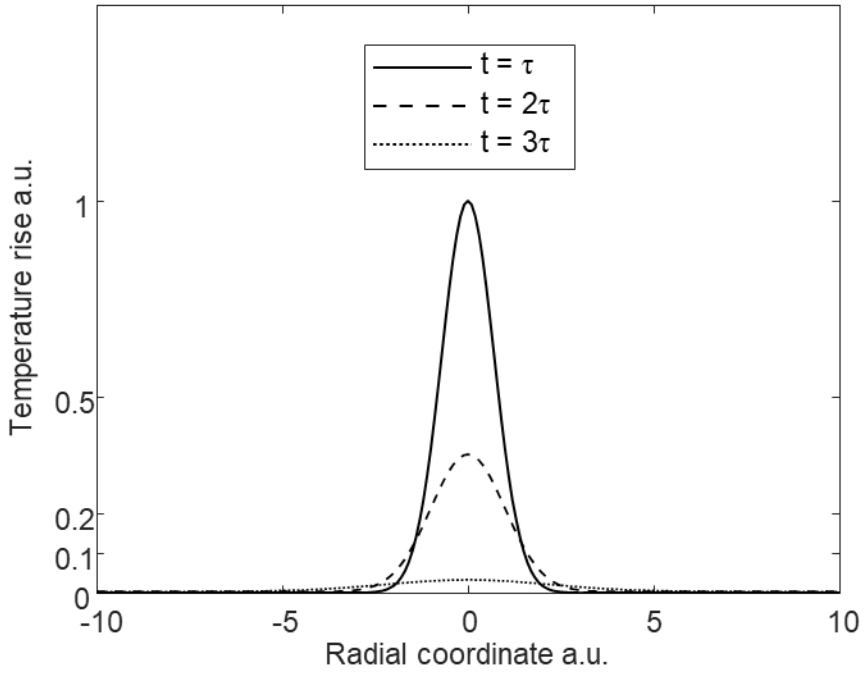

Figure 1.11 Radial distribution of the temperature response to a pulsed point-source excitation. Both coordinates are normalised in arbitrary units.

Green's function $G_T(r,t)$ for heat diffusion can therefore be written as:

$$G_T(r,t) = \frac{1}{(4\pi Dt)^{n/2}} exp\left(-\frac{r^2}{4Dt}\right) \qquad \textit{Equation 1.7}$$

where $n = 1, 2$ or 3, and $r = |x|, \sqrt{x^2+y^2}$ or $\sqrt{x^2+y^2+z^2}$ respectively for 1D, 2D or 3D heat diffusion.

In the presence of a source term $Q(\vec{r},t)$ which has a structure in both space and time, the temperature solution $T(\vec{r},t)$ to Equation 1.1 can then be obtained by a convolution over space and time of the term $\frac{Q(\vec{r},t)}{\rho C}$ with Green's function $G_T(r,t)$ as expressed in Equation 1.7. In our case, the spatial and temporal dependencies in $Q(\vec{r},t)$ can be separated, to write $Q(\vec{r},t) = \Gamma(\vec{r})\Pi(t)Q$, and the spatial distribution $\Gamma(\vec{r})$ and time dependence $\Pi(t)$ can be treated separately.

1.2.3. Step response for a point source

An interesting case is that of a point-like heat source $\Gamma(\vec{r}) = \delta(r)$ applied from t=0 onwards, e.g. a focused laser beam being turned on at t=0. In this case, $\Pi(t) = H(t)$, with H(t) the Heaviside step function, and:

$$T(r,t) = \frac{Q}{\rho C} G_T(r,t) * H(t) = \frac{Q}{\rho C} \int_0^t G_T(r,t')dt' \qquad \textit{Equation 1.8}$$

This yields:

$$T(r,t) = \frac{Q}{\rho C} \frac{erfc\left(\frac{r}{\sqrt{4Dt}}\right)}{4\pi D r} \qquad \textit{Equation 1.9}$$

where $r = \sqrt{x^2 + y^2 + z^2}$ in the 3D problem. For an arbitrary distance r_0 to the heat source, the time dependence of this temperature solution is plotted in arbitrary units in Figure 1.12. As expected, temperature rise strongly slows down and tends towards a steady-state (time independent) value:

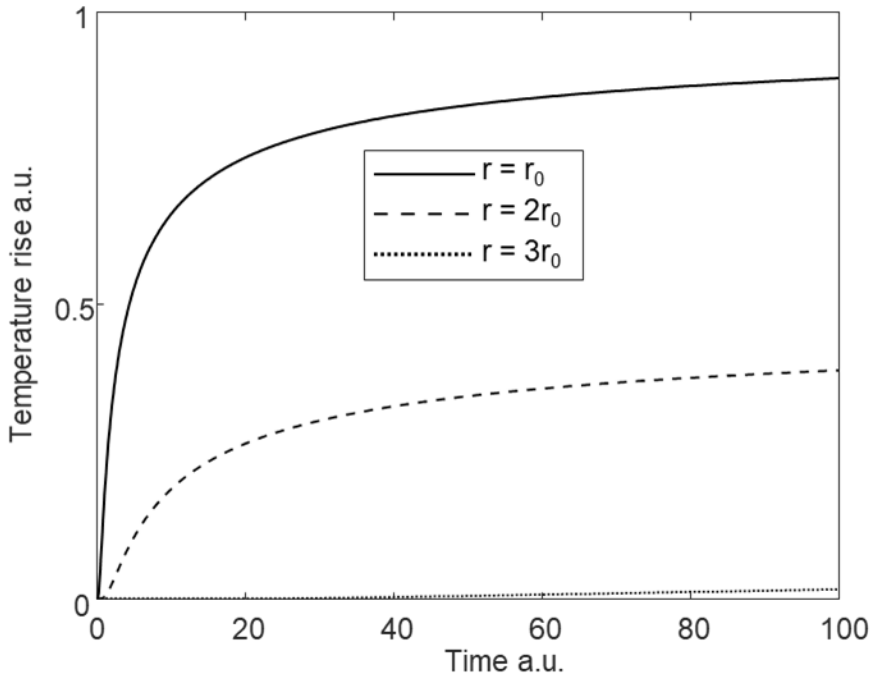

Figure 1.12 Transient temperature response to a point-like step heat source at various distances from the source

1.2.4. Steady-state, point-source response

For a continuous point source $\Gamma(\vec{r}) = \delta(r), \Pi(t) = 1$, we obtain:

$$T(r) = \frac{Q}{\rho C} \lim_{t\to\infty} \frac{erfc\left(\frac{r}{\sqrt{4Dt}}\right)}{4\pi Dr} = \frac{Q}{\rho C} \frac{1}{4\pi Dr} \qquad \textit{Equation 1.10}$$

Therefore, the radial temperature dependence at a distance r from a point source is simply, to a constant factor, a 1/r function, a familiar result in thermal sciences. For e.g. $Q = 4\pi D\rho C$, this function is plotted in Figure 1.13.

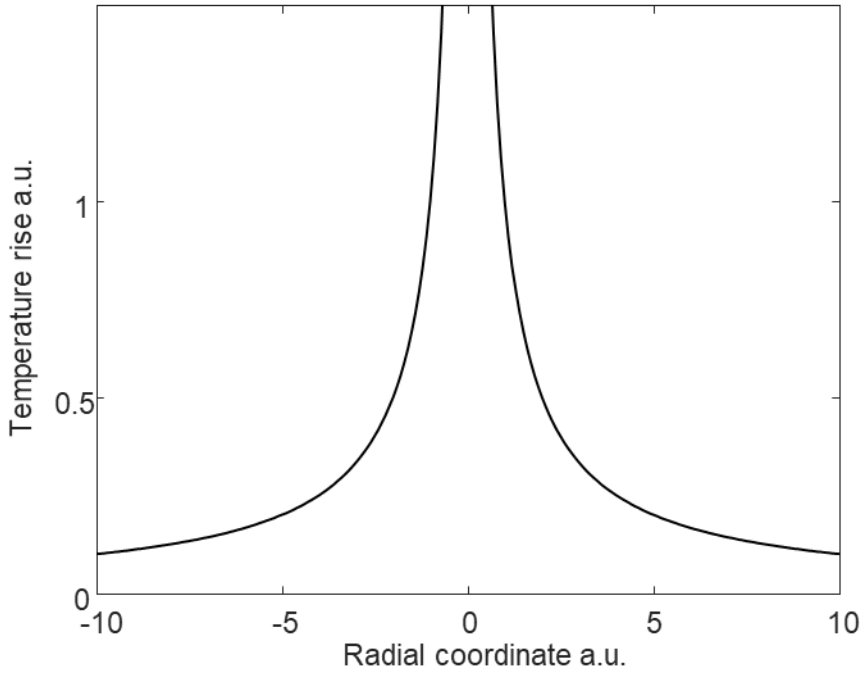

Figure 1.13 - Temperature profile around a continuous point source.

The thermal diffusivity is defined as $D = \kappa/\rho C$, where κ is the thermal conductivity ($Wm^{-1}K^{-1}$). We define here the thermal Green's function in steady-state:

$$G_T^{ST} = \frac{1}{4\pi\kappa r} \qquad \textit{Equation 1.11}$$

For a steady-state system, the temperature distribution is thus the convolution of the heat sources spatial distribution with the thermal Green's function in steady-state G_T^{ST}. This result will be used in Chapter 3 and Chapter 4.

1.3. Photo-induced thermal effects in 2P optogenetics

As described in section 1.1, 2P optogenetic photostimulation induces local thermal effects, which can now be described quantitively using the formalism introduced in Section 1.2. From the discussion of Section 1.2.2, the temperature response can be modelled as the convolution of the thermal Green's function $G_T(r,t)$ with the spatiotemporal distribution of the heat source $Q(\vec{r},t) = \Gamma(\vec{r})\Pi(t)Q$. In our case, which is weak absorption (linear coefficient: α), the heat source distribution Q is proportional to the light intensity distribution I: $Q = \alpha I$. The heat source is then defined linearly by the spatiotemporal distribution of light intensity.

For holographic illumination, the description of the light source $\Gamma(\vec{r})$ must take into account the shape and position of the holographic spots, but also the distortions induced by light propagation in the brain, which is a strongly scattering tissue. In the holographic process, a given phase profile is applied on an SLM and projected on the sample to produce constructive interference in the regions which must be illuminated, and destructive interference everywhere else. This complex phase profile is typically determined using an iterative procedure called Gerchberg-Saxton algorithm[38,65], and the projected optical field is written:

$$E_{SLM}(r,t) = A(x,y)e^{i\varphi(x,y)}$$

with A the amplitude distribution sent to the SLM and φ the phase introduced by the SLM.

In a homogeneous transparent medium, the propagation of this wave to any sample plane can be simulated using the angular spectrum method[66]. To model the scattering medium, we have used the so-called "Beam Propagation Method"[67–69]. This method consists in propagating the field through the medium in a series of finite discreet "steps" and applying a random thin phase mask at each of these steps. The statistics of this random distortion was based on optical measurements of the attenuation in acute brain slices of various thicknesses[41,70]. Using these parameters, we were able to realistically model the 3D distribution of light in the mouse brain, as shown in Figure 1.14(b). A full description of this procedure, as well as the detailed code and validation of its outcome by comparison to experiments, is shown in Annex 1 to this manuscript.

Precisely, Figure 1.14 shows the modelling of the temperature rise induced by 100 two-photon optogenetic holographic spots focused at various 3D positions inside 300µm×300µm×300µm volume. These 100 spots were chosen using a 3D image of a mouse brain and arbitrarily selecting target neurons. In Figure 1.14(c), heat diffusion in the volume of the brain is clearly visible, and collective contributions from these heat sources lead to higher

temperature rises at the centre of the volume where the 100 spots are focused, and lower temperatures near the edges of this region[63].

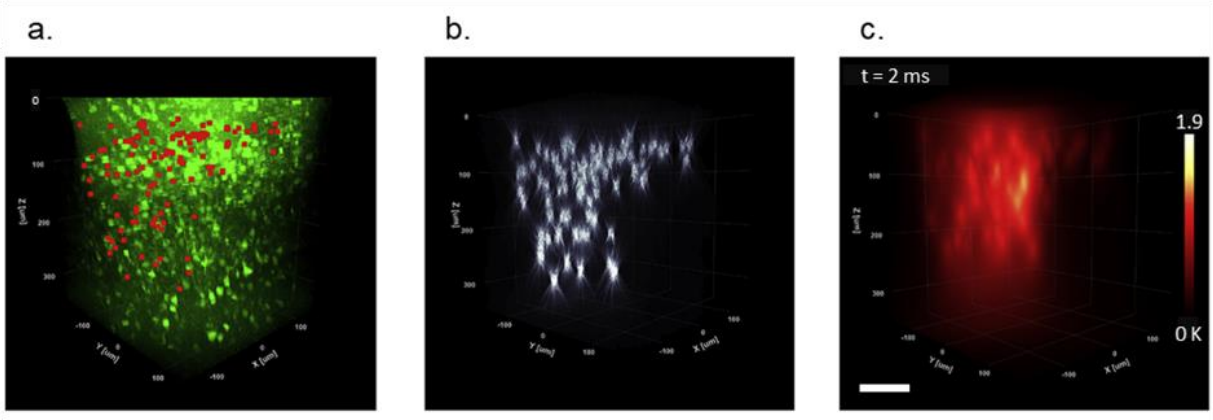

Figure 1.14 Simulated temperature rise produced by multiple holographic spots with power and duration conditions typically used for in vivo action potential stimulation in mice. (a) 3D view of an in vivo two-photon fluorescence stack of the 2/3 layer in the mouse visual cortex. The sample is labelled with GFP, and the position of 100 holographic spots is marked in red. (b) 3D spatial distribution of irradiance produced by these 100 holographic spots (each spot is 12 µm in diameter and receives 0.1mW/µm^2 at λ=1030nm). (c) 3D spatial distribution of the temperature rise produced by these holographic spots. Scale bar: 100µm. (Adapted from ref [63])

Using this model, the predicted temperature rises under the illumination conditions typically used to evoke an action potential, i.e. P = 11mW, t = 3ms, with a spot diameter of 12µm, is shown in Figure 1.15(a,b), revealing a maximum temperature rise of about 0.3 K which, as expected, varies linearly with the optical power (Figure 1.15(b)) and increases for longer pulses (Figure 1.15(c)). When trains of pulses are applied (10 pulses in (Figure 1.15(c)), the accumulation of heat, which does not entirely dissipate between one pulse and the next, is visible as an increase in the temperature baseline, the more important the longer is the illumination time.

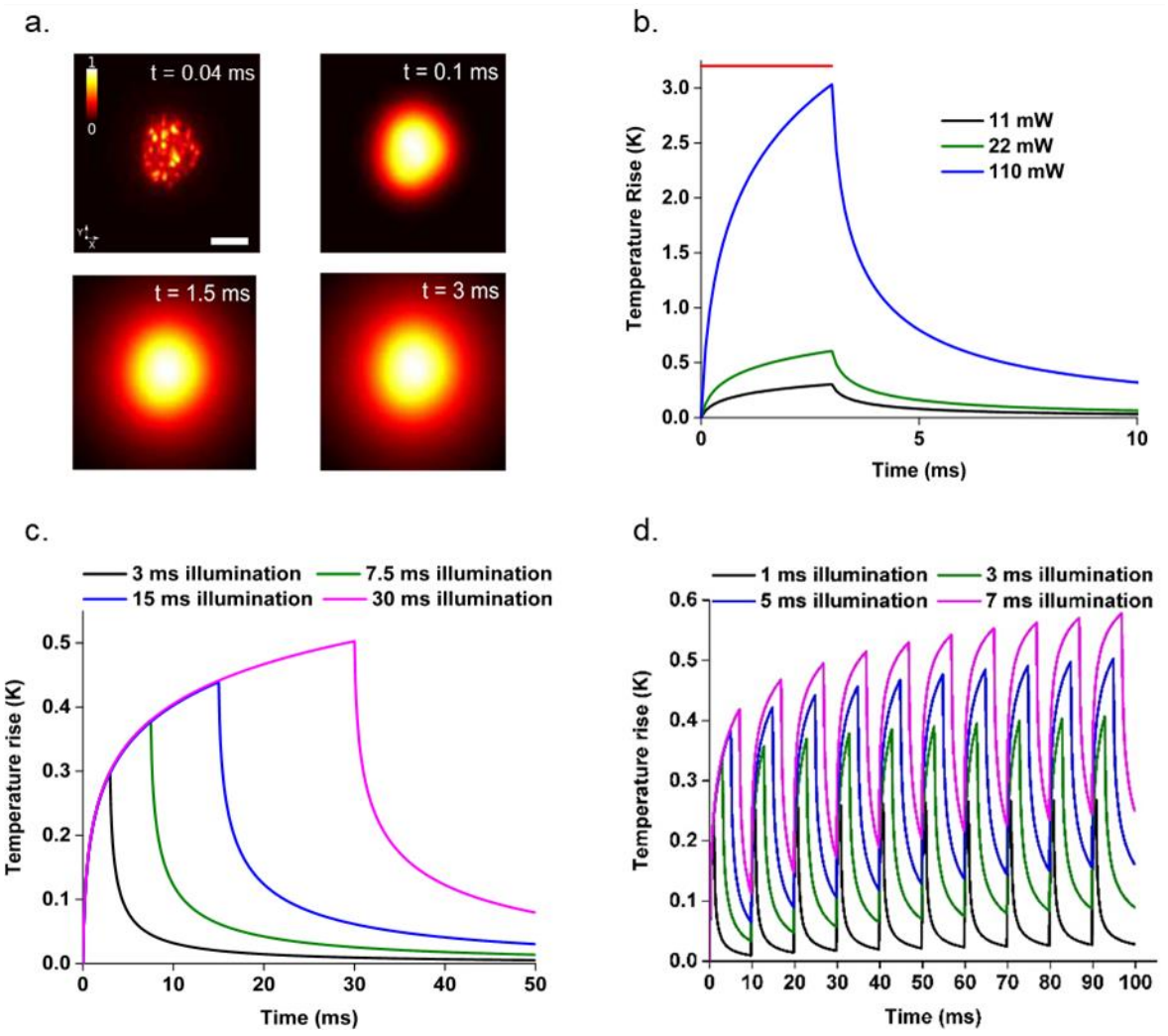

Figure 1.15 Spatial-temporal evolution of the temperature rise generated by a speckled holographic illumination pattern and holographic simulations with varying parameters. (a) 2D spatial distribution of the temperature (normalised) after 0.04ms (time step used in simulation), 0.1 ms, 1.5 ms and 3 ms of illumination. Scale bar = 10 µm. (b, c, d) Calculated temperature in the centre of the spot for a λ=1030 nm, 12 µm diameter holographic spot in vivo; (b) temperature for various optical powers and an illumination time 3 ms; (c) Temperature for variations of illumination durations, with an optical power 11 mW; (d) Same peak power 11mW and various pulse durations, and a 100 Hz repetition frequency.

1.4. Conclusion

In this chapter, we focused on the importance of the heating induced under a typical optogenetic experiment.

In order to predict the magnitude of this effect, we have described a theoretical model previously developed by the Emiliani's lab and have shown how the model enables to predict the spatial and temporal distribution of the temperature rise induced by the illumination of single or multiple targets under the illumination conditions typically used in a 2P optogenetic experiment.

In the next chapter, we will describe the experiments to validate this model *in vitro* using Er/Yb co-doped glass particles embedded in an agar gel and *in vivo* mice brain using a novel temperature endoscope (Chapter 2). Later on, in Chapter 3, we will present the development of a reconfigurable microscale temperature control technique that is adaptable to study the thermal response of cells, and show proof of principle experiments. Supported by the same thermal diffusion theory, we introduce in Chapter 4 the application of a thermal lens device applied to allow simultaneous, multiplane neuron imaging.

Chapter 2

In vivo Temperature Measurement During Two-Photon Optogenetics

Summary

2.1. Introduction

As shown in the previous chapter, the expected simulated temperature rise caused by 2P optogenetic stimulation is of the order of few Kelvins, with a millisecond rising time. To measure the temperature changes with this degree of precision, we propose to use rare-earth-doped glass particles whose photoluminescence spectrum contains two bands that are thermally coupled. We use these particles to validate the model first *in vitro* and then *in vivo.* To this end, we will present a new optical thermometry method which we will call "thermal endoscope", since it uses optical fibre, although it doesn't allow imaging. This system has sub-0.1 K temperature sensitivity, millisecond temporal resolution and single neuron (10–20 micrometres) spatial resolution and enables temperature measurement *in vivo* mice brain. In this chapter, we will first describe several classical thermometry methods and then introduce luminescence thermometry. We will focus on the application of luminescence thermometry for 2P optogenetics temperature evaluation. We will show the result for *in vitro* and in *vivo* temperature measurements under 2P optogenetics holographic spot stimulation and compare it with the simulation model.

2.2. State of the art on temperature measuring methods

There is an extensive range of techniques to measure temperature, based on diverse phenomena such as thermal expansion, thermoelectricity, temperature-dependent variation of electrical conductors' resistance, fluorescence and its spectral characteristics[71]. Depending on their degree of invasiveness, they can be divided into 3 categories:

1) *Invasive.* The measuring device is in direct contact with the sample. Techniques mainly include thermal expansion (gas, liquid, solid) devices[72–77], thermoelectric devices and thermocouples[78,79], electrical resistance devices [80], semiconductor devices[81], fibre optics probes[82,83] and capacitance thermometers[84]. Note that invasiveness can be defined as mechanical, but also thermal (i.e. measurement disrupts the temperature of the sample).
2) *Semi-invasive*. The sample of interest is treated in a way that enables remote observation using contrast agents or transducers. Techniques include thermographic phosphors (quantum dots[85,86], organics dyes[87–90], metal nanoparticles[91], Ln^{3+} based phosphors[92–95], thermoresponsive polymers[96]), thermochromic liquid crystals[97,98], heat-sensitive paints[99].
3) *Non-invasive.* The temperature of the sample is observed remotely, with or without additional stimulation of the sample. Those technologies mainly include optical related methods- infrared thermography[100–102], refractive index-based methods[103,104], absorption and emission spectroscopy[105,106], spontaneous Rayleigh and Raman scattering[107–110], Coherent anti-stokes Raman scattering[111], degenerate four-wave mixing[112] and laser-induced fluorescence thermometry[113].

All those techniques have their strengths and drawbacks, as summarised in Figure 2.1. A few of them are practical for *in vivo* temperature measurement and have the potential to fulfil the requirement of sub-0.1 K temperature accuracy, millisecond temporal resolution and tens of µm spatial resolution at the same time. Thermocouples generally have fast temporal responses and high sensitivity. They are probably one of the most commonly applied temperature measurement techniques [114], although they are invasive mechanically (usually hundreds of µm diameter) and thermally (metallic material). Infrared thermometry is another method widely used to study the photoinduced temperature rise in tissue [115], since it has the advantage of being non-invasive and entirely passive (no external stimulation needed). Thermographic fluorophore-based methods are relatively new approaches. They are performant in terms of temperature sensitivity, and many types of fluorophores are available for various

applications and temperature ranges. They have been widely applied to perform nanoscale thermometry in biological samples[116,117].

Method	Minimum temperature (°C)	Maximum temperature (°C)	Response	Transient capability	Sensitivity	Accuracy
Gas thermometer	about −269	700	Slow	No	···	A standard
Liquid-in-glass thermometer	−200	600	Slow	Yes	1 °C	±0.02–±10 °C (ind) ±0.01 °C (lab)
Bimetallic strip	−73	540	Medium	Yes	···	±1 °C
Thermocouple	−270	2300	Very fast	Yes	±10 μV/°C	±0.5–±2 °C
Suction pyrometer	−200	1900	Very fast	Yes	···	±5 °C of reading
Electrical resistance device	−260	1064	Fast	Yes	0.1 Ω/°C	The standard above 13 K
Thermistors	−100	700	Fast	Yes	10 mV/K	±0.01–±0.05 °C
Semiconductor devices	−272	300	Very fast	Yes	±1%	±0.1 °C
Fiber optic probes	−200	2000	Fast	Yes	10 mV/°C	0.5 °C
Capacitance	−272	−170	Fast	Yes	Good	Poor
Noise	−273	1500	Fast	Yes	Good	Good
Chemical sampling	5	2100	Slow	No	···	±25 K
Thermochromic liquid crystals	−40	283	Medium	Yes	±0.1 °C	±1 °C
Thermographic phosphors	−250	2000	Very fast	Yes	~0.05 °C	0.1%–5%
Heat sensitive paints	300	1300	Slow	No	···	±5 °C
Infrared thermometer	−40	2000	Very fast	Yes	~0.1 °C	±2 °C
Two color	150	2500	Very fast	Yes	1 °C/mV	±1%(±10 °C)
Line scanner	100	1300	Very fast	Yes	···	±2 °C
Schlieren	0	2000	Fast	Yes	N/A	N/A
Shadowgraph	0	2000	Fast	Yes	N/A	N/A
Interferometry	0	2000	Fast	Yes	N/A	N/A
Line reversal	727	2527	Very fast	No	Line of sight avg.	±10–15 K
Absorption spectroscopy	20	2500	Very fast	No	Line of sight avg	15%
Emission spectroscopy	20	2700	Very fast	Yes	Line of sight avg.	15%
Rayleigh scattering	20	2500	Very fast	No	0.1 mm^3 in 100 °C	1%
Raman scattering	20	2227	Very fast	No	0.1 mm^3 in 100 °C	7%
CARS	20	2000	fast		1 mm^3 in 50 °C	5%
Degenerative four wave mixing	270	2600	Very fast	Yes	1 mm^3 in 50 °C	10%
Luminescence	20	200	fast	Yes	1.5 nm in 200 °C	±5 °C
LIF	0	2700	Very fast	No	···	10%
Speckle methods	27	2100	Very fast	No	···	6%
Acoustic thermography	−269	2000	Very fast	Yes	···	4%

Figure 2.1 Guide to temperature measurement technique identification(Red rectangle: invasive, blue rectangle: semi-invasive, green: non-invasive.) (Adapted from [71])

In the following state-of-the-art section, we focus on three methods, which have received the most attention for temperature measurement in biological samples: thermocouple, infrared thermographic camera, and luminescence thermometry.

2.2.1. Classical thermometric methods for *in vivo* measurement

2.2.1.1. Thermocouple

The thermocouple is a widely used temperature sensor based on the Seebeck effect [71,118]: a temperature gradience across the conductor can build up an electrical potential (dV). It is mathematically expressed using the Seebeck coefficient of the conductor S(T):

$$dV = S(T)dT \qquad \textit{Equation 2.1}$$

In order to measure this potential, as shown in Figure 2.2, two conductors of different materials are put in contact to form a junction (at sensed temperature, T_{sense}). A temperature-dependent potential appears between point a and b if the conductors have different Seebeck coefficients (S_A and S_B). Other junctions are necessarily formed (at T_{ref}, with metal C, and T_{meter} is the temperature of the voltmeter), but their effects will be cancelled out in the calculation (Equation 2.2). While T_{ref} and the Seebeck coefficient curves $S_A(T)$ - $S_B(T)$ are often already known, one can deduce the temperature T_{sense} from the following equation:

$$V = \int_{T_{ref}}^{T_{meter}} S_C(T)dT + \int_{T_{sense}}^{T_{ref}} S_B(T)dT + \int_{T_{ref}}^{T_{sense}} S_A(T)dT + \int_{T_{meter}}^{T_{ref}} S_C(T)dT = \int_{T_{sense}}^{T_{ref}} (S_B(T) - S_A(T))dT \qquad \textit{Equation 2.2}$$

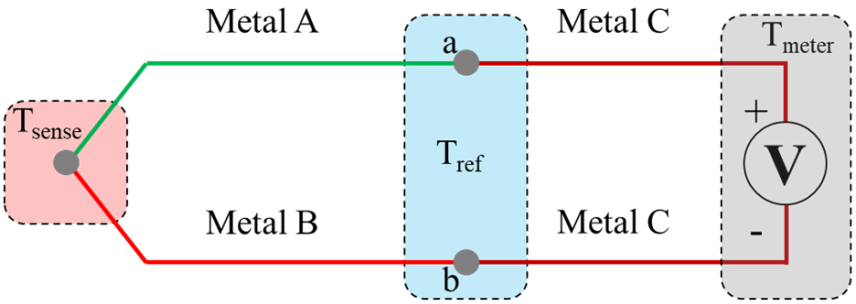

Figure 2.2 Illustration of standard thermocouple measurement configuration. The measured voltage can be used to calculate T_{sense}, given that T_{ref} is known.

This common technique has been applied in several studies to evaluate temperature rise during optogenetics experiments[114,119,120]. Figure 2.3 shows an example of using a thermocouple to measure temperature rise induced by fibre illumination in tissue, the distance between the fibre and thermocouple is around 1mm[114]. Although the proposed problems in those studies are solved, there are still a few limits and drawbacks to thermocouples:

- The size of most commercial thermocouples is too large. Needle-like thermocouples have diameters of typically hundreds of microns, making them physically invasive in the context of brain studies (e.g. typical diameter used for *in vivo* applications: 330 µm[114], 220 µm[119] and 500 µm[120]). Even for the smallest commercial thermocouple available[121], the diameter is 80µm, far from the 10 to 20 µm which are necessary to evaluate the temperature evolution caused by a ~10 µm optogenetics holographic spot in brain tissues. There are very recent publications on the fabrication of microscale thermocouples using lithography that reduced massively the size[122,123], but no *in vivo* application has been demonstrated so far.
- Due to the high thermal conductivity of most metals(or semiconductors), thermocouples are thermally invasive: by "draining" heat from the investigated region, they are strongly perturbative to the temperature measurement—for example, the J-type thermocouple consists of constantan/iron pair with thermal conductivities of 23 $W.mK^{-1}$ and 80 $W.mK^{-1}$ respectively[124], while that for water is only 0.53 $W.mK^{-1}$. Heat will therefore diffuse preferentially along the thermocouple. In the context of microscale, small and fast temperature variation, this will potentially affect the temperature measurement.

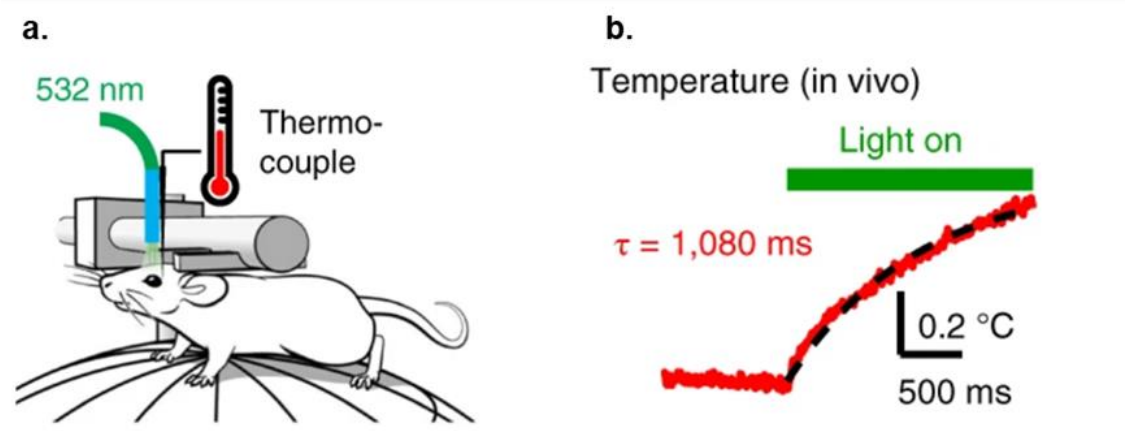

Figure 2.3 Example of temperature measurement using a thermocouple during fibre guided 1P optogenetic stimulation. (Adapted from ref [114])

2.2.1.2. Infrared thermographic camera

Infrared imaging (Figure 2.4) is a non-invasive method based on Max Planck's blackbody radiation principle. By measuring and analysing the thermal radiation of a target object, one can deduce the temperature of the object surface.

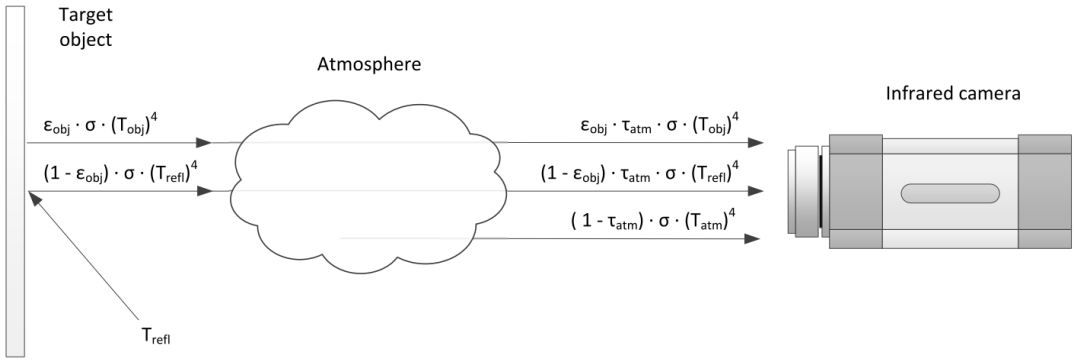

Figure 2.4 Radiation received by an infrared camera. (Adapted from ref[125])

Although a correction factor called emissivity (ε here) should be taken into account, the thermal radiation spontaneously emitted by most ordinary objects (including biological objects) can be approximated as blackbody radiation, which has a specific spectrum of wavelengths that depends on the temperature of the body, as shown in Figure 2.5. Around the temperature of living tissues (30-40 °C), the blackbody emission is essentially in the infrared, with a maximum wavelength given by Wien's law[125] (λ_{max}=b/T, with b=2898 µm.K), at λ=9.3 µm, as shown in Figure 2.5. An infrared camera sensitive to this wavelength range (usually in the 3-5 µm or 8-12 µm wavelength ranges) can detect the emitted thermal radiation to deduce temperature images using the following relation:

$$T_{obj} = \sqrt[4]{\frac{W_{tot} - (1-\varepsilon) \cdot \tau \cdot \sigma T_{refl}^4 - (1-\tau) \cdot \sigma \cdot T_{atm}^4}{\varepsilon \cdot \tau \cdot \sigma}} \qquad \textit{Equation 2.3}$$

where W_{tot} is the total radiation received by the camera, σ is the Stefan-Boltzmann constant (σ=5.67×10^{-8} W/m²·K^4). Other parameters must ideally be taken into account: ε the emissivity of the object, T_{refl} the reflected temperature, τ the transmittance of the atmosphere and T_{atm} the temperature of the atmosphere. In practice, ε and τ are often simply approximated to 1 (which is reasonable in living tissue and in the transmission bands of the atmosphere, respectively), and reflections are experimentally minimised rather than corrected.

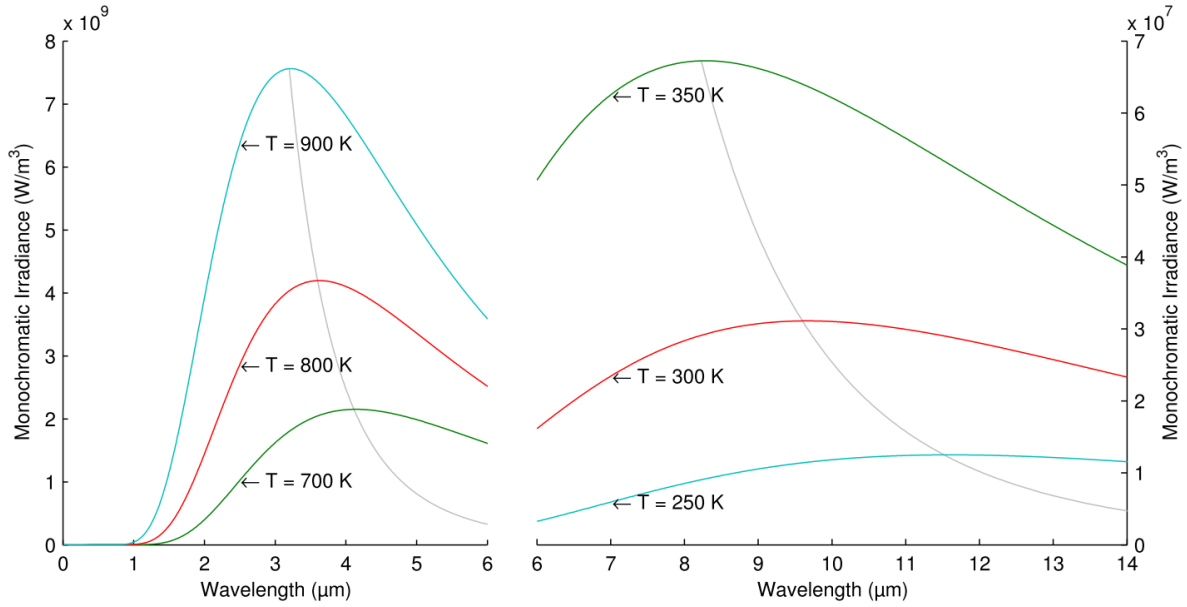

Figure 2.5 Planck's Law: electromagnetic radiation emitted by a blackbody in thermal equilibrium at a given temperature. Radiation emitted by objects with high temperature is mostly in the middle wave infrared (a), while for objects with low temperature, it is mostly the in long-wave infrared range(b). (Adapted from ref[125]*)*

However, while water vapour absorption can be minimised and neglected in the appropriate bands, liquid water is significantly absorbing in the infrared (absorption coefficient being 10^4 to 10^6 m^{-1} in this range). For this reason, the collected infrared radiation only comes from the topmost surface (typ. a few micrometres deep) and carries little information on the temperature of buried structures. Although limited to exposed surface areas, infrared thermography has been applied to studying temperature rise in optogenetic experiments[115], as shown in Figure 2.6. However, measuring temperature changes several hundreds of microns under the brain surface is clearly impossible with an infrared camera.

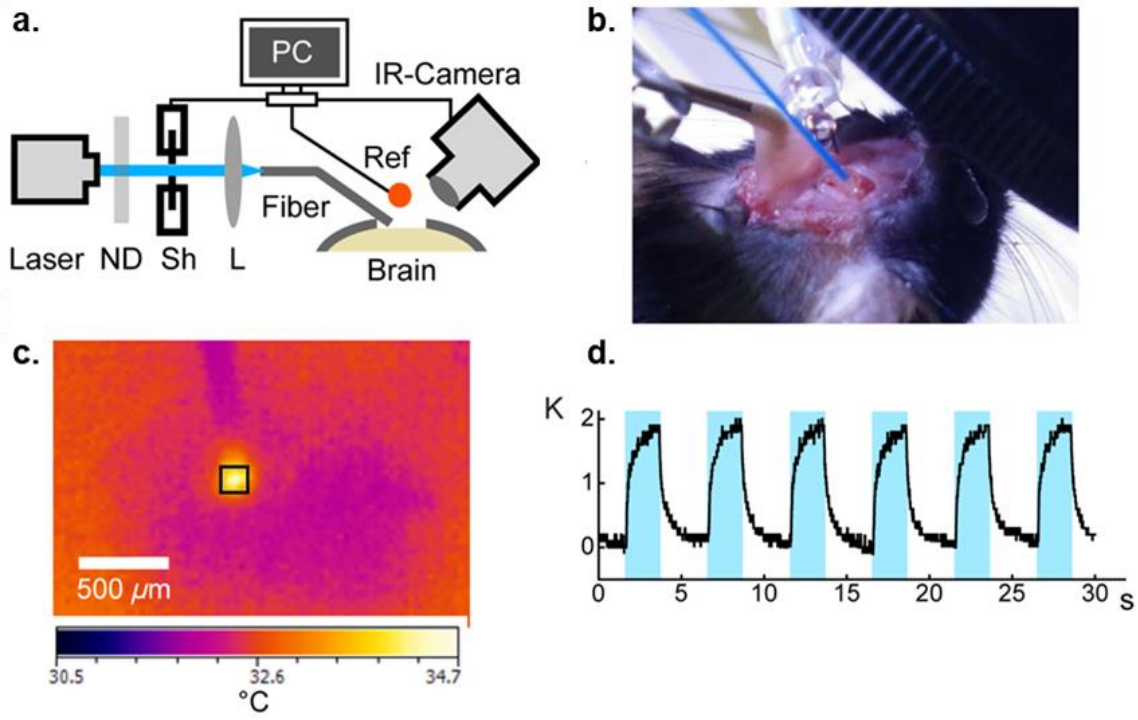

Figure 2.6 Example of using an infrared camera to measure temperature rise on the brain surface induced by fibre guided optogenetic stimulation. (a) Schematic representation of the setup. (b) Close-up view of the craniotomy; fibre is placed on top of the exposed surface of the brain, and the illuminated spot is imaged with the IR-camera; (c) Thermography image of the craniotomy during laser illumination. (d) Example of a temperature-time trace with illumination pulses. (Adapted from ref[115]*)*

2.2.2. Luminescence thermometry

2.2.2.1. General overview

Luminescence is the light emission from excited electronic states of a given atom or molecule populated by an external excitation source, which can be an electric source (electroluminescence), a chemical source (chemiluminescence), a thermal source (thermoluminescence) or a light source (photoluminescence)[126]. The properties of emitted photons are related to the properties and population of electronic states that are involved in this emission process, which depend on the local environment (local field, etc.) of the molecule and particularly on its temperature. Luminescence spectrometry can thus be used to access the temperature of the emitter environment. In the last decade, numerous thermometry methods based on photoluminescence have been proposed.

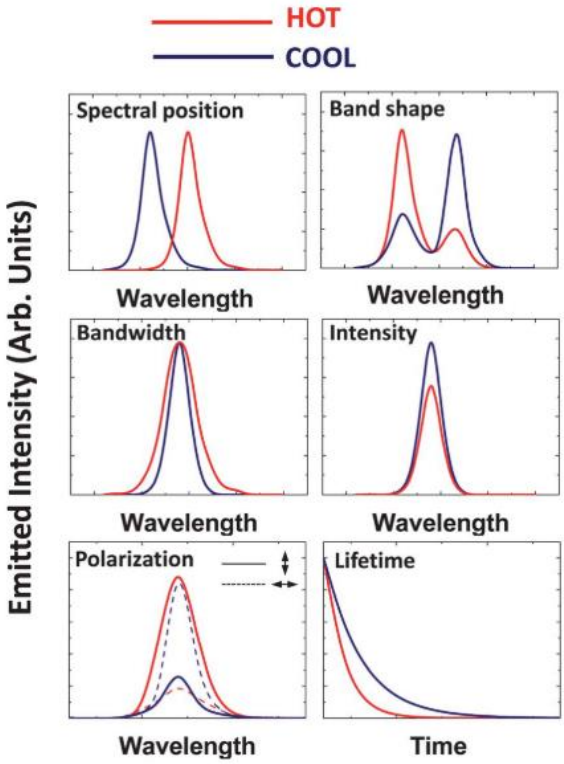

Figure 2.7 Possible effects of temperature on luminescence spectra. (Adapted from ref[126])

As schematically shown in Figure 2.7, a broad range of features of the emitted light can be affected by temperature, and luminescence thermometry methods are thus classified into the following sub-classes[126]:

- *Spectral Luminescence Thermometry* is based on the analysis of the spectral position of the emission lines, which typically changes when the energy difference between two electronic levels is affected by temperature. Based on this phenomenon, the temperature can be deduced from spectral shifts.
- *Band-Shape Luminescence Thermometry*. When the electronic states of emitting lines are close enough in energy, they can be thermally coupled. Temperature variation can then change the electron repartition and the relative intensity between those coupled spectral lines. By measuring the intensity ratio between different lines, one can then deduce the temperature.
- *Bandwidth Luminescence Thermometry*. The temperature increase induces a homogeneous line broadening. Under appropriate conditions, a measurement of this broadening can provide temperature measurements.

- *Intensity Luminescence Thermometry*. Photon emission rates change with temperature, usually through thermal activation and/ or luminescence quenching or the increase of non-radiative decay probabilities.
- *Polarization Luminescence Thermometry*. Molecules illuminated by a linearly polarised light re-emit a luminescence signal that is partially polarised along the same direction. However, the orientation of the molecular dipoles is quickly randomised through thermal agitation, and this orientation is quickly lost, so that partially polarised luminescence is emitted, with a ratio that is temperature-dependent[127].
- *Lifetime Luminescence Thermometry*. Luminescence lifetime τ is the time that emitted luminescence intensity decays to 1/e of its initial value. The variation of this lifetime with temperature can be described through the Mott-Seitz model $\tau(T) = 1/(A_R + A_{NR}(T))$, where A_R the radiative transition rate (independent of temperature) and $A_{NR}(T)$ the non-radiative transition rate described by a Boltzmann law[128] $A_{NR}(T) = A_{NR}(0).\exp(-\frac{\Delta E}{kT})$. Time-resolved luminescence measurement can thus make lifetime thermometry possible.

Among those phenomena, we chose to use *'Band-Shape Luminescence Thermometry'*, which has proved its robustness and versatility in several applications where its relative insensitivity to the excitation intensity proved an important advantage[93,129,130]. Using rare-earth-doped materials provide the additional advantages of good photon yields and robustness against photodamage. Furthermore, the method requires less sophisticated instrumentation than life-time based temperature methods.

2.2.2.2. Rare-earth doped material and upconversion

Lanthanide elements (also called rare-earth elements) have an electronic configuration that gives them interesting spectroscopic properties. As shown in Figure 2.8, rare earth elements have an incomplete electronic shell ($4f^{2\text{-}14}$) shielded from external fields by two complete shells ($5s^25p^6$). Due to this partial screening of the 4f electrons, the energy level scheme of a particular rare-earth ion remains practically unchanged from host to host. Therefore, electrons from the 4f shell can emit luminescence that is only weakly sensitive to the external host environment. For this reason, the position of the atom in the crystal structure has little influence. Among all optically active ions, lanthanides ions are distinguished for the following important characteristics[131]:

- the emission and absorption wavelengths are relatively insensitive to host material of ions;
- long lifetime of metastable states (from hundreds of μs to several ms);
- high quantum efficiency.

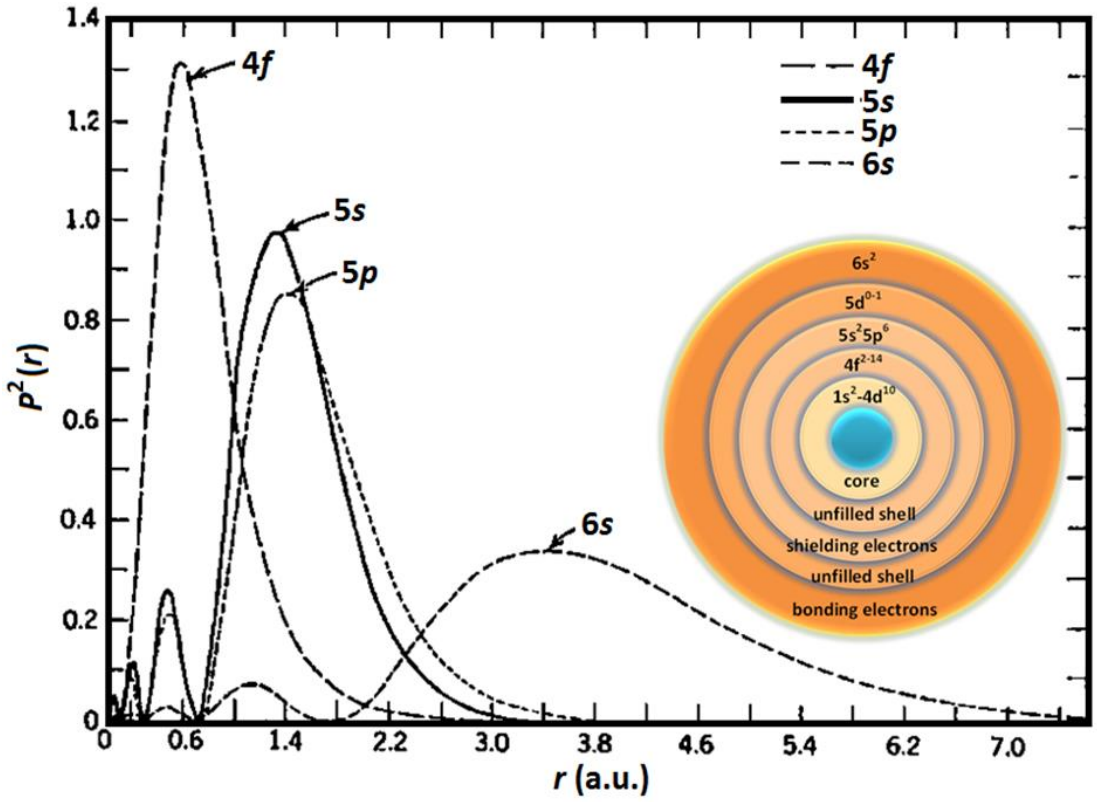

Figure 2.8 Electronic configuration of rare earth materials. (Adapted from [131]*)*

In addition to these properties, rare earth ions possess the interesting capacity to emit a luminescent photon at higher energy than the absorbed photons, which is called "upconversion". During this process, several photons are absorbed one after another to emit one luminescent photon. As opposed to two-photon absorption, in which photons must arrive quasi-simultaneously, this phenomenon relies on electronic energy states with long enough lifetimes that act as intermediaries for upconversion absorption. Thus, there is no need for high photon densities to increase the probability of simultaneous photon arrival. A classical, inexpensive infrared laser can meet the requirement, and no ultrafast laser (which is hardly compatible with optical fibres) is required.

Furthermore, a combination of different rare earth elements in the same crystalline matrix, or co-doping, can considerably increase the luminescence efficiency for the same pumping power. This relies on the difference in absorption cross-section for different dopants. In this thesis, we chose to use a co-doped Erbium/Ytterbium material. Ytterbium, which

exhibits a large absorption cross-section at wavelengths around 976 nm, is used as an efficient intermediary for excitation[132]. Excited Ytterbium then transfers its energy to Erbium by various processes, and predominantly by resonant energy transfer. This interaction will allow the transfer of energy from one system to another, as illustrated in Figure 2.9(c). Since those two elements are co-located in the co-doped host material, energy from the $^4F_{5/2}$ level of Ytterbium can be transferred to the $^4I_{11/2}$ level of Erbium. Erbium at the level $^4I_{11/2}$ can then absorb another photon and be brought efficiently to the state $^4F_{7/2}$.

Another possible mechanism consists of two successive absorption processes of 976nm photons by the same electron, bringing the Erbium ion from its ground state $^4I_{15/2}$ to state $^4I_{11/2}$ with the first absorption and then to $^4F_{7/2}$ with the second absorption.

Afterwards, non-radiative de-excitation brings the ion from the $^4F_{7/2}$ level to states $^2H_{11/2}$, $^4S_{3/2}$ and $^4F_{9/2}$, from which ions can deexcite to the ground state and emit photons at 525 nm, 550 nm and 660 nm.

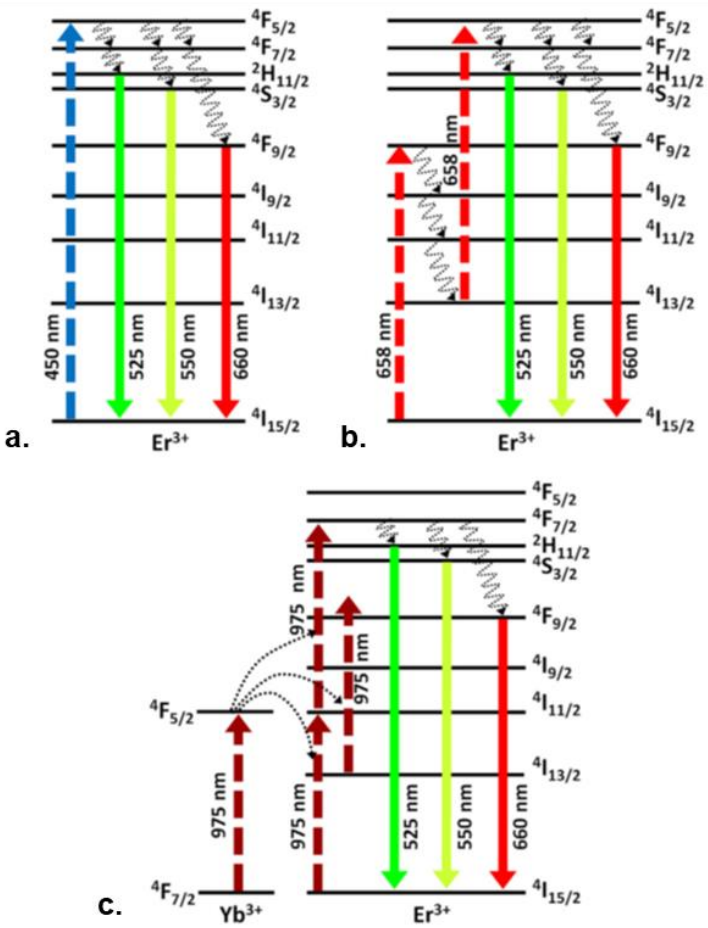

Figure 2.9 Energy band diagram and optical transitions of Er^{3+} ions for different excitation wavelengths; (a) λ_{exc} = 450nm; (b) λ_{exc} = 685 nm; and (c) λ_{exc} = 975 nm, with Ytterbium used as excitation intermediary. (Adapted from ref [93])

2.2.2.3. Principle of luminescence thermometry

In Erbium, as can be seen in Figure 2.9, the $^2H_{11/2}$ and $^4S_{3/2}$ states are energetically very close to each other. As the energy difference of these two states is weak (~800cm^{-1})[133], the population distribution of the two states can be described by the Maxwell-Boltzmann statistics. They are in thermal equilibrium, and the luminescence intensities from the two excited states (λ = 525 nm and λ = 550 nm) respect the following relation[130]:

$$\frac{I_{525}}{I_{550}} \propto \exp\left(\frac{-\Delta E}{kT}\right) \qquad \textit{Equation 2.4}$$

where I_{525} and I_{550} are the integrated luminescence intensities at 525 nm and 550 nm, ΔE is the energy gap between the $^2H_{11/2}$ and $^4S_{3/2}$ states, k the Boltzmann constant, and T the temperature (in Kelvins) of the emitting ions. This expression can be rewritten as $\frac{I_{525}}{I_{550}} = \mathrm{A}.\exp\left(-\frac{B}{T}\right)$, where A and B are constants. If A and B are known, the measurement of the luminescence intensities I_{525} and I_{550} provides a measurement of the temperature of the Erbium ions.

Er-Yb Co-doped crystals or glasses are therefore excellent thermometers, in which Yb is used as an intermediary for efficient excitation and, after energy transfer, the luminescence of Er is used as a sensitive and quantitative temperature reporter.

These ions have been used in various matrices over the last decade. In particular, the first reported use of NaYF4:Er^{3+},Yb^{3+} nanoparticles as thermal nanoprobes in liquids and cells by measuring the spectrum of the temperature-sensitive green luminescence emission was in 2010 (ref[133]).

2.3. Rare-earth particle-based thermometry on model sample

In this section, our goal is to assess the potential of luminescence thermometry (based on Er/Yb co-doped glass particle) for measuring the temperature rise induced by a transient holographic spot that mimics an optogenetic stimulation. In this first step, we carried out the validation of the luminescent-based thermometer in a model system instead of real biological conditions, in which the Er/Yb Co-doped glass particle is at a fixed position, in a transparent medium with known thermal properties, as described in Figure 2.10. In addition to validating the principle and performances of the thermometric concept, this simple setting is particularly adapted to numerical modelling of the temperature field since the optical and thermal properties of the medium surrounding the particle are homogeneous and isotropic. Er/Yb co-doped glass particles (50% GeO2 – 40% PbO – 10% PbF2 – 1%ErF3 – 1%YbF3) have been synthesised at Chimie ParisTech, in the laboratory of Michel Mortier and Patrick Gredin. In the following, we will refer to Er/Yb co-doped glass particle as "Er/Yb particles" for the sake of simplicity.

2.3.1. Description of the setup

As a transparent medium, we used the **water/agar gel** (mass fraction of agar: 0.5%). Since the agar concentration is very low, the optical scattering is negligible, the refractive index is almost the same as water[134], and the thermal properties are similar to those of water (at 20°C, thermal conductivity for 0.5% mass fraction of agar being 0.588 $W \cdot m^{-1} \cdot K^{-1}$, and for water being 0.601 $W \cdot m^{-1} \cdot K^{-1}$)[135]. The gel is rigid enough to avoid any convection, sedimentation or Brownian motion, so that a ~10-µm-diameter **Er/Yb particle** can be kept in the middle of the medium, as shown in Figure 2.11(b). We chose the probe size to obtain sufficient temperature sensitivity and short integration times (4ms); therefore, we measured the temperature rise averaged on a size comparable to the cell soma. The whole sample is surrounded laterally by two layers of silicone rubber isolator (0.5 mm deep each, Invitrogen P24743) and sandwiched between two coverslips (No. 1, 140 µm thickness).

First, to calibrate the temperature probe, we use a **PID-controlled electrical foil heater** integrated with a thermistor (Thorlabs, HT10K) to maintain the global temperature in the agar-gel chamber, as shown in Figure 2.11(c). It applies a constant (or slowly varying) temperature to the entire sample. A thin **thermocouple** (Omega, HYP0-33-1-T-G-60-SMP-M), implemented in the sample close to the probe, is used to precisely measure the reference temperature induced by electrical heating.

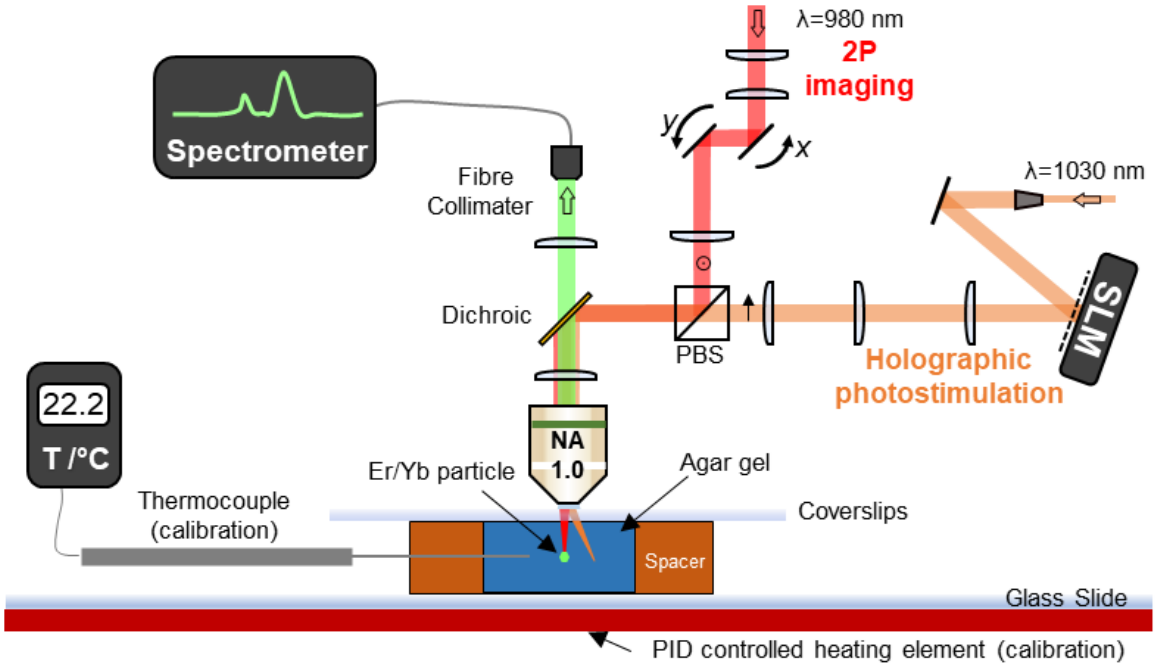

Figure 2.10 Illustration of the experimental setup for temperature measurement on a model sample using Er/Yb particle. 2P scanning imaging path (red) is used to localise and continuously illuminate the Er/Yb particle (green); the fibre collimator collects luminescence light (green path). The holographic photostimulation (orange path) generates a heat-inducing spot of 15-µm-diameter beside the Er/Yb probe. The wide-field imaging path is not shown here. The thermocouple and PID controlled heating element are for calibration purpose.

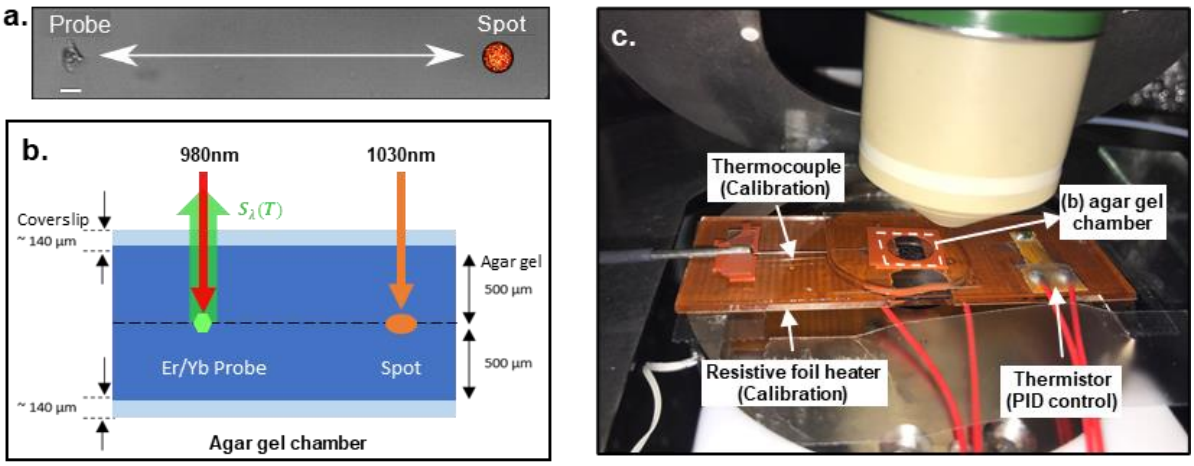

Figure 2.11 Closer view of the sample. (a) Widefield image (xy-plane) of the Er/Yb particle near the holographic spot (illustrative). Scale bar:10µm. (b) Cartoon in xz-plane of the probe and the holographic spot. (c) The agar gel chamber and the calibration setups (thermocouple, resistive foil heater, thermistor).

Secondly, we measure the temperature rise due to the holographic photostimulation spot, using the calibrated Er/Yb probe. The measurements were performed on a system built around a commercial upright microscope (Zeiss, Axio Examiner Z1) coupled with two pulsed infrared excitation paths through a polarizing beamsplitter (PBS), shown in Figure 2.10.

A 1030 nm laser (GOJI, Amplitude Systemes, operated at a repetition rate of 10 MHZ and laser pulse width of ~250 fs) was used to **create a heat-inducing holographic spot** at specific positions near the probe. The laser beam was triggered by an acousto-optic modulator (MQ40-A2, AA Optoelectronic) and expanded to illuminate the screen of the spatial light modulator (LCOS-SLM X10468-07 Hamamatsu Photonics). The SLM plane was then projected by two telescopes (equivalent magnification of 0.5) on the back aperture of a 20x-1.0 NA water immersion Zeiss objective. To maximize output power, the back aperture was underfilled, resulting in the generation of a holographic beam of ~0.5 effective NA. The SLM was addressed with phase profile calculated via Gerchberg-Saxton based algorithm, in order to generate a 15 mm diameter holographic circular spot over different positions of the sample. The zero and higher diffraction orders (>1) were blocked before entering the microscope. The position-dependent diffraction efficiency of the SLM[136] was compensated by adjusting the total laser power for each lateral displacement (Figure 2.13(d)) of the spot. The power (P=500mW) and the shape of the heat-inducing spot (15-µm-diameter) were kept identical at each position.

The same objective was used to excite the Er/Yb particle with **a 980 nm laser** (Mai Tai-Deep See, Spectra Physics, repetition rate 80 MHz, pulse width around 100 fs). The laser beam, modulated by a Pockel cell (350-80, Conoptics), entered a commercial 2P scanning head (VIVO 2-PHOTON, 3i-Intelligent Imaging Innovations) and was focused on the Er/Yb probe by adjusting the position of two galvanometric mirrors. It **illuminated the Er/Yb particle** with a constant average intensity, delivering a constant optical excitation. The absorption of this laser by the medium or the particle generates some spurious heating, but since this heating is continuous, the temperature reaches a new equilibrium T_0 after few seconds. This is not detrimental to measure additive transient temperature changes induced by the optogenetic pulse laser.

During the temperature measurement, luminescence light was collected from the top of the sample through the same objective. It was then collected by the confocal entrance of **a fibre spectrometer** (Avantes, AvaSpec-ULS2048L-EVO). Acquisitions are taken every 4 ms, with an integration time of 2 ms. The position of the glass probe was identified through DIC imaging on a CMOS camera (Thorlabs DCC 1545M) (not shown).

2.3.2. Calibration of the system

From Equation 2.4, the relation between the luminescence spectrum and temperature can be written as:

$$\frac{1}{T} = -\frac{1}{B}.\ln\left(\frac{1}{A}\frac{I_{525}}{I_{550}}\right) \qquad \textit{Equation 2.5}$$

Here, the coefficients A and B strongly depend on the nature of the Er/Yb particle and its doping, but also on its local environment. They need to be determined by calibration whenever one of these parameters changes, but can be considered constant otherwise. Once A and B are known, the absolute temperature can be deduced quantitatively from measurements of I_{525}/I_{550}.

To achieve this calibration, the sample (agar gel chamber) is heated on the PID-controlled heating element (as shown in Figure 2.10 and Figure 2.11(c)). The probe is illuminated constantly, and its luminescence spectrum is measured to derive I_{525}/I_{550} (the integration range for I_{525} and I_{550} are respectively *Band 1*: 510.3 - 529.1 nm and *Band 2*: 535.0 – 575.9 nm, shown in (a)) for various temperature values *T*, as measured by the thermocouple. These measurements were achieved at thermal equilibrium, between 296.6 K and 309.8 K, and repeated five times to increase the reliability of the calibration. A linear fit on $ln(I_{525}/I_{550})$ as a function of *1/T*, shown in (b), yields A = 4.67 and B = 1195.9K with good precision (coefficient of determination R^2= 0.9362).

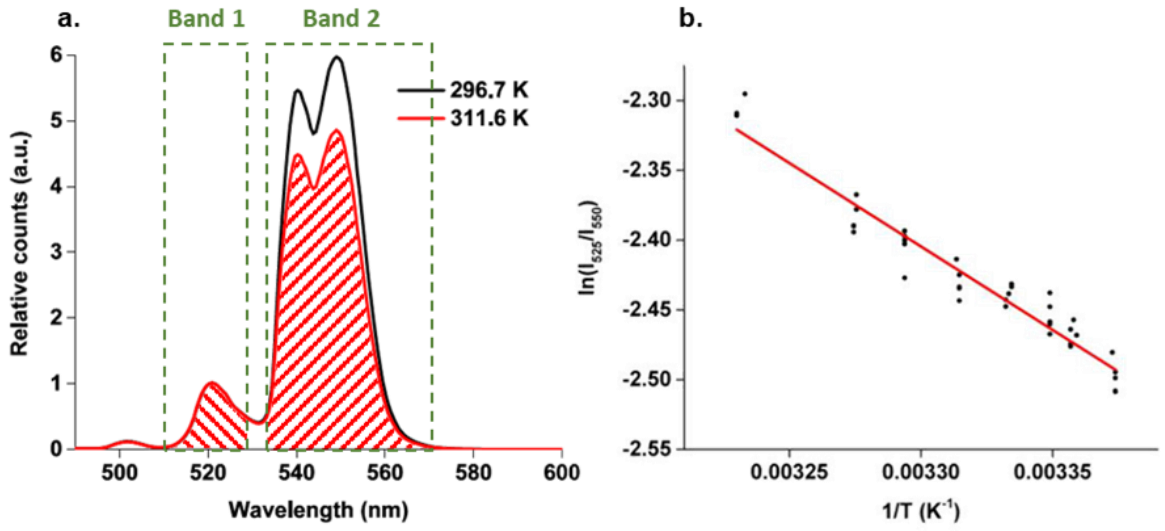

Figure 2.12 (a) Change of luminescence spectrum shape caused by temperature rise and (b) calibration of luminescence thermo-spectroscopy

2.3.3. Experimental results in agar and comparison with numerical simulations

Using the calibrated Er/Yb probe and the holographic photostimulation system (Figure 2.10 and Figure 2.11(b)), we measure the temperature rise induced by a 15-µm-diameter holographic spot (λ=1030nm, P=500mW). In Figure 2.13(a), a single 500 ms laser stimulation pulse with an average power of 500mW (after objective) was applied to the agar-based sample, focused on the holographic spot located 30 µm away from the probe, both at a depth of 150 µm inside the agar gel. The temperature was deduced from the emission band ratio using Equation 2.5 and the calibration coefficients (A and B) given above. Figure 2.13(b,c) show temperature rises induced by two trains of pulses with 50ms-pulse duration and repetition rate of 2Hz and 10 Hz, respectively, using the same peak power and laser-probe distance (30 µm). In Figure 2.13(d), to validate the ability to measure spatial heat distribution, we took the peak temperature rise values at different distances by laterally moving the spot away from the probe; illumination conditions were the same as in Figure 2.13(a).

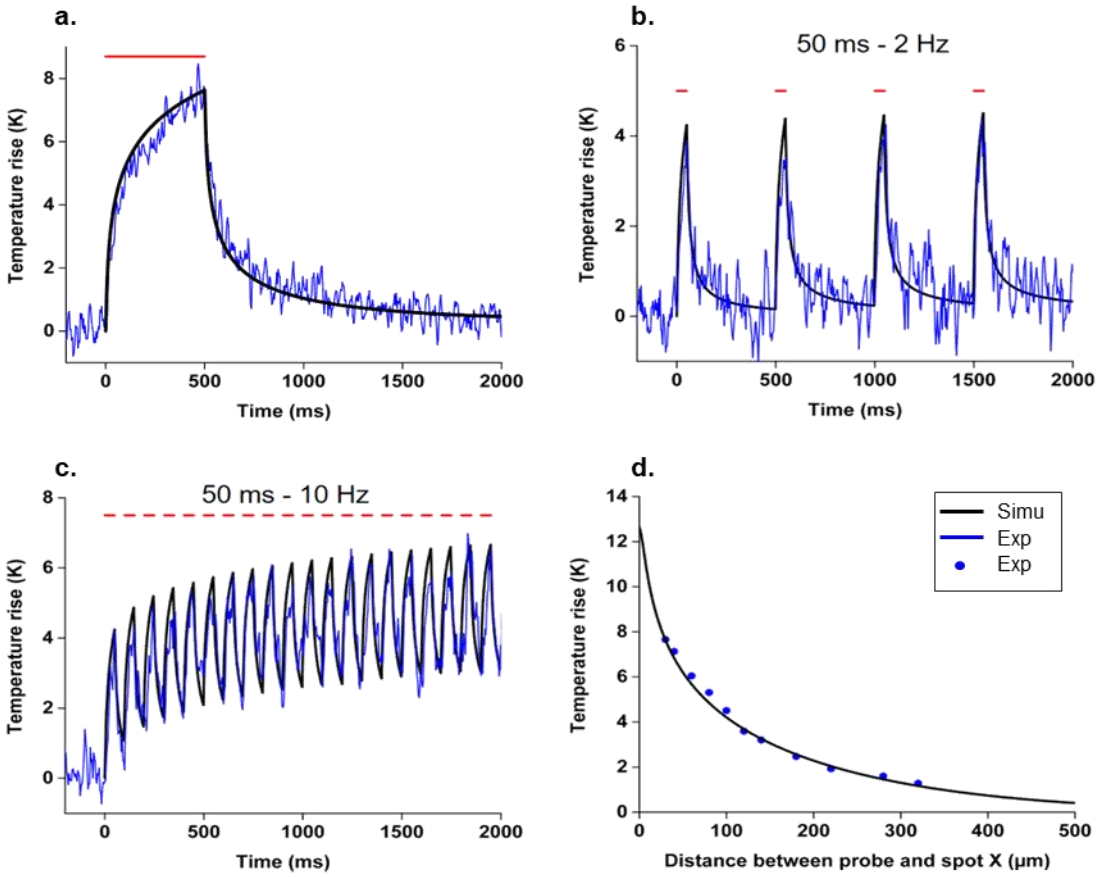

Figure 2.13 Temperature rise induced by a 15-mm-diameter holographic spot (experimental results and simulation). a-c): Time-traces for different pulse durations (a: 500ms, b, c: 50ms) and repetition frequencies (a: single spot, b: 2Hz, c: 10Hz). d): Peak temperature rises as a

function of the distance X between the Er/Yb particle and the holographic spot using the same illumination conditions as in (a). (The red lines represent the excitation pulses; blue trace and point: measurement; black trace: simulation.)

These experimental results were used to validate the model described in Section 1.2 and 1.3 (also in ref[63]). Here, the absorption coefficient[137] ($\alpha = 0.06 mm^{-1}$) and thermal properties of the agar gel were assumed to have the same values as those of water [138,139]. As can be seen in Figure 2.13, our experimental results all fit perfectly with the prediction using no free parameters.

These results show that the use of Er/Yb co-doped particles enables minimally invasive optical temperature measurement with micrometre spatial resolution and millisecond temporal resolution, and also enables to validate the theoretical model previously described. However, in these experiments, to increase the signal to noise ratio, we used much higher power and longer pulse durations than the ones used in typical conditions of *in vivo* 2P optogenetics experiments; and we used a phantom sample whose optical properties might differ from the one of a living mouse brain. As a next step, we then developed an experimental strategy to measure the temperature rise induced at the exact same conditions used for *in vivo* 2P optogenetics.

2.3.4. Limit of the methods for *in vivo* measurement

Using the previously introduced setup to measure the temperature rise under *in vivo* conditions requires focusing the excitation light (to pump the probe) and collecting the evoked luminescence for spectral analysis using an Er/Yb particle placed deep in a living (scattering) brain, and finding the exact position of the probe with respect to the optogenetic excitation spot. Moreover, as the tissue moves during *in vivo* experiments, one has to find a strategy to maintain both the probe and its illumination stable during the experiment. To solve all these challenges, we designed a thermometer endoscope where we fixed the probe at the extremity of an optical fibre and used the fibre both to transmit the excitation and to collect the luminescence, ensuring mechanical and optical stability. Optical glass fibres can be thin enough (up to 125µm diameter) to be compatible with *in vivo* use, and glass has a thermal conductivity ($1\ W.m^{-1}K^{-1}$) which is much closer to that of water ($0.6\ W.m^{-1}.K^{-1}$) than metals (typically 200 to 400 $W.m^{-1}.K^{-1}$). This will ensure minimal thermal invasiveness, i.e., opposite to the case of a thermocouple, glass fibres will not drain heat out of the investigated region.

In the next section, we will describe the system in detail.

2.4. Development of a fibred probe for *in vivo* thermometry

The thermometer endoscope is shown in Figure 2.14. We fix the Er/Yb glass probe at the end of an optical fibre and use the fibre as guidance to illuminate the probe and collect its emission signal.

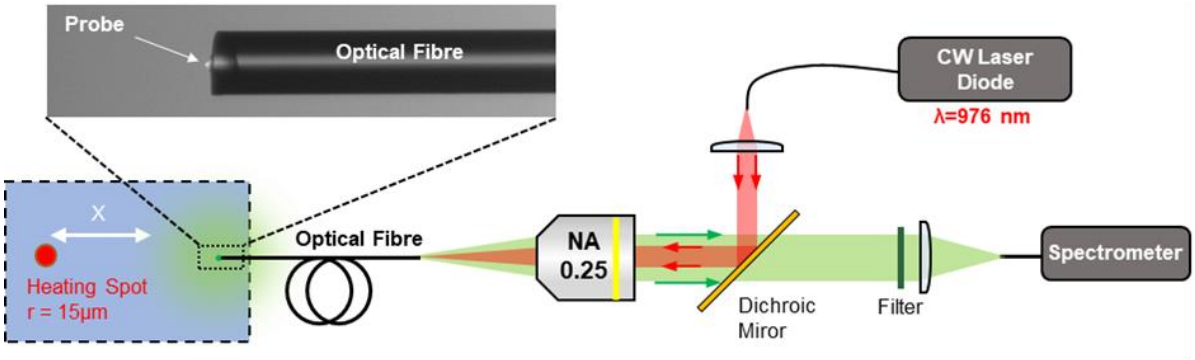

Figure 2.14 Illustration of the fibred luminescence thermometer endoscope. Inset: photograph of the extremity of the fibred probe.

2.4.1. Double-clad optical fibre

Optical fibres are optical waveguides allowing light to propagate over long distances. They are normally classified into two families: multi-mode fibres and single-mode fibres. In multi-mode fibres, light propagates in many different spatial modes, while in single-mode fibre, only one propagating mode is possible. The distribution of energy is thus dimensionally more confined in single-mode fibres than in multi-mode fibres. The light-guiding core shown in Figure 2.15 is much smaller for single-mode fibres than for multi-mode fibres, and light coupling in single-mode fibres requires more stringent coupling conditions. Optical fibres are also characterised by their numerical aperture (NA) value, which determines the angle of the acceptance cone (θ_0), and is given by the refractive indices in the medium (n_0), core (n_{core}) and cladding ($n_{cladding}$) of the fibre: $sin\theta_0 = NA = \frac{1}{n_0}\sqrt{n_{core}^2 - n_{cladding}^2}$.

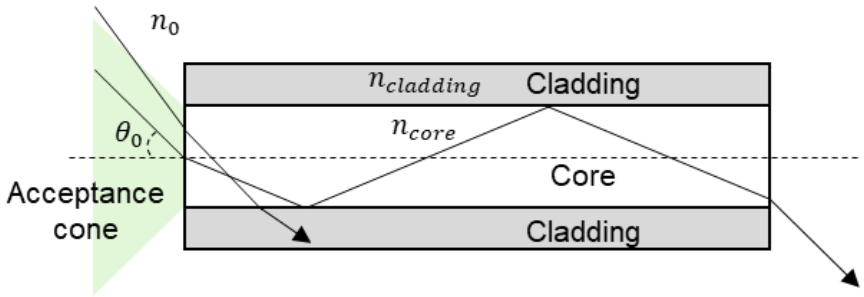

Figure 2.15 Principle of light propagation in optical fibres

Besides these two classical families of fibres, there is another, less common type: double-clad fibres. As shown in Figure 2.16, double-clad fibres have two concentric cores with different refractive indices surrounding the fibre core. In the central fibre, single-mode light can propagate, while multi-mode propagation occurs in the 1st cladding. Each of the two fibres has a different refractive index, and therefore different NA value. A second cladding ensures light confinement, as in classical single fibres. Finally, the whole fibre is often coated with Acrylate, which has no optical role but mechanically protects it.

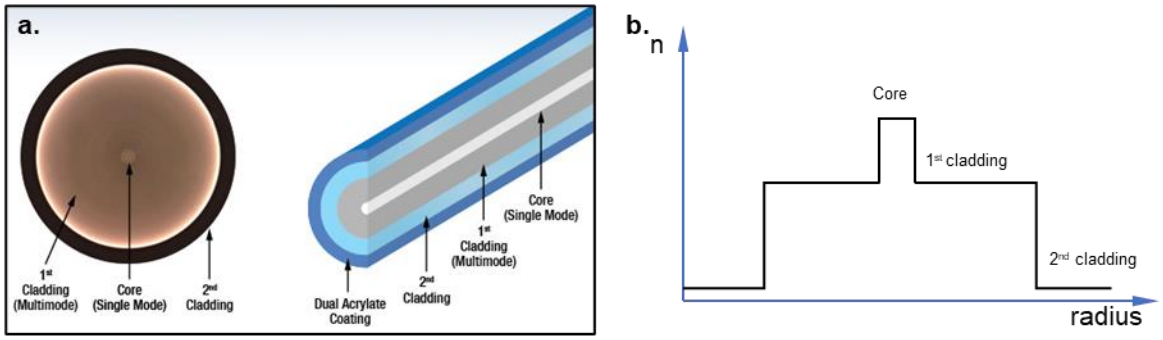

Figure 2.16 (a) Double-clad fibre structure and (b) refractive index profile. (Adapted from ref [140]*)*

2.4.2. The conception of the system

We chose to use the double-clad fibre as a waveguide to both send excitation light to the probe (through the central core), and to collect luminescence light (through the 1st cladding). To maximise photon yield, the probe (with a typical diameter of 10~20 µm) needs to be illuminated as efficiently as possible. The luminescence light should also be collected efficiently. Double-clad fibres are good candidates to fulfil these conditions. The central single-mode core(core diameter = 9.0 µm) ensures optimal spatial confinement of the excitation light on the probe. However, due to its low NA (NA = 0.12), it is relatively inefficient to collect light

emitted in all directions of space by the luminescent probe. The multi-mode fibre corresponding to the 1st cladding has a higher NA and collection angle (NA = 0.2) and a larger collection surface (diameter = 105.0 ± 5.0 µm), and is, therefore, more efficient for luminescence light collection. After propagation in the direction opposite to that of the excitation, this luminescence light is separated from the illumination light path using a dichroic mirror and coupled to a fibred spectrometer for spectrum analysis.

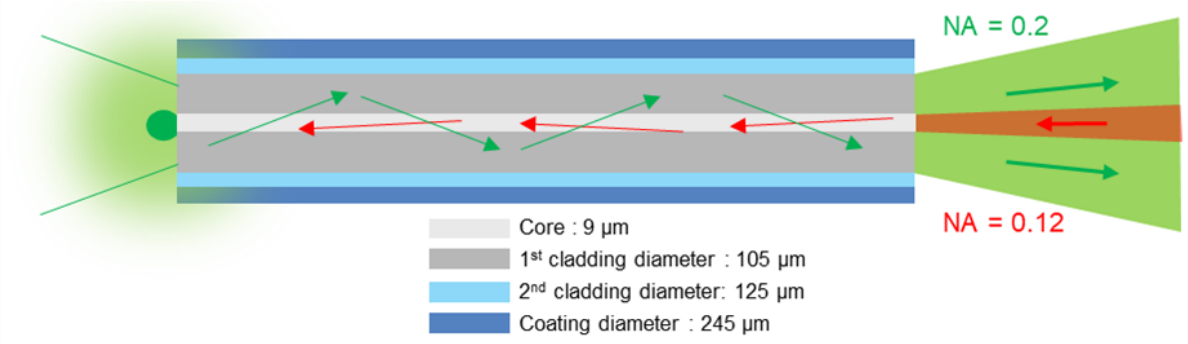

Figure 2.17 Optical path of stimulation and luminescence light in the double-clad optical fibre

2.4.3. Fabrication of the endoscope

The main difficulty in fabricating the endoscope is to attach a luminescent probe properly onto the end of the optical fibre, well superposed with the fibre core. As the probe is around 20 µm (which corresponds to the size of a single neuron), twice the size of the fibre core, the precision needs to be around 10 µm. In order to achieve this, the cleaved fibre is fixed onto an XYZ micro stage on top of a microscope glass slide. Another microscope, perpendicular to the fibre axis, is used to observe along the horizontal direction. The complete process which we optimised is as follows (shown in Figure 2.18):

Step 1 - Move along the z-direction to dip the fibre in a small droplet of UV-curable glue and then move back, leaving only very little glue on the fibre tip.

Step 2 - Change for another slide with Er/Yb particles powder. Send illumination light into the fibre from the distal side and approach the proximal fibre end to the glass slide.

Step 3 - Move the glass slide with the micro stage to select an Er/Yb particle with proper size and maximum luminescence intensity (some particles are more efficient than others) by observing with the microscope camera (from the bottom) and the spectrum of the luminescence light. Once the targeted probe is selected, move it carefully to the centre of the optical fibre

until it is glued to the core of the fibre. Make sure the spectrum of luminescence light is always optimised. Then move the fibre back up.

Step 4 - Use UV light to polymerise the glue in order to fix the probe.

Step 5 - To mechanically and chemically protect the Er/Yb particle, dip the ensemble {fibre + particle} into UV glue as in step 1) to have a very small amount of glue that covers the tip and particle.

Step 6 - Polymerise it with UV lamp.

Several probes were fabricated in each batch to ensure the availability of operational probes, as they can be easily damaged during experiments.

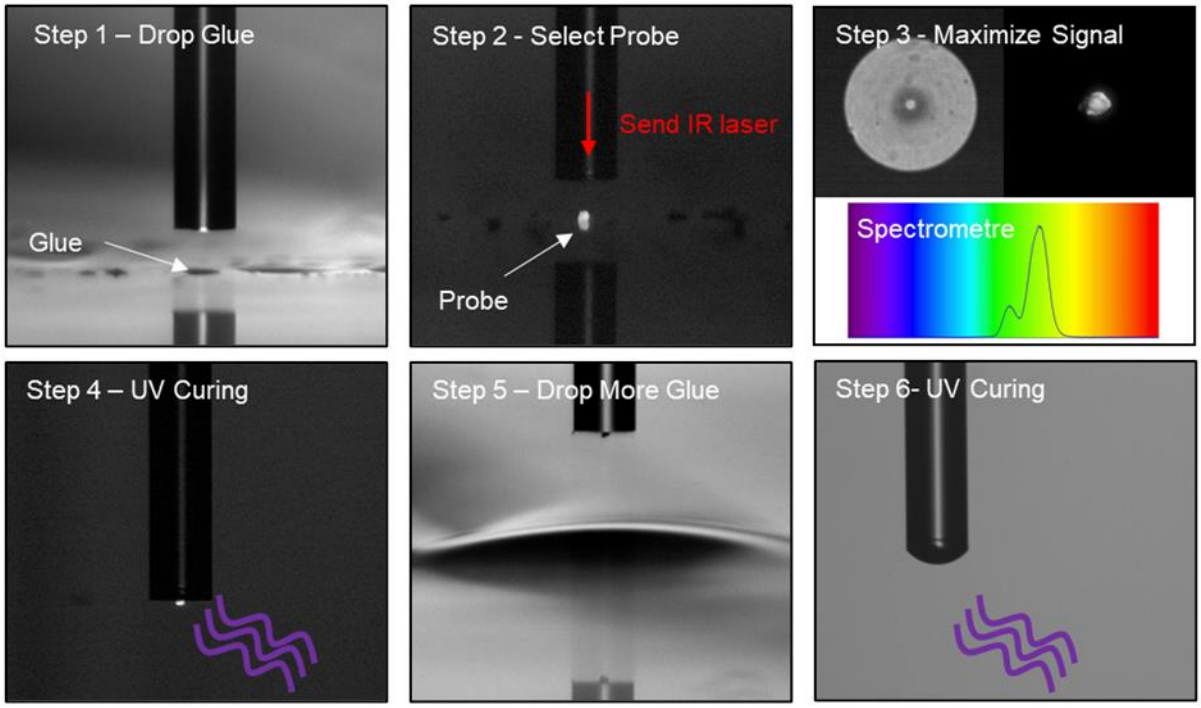

Figure 2.18 Fibred probe fabrication process

2.4.4. Calibration

On the day of the experiment, we performed a calibration in water, using a process similar to the one described for experiments in agar. Instead of an agar gel, the fibred probe is put in water, close to a commercial thermocouple used as a temperature reference (as shown in Figure 2.19(a)). While increasing the water temperature slowly, the spectrum of the luminescence light $S_\lambda(T)$ was recorded every 2ms with an external trigger to the spectrometer, and the temperature of the commercial thermocouple T was recorded every 2s using its internal trigger. The temperature of the water was increased from room temperature to several degrees

above 37°C, to cover the range which is relevant to our studies *in vivo*. After the acquisition, we took 500 spectra acquired in 1s and averaged them to reliably derive the I_{525}/I_{550} value. A linear fit is made on $ln(I_{525}/I_{550})$ as a function of $1/T$ to derive the A and B values which will be used later (as shown in Figure 2.19(b)).

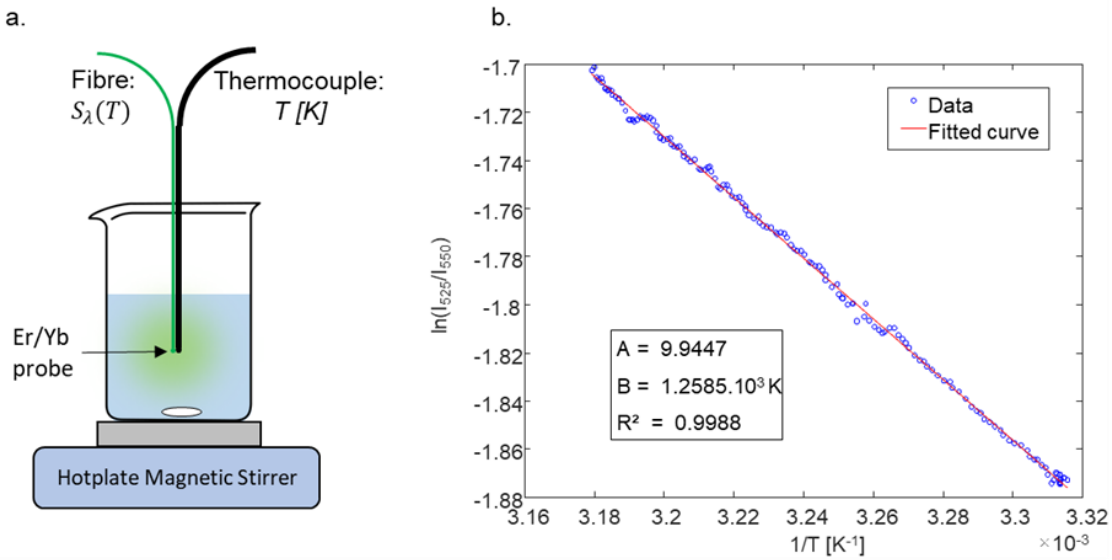

Figure 2.19 Calibration of a temperature probe. (a) Er/Yb fibre probe is put close to the thermocouple and immersed in water; the hotplate heats the water slowly while the fibred system is registering the luminescence spectrum $S_\lambda(T)$ and thermocouple is registering reference temperature T. (b) Calibration curve for finding the parameter A and B.

Also, we realized that it is very important to perform a calibration for each fibre probe on each day of the experiment, as, due to the possible environmental variations on the setup and fabrication variations of the fibred probe, the calibrated values of A and B can significantly vary from a day to another. Figure 2.20 shows the A and B values for 13 different calibrations conducted on different days and different fibre probes in water. If we use calibration for one probe to calculate the temperature rise values of another probe, they may yield variations up to the order of 30% in the experimental result. It is thus essential to calibrate each probe on the day of the experiment.

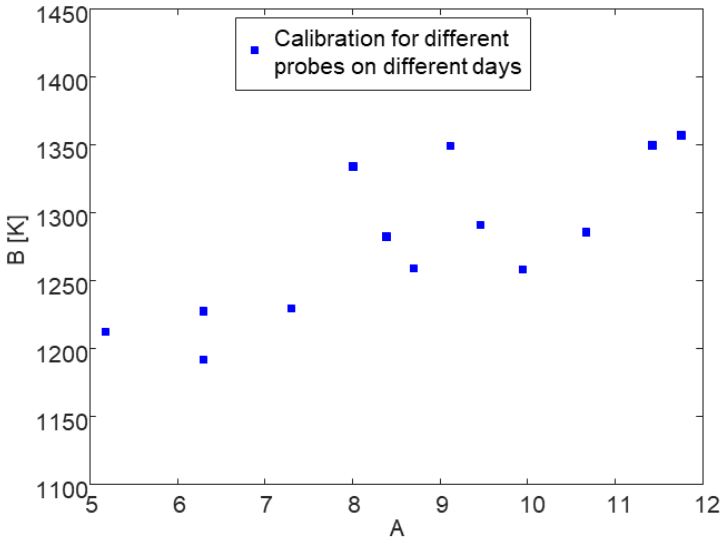

Figure 2.20 Variation of calibrated factors A and B for different probes

2.4.5. Improving the signal to noise ratio for *in vivo* measurement

In typical optogenetics experiments, we use 3-20 ms illumination time and 10-40 mW of excitation power in a holographic spot of ~12 µm diameter. Therefore we need a temperature resolution of the order of a few hundreds of millikelvin, and the temporal resolution should be in the tens of milliseconds range. It is, therefore, crucial to optimise the signal to noise ratio of our *in vivo* measurement for short acquisition time. In the following part, we discuss how the integration time of the spectrometer, the illumination laser power, and the "periodic" averaging method are chosen to improve the SNR, notably by decreasing noises, which we characterise through the standard deviation of temperature σ_T.

2.4.5.1. Integration Time

The uncertainty of our temperature measurement can be derived from Equation 2.5:

$$\sigma_T = \frac{T^2}{B}\left[\frac{\sigma_{N_{525}}}{N_{525}} + \frac{\sigma_{N_{550}}}{N_{550}}\right] \qquad \textit{Equation 2.6}$$

where N_{525} and N_{550} are numbers of photoelectrons collected by the spectrometer for the two peaks at λ = 525 nm and 550 nm, respectively.

To maximise the SNR, we used a more sensitive spectrometer based on Czerny-Turner optical design (Andor, Shamrock 500i coupled to an EMCCD-camera Ixon 888) with a grating optimised to minimise optical losses in the λ = 500-600 nm wavelength range of interest.

Furthermore, the excitation power of the Er/Yb particle is chosen so as to work in a regime where a large number of photoelectrons is detected (typ. 10^6-10^7) in each band. In such conditions, we work in a regime limited by the photon noise σ_{SN} and the camera reading noise (typ. 10) σ_{read} can be neglected:

$$\sigma_{N_{550}} = \sqrt{\sigma_{SN,550}^2 + \sigma_{read}^2} \approx \sqrt{\sigma_{SN,550}^2} = \sqrt{N_{550}} \qquad \textit{Equation 2.7}$$

$$\sigma_{N_{525}} = \sqrt{\sigma_{SN,525}^2 + \sigma_{read}^2} \approx \sqrt{\sigma_{SN,525}^2} = \sqrt{N_{525}} \qquad \textit{Equation 2.8}$$

Considering $N_{550} = \Phi_{550} * t_{int}$ and $N_{525} = \Phi_{525} * t_{int}$ where Φ_{525} and Φ_{550} are the flux of photoelectrons in each band and t_{int} the integration time, we can derive the temperature measurement noise as:

$$\sigma_T = \frac{T^2}{\sqrt{t_{int}}B}\left[\frac{1}{\sqrt{\Phi_{525}}} + \frac{1}{\sqrt{\Phi_{550}}}\right] \qquad \textit{Equation 2.9}$$

Therefore, we expect the standard deviation of temperature to be inversely proportional to the square root of the integration time, which is in good agreement with the experimental measurements shown in Figure 2.21.

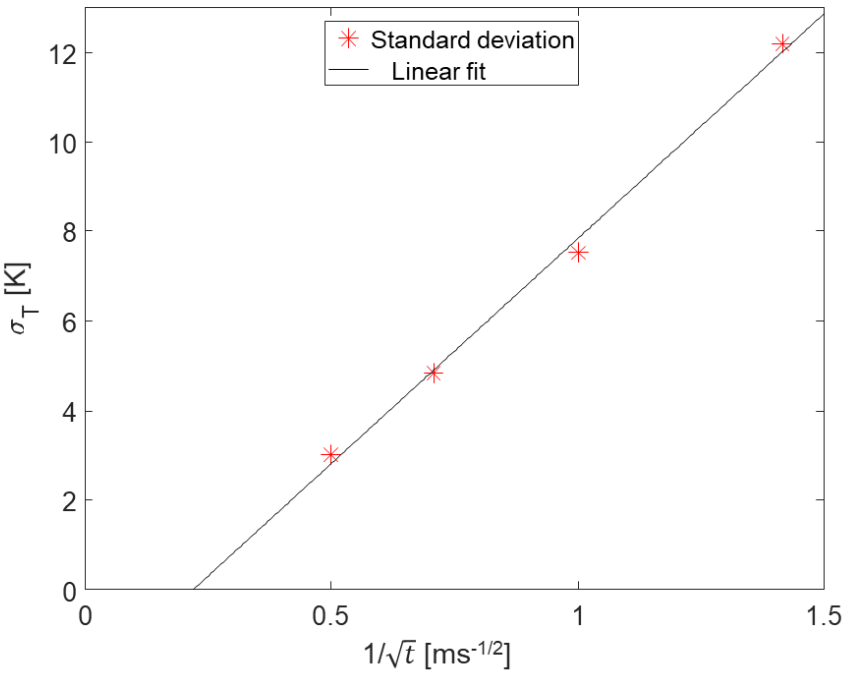

Figure 2.21 Standard deviation of the measured temperature as a function of the square root of the integration time of the spectrometer

For integration times in the 0.5–4ms range, the standard deviation for a typical measurement is well above the 1K scale. It is not sufficient for detecting temperature variation during an optogenetics experiment. Moreover, other averaging techniques are necessary in order to reach such performances while achieving millisecond temporal resolutions.

2.4.5.2. Illumination laser power

By increasing the illumination laser power on the Er/Yb particle probe, we can increase the luminescence intensity emitted by the particle, thus increasing the number of collected photons. Here, we study the relation between luminescence intensity and excitation laser power. The luminescence intensity of the two emission lines was measured for excitation laser powers from 2.28e-2 to 6.73 mW, as shown in Figure 2.22.

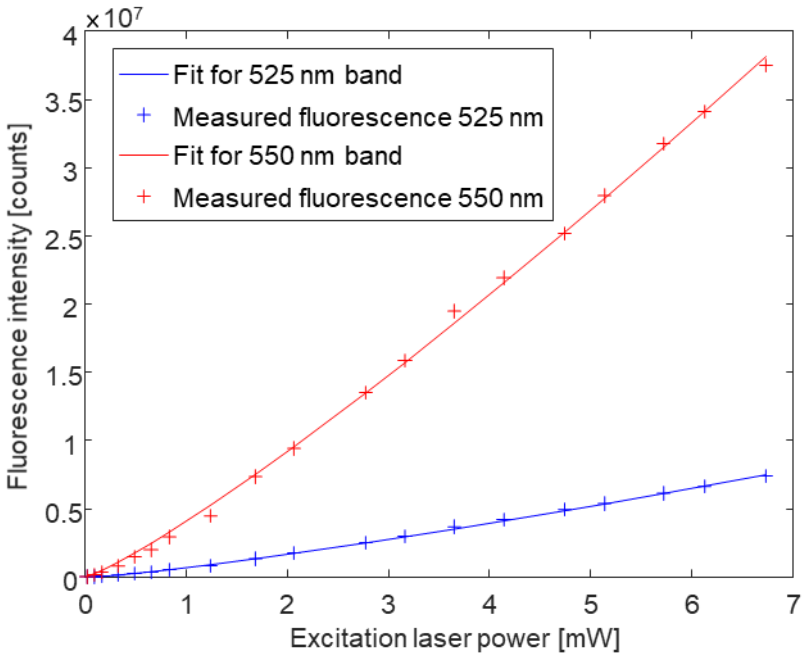

Figure 2.22 Increase in luminescence intensity with excitation laser power

The measurement results are fitted separately for each emission band (λ=525 or 550nm) with a power law: $I_\lambda = a_\lambda I_{laser}^{b_\lambda}$. the coefficients a_λ and b_λ in this measurement are a_{525}=7.22.10^5 and b_{525}=1.23 for the λ=525 nm line, and a_{550}=4.07.10^6 and b_{550}=1.17 for the λ=550 nm line. These values are consistent with those measured in other works[141,142] and, as clearly visible in Figure 2.22, the upconversion phenomenon obeys the power law. We can thus improve the signal by increasing the incident pumping laser power, and therefore use shorter integration times.

However, when increasing the illumination laser power, the local temperature of the Er/Yb particle increases. This is mainly due to the absorption and nonradiative de-excitation in the Er/Yb particle. This temperature increase is therefore related to the chemical composition of the material and increases linearly with the incident laser power. In Figure 2.23, we compared probes made using a glass of "50 GeO_2 - 40 PbO - 10 PbF_2 - 1 ErF_3 - 1 YbF_3" treated under 390°C for 10 hours (Er:Yb=1:1, called "composition 1" in Figure 2.23); and "PbO GeO_2 PbF_2 – Yb 20 Er 5" treated under 360°C for 4 hours (Er:Yb=5:20, "composition 2").

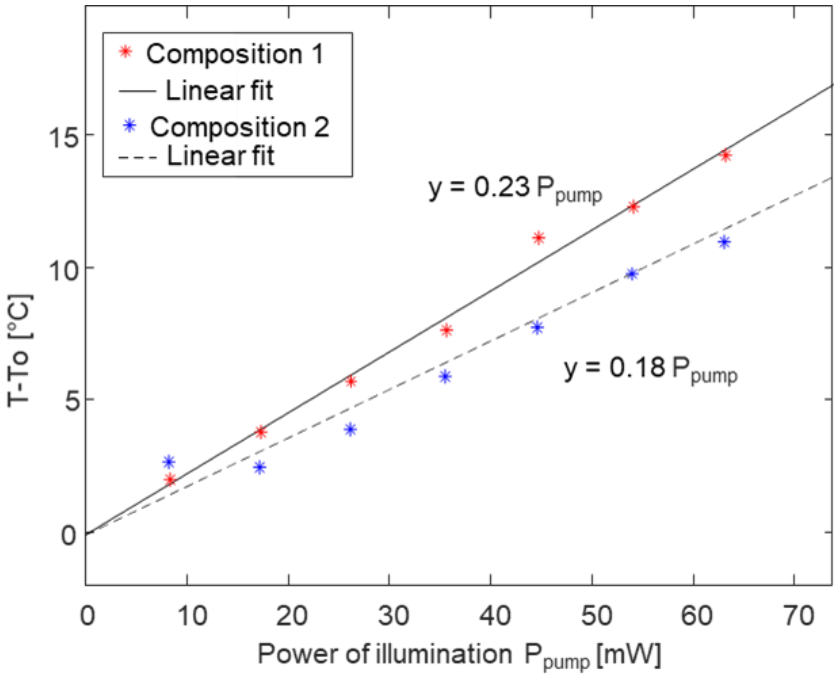

Figure 2.23 Temperature baseline increase with the excitation laser power, in 2 materials with different chemical copositions: 50 GeO_2 - 40 PbO - 10 PbF_2 - 1 ErF_3 - 1 YbF_3 treated under 390°C for 10 hours (composition 1) and PbO GeO_2 PbF_2 – Yb 20 Er 5 treated under 360°C for 4 hours (composition 2)

Although it should stay within reasonable limits to avoid interference with cell or tissue metabolism, this offset does not influence the temperature measurement as we are usually interested only in fast transient temperature rises induced by the optogenetic stimulation, but not in the absolute temperature. All the following experiments have been carried out with composition 2.

2.4.5.3. Periodic averaging

Averaging is clearly an efficient way to increase SNR. In order to maintain sufficient time resolution while allowing as many averages as necessary to obtain the desired signal-to-noise ratios, we used a time sampling strategy which is typically used in e.g. pump-probe experiments based on periodic excitation. The method is illustrated in Figure 2.24. For each optogenetic pulse (pulse duration t_{pulse} = 30 ms), n spectra S_i (with i=1 to n, here n=125) are acquired out at a fast rate (period $t_{sampling}$= 2ms). The spectrum S_i (and temperature Ti) therefore corresponds to a delay $t_i = i.t_{sampling}$ with respect to the start of the optogenetic laser pulse. This process can then be repeated as many times as necessary (here, N=500 times). Each of the N spectra labelled S_i corresponds to the same delay with respect to the excitation pulse and can therefore be averaged together. This averaged spectrum $\langle S_i \rangle$ clearly offers a measurement of temperature at the instant $t_i = i.t_{sampling}$ with a much better SNR than a single spectrum S_i as discussed in Figure 2.25. As illustrated in Figure 2.24, the necessary signals are driven by an Arbitrary Function Generator. By averaging the temperature rise time-trace with N=500 times, the noise is massively decreased.

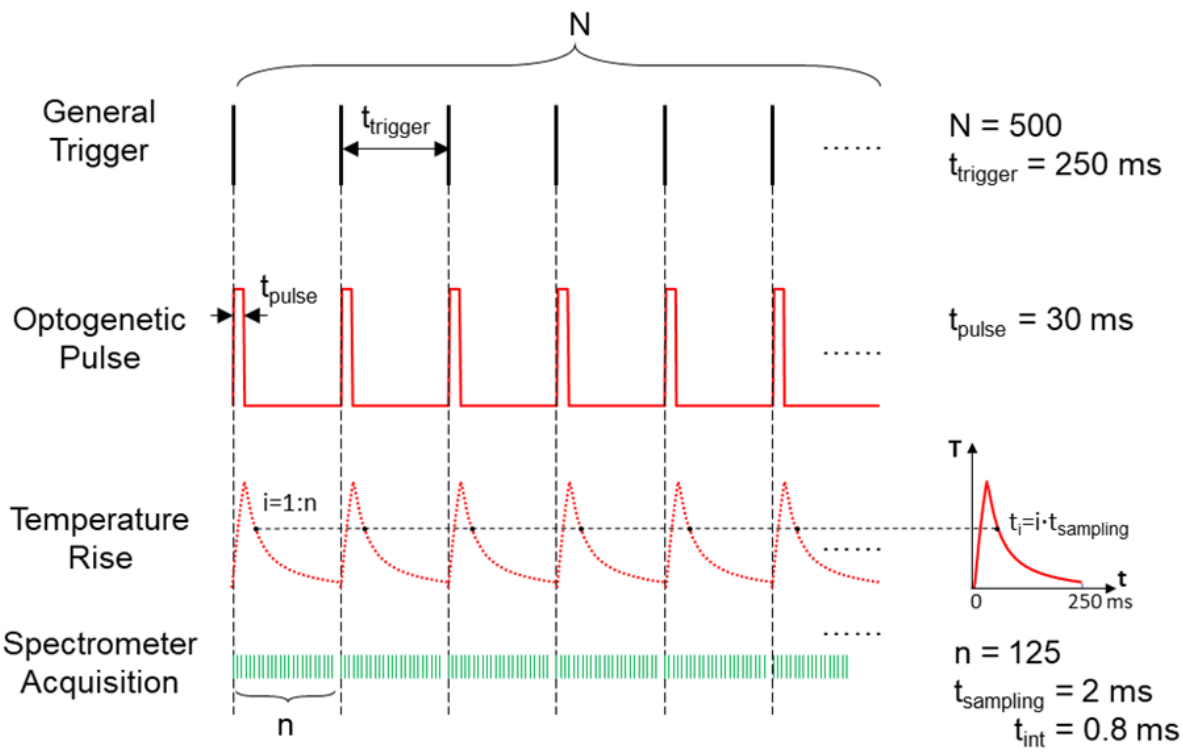

Figure 2.24 Principle of the triggering scheme used for time-resolved spectra averaging. One time-trace is the averaging result of N traces, and each trace is sampled by n times. Period t_{triger} is chosen so that the photoinduced temperature peak can drop close to 0.

In Figure 2.25, we plotted the measured standard deviation of temperature σ_T under different numbers of average. It shows that the standard error can be reduced massively by averaging measurements. For 500 spectra averaged, the temperature noise σ_T reaches 0.05K (for a pump power P_{pump}=60mW and an integration time t_{int}=0.8ms).

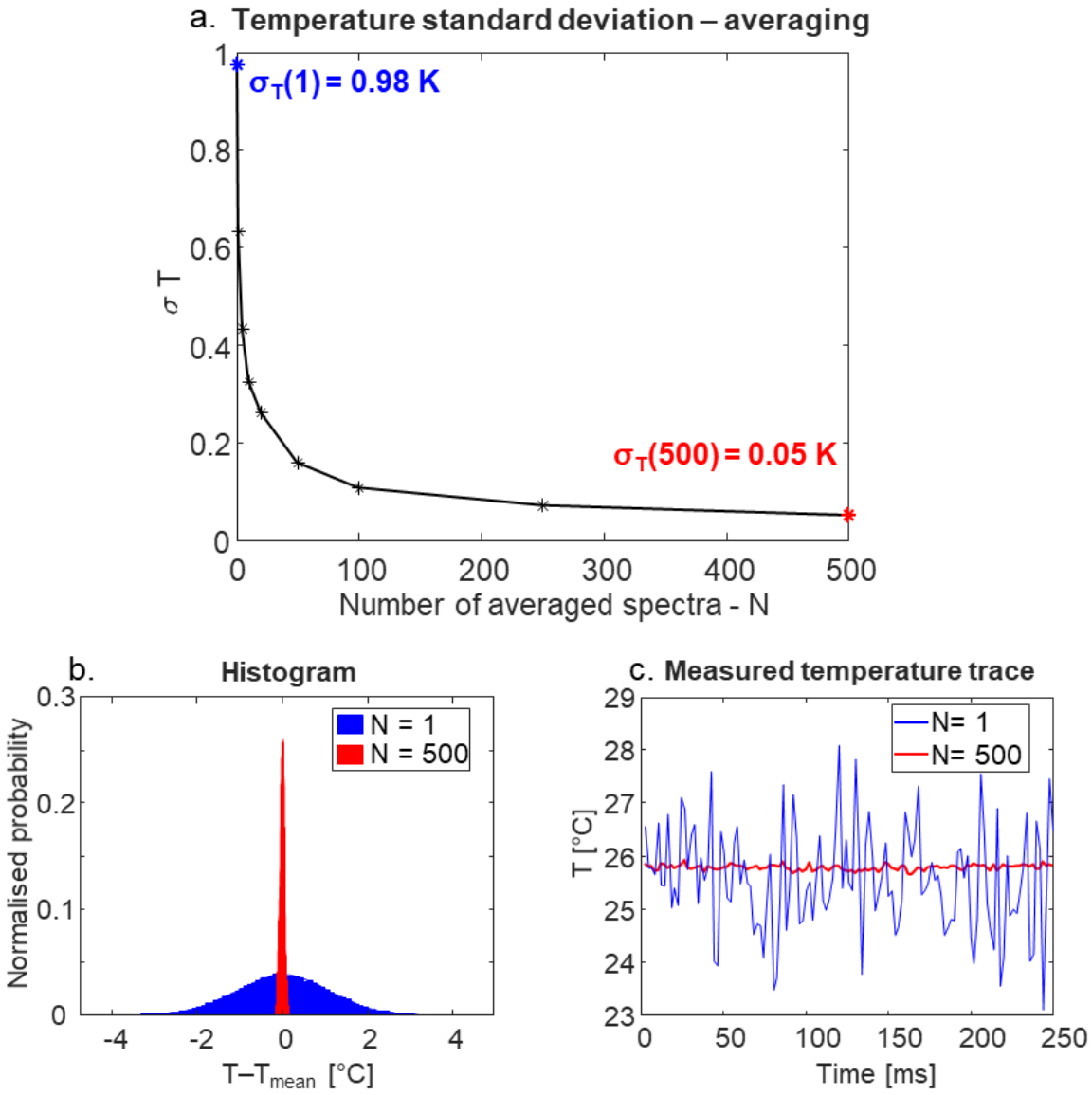

Figure 2.25 Temperature noise reduction by averaging. (a) Evolution of the standard deviation of temperature with the number of averaged spectra (N), measured for 0.8 ms integration time. (b) Histogram of temperature variation from the mean temperature; (c) Temperature trace at thermal equilibrium in water during 250 ms. For two different number of average (N = 1 and N = 500).

2.5. Validation in water

2.5.1. Coupling to the two-photon optogenetic setup

The two-photon optogenetic setup used for the in vivo experiment has been previously described[143], and it is similar to the one described in section 2.3.1. Briefly, The holographic stimulation path is based on an LC-SLM located in a plane conjugated with the back focal plane of the objective lens, which allows generating one or several 2P holographic spots. The laser is externally gated to quickly modulate the intensity to generate optical holographic pulses or train of pulses with typically 10-50 ms duration. In contrast to section 2.3.1, the thermometry modality is now independent of the 2P scanning path, in the sense that the fibre endoscope allows now both excitation of the Er/Yb probe and collection of the luminescence signal. However, the 2P imaging path is needed to precisely locate in 3D the sensitive area of the thermometric endoscope, e.g. the 15-20 µm diameter Er/Yb particle, within the sample.

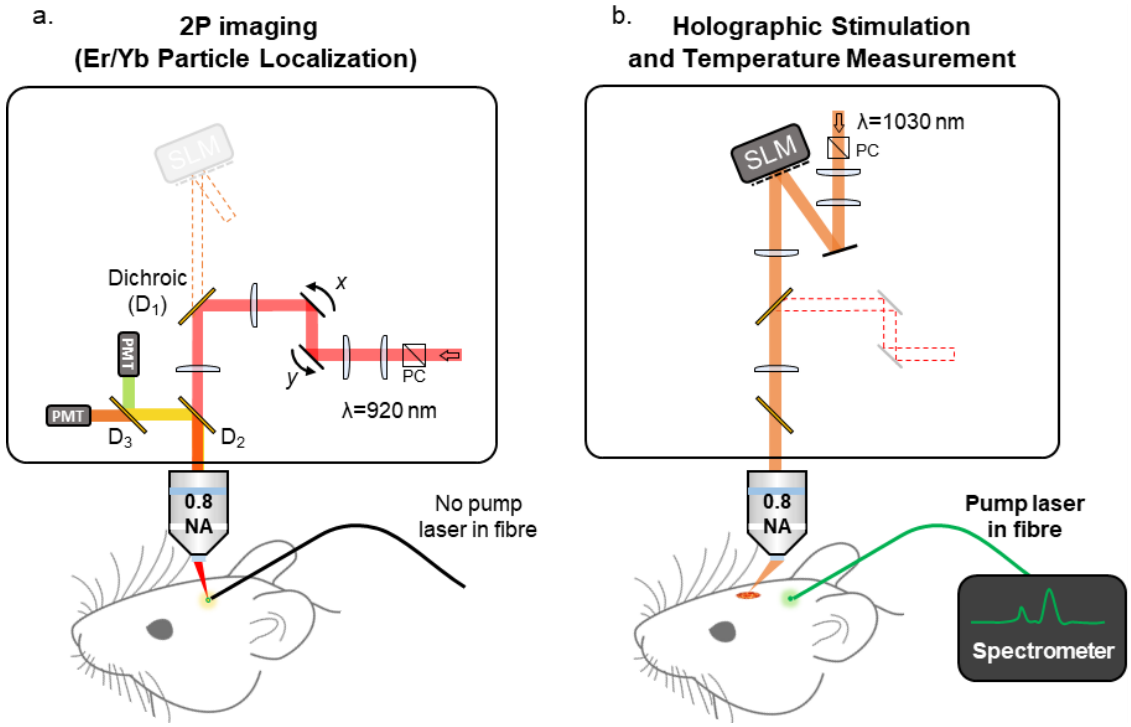

Figure 2.26 Two-photo imaging and holographic stimulation in one setup. (a) while performing the 2P imaging, the pump laser inside the fibre is turned off, and the Er/Yb particle can be located through 2P scanning imaging. (b) while performing the holographic stimulation, the fibre probe measures temperature beside the stimulation spot. A dichroic mirror (D1) combines the two paths.

2.5.2. Experimental process

Before the *in vivo* experiment, a control experiment was conducted in water to validate the system and avoid useless animal sacrificing. The thermometric endoscope was passed through a glass capillary (with a sharpened end prepared by a micropipette puller) held by a micromanipulator oriented with an angle of $\theta_0 = 31°$ to the horizontal plane, as shown in Figure 2.27. Using a water immersion objective (N40X-NIR - 40X Nikon CFI APO NIR Objective, 0.80 NA), the luminescence of the probe allows its localisation when a 2-photon imaging scan is carried out (Figure 2.28).

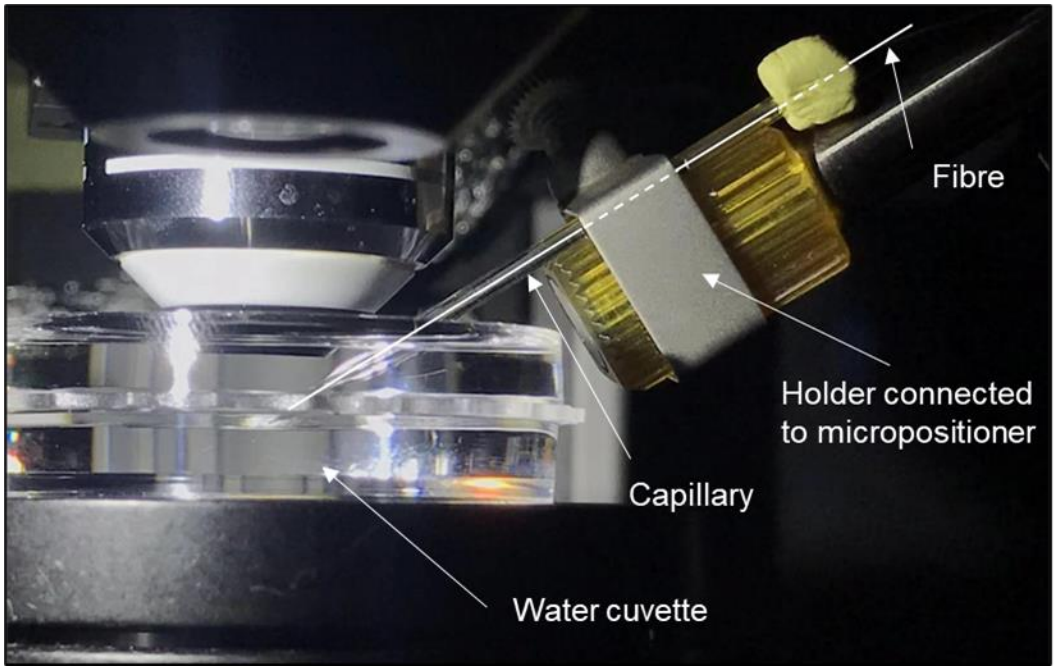

Figure 2.27 Laser- induced temperature rise measurement using fibred Er/Yb particle thermal sensor in a water cuvette

One should note that, when measuring 2P luminescence from the top, the excitation light is refracted by the glass of the fibre (see Figure 2.28(b)). Therefore, as clearly visible in Figure 2.28(a), the 2P image of the luminescent probe is strongly distorted, but also shifted with respect to its actual position. To evaluate and compensate for this effect, we developed a simple model based on geometrical optics (detailed in Annex 2). Our calculation shows that the lateral distance between the holographic spot and the probe is underestimated systematically by ~4µm (considering θ_0=31°), and the depth of the probe is underestimated by ~30µm. Since the temperature varies very quickly with the distance to the holographic spot, this offset was taken into account during experiments and simulations.

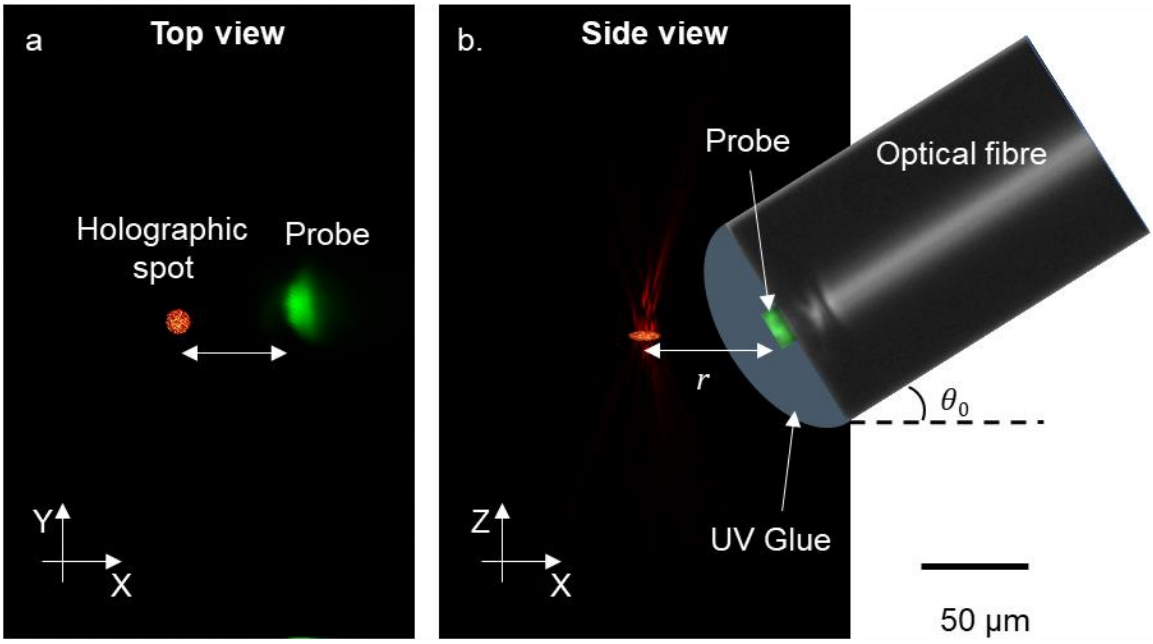

Figure 2.28 (a) Two-photon scanning image of the probe at the end of the optical fibre, in water, viewed from the top, with a schematic indication of the holographic spot position; (b) Schematic of the probe and holographic spot viewed from the side. $\theta_0 = 31°$ *is the angle of the fibre to the x-axis. The optical axis of the microscope objective is along the z-direction. The 2P image of the probe (a) is refracted by the fibre while scanning from the top (z-direction).*

2.5.3. Experimental conditions

During the temperature measurement, the probe is continuously illuminated by a pump laser through the fibre core (λ = 976nm, P = 63.1mW at the exit of fibre), while the luminescence light is collected through the 1st cladding of the fibre. A 12µm diameter holographic spot is then periodically projected at a chosen distance from the temperature probe (pulse duration t_{pulse} =30 ms, a repetition rate of 4 Hz, an average power of P=170 mW). After each optogenetic pulse, a series of n=125 spectra $\mathbf{S_i}$ is acquired at a frequency of 500 Hz (period: $t_{sampling}$=2 ms) with an integration time of t_{int}=0.8 ms. After N=500 optogenetic pulses, spectra acquired at the same delay are averaged. The calibration (A, B) described above is then applied to these n=125 spectra $<\mathbf{S_i}>$ to obtain 125 values of the temperature rise at instants t_i=i.$t_{sampling}$. The signal to noise ratio is highly improved by averaging these 500 time-traces to obtain a single 125-points time-trace, as the error is decreased to 0.05 K.

2.5.4. Result and comparison with the simulation

Figure 2.29 shows the evolution of temperature during the 250 ms following a laser pulse. During this typical optogenetic stimulation, we observe a maximum temperature rise of about 0.6 K. The averaging of 500 experiments gives a high temperature and time sensitivity to resolve this temperature rise time-trace (following the protocol shown in Figure 2.24). In order to remove the remaining DC components to the temperature, this signal is processed by assuming that the temperature rise at the end of the measurement (25 points, between 200 and 250 ms after the pulse) reaches 0, as shown in Figure 2.29(a) (hollow circles).

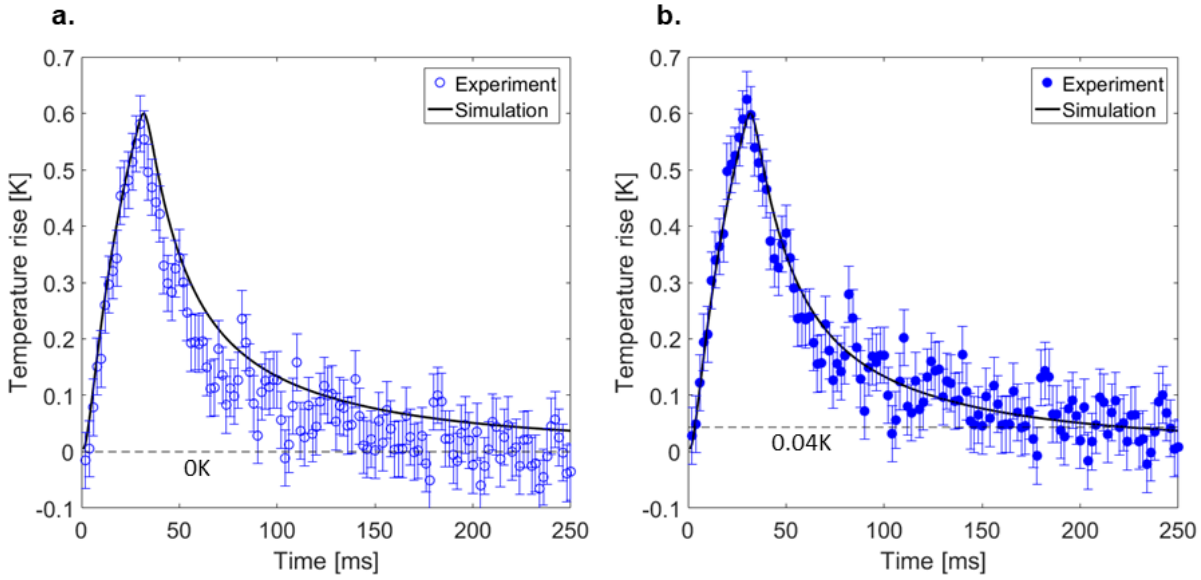

Figure 2.29 Measured and simulated time-trace of the temperature rise caused by a single holographic spot in water (P = 177mW, t_{pulse} = 30ms, D = 12µm, distance from the probe r= 73µm). The two sets of measurement points represent the same data (a) without, or (b) with compensation of a temperature baseline of 0.04 K. The error bar here contains the measurement sensitivity of the system which is 0.05 K.

These experimental results were compared to the simulation described in Section 1.2, with improvements in terms of calculation speed and proper handling of the cyclic boundary condition effect (aliasing) linked to the representation of an infinite medium in a finite calculation space (see in Annex1).

Temperature offset (0.04K): To compare the measured transient temperature rise (ΔT) with the model, we need to subtract the baseline temperature value from the experimental data. Our temperature time-trace is acquired by the periodic averaging, as discussed in Section

2.4.5.3. In Figure 2.29(a), we assumed that the steady-state (ΔT=0) is reached 200 ms after the optogenetic pulse. Thus, we approximated the baseline temperature as the average value of the measured temperature between 200-250ms and removed it from the experimental results (shown in hollow circles). However, simulations show that (black line in (a) and (b) is the same simulation), the average value between 200-250ms is 0.04K, slightly over 0. For this reason, data processing in Figure 2.29(a) that assumed a steady-state, which is not perfectly reached, suffer from a slight offset.

The model shows that reaching ΔT=0 K would require measurements at delays well beyond 250 ms, which cannot be measured on our setup since the buffer of the spectrometer cannot withstand a greater number of spectra. Therefore in Figure 2.29(b), we show the same data to which a positive 0.04 K has been applied (full blue dots). Taking this offset into account, the agreement between measurements and simulation is particularly good, both in terms of maximum temperature rise value and decay dynamics.

2.6. *In vivo* experiments

2.6.1. The simulation method for scattering medium

After having validated our model with the experiment in water, we performed the experiment *in vivo* mice brain. In this case, the temperature probe can only provide measurements at some finite distance $r \geq 60\ \mu m$ from the centre of the holographic spot (depending on the inserting angle and probe fabrication, as shown in Figure 2.28). This requires us to precisely estimate, from these measurements at distance r, the temperature rise inside the spot. To this end, we have adapted the simulation code to take into account the spatial distribution of the heat source on and, due to the scattering, right outside the holographic spot. Scattering at the macroscopic scale is characterized by two parameters (l_s: scattering coefficient, g: anisotropy) which have been measured or estimated for various biological tissues in literature[144]. We will use the *in vivo* measurements outside of the holographic spot to validate this model and then use it to estimate the exact temperature rise value inside the spot.

Figure 2.30 shows the simulation process. It consists of mainly two parts: 1) building the holographic spot heat source and 2) calculating the temperature map caused by heat diffusion.

1) The field on SLM is calculated through an iterative Gerchberg-Saxton algorithm. A Fourier transform of this field E_{SLM} provides the non-scattered field distribution in the focal plane. Using Fresnel propagation, we can back-propagate the field on the focal plane to the tissue's surface. From this field $E_{surface}$, we then use the "Beam Propagation Method" and add scattering effect, to propagate forward step by step. The scattering effect is materialised by multiplying the previous field with the complex transmission of a random phase mask characterised by l_s and g at each finite step of the propagation. In this way, the 3D distribution of the holographic spot $\boldsymbol{I}$ in scattering tissue is simulated.
2) For weak absorption, the heat source distribution $\boldsymbol{Q}$ is proportional to the light intensity distribution: $\boldsymbol{Q} = \alpha \boldsymbol{I}$, with α the absorption coefficient. As discussed in Section 1.2.2, the induced temperature rise can be expressed as the convolution of the heat diffusion equation Green's function $G_T(r,t)$ by the heat source $\boldsymbol{Q}(r,t)$ whose spatial and temporal dependencies can be treated separately in our case: $\boldsymbol{Q}(r,t) = \Gamma(r)\ \Pi(t)$. We first calculate the convolution for the spatial distribution $\Gamma(r)$ in the Fourier space through multiplication while considering an impulsive source in time (e.g. simulation time step dt=1ms). Then, for different pulse shape, a linear summation can realise the convolution for temporal term

Π(t). To solve the boundary effect in Fourier space while heat reaches the border of the simulated volume, and 'adapted voxel' method is used to enlarge the voxel size with time steps. More details could be found in the Annex 1.

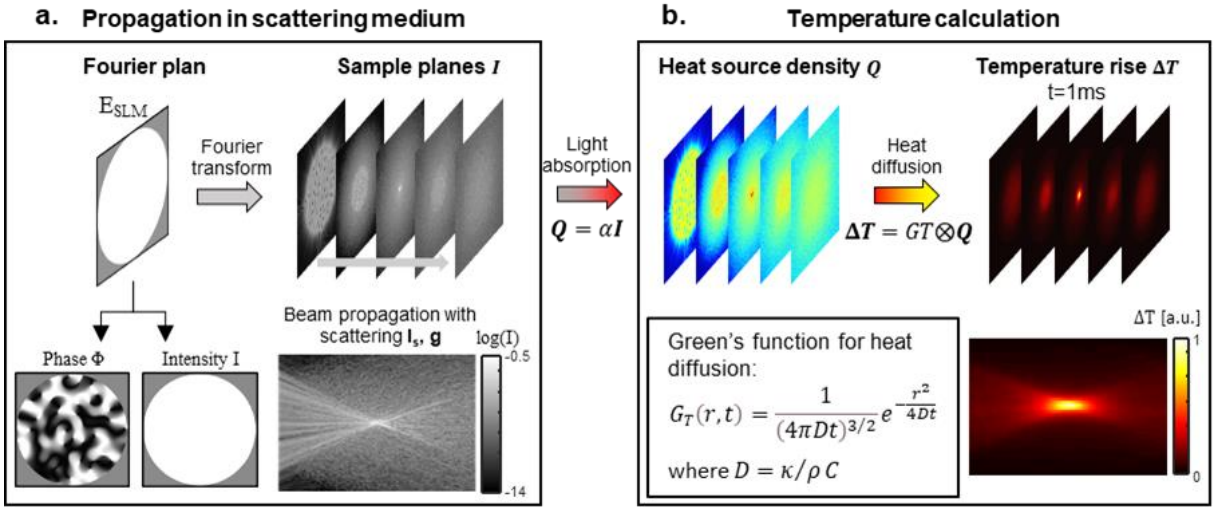

Figure 2.30 Simulation process. (a) Simulation of a holographic spot in scattering tissue, using the beam propagation method. (b) Temperature simulation using the convolution of Green's function of heat diffusion with the heat source Q.

Once the 3D spatiotemporal map of the temperature rise is calculated, we can average this distribution inside a sphere that represents the position and size of the Er/Yb probe to simulate the time-traces measured in experiments.

2.6.2. Experimental methods

Transgenic mice of cortical expression of the calcium indicator GCaMP6s were used during the *in vivo* experiments. They are 10-15 months old mice of the mouse line GP4.3 (The Jackson Laboratory). A craniotomy at the primary visual cortex was prepared on the day of the experiment. Cortical neurons expressing the fluorescence protein of GCaMP6s help indicate the surface of the brain tissue and depth of Er/Yb particle beneath the brain by performing 2P imaging. The mice preparation, 2P imaging and 2P optogenetic stimulations were operated by I-Wen Chen, postdoc in the Emiliani's team. During experiments, mice were anesthetised with isoflurane (2% for induction and 0.5–1% for experiments) and head-fixed under the water immersed microscope objective.

In vivo experiments require much caution to minimise damage and bleeding during the penetration into brain tissues. A sharp glass capillary (pulled by micropipette puller and broken

with a ceramic cutter at suitable diameter to let passe the fibre probe) held by a micromanipulator is used to pierce the tough first layer of the brain surface, the meninges. This capillary is then used to protect and guide the fibred probe during the first steps of its insertion into the brain tissue. Figure 2.31(b) shows while using the sharp end of the glass capillary to pierce the meninges, the fibre probe stays inside the capillary (the bright spot is the illuminated probe while it is not yet penetrated into the tissue). Figure 2.31(c) shows that, after the capillary has entered the tissue, it stays in its position, and the fibre probe is pushed into the tissue with the guidance of the capillary. The fibre probe was positioned at 200~300 µm beneath the brain surface. We can see the change of the bright spot compared to Figure 2.31(b), as tissue scatters the luminescence light from the probe in Figure 2.31(c).

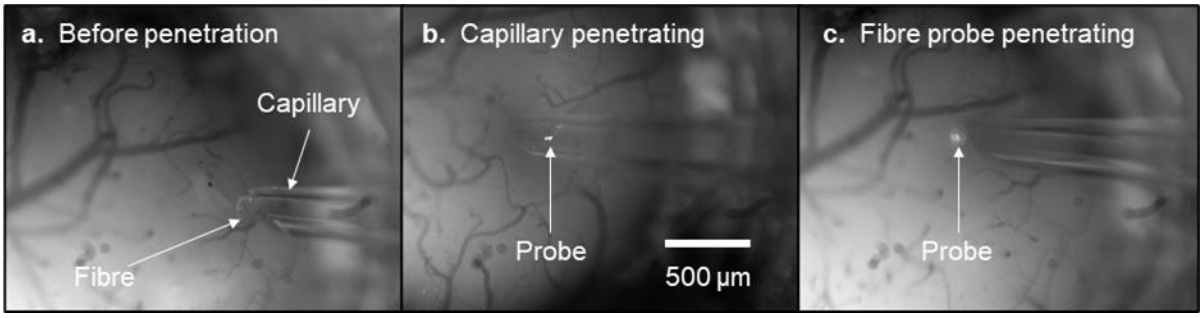

Figure 2.31 Widefield images of thermal 'endoscope' insertion process into the brain. On the left image(a), the glass capillary is visible, and the probe is slightly out of the capillary. In the middle(b), the luminescent particle at the tip of the probe is illuminated and clearly visible. The probe stays inside the capillary while the capillary tip is penetrating the meninges. On the right images(c), the luminescent particle stays illuminated as the probe is inserted through the meninges with the cut pierced by the capillary tip. The scale bar is 500 µm.

As shown in Figure 2.31(c) and Figure 2.32(a), the brain tissue is optically scattering, particularly at visible wavelengths. For this reason, we used 2-photon scanning imaging, which is less prone to scattering, to localise the probe, shown in Figure 2.32(b). Once the probe is localised, two-photon holographic laser pulses of a 12 µm-diameter spot are focused under the brain surface, at the depth at which the temperature probe is inserted. The measurement protocol described earlier, in water, is applied to obtain the corresponding temperature rise.

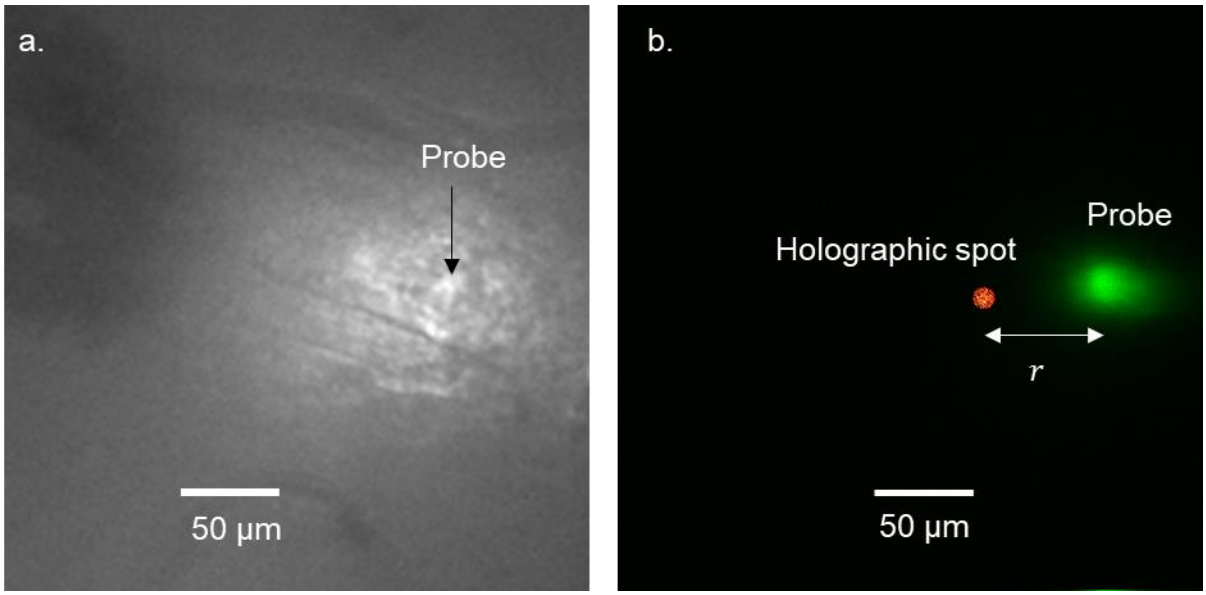

Figure 2.32 Widefield and 2-photon scanning images of the probe after insertion in brain tissues. In (a), the broad bright spot corresponds to the luminescence of the probe, which is scattered by brain tissue, as the Er/Yb particle is excited by IR light sent through the fibre. Accurate localisation of the probe is difficult to achieve because of this scattering. (b) The same probe, imaged (false colours) using a scanned 2-photon illumination. The red spot is a schematic indication of the holographic spot position. The probe is situated 330 µm below the brain surface and around r=75 µm away from the optogenetic holographic spot. Scale bars are 50 µm.

2.6.3. Results and comparison with the simulation

2.6.3.1. Single-pulse

We started by measuring the temperature rise induced by a stimulation spot of a wavelength **λ = 1030nm**, diameter **D = 12µm,** average power at objective exit **P = 180mW,** pulse duration $\mathbf{t_{pulse}}$ **= 30ms,** at depth **z = 330µm** under the brain surface. We found that the maximum temperature rise measured at a distance **r = 75µm** from the holographic spot centre was **ΔT = 1.06 ± 0.05K**, as shown in Figure 2.33.

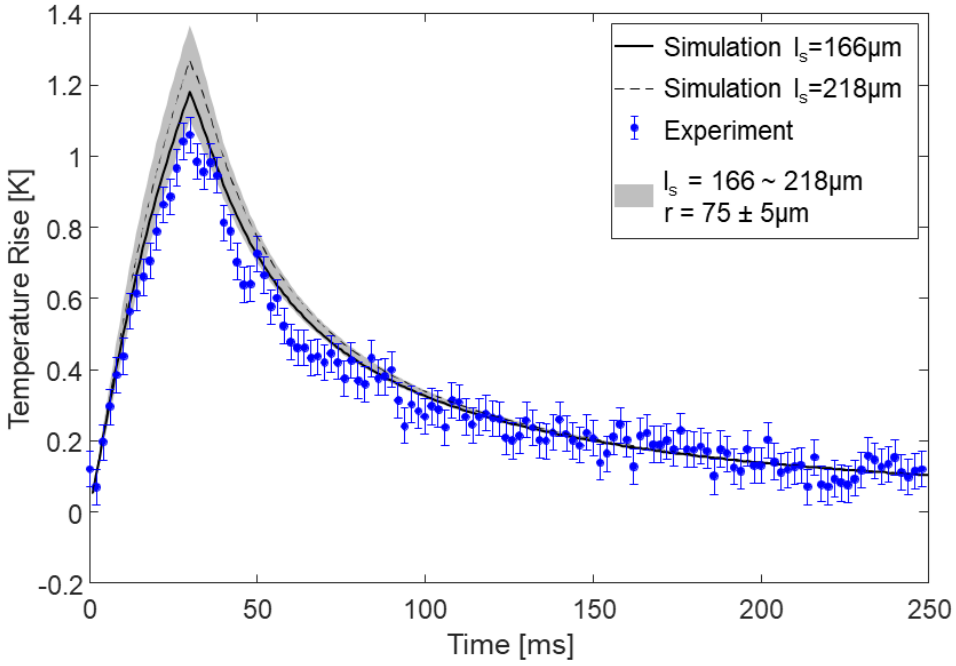

Figure 2.33 In vivo temperature rise measured 75 µm away from a 180mW-30ms holographic spot focused 330 µm below the surface of a live mouse brain. Blackline: simulation result with r =75µm, l_s = 166µm; black dashed line: simulation result with r =75µm, l_s = 218µm; the grey area is the error bar induced by uncertainty on the distance (r = 75±5µm) and scattering length (l_s varies between 166 and 218 µm, depending on the authors).

This temperature rise is higher than what measured in water for similar illumination conditions (Fig. 2. 29), which is consistent with the fact that, although their thermal properties are very similar, at 1030 nm wavelength, brain tissues have three times higher optical absorption coefficient than water[137] (α_{brain} = 0.06 mm^{-1}). Another feature that distinguishes the two conditions (water and brain) is that brain tissues are highly scattering even in the infrared range; as a result, the photons are deviated by their ballistic trajectory generating heating in a broader region. The effects of scattering and consequent heat broadening are taken into account in the simulation with two parameters: the scattering length l_s and the scattering anisotropy g (see for more details the Annex 1). The simulations shown in Figure 2.33 have been obtained by using two values of the scattering length found in the literature, l_s = 166µm (human grey matter[137]) and ~ 218µm (model for mouse cortex[145]). While for the anisotropy factor, we use its value g ≈ 0,9, reported for different types of tissues[137]. Higher *ls* means less scattering, thus inducing a **ΔT** more localised around the holographic spot. The black line in Figure 2.33 is the simulation with l_s = 166 µm, r =75µm, which fits better the experiment than for l_s = 218µm. In the following simulations (Figure 2.34, Figure 2.35 and Figure 2.36), we will therefore only use l_s

= 166 µm. The uncertainty on probe position (±5µm) also plays a role in determining the exact temperature rise, as we will see below.

Next, we measured the dependence of the temperature rise on the excitation power and pulse duration. Figure 2.34 shows time-traces (dots) for different pulse powers **P=180, 90 and 45 mW** (other condition stays the same as Figure 2.33). Here, the peak values are proportional to the laser power of the holographic spot, indicating that power and temperature rise have a linear relationship consistent with the theoretical predictions (solid line and described in Section 1.2).

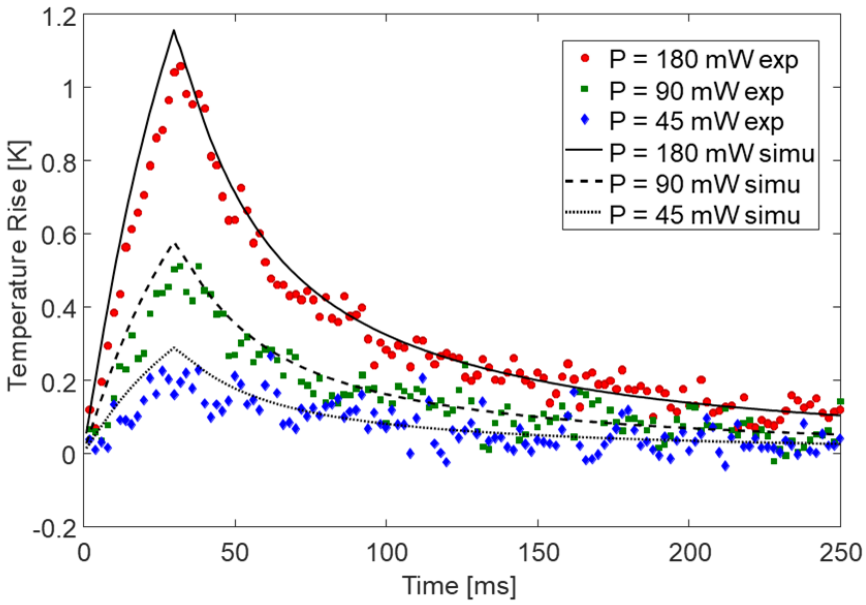

Figure 2.34 Temperature rises for different laser powers (other conditions stay the same as Figure 2.33)

Figure 2.35 shows the **ΔT** time-trace for different pulse durations $\mathbf{t_{pulse}}$ **= 10, 20 and 30 ms** (other condition stays the same as Figure 2.33). The time constants of the temperature rises are similar, as expected, and longer pulse durations lead to higher maximum temperature rises. Precisely, for short pulses, the heating remains confined in the excitation spot and the temperature increases nearly linearly with the pulse duration. For longer pulses, diffusion of the heat out of the illuminated spot produces a sublinear dependence of **ΔT** on the pulse duration $\mathbf{t_{pulse}}$, which follows a $erfc\left(\frac{r}{2\sqrt{Dt}}\right)$. The peak value of the temperature is therefore not proportional to the pulse duration. For long pulse durations, this value tends towards the DC temperature induced by a continuous laser. The rise and decay fit perfectly with the simulation, which means the thermal diffusivity $D = \kappa/\rho C$ are well represented in the model.

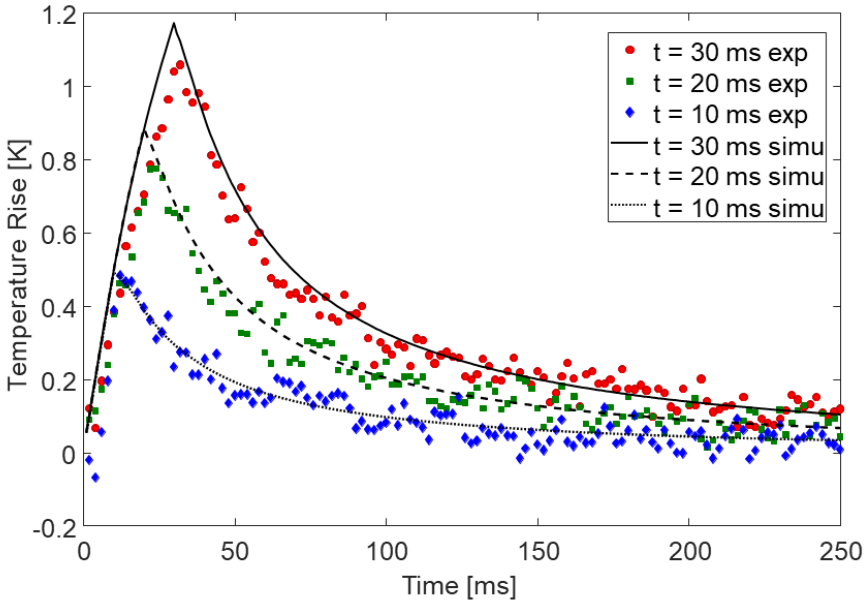

Figure 2.35 Temperature rise (experiment and simulation) for different pulse durations t_{pulse} (other conditions stay the same as Figure 2.33)

2.6.3.2. Heat accumulation of pulses train

The linearity of heat diffusion allows us to simulate multi-pulse heating by a linear summation of sequential pulses. Figure 2.36 shows temperature rises for five pulses of 10-ms (power P = 180 mW) with variable repetition rates. For 10 Hz stimulation, the heat dissipation after each photostimulation pulse is fast enough to bring the cell back to the equilibrium temperature before the arrival of the next photostimulation pulse. Increasing the stimulation repetition rate generates a heat accumulation after each photostimulation, which at a high repetition rate (40Hz), makes the contribution of each pulse hardly distinguishable. In this case, the peak temperature is about two times higher than the peak reached at 10 Hz repetition rate.

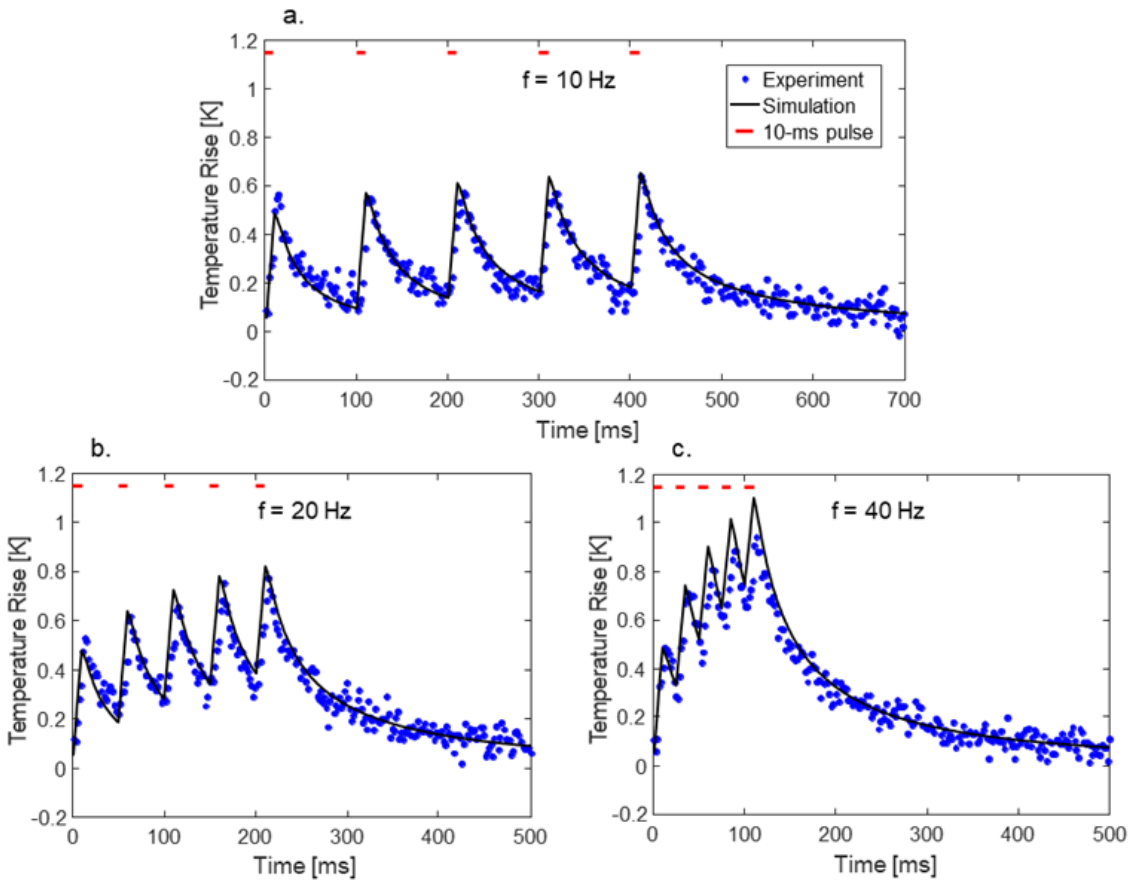

Figure 2.36 Temperature rise caused by a 5-pulses train with different repetition rates.

2.6.3.3. Evolution of the maximum temperature rise with distance

The most relevant information to define the heating during our optogenetic experiment is the maximum temperature reached on the stimulated cells. Clearly, this temperature is reached at the end of the excitation pulse, and at the centre of the holographic spot. However, measurements within the holographic spot are not possible with our temperature endoscope, since the 2-photon excitation would contribute to the excitation of the luminescent material and change the calibration and temperature measurement. We can, however, use our thermal model to extrapolate from the measurements carried out at a known distance from the sample, the temperature rise at the centre of the spot. Figure 2.37 shows the measured maximum temperature rise value at different distances of the probe from the centre of the holographic spot. Each point corresponds to the peak of the corresponding time traces like those of Figure 2.33, acquired at various known distances from the centre of the holographic spot. Simulations were carried out using two different l_s values: 166 and 218 µm, in order to indicate margins of error related to this value (in grey). The error bar on experiment results stands for σ_T=0.05K

(vertical) and uncertainty on the distance σ_r=*5µm* (horizontal). It is worth mentioning that time-traces at all these positions fit the simulations equally well, as in Figure 2.33

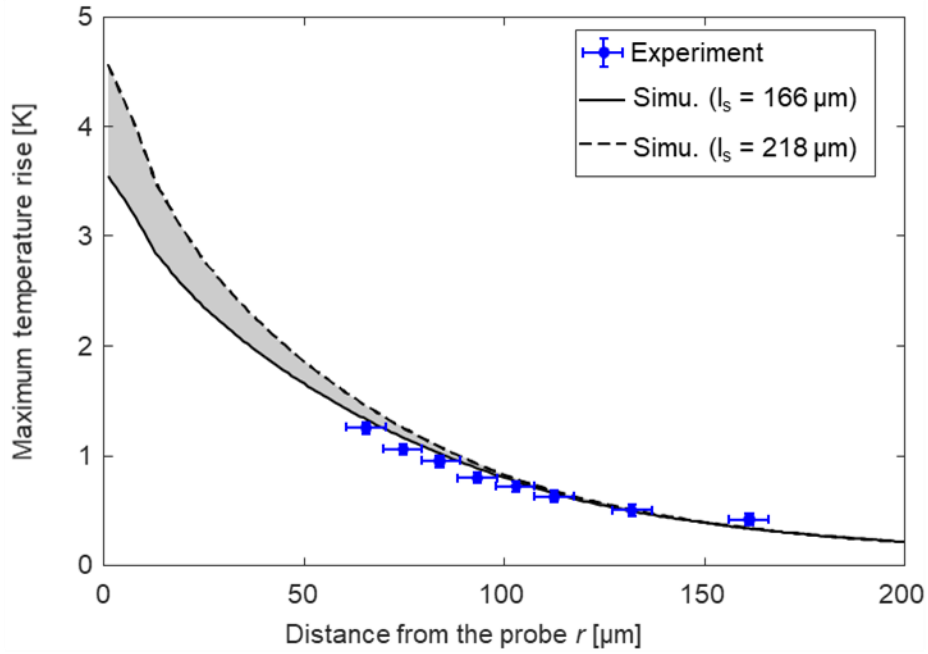

Figure 2.37 Maximum temperature rise at different distances from the holographic spot.

Consistent with the findings reported in Figure 2.35, Figure 2.37 shows that simulation results for l_s = 166 µm indicate a better agreement with the measurements than for l_s=218µm (except for l_s, all other simulation parameters are fixed). With this curve, our evaluation of the maximum temperature rise at the **centre** of a 12-µm diameter holographic spot is around 3.5K (**P = 180mW, t_{pulse} = 30ms**). This means that for a typical *in vivo* 2P optogenetics holographic stimulation (**λ = 1030nm**, **NA = 0.8**, **P = 10 - 50mW, t_{pulse} = 10 - 30ms**), the maximum temperature rise in the **centre** will not exceed a single K, as shown by simulation in Figure 2.38 and Figure 2.39 and summarised in the following table:

Table 1 Expected maximum temperature rise induced by a 12µm-diameter holographic spot at z=330µm under brain surface for different power(objective exit) and pulse duration. ΔT_{max} [K]

t_{pulse} [ms]	Maximum temperature rise ΔT_{max} [K]	
	P = 10 mW	P = 50 mW
10	0.14	0.70
30	0.20	0.99

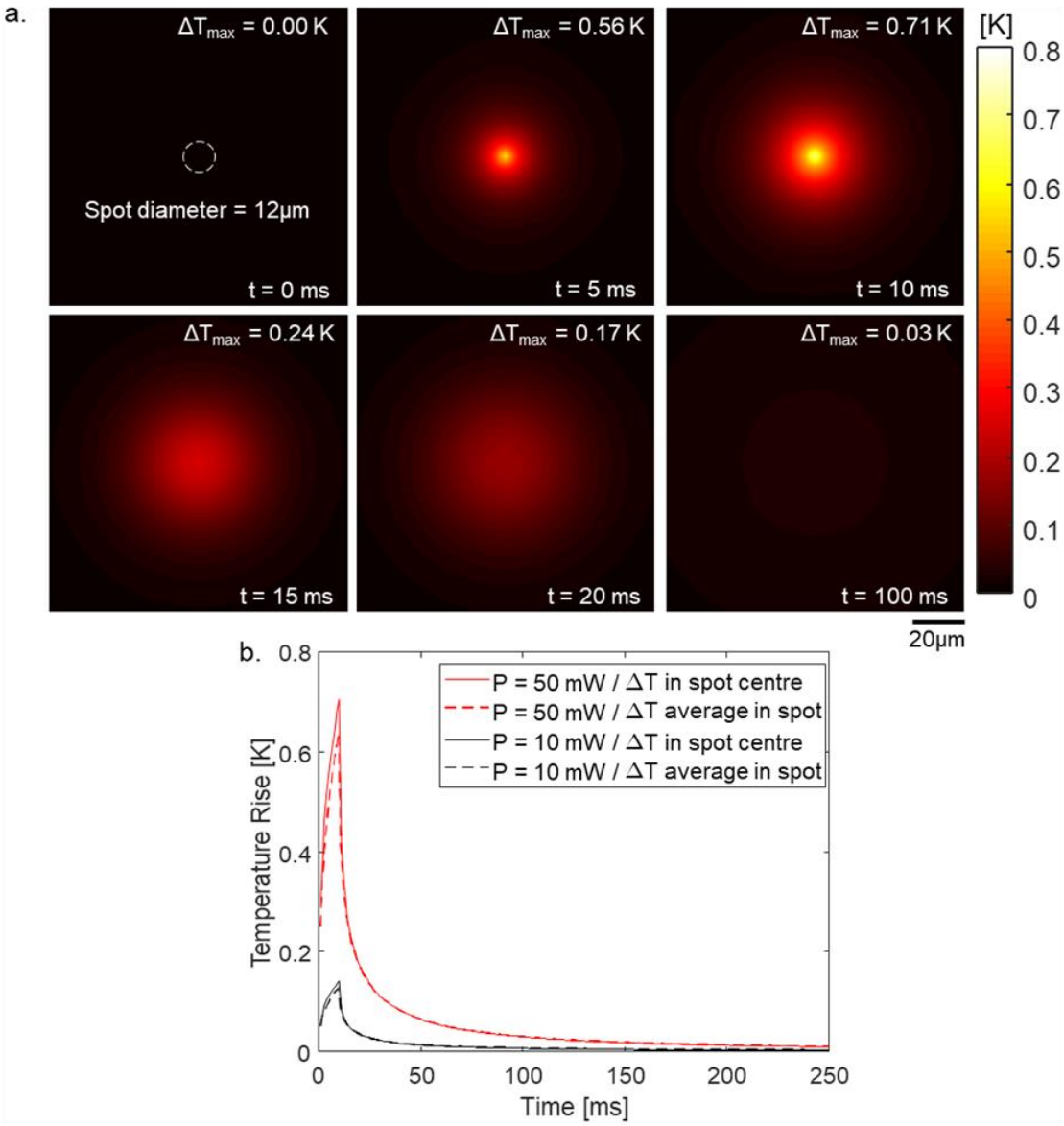

Figure 2.38 Expected temperature rise induced by a ***10ms-pulse duration****, 12μm-diameter, holographic spot at 330μm deep from the brain surface. (a) Temperature maps on the focal plane at different time delays from the start of the pulse; the pulse power is 50mW. (b) Temperature time-trace on the spot, the average value within the spot area (dashed line) and maximum value in the centre (line); red for 50mW pulse power and black for 10mW pulse power. Using scattering coefficient* l_s *=166μm, g = 0.9.*

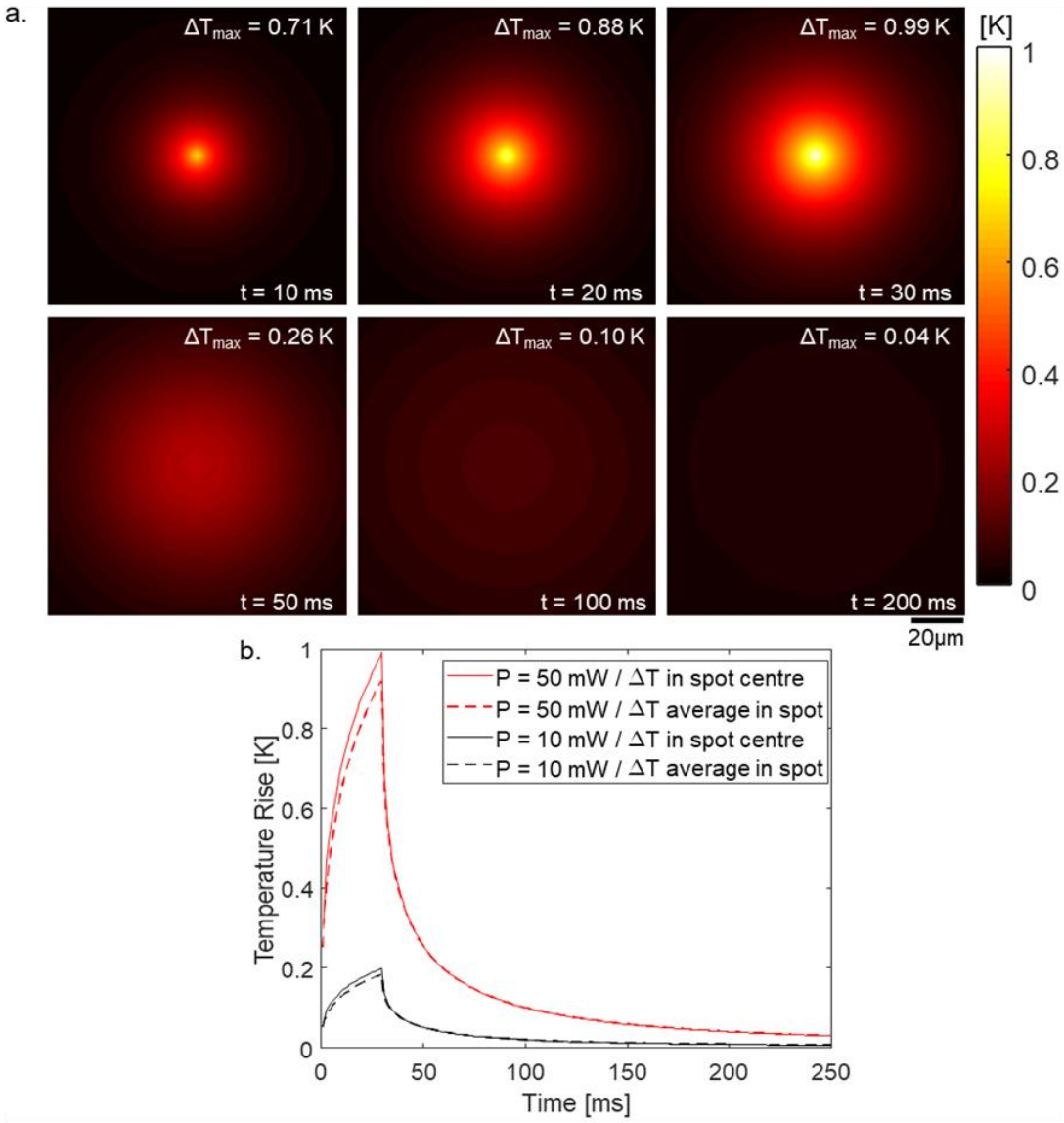

*Figure 2.39 Expected temperature rise induced by a **30ms-pulse duration**, 12µm-diameter, holographic spot at 330µm deep from the brain surface. (a) Temperature maps on the focal plane at different time delays from the start of the pulse; the pulse power is 50mW. (b) Temperature time-trace on the spot, the average value within the spot area (dashed line) and maximum value in the centre (line); red for 50mW pulse power and black for 10mW pulse power. Using scattering coefficient l_s =166µm, g = 0.9.*

2.7. Conclusion

We have designed and implemented an experimental system to measure *in vitro* and *in vivo* the temperature rise caused by microscale holographic illumination with a thermal sensitivity that can reach 0.05 K and millisecond temporal resolution.

The system uses the temperature dependence of the luminescence from Er/Yb glass particles to measure local temperature rises induce by two-photo illumination.

At first, we have embedded the Er/Yb glass particles in an agar solution and water and optimized the model parameters to reproduce the experimental data. Secondly, we have extended the use of our system for *in vivo* experiments in mice brain.

To this end, we have demonstrated a thermal endoscope where an Er/Yb glass particle is glued at the tip of a double-clad fibre inserted in a glass micropipette placed into the brain using a micromanipulator. A 12µm-diameter holographic spot was generated at 330µm under the brain surface using a 1030nm laser. For a single pulse of 180mW-power and 30ms-duration sent to the holographic spot, we observed at 66 µm away from the spot centre a maximum temperature rise of 1.25K at the end of 30ms illumination. Using our simulation model validated by the experimental data, we estimate the maximum temperature rise at the centre of the spot as 3.5K after 30ms illumination. For typical *in vivo* 2P optogenetic experiments, 5-30ms pulse duration and 10-50mW laser power is usually used. We estimate for a single stimulation pulse with 10ms-duration, the maximum temperature rise on the spot is 0.71K for 50mW-power (0.14K for 10mW-power); for 30ms-duration, the maximum temperature rise on the spot is 0.99K for 50mW-power (0.20K for 10mW-power). To our knowledge, such 2P optogenetics-induced temperature rises had never been measured so far.

We also show that, for a train of optogenetic stimulation pulses, the repetition rate should be limited in order to avoid heat accumulation from one pulse to the next. The heat accumulation is a linear process thus easy to deduce from our single pulse model. This simulation model can, therefore, predict the temperature rise caused by multiple pulses with various pulse durations or repetition rates.

This temperature endoscope was explicitly developed to predict temperature rise under a 2P optogenetics experiment but is actually quite versatile. It can also be applied in many other contexts, for example, to measure the temperature rise caused by 2P/3P imaging. The design of the endoscope can also be adjusted for different needs. For example, the double-clad fibre structure can be replaced by a thinner fibre structure, such as single-mode fibres or fibres with a tapered tip, particularly if lower sensitivities are acceptable (since thinner fibres will collect

luminescence less efficiently. With a thinner probe, one can measure closer to the target and cause less damage but sacrifice fast temporal resolution or thermal sensitivity.

---

1) The results presented in Section 2.3 of this chapter have been published in:

Temperature Rise under Two-Photon Optogenetic Brain Stimulation

Cell Reports **2018** 24 (5), 1243-1253.e5, DOI: https://doi.org/10.1016/j.celrep.2018.06.119

2) The rest of the results presented are collected in a manuscript in preparation.

Chapter 3

Reconfigurable Microscale Temperature Control

Summary

3.1. Introduction

In the previous chapter, we have demonstrated an experimental system to measure photoinduced temperature variations inside the brain with high temperature and spatiotemporal resolution. These experiments enabled the validation of a previously developed theoretical model to predict the temperature rise under different illumination conditions to prevent eventual thermal damages when designing an optical experiment on biological preparation.

Although the literature on thermal photodamage effect is very rich, only very few pieces of information are today available on the effects of small (few Ks) temperature increases on, e.g., the electrophysiological properties[114] of small cellular compartments (dendrites, axon, cell soma). Such effects are also the main focus of an emerging field in neuron science, called thermogenetics[146–148], where controlled heating is applied to locally modify neuronal activity. Also, the effects of local heating on organs, non-neuronal cells or organelles are of much interest to understand hyperthermia (e.g. surgery, or cancer cell destruction) and heat-induced metabolic changes. In all of these cases, an essential first step is to be able to deliver heat to living cells or organelles in a careful and localised fashion, in order to reach the targeted purposes efficiently, with minimal perturbation or damage to surrounding tissue. It is thus important to control precisely the spatial extent of temperature rises.

In addition to spatial control, temporal aspects are also essential. Some biological activities, such as, e.g. action potential onset in neurons, happen at the millisecond scale. Being able to modify the temperature on similarly short time scales is important. There are existing temperature control techniques at different scales based on different physics: heating ovens, chambers, chucks or stages, using various heat sources (electrical, optical, chemical, phase transitions…) and various means to carry heat to the target (diffusion in conductive materials, fluid transport…). However, very few techniques are suitable for biological applications. They either take too long to reach thermal equilibrium (thermalizing an incubator, or an entire microscope, takes minutes to hours), due to the large heated volume or cannot heat locally and homogeneously at the microscale. Due to thermal diffusion, the spatial and temporal aspects are intrinsically interwoven, and a faster and local thermal response adapted to cell activities is required.

Here we introduce a new temperature control technique using thermo-plasmonic nanoparticles as efficient optical absorbers to generate thermal effects associated to light shaping, which allows to control the local temperature at microscale reconfigurably with short response time and high precision. The applications of thermo-plasmonic gold NPs in biology

have already drawn much attention for decades. Gold NPs are stable and have excellent biological compatibility[149–151]. They display resonances that can be tuned from visible to NIR by modifying their morphology and size. Gold also has rich surface chemistry that allows functionalisation with various chemical compounds. This feature allows targeting chosen locations, cells, or organ types in the body. For example, it has been applied to the thermotherapy of cancers[152,153] using gold nanoshells. It can also be applied to neuron thermal activation by binding gold NPs to neuronal membrane proteins[154].

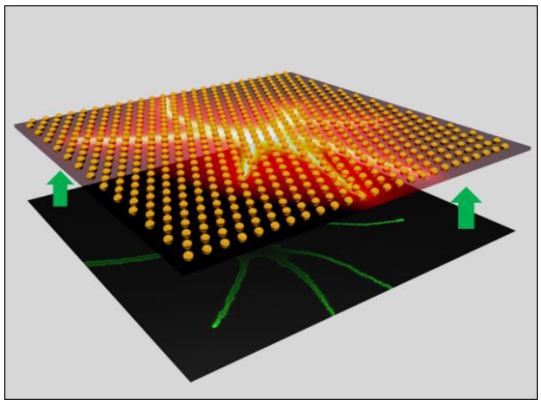

Figure 3.1 General illustration of microscale reconfigurable temperature control by light shaping. The upper layer is a substrate with a homogeneous thermo-plasmonic NPs carpet. The light pattern (in green) is projected on this layer to create temperature variations on it.

In this chapter, we will first introduce the physics and recent applications of plasmonic thermal effects in gold NPs. Then we will present an existing deterministic method that uses gold NP assemblies as light-to-heat transducers to control temperature rises at the microscale[155]. In this method, a pre-engineered array of NPs is employed, in which the collective heating effect caused by heat diffusion is carefully managed to obtain the desired heat distribution. Gold NPs are distributed on a substrate into a pattern that leads to a desired temperature rise result under homogeneous light illumination. However, this temperature pattern is fixed.

Inspired by this method, we will introduce a new method that tailors the illumination light intensity instead, while using homogeneous gold NPs distribution, as shown in Figure 3.1, to achieve the same purpose but in a reconfigurable manner. By changing the projected light pattern, temperature patterns can be tuned at will. This new method is demonstrated experimentally on a planar surface while the temperature map is measured using a wavefront sensing technique[103,104].

3.2. Plasmonic thermal effect of gold nanoparticles

3.2.1. Modelling of light absorption by a single particle

Plasmonic heating is caused by an enhanced light absorption during the surface plasmonic resonance process. Gold nanoparticles (NPs) feature remarkable optical properties allowing plasmonic processes. They support resonances in electron plasma-photon known as Localized Surface Plasmons (LSPs) that can be excited upon illumination. This strong electronic movement in a lossy, or resistive, metal such as gold induces Joule heating. Depending on the morphology and dielectric environment of the NPs, those resonances can be tuned from the visible to the near-infrared frequency range. LSPs are responsible for the enhanced absorption and scattering of light in these NPs, which was considered as an unwanted effect for a long time. However, it was realized recently that this effect can transform the NP into a remotely-controllable nano heat source, providing a powerful way of thermally-induced phenomena at the nanoscale.[156,157]

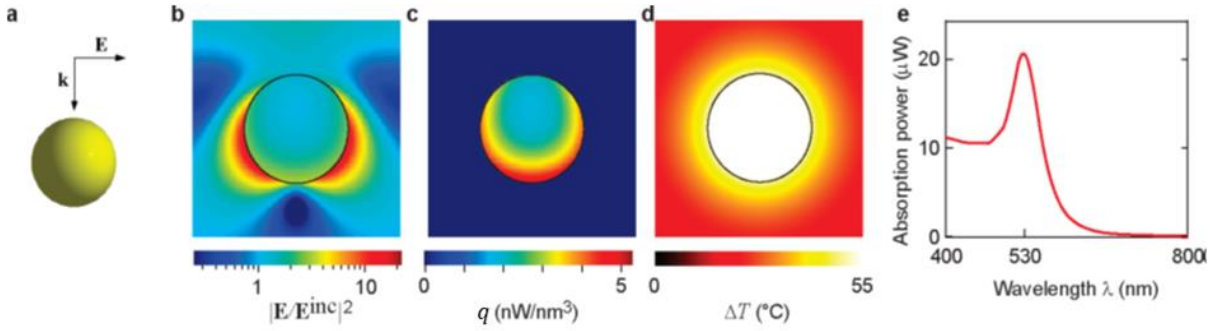

Figure 3.2 Photothermal heating of a 100 nm gold nanosphere placed in water. (a) Schematic view of a nanosphere with the external electric field E and wavevector k of the illumination light, (b) electric near-field intensity normalized to the incident field intensity, (c) heat generation density, and (d) equilibrium distribution of temperature increases for a light wavelength of λ=530 nm, (e) absorption power as a function of light wavelength. The light incident intensity is 1 mW/μm² for all cases. (Figure adapted from ref[157]*)*

To present the physics of plasmonic heating, we consider a simple model: a gold nanosphere with complex relative permittivity $\varepsilon(\omega)$ is immersed in a transparent dielectric medium of real relative permittivity $\varepsilon_s = n_s^2$, n_s being the refractive index. This nanosphere is illuminated by a light with a complex amplitude $\mathbf{E_0}(\mathbf{r})$, defined such that $\mathbf{E_0}(\mathbf{r},\mathrm{t}) = Re\left[\mathbf{E_0}(\mathbf{r})\mathrm{e}^{\mathrm{i}\omega\mathrm{t}}\right]$; ω is the angular frequency, defined as $\omega = c_0 k_0 = \frac{c_0 k}{n_s}$, where c_0 is the speed

of light in vacuum, k_0 and k are the wave vectors in free space and in the medium, respectively, as illustrated in Figure 3.2(a).

LSPs are generated by the interaction between light and conductive NPs of a size comparable to or smaller than the light wavelength. Here, the sphere radius *R* is much smaller than the wavelength (tens of nm), and the NPs can be considered as an electromagnetic dipole. Under this assumption, the sphere polarizability reads:

$$\alpha(\omega) = 4\pi R^3 \frac{\varepsilon(\omega) - \varepsilon_s}{\varepsilon(\omega) + 2\varepsilon_s}. \qquad \textit{Equation 3.1}$$

and relates the complex amplitude of the polarization vector of the NP to the excitation field via $\mathbf{P} = \varepsilon_0 \varepsilon_s \alpha \mathbf{E_0}$. From Equation 3.1, the resonance occurs at a frequency ω where the bottom part of the fraction approaches zero, i.e. $\varepsilon(\omega) \approx -2\varepsilon_s$. This can occur at visible frequencies in some noble metals and leads to a high polarizability value $\alpha(\omega)$. However, the dipolar approximation only holds for small particles. More complex models are required for larger spheres, such as the Mie theory, which considers retardation effects in particles with non-negligible sizes compared to the wavelength. For NPs with more complex geometries, numerical simulations such as *discrete dipole approximation (DDA)* can be used to find the resonance wavelength[158].

This plasmonic resonance is responsible for peaks in both light absorption and scattering. For example, in a spherical gold NP with a diameter smaller than 30 nm in water, this resonance occurs around λ=530 nm[159]. The efficiency of these processes can be described by the following absorption (σ_{abs}) and scattering (σ_{scat}) cross-sections:

$$\sigma_{abs} = kIm(\alpha) - \frac{k^4}{6\pi}|\alpha|^2 \qquad \textit{Equation 3.2}$$

$$\sigma_{scat} = \frac{k^4}{6\pi}|\alpha|^2 \qquad \textit{Equation 3.3}$$

$$\sigma_{ext} = \sigma_{abs} + \sigma_{scat} = kIm(\alpha) \qquad \textit{Equation 3.4}$$

Depending mostly on the morphology of NPs, the relative efficiency of absorption and scattering processes is often quantified by the photothermal efficiency $\mu = \frac{\sigma_{abs}}{\sigma_{scat}}$ [160,161]. For example, in water, for gold NPs smaller than 90 nm, absorption is the dominant effect, while for larger gold NPs, scattering dominates. According to this property, one can design NPs that are optimised for light absorption and heat conversion.

Using the absorption cross-section σ_{abs}, the power absorbed by a NP illuminated with an irradiance *I* reads:

$$Q = \sigma_{abs} I \qquad \textit{Equation 3.5}$$

It can also be derived from the heat power density $q(\mathbf{r})$ inside the NP such that $Q = \int_V q(\mathbf{r})\, d^3r$, with V the spatial domain limited by the volume of the NP. $q(\mathbf{r})$ is generated via the Joule effect and reads[162,163]:

$$q(\mathbf{r}) = \frac{1}{2} Re[\mathbf{J}^*(\mathbf{r}) \cdot \mathbf{E}(\mathbf{r})] \qquad \textit{Equation 3.6}$$

where $\mathbf{J}(\mathbf{r}) = i\omega\mathbf{P}$ is the electronic current density, and **E** is the electrical field inside the NP. As $\mathbf{P} = \varepsilon_0 \varepsilon(\omega)\mathbf{E}$, $q(\mathbf{r})$ is finally:

$$q(\mathbf{r}) = \frac{\omega}{2} \varepsilon_0 Im\big(\varepsilon(\omega)\big)|\mathbf{E}(\mathbf{r})|^2 \qquad \textit{Equation 3.7}$$

3.2.2. Heat diffusion for a single particle model

For a single gold NP under continuous-wave illumination, the steady-state temperature distribution $T(\mathbf{r})$ inside and outside of the NP should then be resolved with the heat diffusion equation:

$$-\kappa_{gold} \nabla^2 T(\mathbf{r}) = -q(\mathbf{r}) \text{ for } |\mathbf{r}| \leq R \qquad \textit{Equation 3.8}$$

$$\kappa_{water} \nabla^2 T(\mathbf{r}) = 0 \text{ for } |\mathbf{r}| > R \qquad \textit{Equation 3.9}$$

Here, we consider a single NP immersed in water and a visible-range illumination. The light absorption in water can be neglected at the wavelength we use (532 nm); Equation 3.8 and Equation 3.9 only considers heat sources inside the sphere ($|\mathbf{r}| \leq R$). The large thermal conductivity of gold ($\kappa_{gold} = 318\ Wm^{-1}K^{-1}$), its large contrast with the conductivity of water ($\kappa_{water} = 0.6\ Wm^{-1}K^{-1}$), and the small size of the particle mean that the temperature can be considered homogeneous inside the particle although $q(\mathbf{r})$ is not necessarily uniform. In other words, heat diffuses so fast inside the NP that the temperature inside the NP is nearly uniform compared to the temperature distribution in water. This Uniform Temperature Approximation

(UTA) is commonly used to solve the problem[157]. Under this approximation, the temperature increases in the particle and in the surrounding medium, deduced from the heat diffusion equation, can be approximated as[164]:

$$\Delta T(\mathbf{r}) \approx \Delta T_{NP} = \frac{Q}{4\pi\kappa_{water}R} \text{ for } |\mathbf{r}| \leq R \qquad \textit{Equation 3.10}$$

$$\Delta T(\mathbf{r}) = \frac{Q}{4\pi\kappa_{water}r} = G_T^{ST}.Q \text{ for } |\mathbf{r}| > R \qquad \textit{Equation 3.11}$$

where $\Delta T_{NP} = \frac{Q}{4\pi\kappa_{water}R}$ is generated by the absorbed power $Q = \sigma_{abs}I = \int_V q(\mathbf{r})\, d^3r$ in a homogeneous medium of thermal conductivity κ_{water}, G_T^{ST} is the thermal Green's function in steady-state $G_T^{ST} = \frac{1}{4\pi\kappa_{water}r}$ defined in Chapter 1 (Equation 1.11). The temperature diffuses as $\frac{1}{r}$ outside of the NP heat source. Taking $R = 1$ and $\Delta T_{NP} = 1$, the temperature increase has a radial distribution which is shown in Figure 3.3.

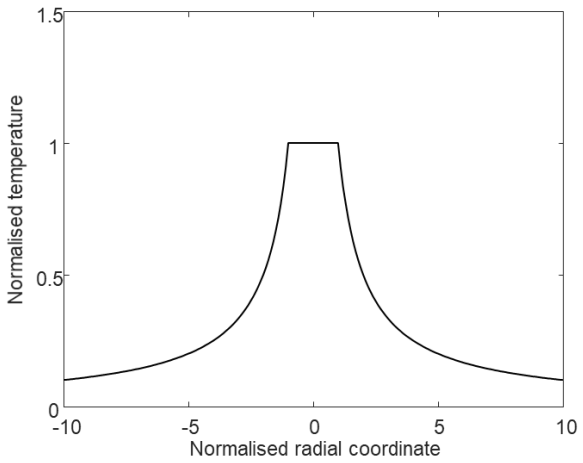

Figure 3.3 Temperature profile with a spherical gold NP heat source, according to Equation 3.10 and Equation 3.11, using normalised coordinates $R = 1$ *and* $\Delta T_{NP} = 1$.

When modelling the 2D temperature induced by a collection of nanoparticles, collective effects must be taken into account. This can be achieved by calculating the convolution of the heat source distribution with the thermal Green's function in steady-state G_T^{ST}, as discussed in the following sections.

3.3. Reconfigurable temperature control using light shaping

3.3.1. Temperature shaping by gold nanoparticles assemblies

By distributing gold NPs into the targeted medium and using light at a wavelength overlapping their plasmonic resonance, one can efficiently heat the NPs as well as the surrounding medium. Since heat is a diffusive phenomenon, it is harder to manipulate than light, which is a propagating phenomenon, but using NPs as light-to-heat transducers offers an efficient way to turn a light distribution into a heat distribution. However, the relation between light absorption and the temperature is not straightforward because of heat diffusion: uniform light absorption does not lead to uniform temperature distribution, an issue that needs to be carefully addressed.

To solve this issue, we calculate an appropriate **Heat Source Density** (HSD) to pre-compensate heat diffusion and create a temperature profile that optimally approaches desired values. This approach has been proposed and demonstrated experimentally by Baffou et al. in 2014 by locally engineering the light absorption of the substrate[155]. Assemblies of metal NPs were fabricated by e-beam lithography[165] on a thermally insulating, 2D substrate, with a local density of absorbers matching the desired HSD. Homogeneous illumination of these assemblies then yielded the desired temperature distribution. The average temperature could be changed easily by tuning the optical intensity. However, the temperature distribution could not be modified after e-beam fabrication: the thermal pattern was fixed.

Here, we show that a homogeneous array of plasmonic NPs on glass can also be used to obtain a chosen temperature pattern. Instead of shaping the substrate itself, we propose to use an absorbing layer that is homogeneous at the wavelength scale and to pattern the illumination to produce the desired HSD, as illustrated in Figure 3.1. Among the various available light-patterning techniques, we chose to use a phase Spatial Light Modulator (SLM) as it provides interesting speed and good power-efficiency. Using it to engineer the wavefront properly in the Fourier plane, we created chosen intensity patterns in the image plane to illuminate the homogeneous NPs array.

3.3.2. Collective effects in heat diffusion

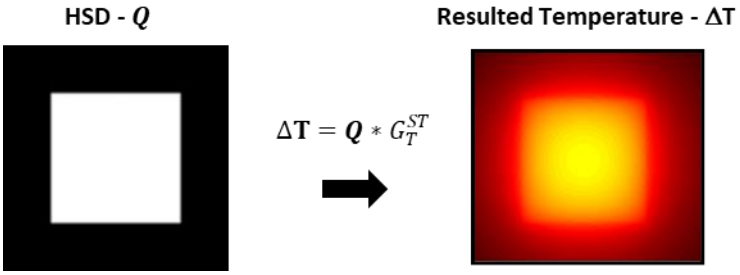

Figure 3.4 Calculated temperature rise (right) induced by a homogeneous HSD applied within a square region (left). The temperature is clearly higher at the centre of the square region than at the edges.

Here, we aim at creating a 2D temperature pattern in a microscopic region of a macroscopic sample with thermal conductivity κ. The whole sample typically has cm-range dimensions. It can therefore be assumed to remain at a constant bulk temperature T_0, or can be actively stabilized at T_0 if necessary. The 2D domain of interest (***D***), where $\Delta T(r)$ is targeted, is meshed using N identical square units, each with an area a^2 and an identical average absorption cross-section σ, since the substrate has a homogeneous absorption at the scale of a (the number of absorbing nanoparticles within a^2 is large enough to neglect variations). For each unit cell i, we note Q_i the heat source (in W) and ΔT_i the temperature rise. The ΔT_i distribution in the sample is actually the convolution of the HSD with the thermal Green's function in steady-state $G_T^{ST} = \frac{1}{4\pi\kappa_{water}r}$, as mentioned in Chapter 1 (Equation 1.11).

A relatively natural idea in order to obtain a homogeneous temperature within a chosen domain of interest ***D*** (e.g. a square) would be to apply a homogeneous HSD within the domain of interest ***D***. However, as shown in Figure 3.4, simulations indicate that the resulting temperature increase profile has a hot centre. It is not hard to understand that the centre receives thermal contributions from all neighbouring heat sources within the square domain, whereas the edges of the square, for instance, do not. These collective effects have been discussed in detail in ref[166].

3.3.3. Pre-compensating the collective effect

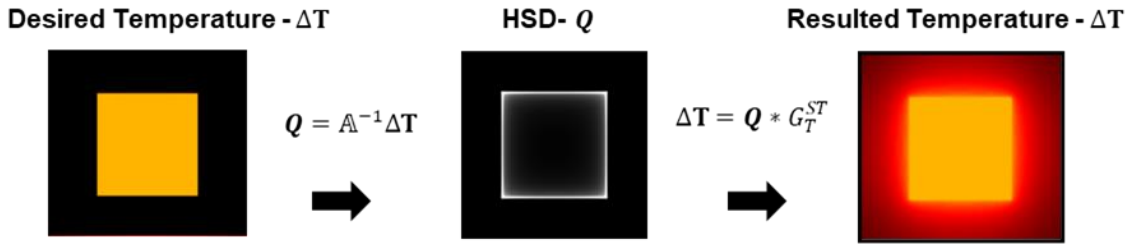

Figure 3.5 Calculated HSD yielding a homogeneous temperature rise within a targeted area and resulting temperature rise.

If the temperature is obtained by the convolution $\boldsymbol{\Delta T} = \boldsymbol{Q} * G_T^{ST}$, it appears reciprocally that the HSD Q_i which must be applied to a sample in order to obtain a chosen temperature pattern $\boldsymbol{\Delta T}$ can be calculated by deconvolving by G_T^{ST}. This deconvolution can be computed numerically by a matrix inversion restricted to the domain $\boldsymbol{D}$, as described in ref[155]. When applying a spatial HSD noted $\mathbf{Q}$ in vector form ($\mathbf{Q} = (Q_i)_{i\in[1,N]}$), where "$i$" designates one of the N location coordinates, the resulting temperature increase distribution $\mathbf{\Delta T}$ ($\mathbf{\Delta T} = (\Delta T_i)_{i\in[1,N]}$) can be calculated using a simple matrix multiplication: $\mathbf{\Delta T} = \mathbb{A}\mathbf{Q}$, where $\mathbb{A}$ is an $N \times N$ coupling matrix defined by:

$$\mathbb{A}_{ij} = \begin{cases} \frac{\ln(1+\sqrt{2})}{\pi\kappa a}, i = j \\ \frac{1}{4\pi\kappa r_{ij}}, i \neq j \end{cases} \qquad \textit{Equation 3.12}$$

Each term $\mathbb{A}_{ij}$ corresponds to the contribution of the heat deposited in region j to the temperature of region i, with r_{ij} the distance between these two regions. Inverting this matrix $\mathbb{A}$ provides a way to calculate the HSD $\mathbf{Q}$ yielding the desired temperature map $\mathbf{\Delta T}$, which writes: $\mathbf{Q} = \mathbb{A}^{-1}\mathbf{\Delta T}$.

3.3.4. Temperature shaping implementation

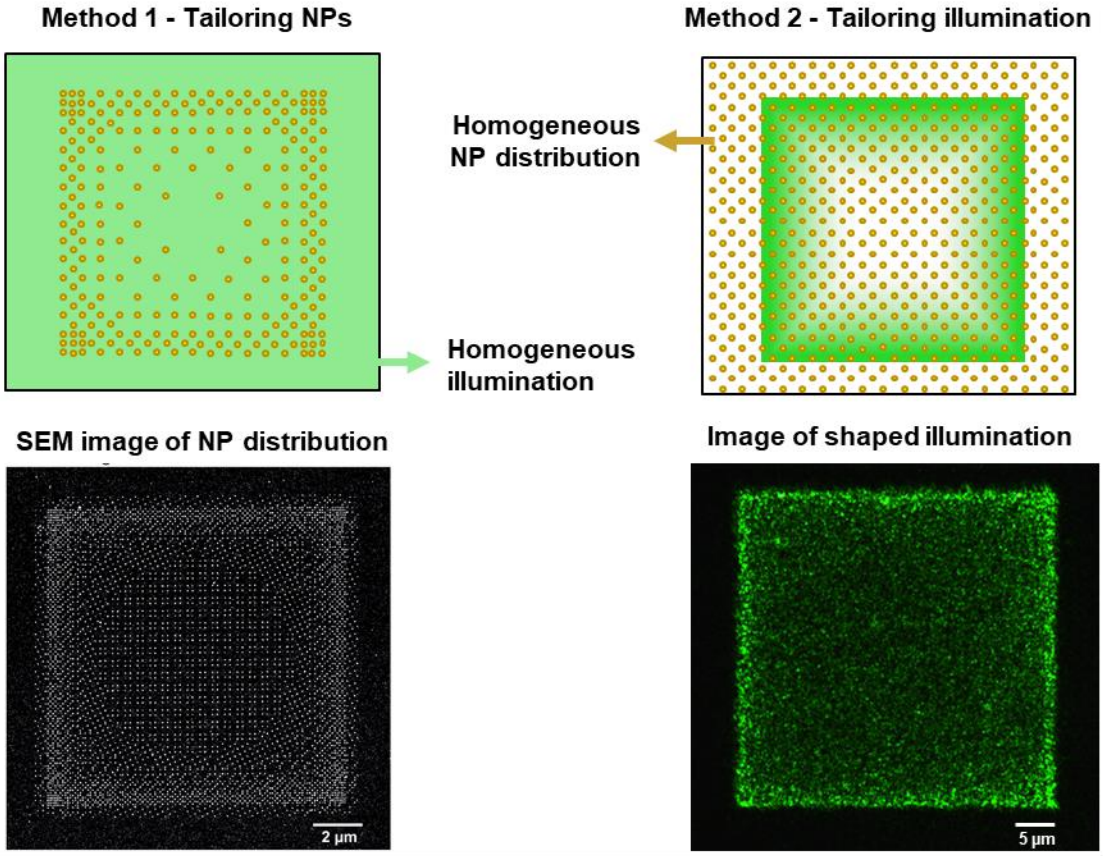

Figure 3.6 Comparison of two temperature shaping methods. Method 1(left column): NP distribution tailoring while using a homogeneous illumination (top left sketch). The SEM image (bottom) of NP distribution is adapted from ref [155]*. Method 2(right column): Illumination tailoring on a homogeneous NP substrate (top right sketch). The experimental image of the corresponding shaped illumination (bottom right) shows the backscattering by the substrate, which reflects the illumination pattern. The inhomogeneity of light intensity is due to speckle, which will be discussed later in 3.5.4.1.*

As mentioned at the beginning of 3.3.1, there are two ways to obtain a tailored HSD: tailoring the distribution of NPs or tailoring the intensity of illumination. The 1st method is illustrated in Figure 3.6 (left): metal NPs are patterned by lithography on a 2D substrate to reproduce the calculated HSD. Under homogeneous illumination at their plasmonic resonance wavelength, the desired temperature rise can be created. This method developed by Baffou et al. in 2014 was named TSUNA for "Temperature Shaping Using Nanoparticle Assemblies"[155]. It is deterministic and effective. However, e-beam lithography is costly, and once the pattern is determined and fabricated, it cannot be changed. This feature is particularly problematic for

biological applications since the position and shape of the cells (or organelles) is not known in advance.

Instead of shaping the NP distribution, we chose to shape the light distribution under the microscope and use a distribution of plasmonic NPs homogeneous on the planar substrate (Figure 3.6–Method 2). As $Q = \sigma_{abs} I$, the light intensity pattern is identical to the HSD pattern. The substrate absorbs the light energy at the resonant wavelength and creates a designed temperature map. Following a workflow that will be discussed in 3.4.3, one can change the temperature map at will.

3.4. Experimental setups and methods

3.4.1. Optical path of the setup

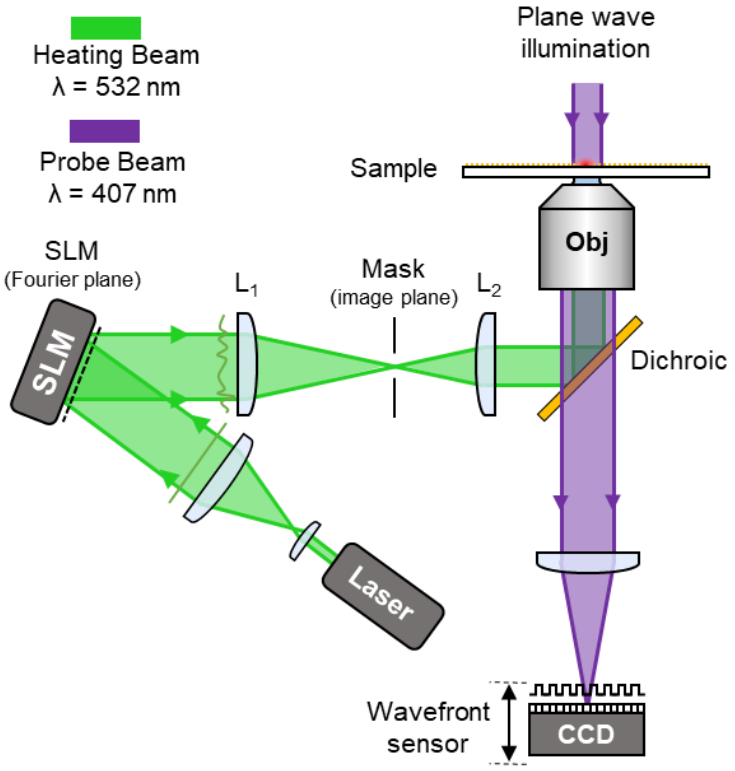

Figure 3.7 Experimental setup for temperature shaping and temperature imaging

The optical path of the experimental setup is shown in Figure 3.7. There are two beams combined in this setup for separated functions: a heating beam at λ = 532nm and a probe beam at λ = 407nm. The heating beam is a plane-wave coming out of the laser source and is expanded to illuminate all the SLM pixels. The SLM modifies the wavefront and projects the desired light intensity pattern, identical to the HSD pattern, onto the sample plane to illuminate the homogeneous surface absorber. There is an intermediate image plane between the SLM and objective, where a spatial mask cancels higher-order images and the 0-order diffraction peak. Another plane-wave passes through the sample from the top of the sample, illuminating a region that includes the heated sample. The sample is then imaged on a wavefront sensor for further thermal imaging analysis based on wavefront sensing.

3.4.2. Homogeneous surface absorber

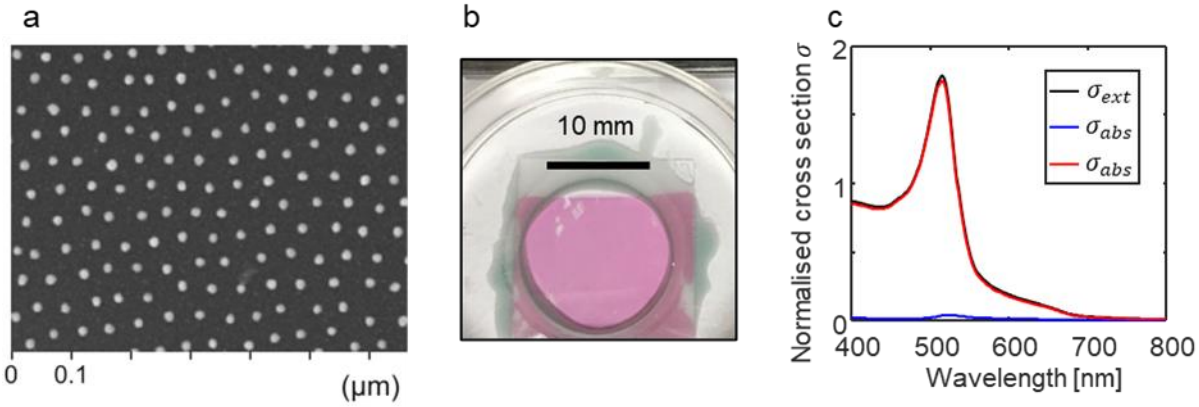

Figure 3.8 (a) Example of a SEM image of a quasi-hexagonal array of gold NPs obtained by diblock copolymer lithography (adapted from ref[166]*). (b) Image of the sample fixed in a petri dish (a window is opened at the centre of the petri dish), taken by a simple cell phone camera with white background. (c) Cross-section of extinction, absorption and scattering for spherical gold nanoparticles of 28 nm-diameter, normalised by πR² where R is the radius of the sphere. The calculation is done using the Mie theory*[167].

In order to efficiently convert optical intensity into heat, the substrate has to be covered with a homogeneous surface absorber, ideally with narrow-band absorption to allow transmission imaging at other wavelengths. We used a substrate consisting of an array of 28 nm-diameter spherical gold NPs on a glass coverslip, with uniform quasi-hexagonal distribution; an example is shown in Figure 3.8(a), and a 72 nm average interparticle distance. The sample was made by diblock copolymer micellar lithography, based on a protocol developed by J. Polleux[165]; an image is shown in Figure 3.8. Under illumination at NP resonance wavelength, near λ = 532 nm, much of the optical energy is converted into heat, an efficient process sometimes called thermo-plasmonic conversion. This localized heat then diffuses into the surrounding medium. The non-percolated gold NPs are not expected to substantially change the lateral heat diffusivity, which is essentially that of the glass substrate. The plasmonic resonance wavelength of the particles is well adapted to efficient absorption over a relatively narrow band near λ= 532 nm, and the biocompatibility of the NP system is excellent[156].

There are two distinct regimes describing the temperature repartition for a gold NPs array under CW illumination: a) the temperature confinement regime, where the temperature increase is confined to the vicinity of each nano heat source, and b) the temperature

delocalization regime, where temperature is smooth throughout the whole illuminated region[166]. Figure 3.9 shows examples of the two regimes. Figure 3.9(a) is in the temperature confinement regime, whereas Figure 3.9(b) in the temperature delocalization regime. A factor ζ is defined in the publication of Baffou et al. 2013[166] to predict which regime applies (for a 1D array: $\zeta_1 = \frac{p}{2Rln(N)}$, for 2D distribution: $\zeta_2 = \frac{p^2}{3LR}$, where *p* is the interdistance, *R* the radius of nanosphere, *L* the characteristic size of the illuminated area and *N* the number of particles). The interparticle distances, the diameter of NPs and number of illuminated NPs (or characteristic size of the illuminated zone) can all contribute to this factor. In our case, the size of the NP is driven by the resonance wavelength (28 nm and 532 nm respectively), and the interparticle distance is the main parameter to reach the temperature delocalization regime (b), which ensures a smooth temperature all over the NP carpet under CW illumination despite the nanometric size of the NPs. With a 72 nm interdistance, ζ is much smaller than 1, which means that we are in the temperature delocalization regime and the NPs layer can be considered as a spatially homogeneous absorbing layer.

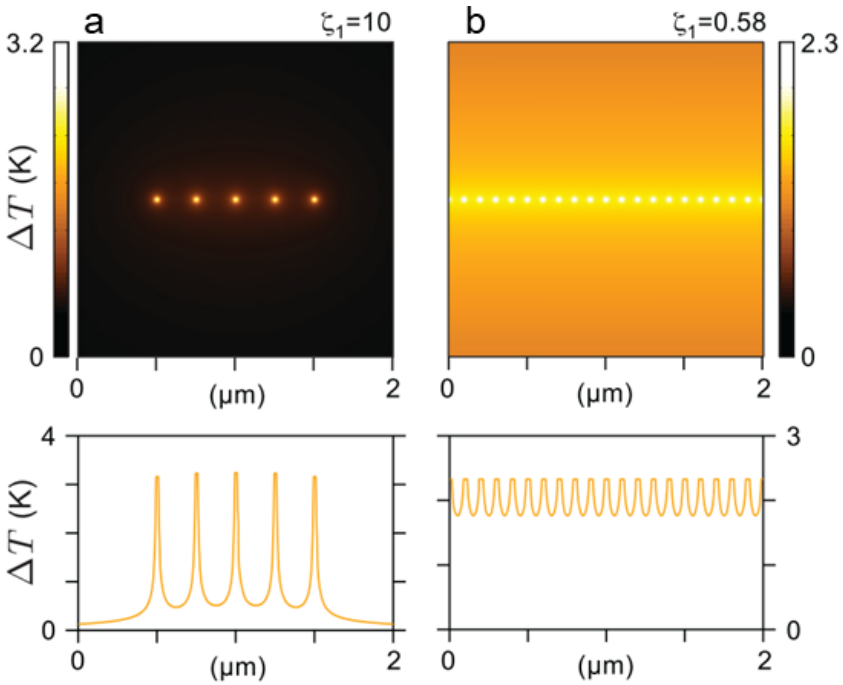

Figure 3.9 Calculated temperature distribution across a NP chain with different interparticle distances, illuminated in CW regime. (a) 5 NPs with 15nm diameter and 250nm interparticle distance; (b) 1001 NPs (only a few shown in the figure) with 25nm diameter and 100nm interparticle distance. (Figure adapted from ref[166]*)*

3.4.3. Phase-only SLM and Gerchberg-Saxton algorithm for light shaping

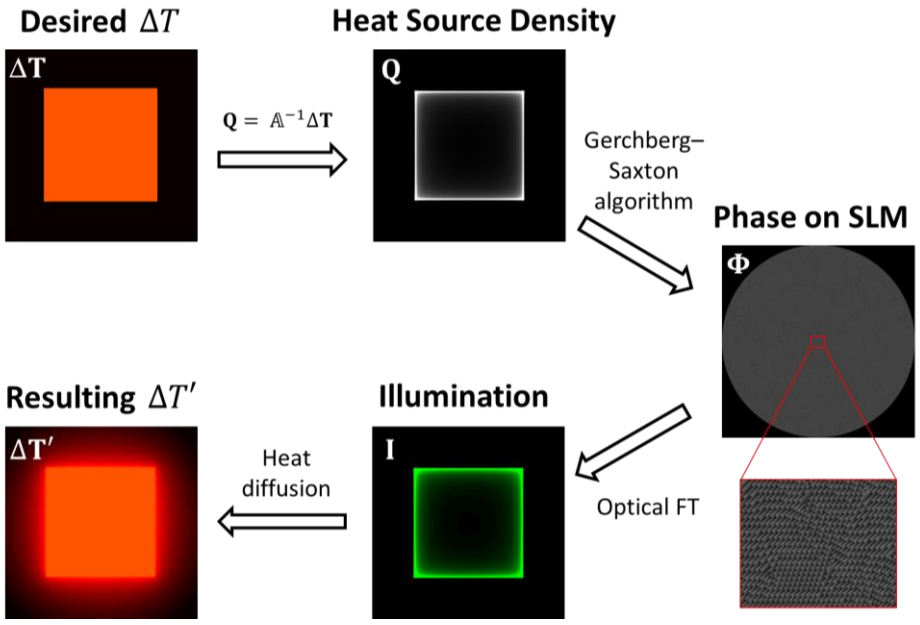

Figure 3.10 Reconfigurable temperature-shaping workflow (calculated images). $\Delta \boldsymbol{T}$ *is the desired temperature increase distribution;* $\boldsymbol{Q}$ *is the associated HSD distribution;* $\boldsymbol{\Phi}$ *is the corresponding phase distribution in the Fourier plane of the illumination pattern;* $\boldsymbol{I}$ *is the light intensity distribution in the sample plane;* $\Delta \boldsymbol{T}'$ *is the resulting temperature increase distribution.*

As discussed in Section 3.3.4, the HSD (Heat Source Density) can be created by projecting onto the surface an optical intensity pattern $\mathbf{I} = \frac{\mathbf{Q}}{\sigma}$. While several techniques allow light patterning, parallel illumination techniques based on SLMs have the advantage of offering much higher temporal resolution compared to scanning-based methods. Acting either on the phase or the intensity of the incident beam, SLMs provide in both cases an arbitrarily-defined intensity distribution of light in the focal plane of the objective. The main drawback of intensity modulators (such as Digital Mirror Devices) is an extremely poor efficiency when creating sparse targets, as most of the light is rejected out of the optical path and does not reach the sample. Here, we modulate the phase using a Liquid Crystal SLM in order to preserve light power and efficiently generate heat sources.

The appropriate phase pattern $\boldsymbol{\Phi}$ (see Figure 3.10) is displayed on the SLM located in the Fourier plane of the microscope and illuminated by a plane wave. We use the iterative Gerchberg-Saxton algorithm[65], which is one of the most common numerical techniques to calculate $\boldsymbol{\Phi}$. As shown in Figure 3.7, this pattern is projected by lens L_1, which acts as a Fourier transformer, and imaged in an intermediate plane where a low-pass spatial filter mask cancels

unwanted higher diffraction orders and zero-order diffraction peak. After the lens L_2 and the microscope objective, the desired intensity pattern **I** (see Figure 3.10) is projected in the substrate plane and generates the temperature distribution $\Delta\mathbf{T}'$ (see Figure 3.10). Within the chosen domain of interest ***D***, this algorithm provides the targeted temperature map ($\Delta\mathbf{T}' = \Delta\mathbf{T}$). One should note, however, that since the temperature distribution is not constrained outside of ***D***, temperature freely decays in $\frac{1}{r}$ due to thermal diffusion outside of ***D***.

Moreover, since we only use heat sources, and no cooling sources (all values in the **Q** vector are strictly positive), some desired shapes with temperature gradients steeper than the $\frac{1}{r}$ decay imposed by diffusion are impossible to reproduce[155]. Finally, we must note that the method is only adapted to 2D temperature control. A temperature decay also appears along the vertical *z*-direction away from the targeted plane, and depends on *z* and on the lateral size of the target[155], but is not controlled in the present configuration.

3.4.4. Temperature imaging using wavefront sensing

To test the reliability of the heating result, we used a wavefront-imaging-based temperature imaging method to measure and validate the temperature variation maps caused by nanoscale heating sources. This method was originally proposed by Serge Monneret and first demonstrated by Guillaume Baffou and Pierre Bon in 2012[103]. The refractive index of most materials is temperature-dependent. As shown in Figure 3.11(a), temperature changes in the medium surrounding the NPs will therefore cause refractive index variations, which can be measured to deduce temperature. To probe the refractive index, we use a plane wave at a wavelength away from the NP resonance, for which the NP carpet is mostly transparent. The thermally-induced refractive index variations modify this plane wavefront and leave a fingerprint of the temperature distribution. We use a high-resolution wavefront sensor (SID4, Phasics) to analyse this perturbated wavefront, from which we deduce the temperature using a dedicated calculation.

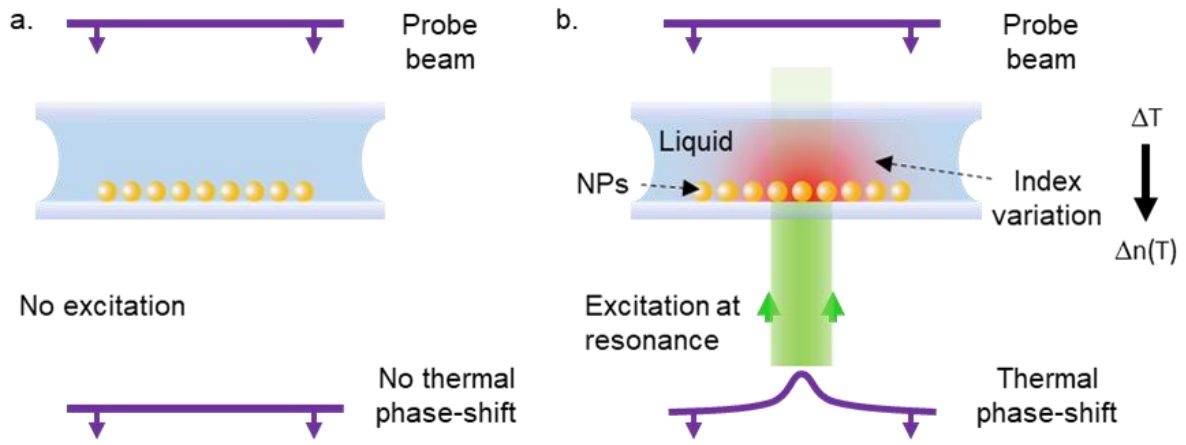

Figure 3.11 Temperature imaging using wavefront sensing. (a) In the absence of excitation light, the probe beam has no thermally-induced wavefront distortion. This is considered as the "reference" wavefront. Note that the static refractive effects induced by the particles and the optics are neglected in this scheme. (b) While the sample is illuminated by light at the plasmonic resonant frequency, the increase of temperature in the medium changes the local optical refractive index. A plane wave that is out of resonance with the NPs will be deformed by the local variation of the refractive index. This phase-shift contains temperature information.

3.4.4.1. Thermo-optical effects

The main principle behind this thermometry method is the thermo-optical effect. The refractive index of most materials is temperature-dependent, and the relation can be described by a Taylor expansion of the refractive index with temperature[168]:

$$n(T) = n(T_0) + (T - T_0) \cdot \frac{\partial n}{\partial T}(T_0) + \cdots + \frac{(T - T_0)^m}{m!} \cdot \frac{\partial^m n}{\partial T^m}(T_0) + o(T^m) \qquad \textit{Equation 3.13}$$

In our experiment, we use glycerol as the thermo-responsive liquid to increase the thermo-optical effect and improve the signal to noise ratio of the measurements. For temperature rises below typ. 60°C, we can limit ourselves to the first term of the Taylor Series[169]. This linear approximation is commonly used with most materials, over limited (a few tens of K) temperature ranges:

$$n(T) = n(T_0) + (T - T_0) \cdot \frac{\partial n}{\partial T}(T_0) \qquad \textit{Equation 3.14}$$

Thus, we have:

$$\Delta n = n(T) - n(T_0) \approx \frac{dn}{dT}(T_0) \cdot \Delta T, \qquad \textit{Equation 3.15}$$

with $\Delta T = T - T_0$. In order to describe the wavefront perturbation caused by the temperature rise in the sample, we need to apply Equation 3.15 to a 3-dimensional space. While the probing beam passes through the heated region, the refractive index variation in the medium will induce an **Optical Path Difference** (OPD), as illustrated in Figure 3.11(a). This OPD is the integral of the refractive index change Δn along the optical path. It can be measured in one plane after propagating through the sample.

To further simplify the demonstration, we first consider the case of a single nano-heater and consider it as a point source. In cylindrical coordinates, ρ being the radial coordinate, with a z-axis corresponding to the optical axis, as shown in *Figure 3.12*, the wavefront perturbation OPD(ρ) reads:

$$OPD(\rho) = \int_{-\infty}^{+\infty} \Delta n(\rho, z) dz \qquad \textit{Equation 3.16}$$

It is worth mentioning that experimentally, while the probe wave propagates through the sample, it accumulates a thermo-optically-induced OPD in the glass substrate[170] ($\frac{dn}{dT}$ = 3 .10^{-6} K^{-1}) and in a thin layer (thickness h = 1 mm) of glycerol[169] ($\frac{dn}{dT}$ = -2.3 .10^{-4} K^{-1}). Light then propagates in air ($\frac{dn}{dT}$ = -0.7 10^{-8} K^{-1}), or immersion media (water, oil) before it reaches the objective, but the fast 1/z longitudinal decay of temperature means that their contribution to the thermo-optical OPD is negligible. In the sample itself, considering the large difference between the thermo-optical coefficients (2 orders of magnitude), the wavefront distortion in glass is negligible, and we can safely assume that only the glycerol layer contributes to the thermo-optical OPD.

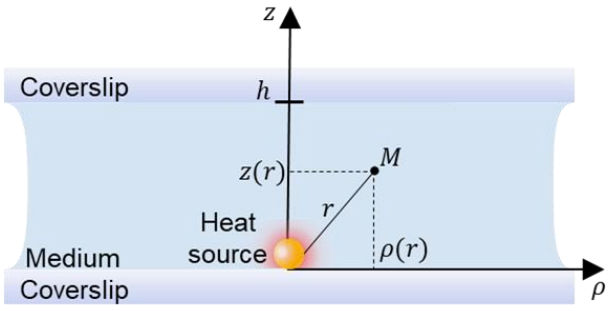

Figure 3.12 Coordinates for calculating the wavefront perturbation OPD(ρ)

Relating the heating and thermo-optical terms from Equation 3.11, Equation 3.15 and Equation 3.16, we have:

$$OPD(\rho) = \int_0^h \frac{dn}{dT}(T_0)\frac{Q}{4\pi\kappa\sqrt{\rho^2+z^2}}dz$$
$$= \frac{Q}{4\pi\kappa}\frac{dn}{dT}(T_0).\sinh^{-1}\left(h/\rho\right) \qquad \textit{Equation 3.17}$$
$$= Q.G_{OPD}$$

with $G_{OPD}(\rho) = \frac{1}{4\pi\kappa}\frac{dn}{dT}(T_0)\sinh^{-1}\left(h/\rho\right)$ and Q the point heat source term. Since the heat source is defined by a Dirac distribution in the point source approximation, the G_{OPD} function corresponds to the Green's function for the thermal OPD distribution. Experimentally, the particles are in contact with a glass slide on one side, and immersed in a liquid on the other. In this case, the thermal conductivity to be considered is the mean value between that of glass κ_{glass} and liquid κ_{liq}: $\kappa = (\kappa_{glass} + \kappa_{liq})/2$.[104]

Now that we have solved the thermo-optical problem for a point source, any set of heat sources distributed in a 2D plane with a distribution map $Q(x,y)$ can also be modelled. The resulting OPD is then the convolution $Q(x,y)$ with Green's function for the optical path difference, G_{OPD}. If we change to a Cartesian coordinate system, and under the linear approximation of Equation 3.15 while the temperature is under 60°C, the $OPD(x,y)$ caused by a heat source distribution $Q(x,y)$ writes:

$$OPD(x,y) = \iint Q(x_0,y_0)G_{OPD}(x-x_0,y-y_0)dx_0\mathrm{d}y_0$$
$$= Q(x,y) * G_{OPD}(x,y) \qquad \textit{Equation 3.18}$$

Equation 3.18 clearly shows that $OPD(x,y)$ is the convolution of $Q(x,y)$.with $G_{OPD}(x,y)$. Therefore, the heat source distribution $Q(x,y)$ can be determined by a deconvolution. An optical measurement of wavefront perturbations can therefore give access to the heat source term, and therefore, as shown below, to the temperature.

3.4.4.2. Wavefront sensing

We use a shearing interferometry-based wavefront sensor (Phasics, SID4 [171,172]) in order to obtain the perturbation $OPD(x,y)$[103]. In Figure 3.7, the optical path corresponding to this measurement arm is coloured in violet. The sample is illuminated by a halogen lamp spectrally filtered around λ = 407nm (Δλ = 40 nm), a wavelength at which the absorption by gold nanoparticles is much lower than at resonance (532 nm). With a total power of the order of the mW, this illumination can be safely assumed to be thermally non-perturbative. We use a Köhler illumination with a closed aperture diaphragm to maximize the spatial coherence and illuminate the sample with a quasi-plane wave. However, wavefront distortions in the setup need to be considered: a first reference phase image is acquired before any heating is applied Figure 3.11(b), and the measured wavefront is subtracted from the subsequent acquisitions in order to extract the thermally-induced wavefront distortions.

3.4.4.3. Retrieving temperature from wavefront images

In the previous two sections, we have deduced the relation between wavefront distortion and explained the experimental way to acquire wavefront images (OPD image). Now we show how to retrieve the temperature map out of the wavefront images numerically.

Transforming Equation 3.18 in the Fourier space, we have:

$$TF(OPD)(v_x, v_y) = TF(Q)(v_x, v_y) \cdot TF(G_{OPD})(v_x, v_y). \qquad \textit{Equation 3.19}$$

Theoretically, once the OPD image is acquired by the wavefront sensor, one can get the heat source distribution image in the Fourier space by $TF(Q)(v_x, v_y) = TF(OPD)(v_x, v_y)/TF(G_{OPD})(v_x, v_y)$. However, in practice, the noises will be amplified when the value of Green's function G_{OPD} approaches zero. For this reason, we apply a filtering method that has been implemented by Baffou et al.[103] to regulate these noises. The idea is to use an intermediate function $\bar{G}$ which consists of a Tikhonov factor α_T, as defined by the following relation:

$$\frac{1}{\bar{G}(v_x, v_y)} = \frac{1}{TF(G_{OPD})(v_x, v_y)} \cdot \frac{1}{1 + \frac{\alpha_T}{\left|TF(G_{OPD})(v_x, v_y)\right|^2}} \qquad \textit{Equation 3.20}$$

The Tikhonov factor $\alpha_T > 0$ is defined empirically for each measurement. Using this regulation, we get $\frac{1}{\bar{G}(v_x,v_y)} \approx 1/TF(G_{OPD})(v_x, v_y)$ when the value of $TF(G_{OPD})(v_x, v_y)$ is large enough compared to α_T, and 0 when it's not the case, which means that noise amplification is avoided. By deconvolution of the measured optical path difference $OPD_{measure}$, we then have:

$$Q(x,y) \approx TF^{-1}\left[\frac{TF(OPD_{measure})}{\bar{G}}\right](x,y). \qquad \textit{Equation 3.21}$$

From the $Q(x,y)$ map and Equation 3.11 we can retrieve the temperature increase map $\Delta T(x,y)$:

$$\Delta T(x,y) = Q(x,y) * G_T^{ST} \qquad \textit{Equation 3.22}$$

This wavefront-sensing-based system can provide quick access (10 fps) to the temperature distribution in the sample, with a spatial resolution limited by both diffraction (λ/NA under spatially coherent illumination) and deconvolution inaccuracies. The phase resolution of the wavefront sensor for a single camera frame is 2 nm, which translates into a temperature resolution of the order of 1K and can be improved at the expense of temporal resolution upon averaging.

3.5. Results

3.5.1. Uniform temperature increase control

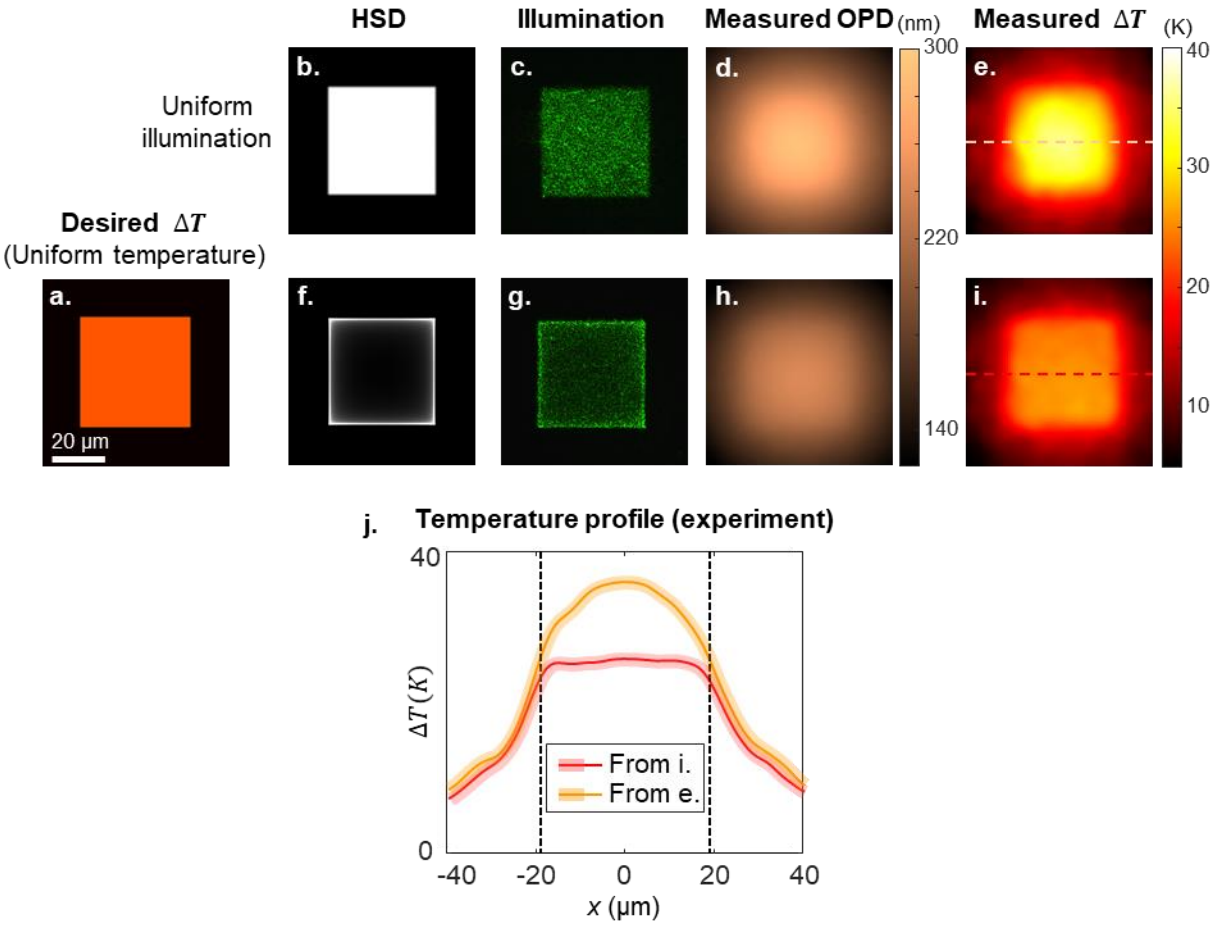

Figure 3.13 Photothermal stimulation shaping and thermal imaging process. (a) Desired temperature increase pattern; Two Heat Source Density maps are compared: (b-e) correspond to the case of uniform illumination while (f-i) correspond to the case of a calculated illumination (b,f) applied HSD; (c,g) Experimental reflectance images of light distribution in the sample plane; (d,h) OPDs measured by wavefront sensing; (e,i) temperature increase distributions retrieved from OPD; (j) Comparison of the temperature increase profiles. Scale bar: 20 µm.

In order to illustrate the possibilities of the method for shaping temperature, we start by imposing either a homogeneous HSD (Figure 3.13(b)) or a precalculated HSD (Figure 3.13(f)) leading to a uniform temperature (Figure 3.13(a)) over a square region of 40 µm × 40 µm. After calculating and displaying the appropriate phase pattern on the SLM, a uniform light intensity I = 8 µW.µm^{-2} is sent onto the sample in this square region (Figure 3.13(c)) and constitutes the

HSD (note the speckling effect due to the coherent laser source). As shown in Figure 3.13(b-e), an uniform illumination HSD (Figure 3.13(b-c)) does not yield a uniform temperature distribution since collective effects induced by heat diffusion lead to higher temperatures at the centre than on the edges of the square (Figure 3.13(e)). The orange profile in Figure 3.13(j) clearly shows the bell-shaped thermal response of the system, with a temperature increase varying between 29.4 K and 36.3 K over the heated region. As discussed above, HSD engineering can compensate for this effect. Figure 3.13(f,g) show the calculated and experimental HSDs which yield a constant temperature rise ΔT over the square region when imposing $I \leq I_0$ at any position. As expected, the highest HSD is found near the edges, where lateral heat dissipation is strongest. The resulting temperature distribution (Figure 3.13(i,j)) reaches the constant targeted value (ΔT = 25 K) within the designated square region (standard deviation: 1.3 K). In both cases (uniform HSD and uniform ΔT), the absolute temperatures profiles are in good agreement with the expected values.

3.5.2. Temperature control with different locations and values

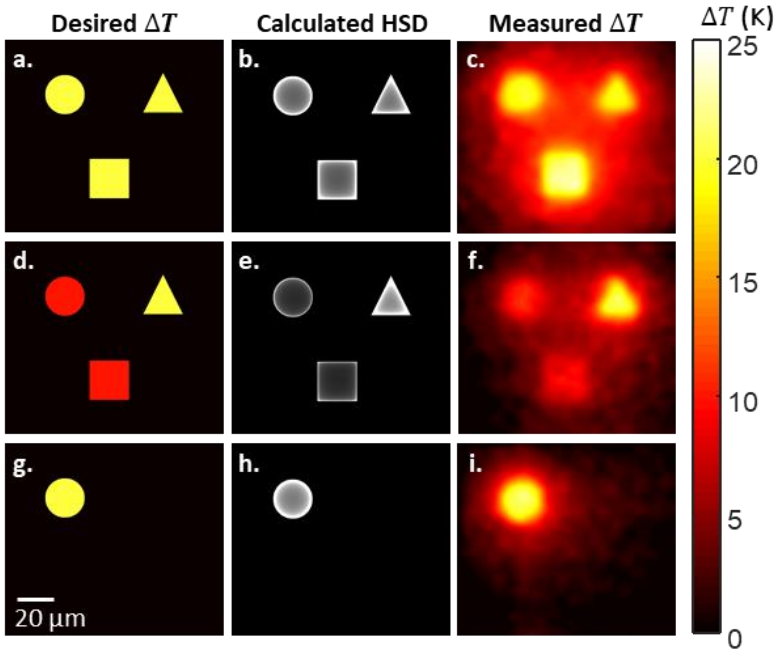

Figure 3.14 Temperature control at different locations and values. (a,d,g) Desired temperature increase distribution; (b,e,h) Calculated HSD; (c,f,i) experimental temperature increase images retrieved from wavefront measurements.

A major advantage of temperature shaping using a SLM is that patterns can be arbitrarily reconfigured in both time and space. Quantitative temperature shaping is illustrated in Figure

3.14, where arbitrary temperature targets ΔT of 20K or 10K are chosen within domains of variable shapes (Figure 3.14 (a,d,g)). The corresponding HSD (Figure 3.14(b,e,h)) and the phase pattern to display on the SLM are calculated using the algorithm described above. After projection on the plasmonic substrate, wavefront measurements yield the temperature images (Figure 3.14(c,f,i)). Heat spreading around the microstructures is clearly visible, particularly in central regions where the distance between heat sources is lower, but the temperature in the targeted regions is homogeneous and quantitatively reaches the desired values within a 15% error, mostly due to NPs sample absorption inhomogeneities, phase measurement noise and deconvolution noise. This shows that single-shot substrate illumination with the appropriate HSD can produce arbitrarily localized temperature rises.

The reduction of the heated area also has the advantage of giving access to faster thermal dynamics, which can typically reach the millisecond range. Indeed, the characteristic time scale τ for generating a stable 2D temperature distribution depends on the typical length l_c of the pattern as follows:

$$\tau = \frac{{l_c}^2}{4D} \qquad \textit{Equation 3.23}$$

with D = 9.2 .10^{-4} cm^{2}s^{-1} the thermal diffusivity of glycerol[173] and D = 3.4 .10^{-3} cm^{2}s^{-1} that of glass, we can assume that glass drives the lateral thermal spread [174]. Considering a square with side length $l_c = 10$ µm, the system therefore reaches a stable temperature profile extremely quickly, within approximately τ = 70 µs. The rise time and fall time of the SLM we use, 10 and 25 ms respectively, are much longer than τ, and are therefore the main temporal limitation here. This can be improved relatively easily using kHz frame rate SLMs which are now available[175].

3.5.3. Towards biological application: selective heating at sub-neuron scale

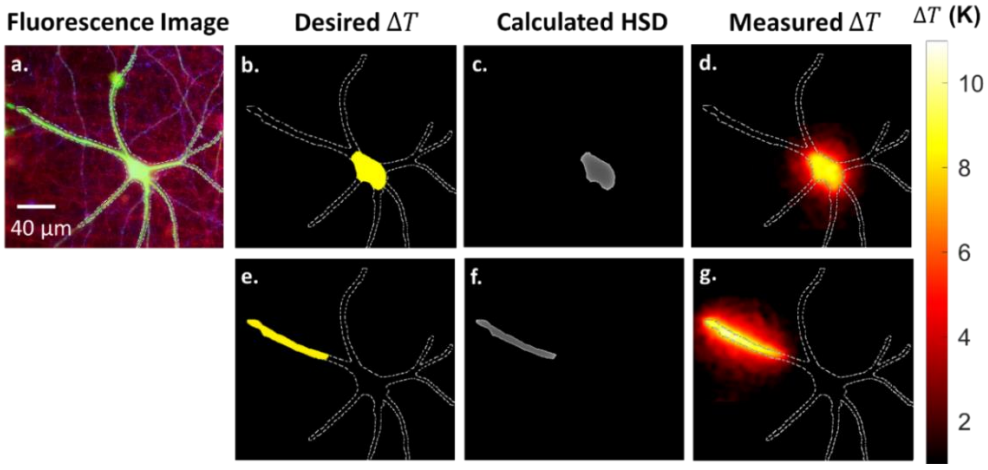

Figure 3.15 Selective heating of different parts of a cultured hippocampal neuron. (a) Confocal fluorescence images of a hippocampus neuron (light green: neuron staining, MAP2). The dashes outline the area of interest, i.e. the neuron. (b,e) Outline of the neuron, with targeted heating areas highlighted in yellow; (c,f) Calculated HSD to heat these areas. (d,g) Experimental temperature increase distribution and outline of the neuron position.

One of the main applications envisioned for this temperature shaping technique lies in the field of biology, where temperature is an essential parameter. In the context of 2P optogenetics, photo-induced local temperature rises could influence neuronal activity: suppress spiking[114], generate action potentials[176], drive the growth of neurites[177] and so on, which should be carefully evaluated. In this section, we show, as a proof of principle, the potential of the reconfigurable temperature control technique that we developed to address these problems.

Here, we propose a methodology combining temperature shaping with fluorescence imaging to thermally target a given population of cells or organelles of interest. Since fluorescence staining is a ubiquitous tool providing excellent specificity, it gives access to biological regions of interest in which local, precise and dynamic temperature control can be performed. The size and shape of the neuron were derived from the image Figure 3.15(a), using neuron staining (MAP2, in green). Note that the red and blue channels in Figure 3.15(a), which represent cytoskeleton (Alpha tubulin) and presynaptic (synuclein) tagging, respectively, were not used here. As shown in Figure 3.15(b,e), the outlines of this image were used to define the thermal stimulation of the substrate with the shape of the soma (Figure 3.15(b-d)) or a dendrite (Figure 3.15(e-g)). Because the noise of the wavefront imaging limits the sensibility for short exposure times, we used a relatively high-power thermal stimulation for clarity, ΔT = 10K.

However, since this heating varies linearly with power, lower laser power can easily be applied to deliver more realistic and precise ΔT values (after a power-ΔT calibration), which can be applied within millisecond-scale times, and are therefore well adapted to biological investigations.

3.5.4. Discussion on homogeneity and reliability

3.5.4.1. Influence of speckle

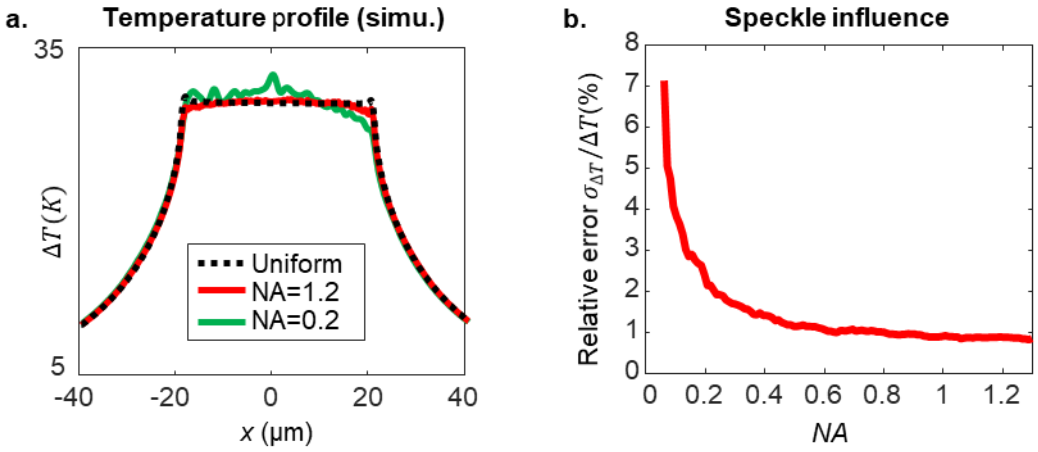

Figure 3.16 2D Inhomogeneity caused by speckle. (a) Temperature rise cross-sections calculated in the presence of speckle distributions associated to NA= 0.2 (green) and 1.2 (red), and in the absence of speckle in the illumination (black dashes). (b) Evolution of the speckle-induced spatial noise with NA, showing the effect of speckle grain-size decrease with NA.

Since a coherent source is used to create our HSDs, the intensity patterns in Figure 3.13(c) and g are clearly affected by speckle. Whether this speckle in turn induces inhomogeneity in the temperature distribution is an important question, driven in part by the size of the speckle grain, which varies as λ /NA where NA is the numerical aperture used to project the pattern. Due to the limited spatial and thermal resolution of the wavefront analyser, this subtle effect is difficult to characterize experimentally. To predict these inhomogeneities, we use the fact that the Gerchberg-Saxton algorithm imposes the intensity (that of the target pattern), but leaves the phase (which is displayed on the SLM) as a free parameter, thus producing after Fourier transformation a speckle pattern representative of the experimental one for a given NA. Figure 3.16(a) shows temperature profiles obtained by convolving the Fourier transform[103] of Gerchberg-Saxton solutions for various NA values with the thermal Green's function G_T^{ST}, thus producing realistic, speckle-affected temperature profiles. For a low NA =

0.2 (green line), local temperature inhomogeneities are clearly visible, with a relative error $\frac{\sigma_{\Delta T}}{\Delta T}$ = 2% with respect to the targeted temperature rise ΔT. However, these relative variations quickly fall below 1% and become negligible in practice for NA > 0.5, as shown in Figure 3.16(b). In our experiment, we used microscope objectives with NA = 0.85 (Olympus, UPlanSApo, 20x) or NA = 1.42 (Olympus, oil immersion Plan Apo N 60x) to minimize this effect. Several strategies can be proposed to reduce speckle and improve temperature homogeneity. Experimentally, speckle scrambling using e.g. a rotating diffuser is of course possible if time-resolution is not an issue. Alternatively, it is possible to improve the Gerchberg-Saxton algorithm by removing optical vortices responsible for intensity zeros. Such a control of both phase and intensity at the sample requires modulating both phase and amplitude in the Fourier plane. In practice, however, speckle control is achieved either at the expense of critical optical power losses[178], or of experimental complexity[179].

3.5.4.2. Homogeneity in 3D

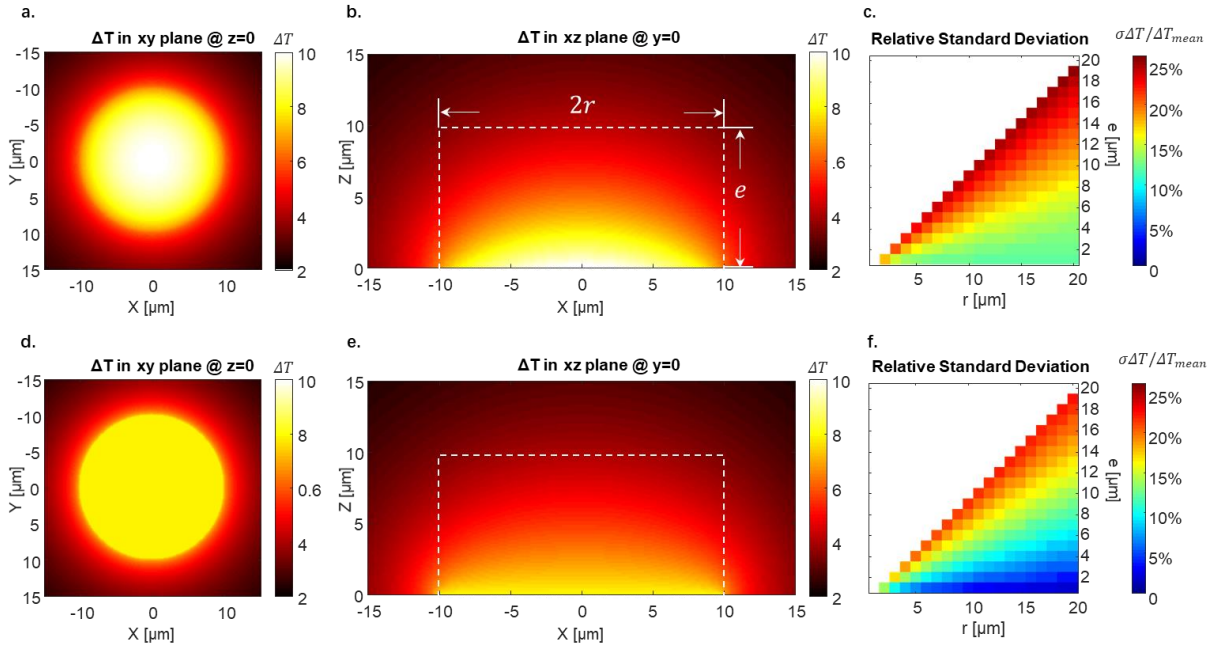

Figure 3.17 3D temperature distribution and temperature homogeneity for a homogeneous (a,b,c) and pre-compensated illumination (d,e,f). (a,d) Temperature increase map in the xy-plane (z=0); (b,e) Cross-section of the temperature increase map in the xz-plane (y=0). The white dashed lines represent the dimension of the assumed cylindrical object (e stands for the thickness and r for the radius of the cylinder). (c,f) Relative standard deviation of ΔT in the cylindrical volume. For both illuminations, the total laser power is the same.

In the previous sections, we essentially focused on the optimization of the lateral (x, y) temperature increase map. However, along the longitudinal (z) direction, there is also clearly a temperature distribution. This can be important in cases where e.g. a relatively thick adherent cell body needs to be brought to a constant temperature. While ΔT(z) cannot be measured using the OPD method, we propose to model it. Here we report simulation results describing the 3D temperature distribution generated by heating an absorbing nanoparticles layer with a homogenous (Figure 3.17(a-c)) and thermally pre-compensated illumination (Figure 3.17(a-c)). We consider a disk shape target area with radius r. For a homogeneous illumination, the temperature distribution in the nanoparticle plane ($z = 0$) is not homogeneous (see Figure 3.17(a)). As described in the main text, it is however possible to calculate an illumination pattern leading to a uniform temperature distribution in the plane $z = 0$ (see Figure 3.17(d)).

Figure 3.17(b,e) show respectively the temperature distributions along the propagation direction of the heating beam (z-direction) for a homogeneous (b) and pre-compensated (e) illumination. In both cases, temperature decreases away from the heating plane. Let us now estimate the temperature homogeneity inside a cylindrical volumetric object with radius r and thickness e, represented by a dashed line rectangle in Figure 3.17(b,e). To this aim, we defined the Relative Standard Deviation: RSD=$\frac{\sigma_{\Delta T}}{\Delta T}_{mean}$, with $\sigma_{\Delta T}$ the standard deviation and ΔT_{mean} the average temperature increase inside the cylindrical volume. Figure 3.17(c,f) show the temperature inhomogeneity inside cylinders of variable radii r (horizontal axis) and thicknesses e (vertical axis). Here, we assume $e < r$, since this is typically the case for adherent culture cells which are relatively flat objects[180]. For any value of e and r in the tested range, the values of the RSD, i.e. the temperature inhomogeneity, is larger in Figure 3.17(c) than in Figure 3.17(f): the pre-compensated illumination always provides a better temperature homogeneity than the non-compensated case. Furthermore, it is worth mentioning that Figure 3.17(f) also shows that RSD decreases: the 3D temperature homogeneity improves with the size of the heated region. However, this reduces the lateral spatial resolution of the thermal targeting as spurious heating can potentially be induced in the surrounding structures.

3.5.4.3. Confinement in 3D - comparison with direct IR laser beam heating

As discussed earlier, several methods for local heating coexist. One of the most straightforward and efficient methods is probably to heat water at wavelengths which it absorbs, i.e. in the infrared or near-infrared range. In this section, we compare the 3D temperature

distribution induced by an IR beam focused in water with the one induced when illuminating an absorbing nanoparticle layer.

In this study, we considered a gaussian NIR beam (λ_0 =1.8 µm as in ref[181]) focused in water, with a low numerical aperture, in order to generate a 15µm diameter spot (FWHM) at the sample plane (z=0, see Figure 3.18(a)). For the sake of simplicity, we considered a homogenous medium having the thermal and optical properties of water, and we neglected the intensity depletion of the heating beam during its propagation. Figure 3.18(b) shows the intensity distribution of the focused beam along the propagation direction (z-direction). The large axial extension of the focal volume is clearly visible: $Lz = 2z_r = \frac{\pi.FWHM^2}{(\lambda_0/\mathrm{n}).ln2} \approx 700\mu m$, where z_r stands for the Rayleigh length and n=1.31 the refractive index of water at λ_0.

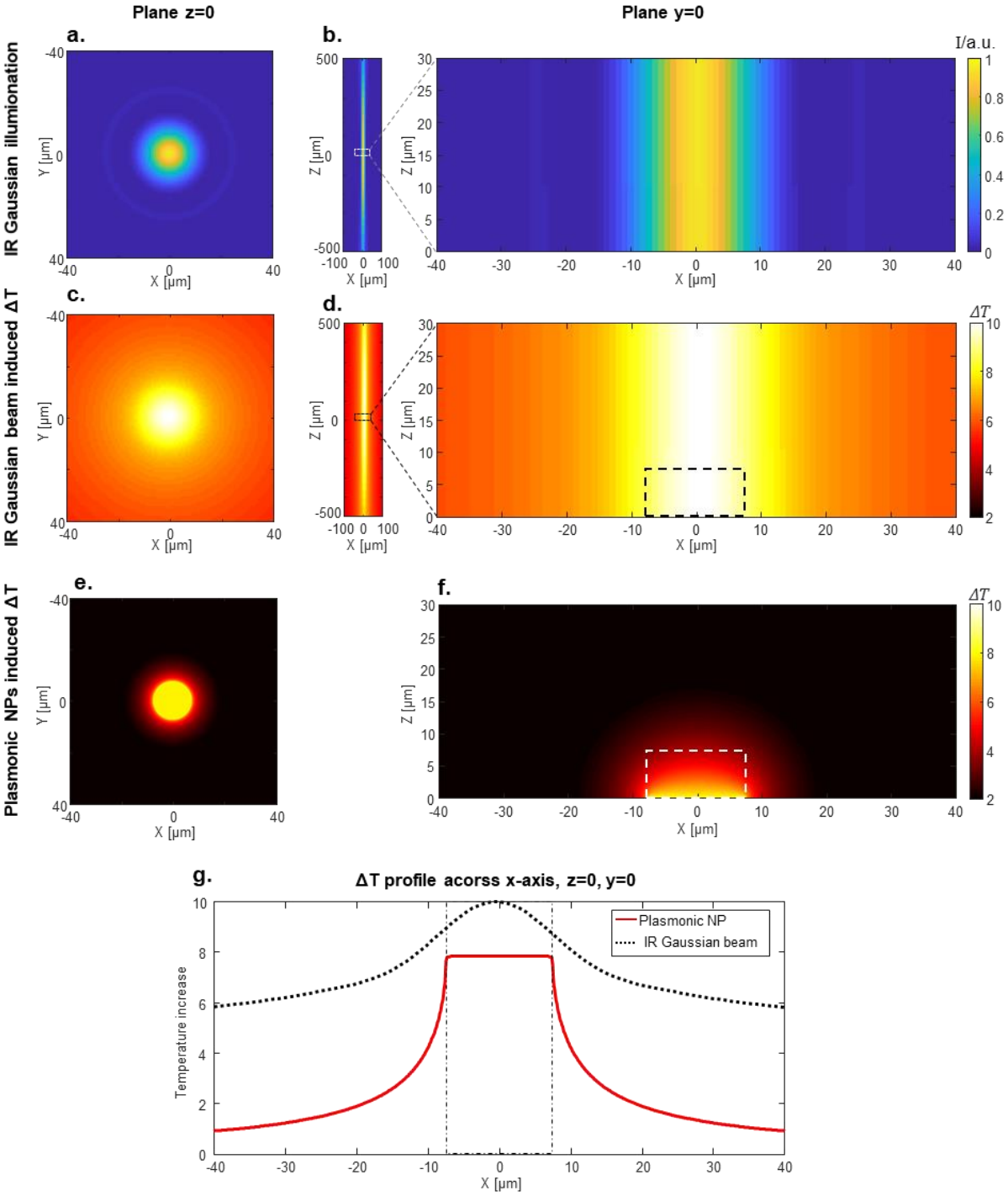

Figure 3.18 Comparison of temperature confinement under focused infrared beam or pre-compensated illumination. (a) Intensity map of a focused infrared beam in the z=0 plane of best focusing. (b) Cross-section of the beam intensity distribution (FWHM=15μm) in the xy-plane (y=0). (c) Temperature map induced by a gaussian beam in the focal plane (z=0) and d) Cross-section of the temperature increase in the xz-plane (y=0). (e) Temperature increase map in the XY-plane of an absorbing nanoparticle layer (z=0) heated by a pre-compensated illumination leading to a 15 μm diameter homogeneous temperature disk; (f) Cross-section of the

temperature increase map in the xz-plane (y=0). (g) Temperature increase profiles along the x-direction (y=0, z=0).

Water absorption of the NIR light (α = 8 cm^{-1} at λ_0) along the beam propagation then results in a temperature increase that can be calculated by convolving the 3D heat source distribution with the 3D thermal Green's function G_T^{ST}. Figure 3.18(c,d) show, respectively, the resulting temperature distribution in the xy-plane (z=0) and the xy-plane (y=0). This volumetric absorption leads to a broad distribution of temperature increase, particularly along the z-axis.

For comparison, we also simulated the 3D temperature distribution generated when illuminating an absorbing layer of nanoparticles located at z=0. Here, we considered a pre-compensated illumination leading to a 15 µm diameter homogeneous temperature disk (same size as the FWHM diameter of the Gaussian beam, see Figure 3.18(e,f). In this case, the temperature is much more confined, not only axially but also laterally. This effect can be clearly seen in Figure 3.18(g), where the temperature profiles in the xy-plane are compared (taken along the dashed lines in Figure 3.18(c,d). This lateral and vertical confinement is particularly important in biological applications as it reduces spurious thermal excitation of the surrounding structures (other cells, for instance) and thus provides a better spatial resolution on the thermal targeting.

3.6. Conclusion

Combining wavefront engineering and thermo-plasmonics, we proposed and demonstrated a method to generate microscale reconfigurable temperature distributions in chosen domains of space. Using a spatial light modulator, we apply a Heat Source Density (HSD) which is calculated to compensate the heat diffusion effects within this domain and obtain the desired temperature profile. We experimentally demonstrate the feasibility of the procedure by imaging the temperature with micrometre resolution using a method based on wavefront-sensing.

We show as proof of principle that this technique has the potential to create heat stimulation targeting different parts of a neuron. If we used adherent neuron cells on a NP substrate, this reconfigurable temperature control technique would allow to select different zones of interest in a neuron, or to create homogeneous temperature rises in a ~10µm thick (z-direction) region above the substrate. As the temperature control setup is quite compact, it is possible to observe at the same time the neuron activities through patch-clamp, calcium imaging or voltage imaging, allowing the observation of electrophysiological responses to thermal stimulation.

There are clearly limitations to the method: temperature gradients steeper than the $\frac{1}{r}$ imposed by heat diffusion are not achievable without using negative heat sources, i.e. local cooling. For similar reasons, the temperature can only be driven in limited domains of space, and will be imposed by $\frac{1}{r}$ diffusion, collective effects (i.e. other neighbouring heat sources), and boundary conditions outside of the domain. Although limited to such microscale domains, overcoming thermal diffusion by pre-engineering thermal sources promises a wide range of applications, for which reconfigurable, fast and accurate temperature shaping is necessary. This includes not only biological applications (e.g. photoinduced thermal perturbation, metabolism stimulation, thermogenetic), but also applications in physics (e.g. phase changes, microscale thermal phenomena), microfluidics and chemistry, where thermal gradients are crucial to drive e.g. reaction kinetics.

The results presented in this chapter have been published in:

Reconfigurable Temperature Control at the Microscale by Light Shaping

ACS Photonics **2019** *6* (2), 422-428, DOI: https://doi.org/10.1021/acsphotonics.8b01354

Chapter 4

Tunable Thermal ‘SmartLenses’: Towards Multiplane Imaging of Neural Activities

Summary

4.1. Introduction

We have seen in the previous chapter (see Section 3.4.4.1) that temperature variations in a material locally change its optical refractive index. A light beam passing through a given material thus experiences a wavefront distortion (or phase-shift) which directly depends on the temperature distribution within the material. We also have seen that the temperature distribution can be precisely shaped at the microscale by pre-compensating heat diffusion. Combining these two concepts, it clearly appears that one can precisely engineer an optical wavefront by shaping the temperature within a thermo-optical material.

Based on this principle, we will introduce in this chapter a novel concept of tunable micro-optics called *SmartLens* (SL). The method, developed in close collaboration with the group of Romain Quidant (ETH Zurich), exploits electrically-induced thermal phase-shifts at the microscale. We will see that the Heat Source Distribution (HSD) generated by engineered microresistors can be optimised to produce free-form tunable wavefront distortions. Individually or in arrays, the SmartLens technique can generate complex functions based on either pure, or a combination of Zernike polynomials, including lenses or aberration correctors of electrically-tunable magnitude. This technology could offer a broad range of potential applications, especially in microscopy.

As this project shares very similar physics with the temperature shaping technique and is of particular interest to the microscopy of neuronal circuits, I have participated in the characterisation and application of this technology in two aspects:

- characterisation of the wavefront engineering performance: focus tuning and Bessel beam generation (published in ref[182]);
- new development based on an **array of SmartLenses**: simultaneous *in vivo* multiplane fluorescence imaging to **monitor brain activity in 3D.**

This chapter focuses on the multiplane imaging part, and we present the Bessel beam generation in Annex 3.

4.2. Background: 3D neuronal imaging

4.2.1. Monitoring neural activities

In the last decades, extensive efforts have been made to develop fluorescent reporters of neuronal activity to decipher the neural code under optical microscopes. Genetics and protein engineering have provided us with a powerful tool — optogenetics. These techniques are arguably one of the major breakthroughs of the beginning of the 21st century. Optogenetics not only provide access to the optical activation of neurons (as described in Section 1.1.2) but also enables converting electrical or chemical activities in neuron into fluorescence signals[183], opening a new horizon for optical investigation of the brain. Among the advantages of using fluorescence compared to electrodes to detect neuron activities, one can mention reduced invasiveness, versatility, and the possibility to investigate a large population of neurons at once on living animals. Figure 4.1(a) shows an example (image acquired by Giulia Faini, post-doc in the group of F. Del Bene) of a wide-field fluorescence image of neuron in living Zebrafish larvae expressing the widely use GcaMP, a genetically encoded calcium indicator (GECI). These kind of indicators are the most widely used fluorescent proteins that respond to the binding of Ca^{2+}. Because an influx of Ca2+ ions always accompanies the generation of action potentials in neurons, the calcium indicators can thus monitor neurons' firing. Besides, there is another type of indicator – genetically encoded voltage indicator (GEVI), protein or chemical compounds whose fluorescence varies with the electrical activities of the neurons, which is even more powerful as it provides faster response time to sub-millisecond. Figure 4.1(b) shows, in another case, the comparison of calcium imaging signal and voltage imaging signal at the same region of interest, while three action potentials were evoked by direct current injection into the cell body. The faster response of GEVI and the faster electrical activity dynamic show clear advantages in time resolution, almost comparable to electrical recording.

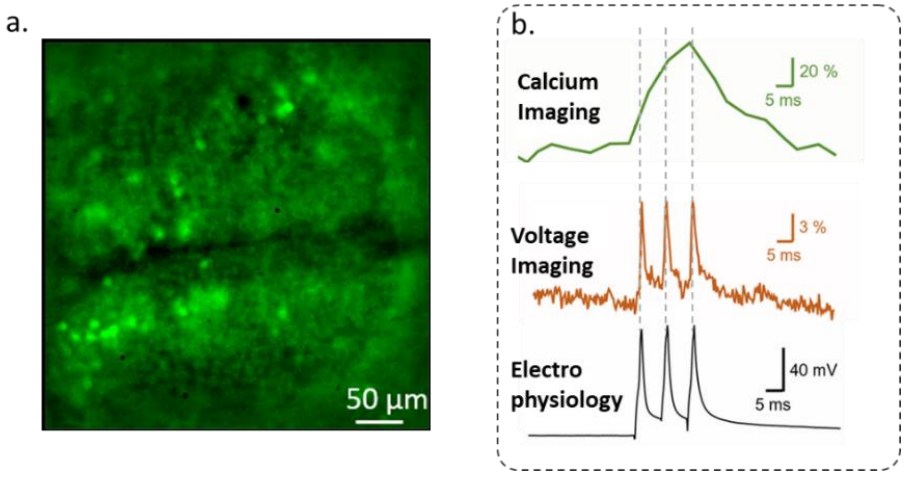

Figure 4.1 (a) Widefield fluorescence imaging of a zebrafish larva brain (Danio rerio) expressing Gcamp6s – courtesy of Giulia Faini, Institut de la Vision. Scale bar: 50 µm. (b) (in another case) Voltage and calcium time-trace from the same region of interest on a basal dendrite of layer 5 cortical pyramidal neuron (adapted from ref[184]). In this illustrative example, three action potentials were evoked by direct current injection into the cell body.

Optical imaging of neuronal activity using $Ca2^{+}$ or voltage indicators requires developing dedicated optical imaging techniques to detect fluorescent signals from multiple targets with cellular resolution deep in living tissue. In particular, neuronal networks have complex and wide three-dimensional structures. It's thus critical to achieve 3D images and detect activities over cellular structures located at different depths. Additionally, resolving spiking activity requires ms temporal resolution (Figure 4.1(b))..

In order to tackle these challenges, several methods have been proposed to achieve volumetric acquisitions over large areas without compromising the acquisition speed or the signal-to-noise ratio (SNR). These methods can be roughly classified into two groups: (i) sequential (or scanning) imaging techniques, in which structures at different depths are imaged quickly one after the other, systematically requiring a delay between subsequent measurements at the same point; (ii) parallel imaging techniques which can image targets at different depths simultaneously. We will discuss the two types of approaches in the following two sections, giving a few examples in a non-exhaustive list.

4.2.2. Sequential imaging-based techniques

In this scheme, most of the instrumental efforts are focused towards the optimization of scanning delays. Increasing the frame rate is, of course, useful in itself, but it is even more essential in order to avoid missing short transient events occurring between frames.

Piezo-controlled objectives and electrically tunable lens (ETL):): In two-photon microscopy or any other laser scanning microscopy, those are the most prevalent Z-scanners in combination with galvanometric mirrors (<10 fps) or resonant XY-scanners (>30 fps)[185]. Piezo-controlled objectives have refocusing ranges of ~ 400 µm, with step and settling times[186] shorter than 20 ms. ETLs have a faster settling time (<10 ms)[187], but still they enable only a limited number of planes if combined with Ca^{2+} imaging and lack the temporal resolution for multiplane voltage imaging.

Spatial Light Modulator (SLM): SLM is a ubiquitous wavefront shaping technique that can be used to obtain fast focus scanning elements as well as scanless parallel elements. Among the various wavefront engineering techniques, liquid-crystal spatial light modulators (LC-SLMs) are the gold standard for dynamic spatial phase control of wavefronts with a high spatial resolution. They can switch focus across > 500 µm while reducing the transition time between different illumination depths into < 3 ms by applying different digital phase masks on the wavefront[188]. Moreover, SLMs are compatible with beam multiplexing and adaptive optics to correct the aberration from the optical system and sample. However, they are highly chromatic since they work in a diffractive regime.

Ultrasound / TAG Lens: Ultrasound lens, or acoustic gradient index of refraction (TAG) lens, is an alternative strategy for high-speed scanning. As opposed to other scanners whose frames are taken from xy-planes, each frame of ultrasound/TAG Lens scanners is taken along yz-planes with a continuous resonance frequency > 450 kHz in the Z direction. To avoid image distortions caused by oscillation instabilities, it needs a phase-locked loop. Eventually, the frame rate can typically[189] reach ~1 kHz.

Random access multiphoton (RAMP) microscopy: This method combines multiphoton excitation with an inertial free scanning mechanism—acousto-optic deflectors(AODs). While using two orthogonal AODs (for X and Y direction), one can steer a multiphoton excitation laser beam in an inertia-free manner, enabling the multiphoton excitation volume to be laterally repositioned to only locations of interest within the microscope's specimen plane with very short latency[190] (~15µs). It dramatically reduces the number of voxels that need to be sampled. Recording *in vivo* neuronal activities in a 500µm×500µm plane up to depths of ~500µm at ~160Hz was realised; combining with piezo axial scanning, 3Hz volume rate is achievable to observe thousands of neurons in large V-FOVs (500µm×500µm×500µm) for single-cell resolution in the mouse neocortex[191]. It can also be combined with an acousto-optic lens to perform 3D random-access multiphoton points measurements at 35–50 kHz. However, the major limitation of AODs based devices is that they

cannot perform full-frame continuous line scanning away from the natural focal plane of the objective, which needs to be overcome for *in vivo* imaging[192].

Light-sheet microscope: Light-sheet microscopy can significantly increase time resolution using full-field (scanning-free) imaging along the XY direction. It uses a thin sheet of light projected into the sample from the side so that only a 2D section of the sample is illuminated, providing, therefore, micrometric optical sectioning. For relatively transparent samples that are not limited by light scattering effects, light-sheet microscopy is very efficient for the functional mapping of circuits across large volumes in (e.g.) transparent samples such as worms, Zebrafish and Drosophila larvae. In fluorophore-labelled samples, the emitted fluorescence signal from one plane is imaged along the direction orthogonal to the light sheet, and the plane of the light sheet is scanned along the z-direction. The volumetric recording of light-sheet scanning can reach >10 vol/s (depending on the size and resolution).[176,193,194]

In general, those sequential (scanning) approaches for 3D imaging share the following features:

- They achieve high resolution in 3D imaging, even deep in living tissue when combined with 2P excitation;
- However, being sequential approaches, they intrinsically suffer from loss of speed. For instance, for the same dwell time per voxel (same acquisition time spent in each location), the acquisition rate f is divided by the number of planes N_{plane}: $f \propto \frac{1}{N_{plane}}$. This limit the overall speed achievable.

4.2.3. Parallel imaging-based techniques

Multiplexed point-scanning microscopy: Instead of increasing the scanning speed, an alternative approach is to increase (multiplex) the number of laser beams, a major route towards parallel imaging. This can be realised in several ways. For example, **temporal multiplexing**[195] separates nanosecond pulse trains into several copies, interleaved in intervals longer than the fluorescence lifetime. These temporally separated beams scan the different fields of views or depths simultaneously. Their fluorescent signals can be distinguished using the time interval separation. The number of multiplexed plane is, however, limited by the fluorescence decay time. **Spatial multiplexing** includes lateral approaches that[196] use N beams to scan N lateral regions simultaneously and N PMTs (multianode PMTs) to detect each emission, respectively. It also includes axial approaches that use computational algorithms to extract multiplanes signals from overlapped images. Multiple focus spots[188,197] or Bessel beam[198] is used to scan

several planes or entire volume, and 1 PMT is used to record the 2D projection of 3D signals. A computational algorithm that considers the prior information of each plane (cell position and calcium indicator kinetics) can efficiently untangle the overlapped images into spatiotemporal signals of the neuron activities. The essential limitation of this method lies in how well crosstalk between different paths and SNR can be optimised. **Spatiotemporal code multiplexing**[199] uses a digital mirror device (DMD) to add temporal patterns on separated beams (to scan different regions), and a single PMT to collect all signals. A decoding algorithm is applied to extracts emission signals that inherited the temporal code. **Wavelength multiplexing**[200] uses multiple beams with different wavelengths to image cells labelled with different fluorophores. Multiple dichroic mirrors separate the multicolour signals. This can be useful for structural imaging or to distinguish activities arising from different cell types expressing two different indicators.

While multiplexing approaches modulate the excitation PSF, the following approaches modulate mainly the detection PSF.

Extended depth of field microscope: the method consists in enlarging the depth of field to image simultaneously objects that are located in different planes. It can be achieved, for example, with a computer-generated hologram (CGH, as mentioned earlier in Section 1.1.3), used on the fluorescence path. The 2P laser beam is then divided into multiple beamlets, precisely illuminating neurons of interest (as many as 100) at different depths. By placing a cubic phase mask in the detection path, fluorescence signals from different depths (up to hundreds of µm range) are all focused on the camera and recorded simultaneously[201–203]. This method has the disadvantage of completely sacrificing axial resolution.

Light field microscopy: Computational imaging allows to extract different imaging depths from a single acquisition. To this aim, a microlens array is positioned before the camera so that richer information encoding the direction and intensity of the emitted light is recorded. With all this direction and intensity information, one can reconstruct a 3D image of the sample. For example, 20 vol/s light-field *in vivo* functional imaging of Zebrafish larval brain spanning 700µm×700µm×200µm is reached using this method[204,205].

Compared to the sequential scheme, the parallel schemes have acquisition speed independent of the number of planes (N_{plane}). In particular, camera-based approaches can reach high acquisition rates up to kHz. They have promising potentials as they can match the fast response of voltage imaging indicators, thus providing higher temporal resolution to observe neuron activities. However, there are also challenges in terms of signal to noise ratio, axial

sectioning and spatial resolution, especially in dense and scattering samples, since existing methods spread the signal over many pixels and/or superimpose it to that of the other planes.

In the next section, we introduce a new wavefront engineering concept, called “SmartLens”, that can be applied for simultaneous multiplane imaging. We will show that this technic could provide several advantages over existing technologies, making it a method worth studying for brain activity investigation.

4.3. Wavefront engineering SmartLenses using thermo-optical effects

4.3.1. Overview of the SmartLens concept

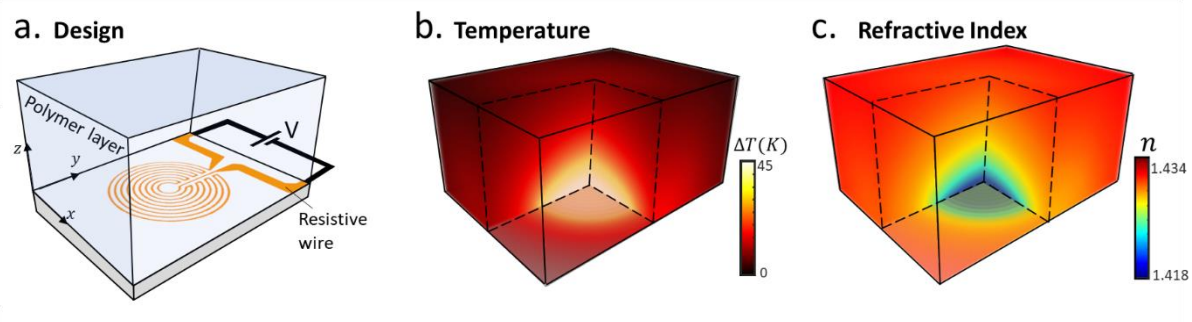

Figure 4.2 Principle of the electrically tunable SmartLens device. Electrically controlled resistive spirals induce a thermal refractive index modulation in the thermal-responsive material. (a) Schematic of a single device design; (b) Calculated 3D distribution of the temperature rise caused by electrical heating of the spiral; (c) Calculated refractive index variation induced by the temperature rise. [182]

The SmartLens (SL) technology exploits electrically-induced thermal phase shifts at the microscale[182]. Figure 4.2 describes the overall concept. A theoretical model enables the precise design of a resistive microwire. Following microfabrication, the device (Figure 4.2(a)) is electrically powered to deliver, through Joule effect, the pre-determined temperature landscape ΔT(x,y,z) into a thermo-responsive polymer (see Figure 4.2(b)). Due to the temperature dependence of its refractive index ($\Delta n(x,y,z) \approx \left[\frac{dn}{dT}\right] \Delta T(x,y,z)$ in the linear approximation, as discussed in Section 3.4.4.1), the polymer experiences a local refractive index modulation (see Figure 4.2(c)) that precisely shapes the incoming light wavefront with the pre-determined pattern.

The SmartLens technology could complement the existing optical shaping toolbox (e.g., SLMs[206], deformable mirrors[207], tunable lens[208–217]) by offering the following advantages:

- **Polarisation insensitivity and quasi-achromaticity**. These are important advantages compared to SLMs, especially for applications involving dim fluorescence signal. Indeed, since the SLMs involve birefringent index modulation, they can only shape one polarisation direction, leading to at least a 50% loss in fluorescence signal[206]. This feature has limited their applicability, especially in imaging. As discussed in ref[182], Smartlenses can potentially reach transmission >90%. Furthermore, SLMs are highly chromatic as they work in a diffractive regime. On the contrary, since SmartLenses work in a refractive

regime, they can then be used over a broad wavelength range to (e.g.) manipulate the wavefront on both the excitation and fluorescence collection paths, as discussed in Section 4.4.1.

- **Transmission mode.** Unlike most SLMs or deformable mirrors, SmartLenses can operate in transmission, allowing compact optical systems that could be integrated into endoscopes or miniature microscopes.
- **Freeform wavefront distortion.** Deformable tunable lenses have found many applications due to their compact design, cost efficiency and transmission operating mode. However, since they are usually based on polymer (or liquid) interface deformations, they are limited in terms of degrees of freedom, making it hard to achieve freeform optical elements. SmartLenses are more versatile in this respect, and the electrical design can be optimised to generate complex functions based on either pure or a combination of Zernike polynomials, including lenses, aberration correctors and other specific optical functions (as an example, see the inverted-axicon in Annex 3). This can be useful to optimise the PSF of our fluorescent multiplane microscope or specific beam generation.
- **Cost-effective.** SmartLenses are relatively easy to manufacture. Since the method requires only one lithographic step, it makes the components relatively inexpensive and easy to fabricate. This would facilitate the dissemination of the technique within biology laboratories and make easily accessible customised designs.
- **Micrometre size.** SmartLenses can be easily arranged in an array because of their micrometre size, which brings many potential benefits. For example, as will be discussed in the next section, an array of lenses with individually tunable focal lengths can be applied to achieve simultaneous focusing in different planes. Interestingly, the small size of the lenses potentially enables to integrate them into fibred endoscope systems.

4.3.2. SmartLenses array for simultaneous multiplane imaging

In the last years, extensive efforts have been made to develop tunable micro-lenses using various approaches, including electromechanical, electromagnetic, optical and thermal actuators or stimuli-responsive hydrogels. Still, only very few works proposed to arrange them in arrays. While the SmartLens technology belongs to the family of microscale wavefront engineering techniques, it can be designed into various optical functions, including lenses whose focal lengths change with voltages. Thus, it can also be classified into the tunable micro-lens family and can be arranged in arrays using classical lithographic methods.

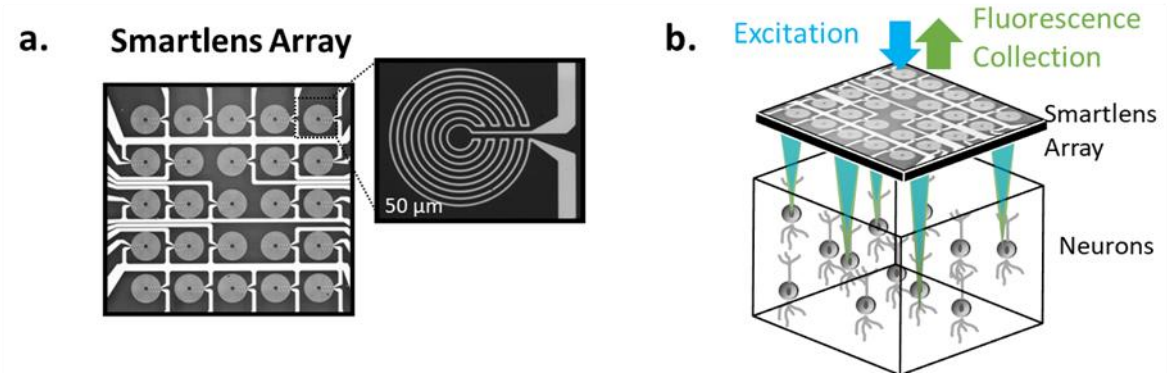

Figure 4.3 (a) Array of 5x5 Smartlenses. (b) Principle of simultaneous multiplane imaging using a SmartLens Array.

The main idea of this chapter is to **use an array of SmartLenses** (see Figure 4.3(a)) **to perform simultaneous multiplane** imaging of brain activities (see Figure 4.3(b)). Indeed, while a single SmartLens already offers a powerful way to control a defocus (or other aberration), additional control possibilities are offered when several SmartLenses are arranged in an array. As a simple example, we recently demonstrated, with R. Quidant's Group, broadband simultaneous multiplane imaging at the macroscale by simply inserting a SmartLens array in front of a standard camera[182]: by tunning each SmartLens independently, the method allows the simultaneous refocusing of several macro-objects located at various distances from the imaging system. Different planes of interest are monitored at the same time, without scanning. Here, we want to adapt this idea in fluorescence microscopy to simultaneously monitor several neurons located in different planes (see Figure 4.3(b)).

4.3.3. SmartLens model and validation

Before demonstrating the imaging system, a series of characterisations are necessary to understand the performances of the SmartLenses. Here we explain the principle of the device, the fabrication process and the characterisation through wavefront imaging.

Electro-thermo-optical model: Similar to the laser pattern determination for temperature shaping in Section 3.3.3, the electrical design also requires theoretical modelling. Briefly, the model, proposed by Pascal Berto in ref[182], considers a spiral electrical geometry (Figure 4.3(a)) modelled by an assembly of N circular wire-loops of radius r_i. The electrical resistance of an infinitesimal wire segment of length dl reads:

$$dR(r_i, T) = \frac{\rho(T).dl}{w(r_i).h_g} \qquad \textit{Equation 4.1}$$

where h_g stands for the wire thickness, $w(r_i)$ the wire width and $\rho(T)$ the electrical resistivity. The electric current flow I through the wire segment locally induces, by Joule effect, a dissipated heat power $dP(r_i,T) = dR(r_i,T).I^2$. An incoming plane wave passing through the polymer accumulates an optical path difference (OPD) that can be calculated, as described in Section 3.4.4.1, by a simple convolution between the dissipated power P and the phase Green's function G_{OPD}:

$$OPD = P * G_{OPD} \qquad \textit{Equation 4.2}$$

It is worth mentioning that, in practice, the model is a bit more sophisticated and takes into account the temperature-dependence of the resistivity.

To validate this model, a SmartLens element is designed and fabricated based on a microfabricated gold wire with a simple electrical geometry: a 200-µm diameter spiral heater with 9 regularly spaced loops of constant width *w* (see Figure 4.4(b)). PDMS was chosen as a thermo-responsive polymer due to its high transparency in the visible region, its thermal stability at high temperature[218], and because it exhibits relatively large refractive index variations with temperature[219] ($[dn/dT] = -4.5 \cdot 10^{-4}\ K^{-1}$).

Using this model, the design is optimized using a genetic algorithm: small variations are added to each generation of design. The electro-thermo-optical model is then used to determine how well this design fits the targeted wavefront. Sub-optimal designs are discarded, and the best ones are kept and reinjected in the optimization, in a process akin to Darwin's natural selection rules.

SmartLens fabrication: This has been performed in R. Quidant's team at ICFO (Barcelona) by Johann Osmond and Laurent Philippet. The samples were produced in one lift-off step, consisting of UV photolithography with a negative resist (Microchemicals AZ nLOF 2020) on a soda-lime wafer. Subsequently, Ti (2 nm) / Au (50 nm) were deposited using e-beam and thermal evaporation, respectively. Lift-off was completed by removing the resist with acetone. Finally, the whole samples were covered with h=1 mm thick of PDMS (Sylgard 184).

SmartLens characterisation: We experimentally measured the thermal OPD using a wavefront sensor (SID4, Phasics S.A.) under a custom-built microscope (×10, NA=0.45) in the same way that we measured optically-induced thermal OPD in Section 3.4.4.2. The SmartLens was illuminated through a Köhler illuminator. To extract the thermal contribution to the OPD, we subtracted the reference wavefront measured while the device was off ($V = 0$) from the wavefront measured when heating the device ($V \neq 0$). Figure 4.4(b) shows a good agreement

between experimental and simulated OPD maps for different applied voltages, thus validating the electro-thermo-optical wavefront modelling. Furthermore, from the thermal OPD measurement, we extracted the experimental temperature map in the plane of the resistor by deconvolution with the OPD Green's function G_{OPD}, as described in Section 3.4.4.3. This measurement also ensures that the ceiling temperature (T = 250 °C for PDMS[218]) is not reached, to avoid damage.

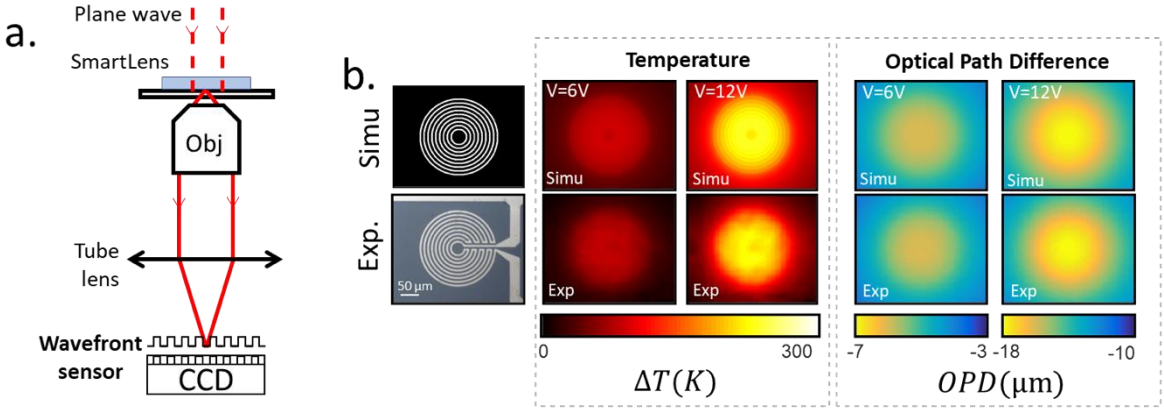

Figure 4.4 Validation of model (adapted from ref[182]*) . (a) Setup for characterization. A plane wave (Köhler illumination) illuminates the SmartLens that is imaged on a high-resolution wavefront sensor. (b) Simulation (top row) and measurement (bottom row) of the temperature and OPD maps for V=6V and 12 V.*

The OPD map in Figure 4.4(b) clearly show that the SmartLenses induce a negative phase curvature, as expected since the thermo-optical coefficient $\frac{dn}{dT}$ of PDMS is negative. Thus, the simple design we chose (9 regularly spaced loops of constant width) acts as a tunable diverging lens.

4.3.4. Dynamic focal range

The experimental OPD profile measured in Figure 4.4 (b) can be approximated [136,188,220] by a parabola $\delta = f_{SL}\left(1 - \frac{x^2}{2f_{SL}^2}\right)$ in order to estimate the focal length f_{SL} of the Smartlens (see Figure 4.5(a) for V=3V). We performed the same measurement on Smartlenses of different diameters D = 10, 50, 200, and 540 µm, all acting as tunable diverging lenses. Figure 4.5 (b) shows, for four spiral sizes, the measured focal length (in log scale) depending on the applied voltage V (in Volts). When the SmartLens is off (V = 0 V), the device acts as a plane-parallel plate (infinite focal length). Interestingly, the focal length $|f|$ decreases faster with the applied

voltage V for smaller heaters, since the radius of curvature of the generated lens is shorter than for bigger heaters. For instance, the vergence of the 200 µm diameter spiral reaches f_{SL}=-2.2mm for V = 12 V, which corresponds to an f-number $|f_{SL}/D|$=11. Furthermore, it is noteworthy that the accuracy and precision of the phase, and thus of the focal length, are only limited by the applied voltage accuracy and precision.

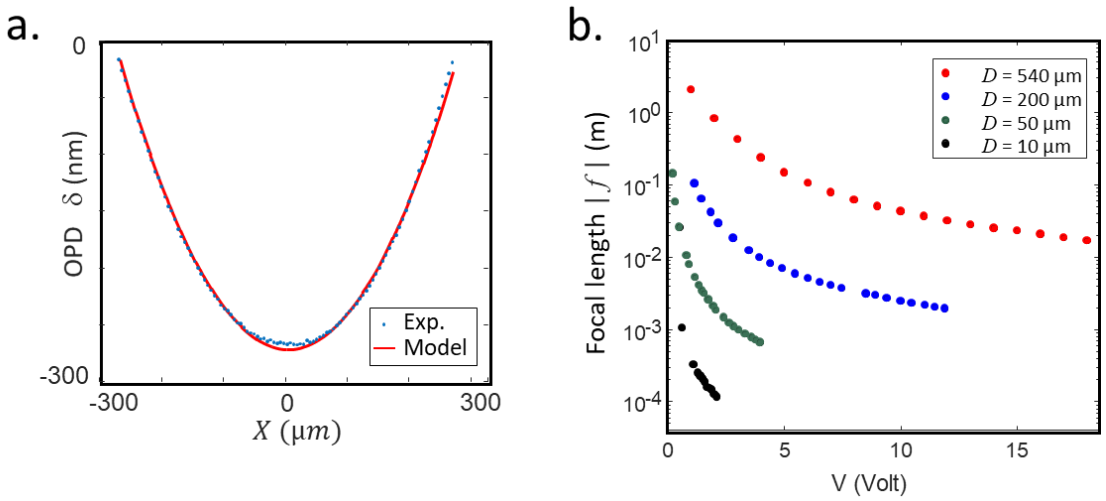

Figure 4.5 Tunability range of SmartLenses for four different sizes. (a) Experimental OPD profile (dots) for a resistor diameter D = 540 µm, V = 3 V. The SmartLens element acts as a diverging lens, and the measured OPD profile is fitted by a parabola (red line) in order to estimate the focal length f. (b) Evolution of focal lengths estimated using the same method for various diameters D, plotted against the applied voltage

When integrated into a microscale array (Figure 4.3(a)), those lenses can be tuned independently and allow focusing on different planes simultaneously. In the following section, we use a diverging SmartLens array to demonstrate focus tuning and multiplane imaging.

4.4. Development of a multiplane imaging fluorescence microscope

As demonstrated at the macro-scale[182], Smartlenses arrays allow the simultaneous refocusing of objects located in different planes, a technique that can be applied to 3D microscopy. This feature is of particular interest in functional voltage imaging, which allows the fluorescence monitoring of the activity of several neurons[221,222]. However, this method is particularly challenging since dim fluorescence signals located in non-deterministic 3D (x, y, z) positions need to be imaged at high frame rates (typ. 1 kHz) with a good SNR to detect short action potentials (typ. 1ms). In this context, a drawback of sequential z-scanning of the imaging plane is the reduction of SNR and temporal resolution[222], and some important events can possibly be missed. Here, we propose to use a SmartLens array for parallel (simultaneous) monitoring of fast transient neuron activity at different depths. This simple strategy will be implemented in 1-photon fluorescence microscopy.

4.4.1. Overview of the setup

I developed the setup with a master student intern, Reda Berrada. The optical path is described in Figure 4.6: a defocusing SmartLens array is inserted in a homemade widefield fluorescence microscope to control both the illumination and imaging paths. A blue LED (λ = 488 nm) excites the fluorescent targets, which are neurons expressing the GcaMP proteins (calcium indicators) in Zebrafish Larvae. Those neurons emit an increase of fluorescence during electrical activities. To excite only the neurons of interest (and therefore reduce the fluorescent background and improve the signal to noise ratio), a **Digital Mirror Device** (DMD) is placed in a conjugated object plane to shape the illumination in the transverse (XY) plane. The illumination light is reflected by a dichroic mirror and projected in an intermediate plane after the SmartLenses array; it is then projected in the sample by a microscope. The **SmartLenses** (SL) **array**, located close to an intermediate image plane (I.P) at a distance Δ, will be tuned electrically to illuminate neurons located at different depths z. Collected fluorescence light crossing the tuned SL on its way back will remain conjugated with the camera. It should be noted that the achromaticity and insensitivity to the polarisation of SLs are crucial here. Parallel methods[37,70,136] (computed holography) based on polarisation-sensitive and chromatic LC-SLM would not allow this implementation. It is also important to mention that this setup is relatively simple, compact and cost-effective.

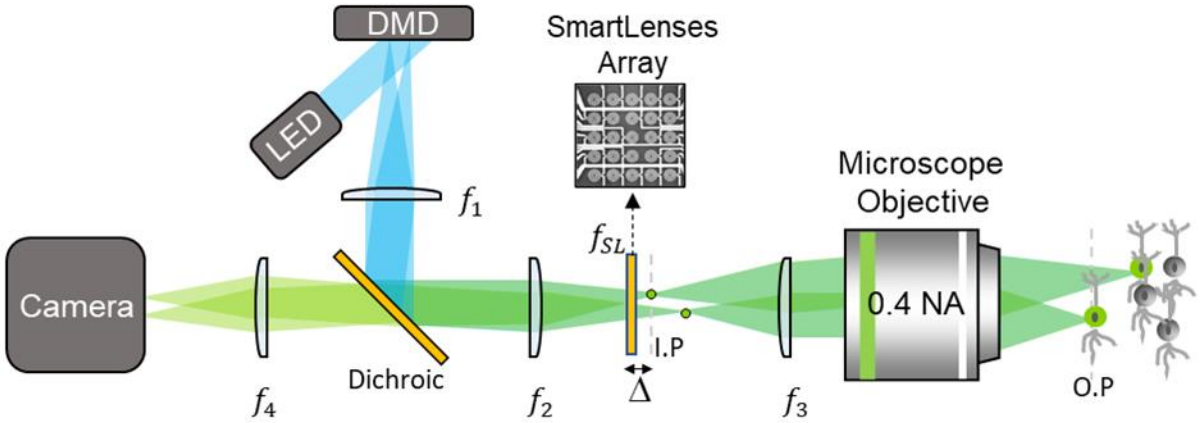

Figure 4.6 Schematic of the simultaneous multiplane imaging microscopy based on a SmartLens array (located close to an intermediate image plane). F_1=f_4=200mm, f_2 = 50mm, f_3 = 125mm, the objective is ×20, water immersed. The dichroic mirror reflects 480 nm excitation light. OP: object plane, IP: intermediate image plane

4.4.2. Modelling and measurement of the axial range

In this section, we study the focal tuning performances of an individual SmartLens (SL), an essential characteristic of the multiplane imaging system. The estimated focal length for SL with a diameter of 540 µm is typically around -40 mm when applying a 10V voltage (Figure 4.5(b)). We placed it in front of an intermediate imaging plane (marked A in Figure 4.7) and measure the defocusing ability ΔZ' (BB') in function with voltage V and distance Δ (O_{SL}A).

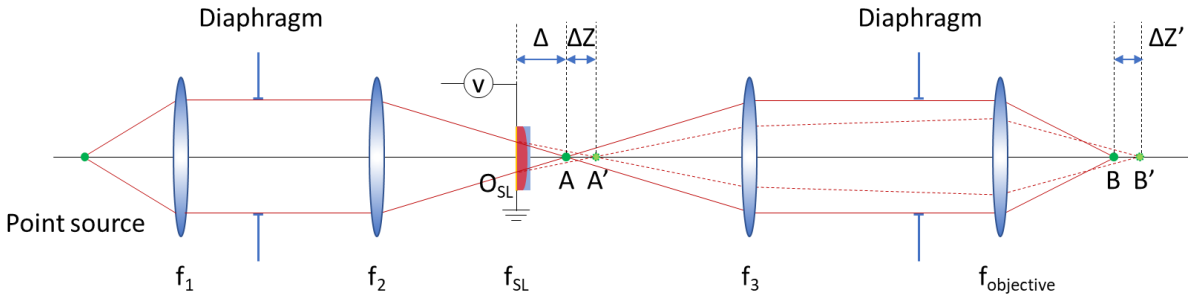

Figure 4.7 Schematic of the SL defocusing setup

Figure 4.7 shows the setup using diverging SLs as defocusing device. F_1-f_2 is a telescope system that brings the image of a point source (i.e. a single pixel of the DMD) to an intermediate plane at position A, allowing space for implementing the SL system. The SL is at plane O_{SL} before the intermediate plane A, Δ is the distance between plane O_{SL} and plane A. When no voltage is applied to the SL, the point source image is in A. The microscope then images the

point source in B. Once a voltage is applied on the SL, it becomes a diverging lens (i.e. with a focal length $f'_{SL}<0$), defocusing the intermediate image from plane A to plane A' and the image from plane B to plane B'. We denote these defocusing values as AA' = ΔZ and BB' = ΔZ'. Using the Gaussian lens formula, ΔZ writes:

$$\Delta Z = -\frac{\Delta^2}{f'_{SL} + \Delta} \qquad \textit{Equation 4.3}$$

For the sake of simplicity, we use the approximation of small ΔZ and $\Delta Z'$values. Thus the relation between ΔZ and $\Delta Z'$ can be represented by the longitudinal magnification M² of the f_3-$f_{objective}$ system: $\Delta Z' = M^2 \Delta Z$ (where $M = \frac{f_{TL}}{M_{objective} f_3}$, $M_{objective}$ the magnification indicated on the objective, and f_{TL} the focal length of the standard tube lens of the microscope, 180 mm). Therefore we have:

$$\Delta Z' = -\frac{\Delta^2}{f'_{SL} + \Delta}\left(\frac{f_{TL}}{M_{objective} f_3}\right)^2 \qquad \textit{Equation 4.4}$$

The value of f'_{SL} being negative, it evolves with applied voltage as shown in Figure 4.5: the higher the voltage, the smaller the value $|f'_{SL}|$, thus the higher the value of $\Delta Z'$. From Equation 4.4, we can also deduce that $\Delta Z'$ increases with the value of Δ. The term $\left(\frac{f_{TL}}{M_{objective} f_3}\right)^2$ shows that smaller magnification of the objective and focal length of f_3 yield a larger defocus $\Delta Z'$. However, Δ cannot increase without limit; it has to be smaller than $|f'_{SL}|$ to ensure that the image B' is a real image; it also needs to be small enough so that the effective diameter of the SL will not limit the pupil of the system, which means that no light passes outside of the SL effective zone (considering a point source on the DMD). Figure 4.8 shows the theoretical and experimental relations between $V_{SL} = \frac{1}{f'_{SL}}$ and $\Delta Z'$ in chosen experimental conditions, and Figure 4.10 shows the PSF of the defocused point source. The experimental defocusing value is higher than the theoretical calculation, as shown in Figure 4.8. However, we consider in the model that the SmartLens is a thin lens located in the plane of the electrical resistor spirals, with a focal length estimated from Figure 4.5(b). In reality, the PDMS layer (Figure 4.2(a)) has a thickness of 1mm, which can induce an error in the estimation of the position of the actual thermal lens. The effect of the thin PDMS layer is not taken into consideration in the model. Also, as the sample that we used here was not yet optimised for aberrations, its focal length

values may have been influenced by the spherical aberration. Moreover, the estimation of focal lengths is not done for the exact SmartLens that we use here. The exact focal length might differ from that measured in Figure 4.5(b) for the same voltage applied. Those could be the reasons explaining the lower defocusing values that were measured, as compared to theoretical expectations.

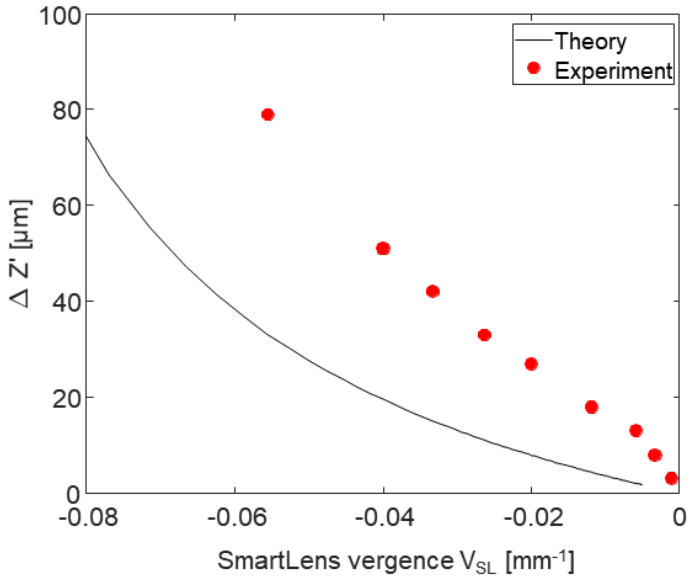

Figure 4.8 Theoretical and experimental relations between V_{SL} and $\Delta Z'$ (with Δ=8mm, the diameter of SL D_{SL}=540µm, f_3=125µm, $M_{objective}$=20, f_{TL}=180mm). f_{SL} is estimated from Figure 4.5(b) for each voltage.

4.4.3. PSF characterization

In order to estimate the axial and lateral extension of the excitation PSF, a single pixel of the DMD (pitch 13.6µm) in the sample plane was imaged with the system described in Figure 4.9. The total magnification of this system is given by $M_{tot} = (f_{obj}f_3)/(f_2f_1)$. It should be noted that under these conditions, the geometrical image size of the pixel ($M_{tot}.s_{pixel}$=0.247µm, with s_{pixel} the pixel size) is negligible compared to the size of the PSF when the latter is limited by diffraction (typ. λ/2NA=0.6µm, considering NA=0.4). The pixel can therefore be considered as a point source. The 3D excitation PSF is then measured using a forward collection path consisting of a microscope objective with a large NA, a tube lens and a camera. For different voltages applied to the SmartLens, the objective is scanned axially to measure the 3D PSF (see Figure 4.9).

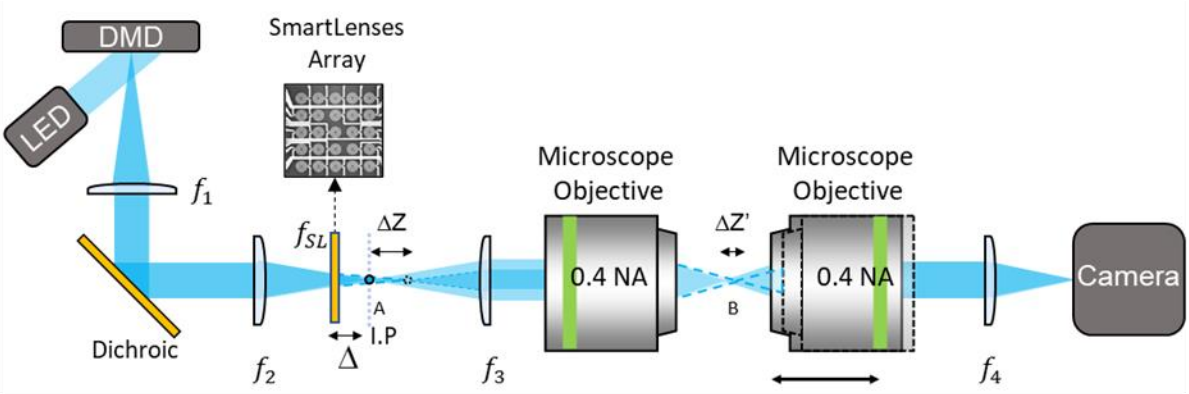

Figure 4.9 Schematic of the PSF characterisation setup. LED source λ = 488 nm, f_1=200mm, f_2 = 50mm, f_3 = 125mm, f_4=250mm. The objectives are both ×20, NA=0.40.

Figure 4.10(c) shows that with this configuration (Δ=8mm, D_{SL}=540µm, f_3=125µm, $M_{objective}$=20, the corresponding tube lens for objective f_{TL}=180mm), we can distinguish different planes with around 10µm z-resolution, which evolves with defocusing depth ΔZ'. With 18V applied to the resistor, we can reach 79µm displacement in the z-direction.

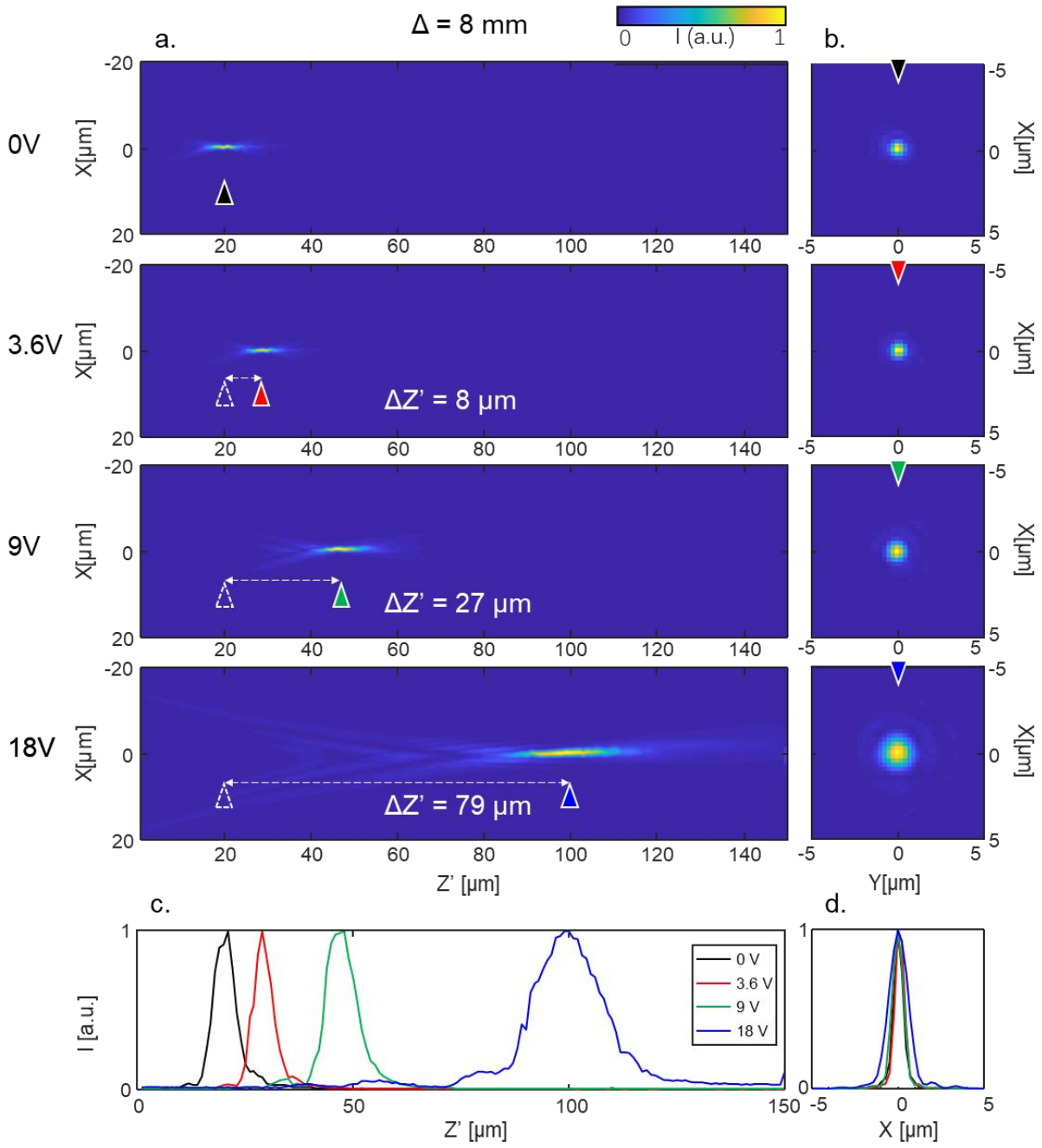

Figure 4.10 Defocused point source, with $\Delta = 8mm$, V = 0V, 3.6V, 9V and 18V. (a) XZ projection of the PSF defocused by SL with different voltages. (b) xy-projection of PSF on focus. (c) PSF profile along the optical axis (z-direction). (d) PSF profile along the x-direction. The excitation source is generated by 1 pixel on the DMD.

4.5. Preliminary results on a Zebrafish

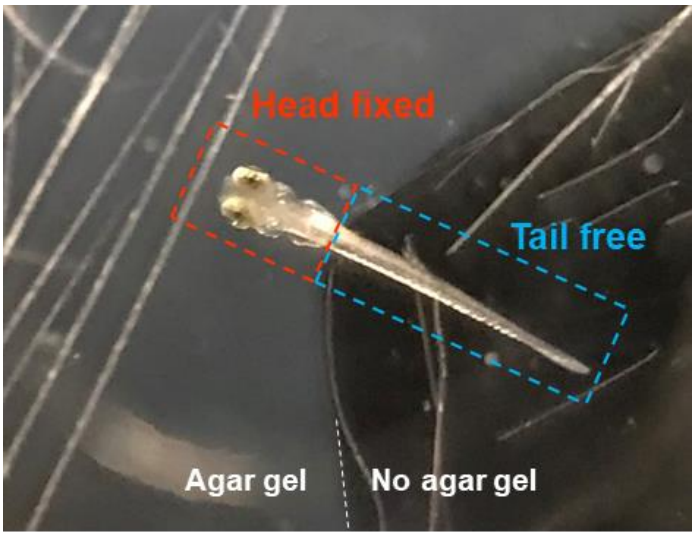

Figure 4.11 6dpf Zebrafish larvae head-embedded in agar gel and free-tailed, maintained in a solution that supports its life

The zebrafish larvae (Danio rerio) are almost transparent, which makes them ideal for *in vivo* fluorescence imaging. Here we investigate 6 days post-fertilization (6dpf) larvae, genetically encoding calcium (Ca^{2+}) indicator GcaMP6s to measure neuronal activity. When a neuron is active and fires an action potential, there is a Ca^{2+} influx into the cell that is sensed by the calcium indicator. This results in an increase in its green fluorescence under blue light illumination ($\lambda = 488$ nm). Here, the head of the fish is fixed in 2% agar gel so that it stays still during the imaging process. The tail of the fish remains free in the liquid so that it can move freely and evoke activities in the nerve system. In order to increase neuronal activity and thus fluorescence signals, we add in the water the drug Gabazine, which blocks inhibitory receptors of the cells and thus enhances activity. The zebrafish larvae sample has been prepared by Giulia Faini (post-doc in the group of F. Del Bene at *Institut de la vision*).

We placed the SmartLens array at Δ=8 mm in front of the intermediate plane, as shown in Figure 4.6. Thus its structure is not visible in the sample image plane. In Figure 4.12*(a)*, we can only see some shadows within the dashed circles due to the optical absorption of gold wires in excitation and collection. When a 0V voltage is applied to the SLs, no lens effect is activated; thus, we only see neurons at the focal plane z = 0. By tuning the voltages individually in chosen Smart Lenses, we can bring neurons located at different depths and different region of the field of view to the same image plane. For example, in Figure 4.12, 11V applied on SL#1 brings neurons at plan z=26µm into focus (positive z means deeper in tissue); 16V applied on SL#2,

neurons at z=42µm are on focus. Figure 4.12 (c) shows that neurons from the three different planes are all observed on the same image when the appropriate voltages are applied individually on different elements.

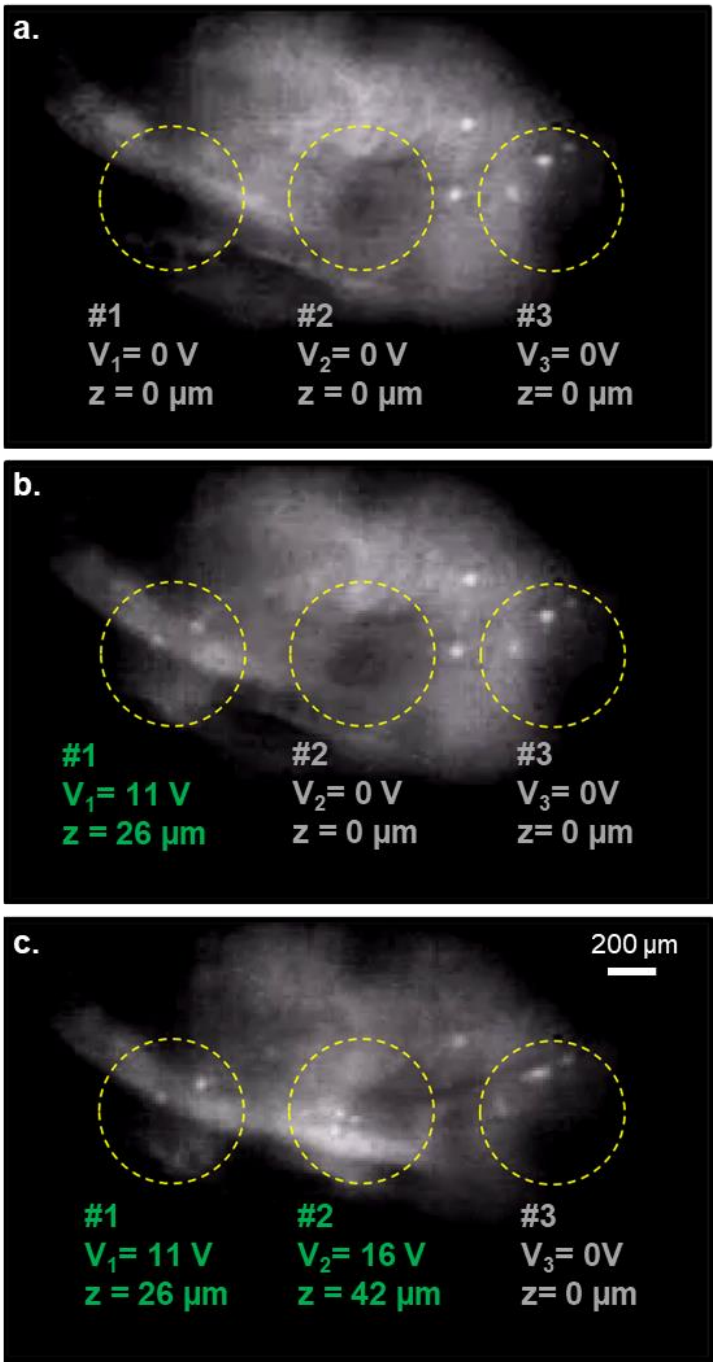

Figure 4.12 Widefield calcium imaging of neuron activities at different depths in the zebrafish larvae. SmartLens elements are tuned with different voltages to focus in different planes. (a) 0V applied on all elements; (b) 11V applied on element #1; (c) 11V applied on element #1 and 16V applied on element #2.

In the images shown in Figure 4.12, a widefield illumination technique was used. This induces background fluorescence signals from the tissue, decreasing the signal to noise ratio (SNR). In order to increase the SNR, we can use a selective illumination of zones of interest using a digital mirror device (DMD). The selective illumination requires taking at first a long image stack, which records all active neurons' positions; thus, one can address interesting zones afterwards. In Figure 4.13(a), widefield imaging outside of the green dashed circle is focused on plane z=0, while the zone in the green dashed circle is focused on plane z=36µm using the activated SL located here. A long stack acquisition of all the neuron activities is taken with this SL element activated (500 images were taken in ~2.5 minutes with a frame rate of 3.278 Hz). The stack is processed by counting the maximum of each pixel (Z-projection through ImageJ); thus, all the neurons which have fired during the acquisition were recorded, both in the plane z =0 (outside the green dashed line circle) and in the plane z=36µm (inside the green dashed line circle). Then, we chose several locations of interest, shown by white dashed squares in Figure 4.13(a). Using the DMD device, calibrated illumination patterns (Figure 4.13(b)) were sent to the sample to illuminate only the chosen neurons rather than the entire imaged field. Figure 4.13(c) shows the resulting patterned illumination: only neurons located in the illuminated zones of interest were possible to give fluorescence light when firing.

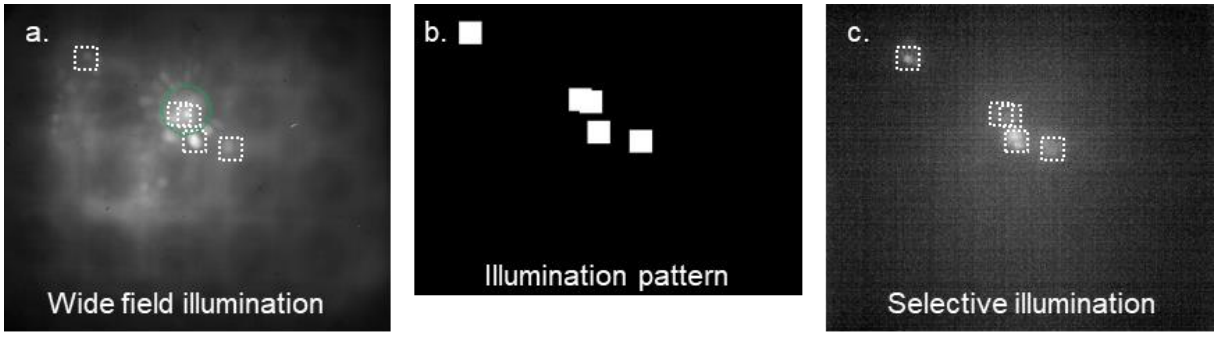

Figure 4.13 Fluorescence images (calcium imaging) under wide-field illumination and selective illumination. (a) 'Z-projection' calculation results of 500 images taken during 2.5 minutes while the whole field is illuminated to capture fluorescence from all active neurons; (b) illumination pattern on the DMD for preselected regions; (c) A fluorescence image taken with an integration time of 0.3s under the selective illumination condition reveals the activity of the illuminated neurons.

Under selective illumination, we observed neuron activities in different planes. In Figure 4.14(a), no SL is activated; thus, the whole image is taken in the plane z = 0. Very few neuron activities appear in z = 0, and there is almost no event detected within 2 minutes in zone 1 and 2.

In Figure 4.14(b), one SL is activated inside the white dashed circle and becomes a diverging lens: zones 3 and 4 stays in the plane z = 0 and zones 1 and 2 are brought to a deeper plane, z=36 µm. We observe neuron activities in zone 1 and 2 at z = 36 µm. In zones 3 and 4, there is no obvious change as we keep looking at the same neurons in the plane z =0, where the activity is low.

This experiment illustrates the possibilities offered by SmartLenses when imaging multiple planes, as it offers the possibility of recording neural spiking in multiple planes, some of which were previously inaccessible.

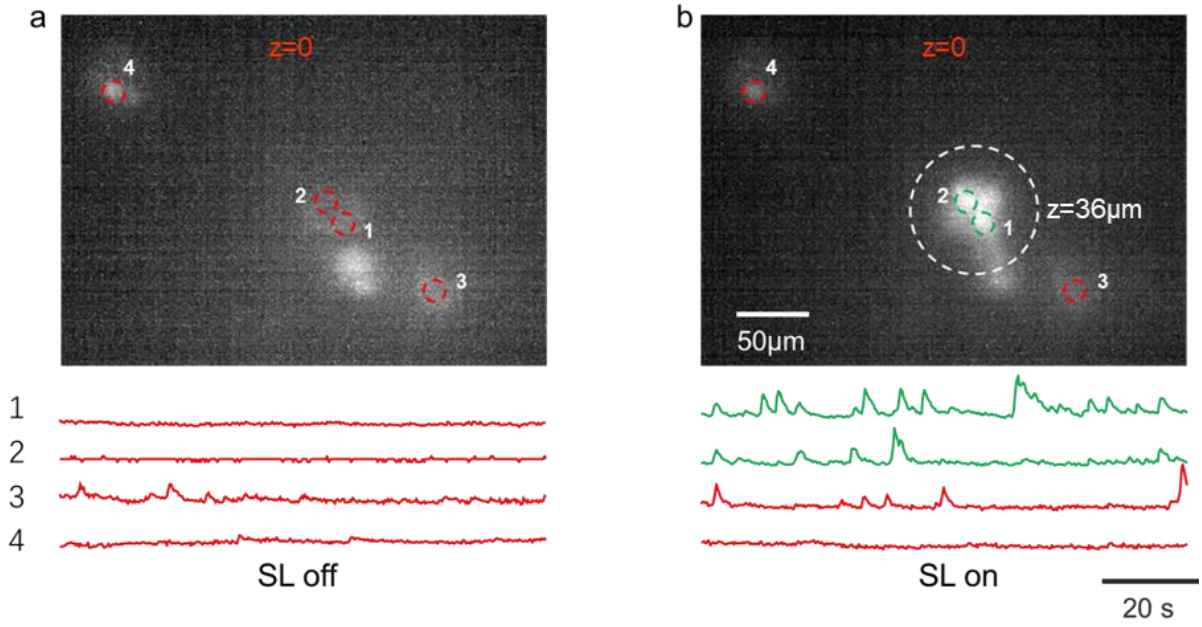

Figure 4.14 Recording spontaneous neuron activities through fluorescent imaging. (a) When the SL is off, the whole image is taken at z = 0. Only very few spontaneous neurons activities are observed at this depth, within zones 3 and 4; no neuron activities are observed inside zone 1 and 2. (b) As the SL is activated inside an effective zone drawn in white dashes, the focusing is locally brought to a deeper plane z = 36µm; very frequent spontaneous neurons activities are observed at zone 1 and 2 at this depth; Zones 3 and 4 stay focused at z = 0: a firing rate similar to that of the initial situation (a) is observed. The time scale bar corresponds to 20 s; the intensity is in arbitrary units.

4.6. Discussion

The results in Figure 4.12 and Figure 4.14 have demonstrated the feasibility of multiplane imaging using the SmartLens device. This proof-of-principle experiment also suggests several points for further improvements.

- **Setup improvement**: The setup shown in Figure 4.6 is not perfectly confocal. The rejection of the fluorescence background would be much better if the fluorescence signal would be imaged back to the DMD. In this condition, the pixels "on" for selective excitation would also serve as a pinhole to reject the fluorescence emitted out of the regions of interest.
- **SmartLens transparency**: So far, our work has focused on (50-nm thick) absorbing gold electrodes leading to a transmission of the order of 65 %, which is detrimental to both the optical excitation and collection. This effect is visible in e.g. Figure 4.13(a), where a defocused shadow of the SmartLens array is clearly visible. This needs to be improved to maximise the signal-to-noise ratio as well as to decrease the integration time (thus increasing the frame rate) of the camera, a critical point in Calcium and Voltage imaging. Preliminary tests on conductive oxides (Indium Tin Oxide – ITO) have demonstrated transmission and absorption at the desired level as well as reduced diffractive effects (only 1.5% of the incident light is diffracted for 25-nm thick ITO electrodes) compared to 50-nm thick gold electrodes. However, this comes at the price of higher SL activation voltage values due to the resistivity of ITO. It is worth mentioning that the use of low absorption ITO would also make it possible to work in a 2-photon excitation regime in order to increase axial sectioning.
- **Thermal crosstalk:** In steady-state, temperature profiles decay with the distance according to the steady-state thermal Green's function. This induces thermal cross-talk between neighbouring SmartLenses. When we activate one SL, we also induce aberrations in the adjacent SLs. For example, in Figure 4.12(c), neuron images in zone #3 are influenced by the activation of the SL located in zone #2. An interesting strategy investigated in R.Quidant's group consists in confining the temperature increase by engineering the thermal diffusivity around the resistor. Adding high thermal conductivity heat sinks around each SL would help mitigate this cross-talk.
- **Improving the PSF**: PSF quality is an important factor for spatial resolution. In SmartLens applications, it can be improved by correcting aberrations through numerically engineering the OPD profile. To reach the desired OPD, one has to solve the inverse problem and find

out the electrical design that gives the proper heat source distribution. In article [182], a genetic algorithm is applied to determine the optimal resistor design leading to the targeted wavefront shape. The variables for one design are the number of wire circles, the radius and the width of each wire circle. The genetic algorithms give stochastic mutation and crossover on each parameter and select the optimal using a merit function. After typically 60 iterations which take around 30 minutes, one effective design can be obtained. The efficiency of this method is discussed in article[182], and various wavefront shapes are acquired experimentally. In Figure 4.15, several different wavefronts are demonstrated: pure defocus, piston, hollow-axicon and vertical astigmatism. It shows a high degree of freedom for wavefront control and broad potential applications. Annex 3 shows an example using the inverted axicon to generate tunable annular and Bessel beam. For our imaging system, where the SmartLens is located in an intermediate image plane, the PSF can also be optimised in advance using this approach to pre-compensate possible aberrations of the system and obtain an optimal PSF.

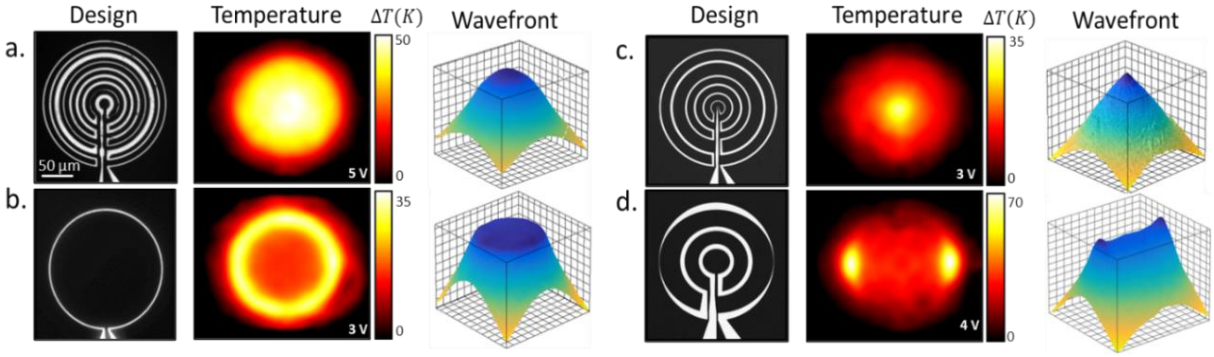

Figure 4.15 Wavefront engineering with SmartLenses - Experimental results obtained on a set of four spiral geometries optimised for four different wavefronts: (a) Pure Defocus (diverging lens). (b) Flat profile (piston). (c) Conical surface (hollow-axicon). (d) Vertical astigmatism. In each case, an optical reflection image of the fabricated spiral design and the corresponding experimental temperature and wavefront is shown.

4.7. Conclusion

We have demonstrated in preliminary experiments that a diverging SmartLens can be easily applied to simultaneous *in vivo* multiplane fluorescence imaging, with a local defocusing range of around 100µm and depth of field of around 10µm. In the present experiments, the heating spirals are made of gold, thus blocking a non-negligible amount of excitation and fluorescence light. To acquire enough photons, we are currently limited to 100-300ms frame integration times. This frame rate can be improved (i) by using a more powerful excitation source and, more importantly, (ii) by using ITO as electrical heating material, since it is almost transparent to visible light and causes little diffraction. Thus, one will not see the 'shadows' as in Figure 4.13(a) and could expect brighter and clearer images as well as higher frame rates. In Figure 4.13 and Figure 4.14, we only activated one of the SmartLenses in the array to observe activities in two planes simultaneously as an example. By optimising the optical system (increasing the defocusing range) and SL positions, massively multiplane imaging is possible. A new set of experiments showing applications of this concept to a biologically relevant problem will be carried out in the near future. Furthermore, this miniature device can be associated with GRIN (Gradient Index) lenses to achieve endoscopic multiplane imaging; it is light enough to be implemented in rodent-wearable microscopes. Last but not least, once the frame time is shortened through the optimisation of transmission, the advantages of simultaneous multiplane imaging can be fully appreciated when it allows the imaging of previously inaccessible millisecond voltage imaging signals in multiple 3D-distributed neurons. As shown in Figure 4.1(b), this will contribute to drawing even more interest towards fast *in vivo* observation of neuron activities in brain circuits.

The results presented in this chapter have been partially published in:

Tunable and free-form planar optics

Nature Photonics **2019** 13(9), 649–656

DOI: https://doi.org/10.1038/s41566-019-0486-3

Conclusion

This work started off centred on the evaluation of the temperature rise induced by two-photon optogenetic stimulation in tissue. This was achieved through luminescence thermometry and a thermal model (Chapter 2). These developments led us to extend the scope towards two other themes, both also connected to optics, thermal phenomena, and the study of neural behaviour: reconfigurable temperature control using thermo-plasmonics (Chapter 3) and simultaneous multi-plane imaging using tunable thermo-optical SmartLenses (Chapter 4). The temperature control technology provides a platform for studying thermal perturbation on cell physiology and metabolism; the multi-plane imaging opens new perspectives for observing brain activities in 3D.

Our luminescence thermometry 'endoscope' was realised by fixing the temperature-sensitive probe (an Er/Yb glass particle) at the extremity of a double-clad fibre, which guides the pumping light to the probe and collects the luminescence light for spectral analysis. This system achieved stable and precise temperature measurements deep (~330µm) inside the brain, with a 2-millisecond temporal resolution, up to ~15µm spatial resolution and 0.05K temperature sensitivity (after 500 averages). There are trade-offs between those parameters.: for example, by increasing the integration time of the spectrometer, one can decrease the noise thus increase the temperature sensitivity, at the expense of a longer temporal resolution; by decreasing the Er/Yb probe size, one can have a finer spatial resolution, however fewer photons are then available which increases the noise. Our system is explicitly developed to measure the millisecond, microscale and sub-Kelvin temperature rise induced by 2P optogenetics stimulation. It can also be applied in many other contexts, for example, to measure the temperature rise caused by 2P/3P imaging, and even broader applications, whenever remote, minimally invasive temperature sensing is required. Depending on the spatial, temporal and temperature sensitivity requirements under different contexts, we can modify the acquisition parameters as well as the structure of the fibre probe. For example, the double-clad fibre structure can be replaced by a thinner fibre structure, e.g. thinner single-mode fibres or fibres with a tapered end, particularly if lower sensitivities are acceptable (since thinner fibres will collect luminescence less efficiently). With a thinner probe, one can measure closer to the target and cause less damage. One can also modify the optical structure at the fibre end to optimise luminescence collection. For example, instead of positioning the probe directly at the centre of the cleaved fibre, one could create a spherical lens (with optical glue, lithography, moulding or

by melting the fibre tip) and then position the Er/Yb probe at the focal point of the lens. Instead of using optical glue, one can also melt the probing material directly on the fibre, which could hopefully increase the illuminating efficiency and decrease loss by surface reflection. One can even add reflective coating around the probe to send more luminescence light to the fibre. On the other hand, now that we have achieved "single-pixel" measurement using one probe situated on the core of a double-clad fibre, it would thus be interesting to increase the pixel number using an optical fibre bundle and realise a thermal endoscope. For this purpose, finer manufacturing would be required to avoid cross-talk. Besides, the luminescence thermometry can be applied on various working mode without the use of an optical fibre as long as stable calibration is provided.

Our *in vivo* temperature measurements have validated a thermal model that simulates photo-induced temperature rises in scattering tissues. The temperature probe cannot measure inside the heat source itself (a 2P optogenetic holographic stimulation spot) because this will influence the light absorption of the tissue and disturb the luminescence of the probe. For this reason, measurements were carried out at various lateral positions (66-200µm) away from the holographic spot, and we varied the pulse duration and power of the holographic spot. The experiments agree well with the thermal model for the chosen scattering coefficients, taken from publications. Using the model, we estimated the maximum temperature rises inside the holographic spot for typical 2P optogenetic stimulation conditions (12µm-diameter, 1030nm-wavelength, 0.8-NA, 330µm deep in the brain, power P at the exit of objective and duration t_{pulse}):

t_{pulse} [ms]	Maximum temperature rise in spot centre [K]	
	P = 10 mW	P = 50 mW
10	0.14	0.71
30	0.20	0.99

Due to the linearity of thermal phenomena with respect to the excitation power and based on these results, we can simulate with a good degree of confidence the temperature rise induced by a train of optogenetic stimulation pulses and multiple spots distributed in space. This model also allows for calculating the photo-induced thermal effect of 2P/3P scanning imaging. Combining the thermal probe and thermal model, we provide a toolbox to evaluate the photo-induced thermal effect in tissue, which we believe will answer most thermal concerns within the optogenetics community.

The reconfigurable temperature control combines wavefront engineering and thermo-plasmonics. It allows to create chosen temperature patterns in a specific domain of space at the microscale (down to sub-cell resolution) to e.g. study the influence of localized heating on cells. We experimentally demonstrated the feasibility of the procedure by imaging the temperature with micrometre resolution using a method based on wavefront-sensing. There are clearly limitations to the method: temperature gradients steeper than the $\frac{1}{r}$ imposed by heat diffusion are not achievable without using (currently unavailable) negative heat sources, i.e. local cooling. For similar reasons, the temperature can only be controlled in limited domains of space, and will be driven by $\frac{1}{r}$ diffusion, collective effects (i.e. other neighbouring heat sources), and boundary conditions outside of this domain. Nevertheless, overcoming thermal diffusion by pre-engineering thermal sources promises a wide range of applications, for which reconfigurable, fast and accurate temperature shaping is necessary. We showed as proof of principle that this technique has the potential to create heat stimulation targeting different parts of a neuron. In adherent neuron cells, we could select various zones of interest (spatially and temporally) in one neuron or for a group of neurons and create homogeneous temperature rises within a limited (~10µm) region above the substrate. As the setup is quite compact and only involves a quasi transparent coverslip on the sample side, it is possible to observe at the same time the neuronal activities through patch-clamp, calcium imaging or voltage imaging, allowing the observation of electrophysiological responses under controlled levels of thermal stimulation. This technique also raises interests in thermogenetics, where heat is used to evoke action potentials. We can imagine a cultured neuron circuit adherent to the substrate, thermally activable by spatiotemporal temperature patterns. The method is reconfigurable so that the stimulation pattern can be adjusted very fast during the experiment, making it possible to observe and adjust neuron stimulations on a coverslip in real-time.

Besides application in biology, this approach can also be used in physics (e.g. phase changes, microscale thermal phenomena), microfluidics and chemistry, where thermal gradients are crucial to drive, e.g., reaction kinetics.

Temperature control at the microscale can also be exploited to make tunable optical devices, which is very useful for 3D imaging. In the last chapter, we have demonstrated that a diverging SmartLens, realised through micro-electrical-resistor heating in a thermo-optical medium, can be easily applied to simultaneous *in vivo* multi-plane imaging. A preliminary demonstration was obtained by implementing a SmartLenses array into a full-field calcium imaging system and has shown great potential. By changing the voltage applied on resistors,

one can obtain a local defocusing range of around 100µm with a depth of field of around 10µm. This preliminary work still leaves several aspects open to optimization. Here, the tested device is made of gold heating spirals, which block a non-negligible amount of excitation and fluorescence light. To acquire enough photons, we are currently limited to 100-300ms frame integration times. This can be improved using ITO as electrical heating material, since it is almost transparent to visible light and causes little diffraction. This solution is being explored, and we can thus expect brighter and clearer images with higher frame rates. Also, by optimising the optical system and SLs position, massively multi-plane imaging should be possible. A new set of experiments showing the applications of this concept to a biologically relevant problem will be carried out in the near future. Furthermore, this miniature device can be associated with GRIN (Gradient Index) lenses to achieve endoscopic multi-plane imaging, or can be implemented in rodent-wearable microscopes. Last but not least, once the frame time is shortened through the optimisation of transmission, the advantages of simultaneous multi-plane imaging can be fully appreciated, allowing the imaging of previously inaccessible millisecond voltage signals in multiple 3D-distributed neurons. We are confident that this will draw even more interest towards fast *in vivo* observation of neuron activities in brain circuits.

Bibliography

1. Miller, D. R., Jarrett, J. W., Hassan, A. M. & Dunn, A. K. Deep tissue imaging with multiphoton fluorescence microscopy. *Curr. Opin. Biomed. Eng.* **4**, 32–39 (2017).
2. Luo, L., Callaway, E. M. & Svoboda, K. Genetic Dissection of Neural Circuits. *Neuron* **57**, 634–660 (2008).
3. Carter, M. E. & de Lecea, L. Optogenetic investigation of neural circuits in vivo. *Trends Mol. Med.* **17**, 197–206 (2011).
4. Connors, B. W. & Gutnick, M. J. Intrinsic firing patterns of diverse neocortical neurons. *Trends Neurosci.* **13**, 99–104 (1990).
5. Apfelstedt-Sylla, E. & Zrenner, E. Electrophysiology. *Clin. Neuro-Ophthalmology A Pract. Guid.* 87–99 (2007) doi:10.1007/978-3-540-32708-0_7.
6. Hodgkin, A. L. & Huxley, A. F. A quantitative description of ion currents and its applications to conduction and excitation in nerve membranes. *J. Physiol.* **117**, 500–544 (1952).
7. Lodish, H., Berk, A., Zipursky, S. L., Matsudaira, P., Baltimore, D. & Darnell, J. The action potential and conduction of electric impulses. in *Molecular Cell Biology. 4th edition* (WH Freeman, 2000).
8. Jin, L., Han, Z., Platisa, J., Wooltorton, J. R. A., Cohen, L. B. & Pieribone, V. A. Single Action Potentials and Subthreshold Electrical Events Imaged in Neurons with a Fluorescent Protein Voltage Probe. *Neuron* **75**, 779–785 (2012).
9. Platkiewicz, J. & Brette, R. A Threshold Equation for Action Potential Initiation. *PLOS Comput. Biol.* **6**, 1–16 (2010).
10. Warden, M. R., Cardin, J. A. & Deisseroth, K. Optical neural interfaces. *Annu. Rev. Biomed. Eng.* **16**, 103–129 (2014).
11. OESTERHELT, D. & STOECKENIUS, W. Rhodopsin-like Protein from the Purple Membrane of Halobacterium halobium. *Nat. New Biol.* **233**, 149–152 (1971).
12. Nagel, G., Szellas, T., Huhn, W., Kateriya, S., Adeishvili, N., Berthold, P., Ollig, D., Hegemann, P. & Bamberg, E. Channelrhodopsin-2, a directly light-gated cation-selective membrane channel. *Proc. Natl. Acad. Sci.* **100**, 13940–13945 (2003).

13. Nagel, G., Ollig, D., Fuhrmann, M., Kateriya, S., Musti, A. M., Bamberg, E. & Hegemann, P. Channelrhodopsin-1: a light-gated proton channel in green algae. *Science* **296**, 2395–2398 (2002).

14. Matsuno-Yagi, A. & Mukohata, Y. Two possible roles of bacteriorhodopsin; a comparative study of strains of Halobacterium halobium differing in pigmentation. *Biochem. Biophys. Res. Commun.* **78**, 237–243 (1977).

15. Boyden, E. S., Zhang, F., Bamberg, E., Nagel, G. & Deisseroth, K. Millisecond-timescale, genetically targeted optical control of neural activity. *Nat. Neurosci.* **8**, 1263–1268 (2005).

16. Zhang, F., Aravanis, A. M., Adamantidis, A., de Lecea, L. & Deisseroth, K. Circuit-breakers: optical technologies for probing neural signals and systems. *Nat. Rev. Neurosci.* **8**, 577–581 (2007).

17. Cardin, J. A., Carlén, M., Meletis, K., Knoblich, U., Zhang, F., Deisseroth, K., Tsai, L. H. & Moore, C. I. Driving fast-spiking cells induces gamma rhythm and controls sensory responses. *Nature* **459**, 663–667 (2009).

18. Zhang, F., Wang, L. P., Brauner, M., Liewald, J. F., Kay, K., Watzke, N., Wood, P. G., Bamberg, E., Nagel, G., Gottschalk, A. & Deisseroth, K. Multimodal fast optical interrogation of neural circuitry. *Nature* **446**, 633–639 (2007).

19. Li, X., Gutierrez, D. V., Hanson, M. G., Han, J., Mark, M. D., Chiel, H., Hegemann, P., Landmesser, L. T. & Herlitze, S. Fast noninvasive activation and inhibition of neural and network activity by vertebrate rhodopsin and green algae channelrhodopsin. *Proc. Natl. Acad. Sci.* **102**, 17816–17821 (2005).

20. Tsai, H. C., Zhang, F., Adamantidis, A., Stuber, G. D., Bond, A., De Lecea, L. & Deisseroth, K. Phasic firing in dopaminergic neurons is sufficient for behavioral conditioning. *Science (80-.).* **324**, 1080–1084 (2009).

21. Szobota, S., Gorostiza, P., Del Bene, F., Wyart, C., Fortin, D. L., Kolstad, K. D., Tulyathan, O., Volgraf, M., Numano, R., Aaron, H. L., Scott, E. K., Kramer, R. H., Flannery, J., Baier, H., Trauner, D. & Isacoff, E. Y. Remote Control of Neuronal Activity with a Light-Gated Glutamate Receptor. *Neuron* **54**, 535–545 (2007).

22. Huber, D., Petreanu, L., Ghitani, N., Ranade, S., Hromádka, T., Mainen, Z. & Svoboda, K. Sparse optical microstimulation in barrel cortex drives learned behaviour

in freely moving mice. *Nature* **451**, 61–64 (2008).

23. Curtis, J. C. & Kleinfeld, D. Phase-to-rate transformations encode touch in cortical neurons of a scanning sensorimotor system. *Nat. Neurosci.* **12**, 492–501 (2009).

24. O'Connor, D. H., Huber, D. & Svoboda, K. Reverse engineering the mouse brain. *Nature* **461**, 923–929 (2009).

25. Ohki, K., Chung, S., Ch'ng, Y. H., Kara, P. & Reid, R. C. Functional imaging with cellular resolution reveals precise microarchitecture in visual cortex. *Nature* **433**, 597–603 (2005).

26. Peron, S. & Svoboda, K. From cudgel to scalpel: Toward precise neural control with optogenetics. *Nat. Methods* **8**, 30–34 (2011).

27. Papagiakoumou, E. Optical developments for optogenetics. *Biol. Cell* **105**, 443–464 (2013).

28. Ronzitti, E., Ventalon, C., Canepari, M., Forget, B. C., Papagiakoumou, E. & Emiliani, V. Recent advances in patterned photostimulation for optogenetics. *J. Opt. (United Kingdom)* **19**, 113001 (2017).

29. Papagiakoumou, E., Ronzitti, E., Chen, I.-W., Gajowa, M., Picot, A. & Emiliani, V. Two-Photon Optogenetics by Computer-Generated Holography. in *Neuromethods* vol. 133 175–197 (2018).

30. Benninger, R. K. P. & Piston, D. W. *Two-photon excitation microscopy for unit 4.11 the study of living cells and tissues*. *Current Protocols in Cell Biology* (2013). doi:10.1002/0471143030.cb0411s59.

31. Rumi, M. & Perry, J. W. Two-photon absorption: an overview of measurements and principles. *Adv. Opt. Photonics* **2**, 451 (2010).

32. Xu, C. & Webb, W. W. Multiphoton Excitation of Molecular Fluorophores and Nonlinear Laser Microscopy. in *Topics in Fluorescence Spectroscopy: Volume 5: Nonlinear and Two-Photon-Induced Fluorescence* (ed. Lakowicz, J. R.) 471–540 (Springer US, 2002). doi:10.1007/0-306-47070-5_11.

33. Denk, W., Strickler, J. H. & Webb, W. W. Two-photon laser scanning fluorescence microscopy. *Science (80-.).* **248**, 73–76 (1990).

34. So, P. T. C., Dong, C. Y., Masters, B. R. & Berland, K. M. Two-Photon Excitation Fluorescence Microscopy. *Annu. Rev. Biomed. Eng.* **2**, 399–429 (2000).

35. Zipfel, W. R., Williams, R. M. & Webb, W. W. Nonlinear magic: Multiphoton microscopy in the biosciences. *Nat. Biotechnol.* **21**, 1369–1377 (2003).

36. Feldbauer, K., Zimmermann, D., Pintschovius, V., Spitz, J., Bamann, C. & Bamberg, E. Channelrhodopsin-2 is a leaky proton pump. *Proc. Natl. Acad. Sci. U. S. A.* **106**, 12317–12322 (2009).

37. Papagiakoumou, E., Anselmi, F., Bègue, A., de Sars, V., Glückstad, J., Isacoff, E. Y. & Emiliani, V. Scanless two-photon excitation of channelrhodopsin-2. *Nat. Methods* **7**, 848–854 (2010).

38. Lutz, C., Otis, T. S., DeSars, V., Charpak, S., DiGregorio, D. A. & Emiliani, V. Holographic photolysis of caged neurotransmitters. *Nat. Methods* **5**, 821–827 (2008).

39. Papagiakoumou, E., de Sars, V., Oron, D. & Emiliani, V. Patterned two-photon illumination by spatiotemporal shaping of ultrashort pulses. *Opt. Express* **16**, 22039 (2008).

40. Oron, D., Tal, E. & Silberberg, Y. Scanningless depth-resolved microscopy. *Opt. Express* **13**, 1468 (2005).

41. Bègue, A., Papagiakoumou, E., Leshem, B., Conti, R., Enke, L., Oron, D. & Emiliani, V. Two-photon excitation in scattering media by spatiotemporally shaped beams and their application in optogenetic stimulation. *Biomed. Opt. Express* **4**, 2869–79 (2013).

42. Chaigneau, E., Ronzitti, E., Gajowa, M. A., Soler-Llavina, G. J., Tanese, D., Brureau, A. Y. B., Papagiakoumou, E., Zeng, H. & Emiliani, V. Two-Photon Holographic Stimulation of ReaChR. *Front. Cell. Neurosci.* **10**, 234 (2016).

43. Chen, I.-W., Ronzitti, E., R., B. L., L., T. D., Zeng, H., Papagiakoumou, E. & Emiliani, V. Parallel holographic illumination enables sub-millisecond two-photon optogenetic activation in mouse visual cortex in vivo. *BioArxiv* 1–21 (2017) doi:10.1101/250795.

44. Picot, A. 2P optogenetics : simulation and modeling for optimized thermal dissipation and current integration. (2018).

45. Upputuri, P. K. & Pramanik, M. Photoacoustic imaging in the second near-infrared window: a review. *J. Biomed. Opt.* **24**, 1 (2019).

46. Boulnois, J. L. Photophysical processes in recent medical laser developments: A review. *Lasers Med. Sci.* **1**, 47–66 (1986).

47. Vogel, A., Noack, J., Hüttman, G. & Paltauf, G. Mechanisms of femtosecond laser

nanosurgery of cells and tissues. *Appl. Phys. B Lasers Opt.* **81**, 1015–1047 (2005).

48. Elwassif, M. M., Kong, Q., Vazquez, M. & Bikson, M. Bio-heat transfer model of deep brain stimulation-induced temperature changes. *J. Neural Eng.* **3**, 306–315 (2006).

49. Hodgkin, A. L. & Katz, B. The effect of sodium ions on the electrical activity of the giant axon of the squid. *J. Physiol. J. Physiol. Online UNIV UTAH* **108**, 37–77 (1949).

50. Reig, R., Mattia, M., Compte, a, Belmonte, C. & Sanchez-Vives, M. V. Temperature modulation of slow and fast cortical rhythms. *J. Neurophysiol.* **103**, 1253–1261 (2010).

51. Stujenske, J. M., Spellman, T. & Gordon, J. A. Modeling the Spatiotemporal Dynamics of Light and Heat Propagation for InVivo Optogenetics. *Cell Rep.* **12**, 525–534 (2015).

52. Plaksin, M., Shapira, E., Kimmel, E. & Shoham, S. Thermal Transients Excite Neurons through Universal Intramembrane Mechanoelectrical Effects. *Phys. Rev. X* **8**, 11043 (2018).

53. Shibasaki, K., Suzuki, M., Mizuno, A. & Tominaga, M. Effects of Body Temperature on Neural Activity in the Hippocampus: Regulation of Resting Membrane Potentials by Transient Receptor Potential Vanilloid 4. *J. Neurosci.* **27**, 1566–1575 (2007).

54. Wells, J., Kao, C., Konrad, P., Milner, T., Kim, J., Mahadevan-Jansen, A. & Jansen, E. D. Biophysical Mechanisms of Transient Optical Stimulation of Peripheral Nerve. *Biophys. J.* **93**, 2567–2580 (2007).

55. Andersen, P. & Moser, E. Brain Temperature and Hippocampal Function. *Hippocampus* **5**, 491–498 (1995).

56. Thompson, S. M., Masukawa, L. M. & Prince, D. A. Temperature dependence of intrinsic membrane properties and synaptic potentials in hippocampal CA1 neurons in vitro. *J. Neurosci.* **5**, 817–24 (1985).

57. Deng, W., Goldys, E. M., Farnham, M. M. J. & Pilowsky, P. M. Optogenetics, the intersection between physics and neuroscience: light stimulation of neurons in physiological conditions. *Am. J. Physiol. Regul. Integr. Comp. Physiol.* **307**, R1292-302 (2014).

58. Thomsen, S. Pathologic Analysis of Photothermal and Photomechanical Effects of Laser Tissue Interactions. *Photochem. Photobiol.* **53**, 825–835 (1991).

59. Dewhirst, M. W., Viglianti, B. L., Lora-Michiels, M., Hanson, M. & Hoopes, P. J. Basic principles of thermal dosimetry and thermal thresholds for tissue damage from

hyperthermia. *Int. J. Hyperth.* **19**, 267–294 (2003).

60. Lepock, J. R. Cellular effects of hyperthermia: Relevance to the minimum dose for thermal damage. *Int. J. Hyperth.* **19**, 252–266 (2003).

61. Fourier, J.-B.-J. *Théorie analytique de la chaleur*. (F. Didot, 1822).

62. Pennes, H. H. Analysis of Tissue and Arterial Blood Temperatures in the Resting Human Forearm. *J. Appl. Physiol.* **1**, 93–122 (1948).

63. Picot, A., Dominguez, S., Liu, C., Chen, I. W., Tanese, D., Ronzitti, E., Berto, P., Papagiakoumou, E., Oron, D., Tessier, G., Forget, B. C. & Emiliani, V. Temperature Rise under Two-Photon Optogenetic Brain Stimulation. *Cell Rep.* **24**, 1243-1253.e5 (2018).

64. Carslaw, H. S., Jaeger, J. C. J., Carslaw 1870-1954, H. S. (Horatio S. & Jaeger, J. C. J. *Conduction of Heat in Solids*. (Clarendon Press, 1959).

65. Gerchberg, R. W. & Saxton, W. O. A practical algorithm for the determination of phase from image and diffraction plane pictures. *Optik (Stuttg).* **35**, 237–246 (1972).

66. Goodman, J. W. Introduction to Fourier Optics McGraw-Hill Series in Electrical and Computer Engineering. *Quantum Semiclassical Opt. J. Eur. Opt. Soc. Part B* **8**, 491 (1996).

67. Cheng, X., Li, Y., Mertz, J., Sakadžić, S., Devor, A., Boas, D. A. & Tian, L. Development of a beam propagation method to simulate the point spread function degradation in scattering media. *Opt. Lett.* **44**, 4989 (2019).

68. Schott, S., Bertolotti, J., Léger, J.-F., Bourdieu, L. & Gigan, S. Characterization of the angular memory effect of scattered light in biological tissues. *Opt. Express* **23**, 13505 (2015).

69. Roey, J. Van, Donk, J. Van Der & Lagasse, P. E. Beam-propagation method : analysis and assessment Ear) = JJJ. **71**, (1981).

70. Papagiakoumou, E., Bègue, A., Leshem, B., Schwartz, O., Stell, B. M., Bradley, J., Oron, D. & Emiliani, V. Functional patterned multiphoton excitation deep inside scattering tissue. *Nat. Photonics* **7**, 274–278 (2013).

71. Childs, P. R. N., Greenwood, J. R. & Long, C. A. Review of temperature measurement. *Rev. Sci. Instrum.* **71**, 2959–2978 (2000).

72. Nicholas, J. V & Webster, J. G. Liquid-in-glass thermometers. in *The Measurement*

Instrumentation and Sensors Handbook (CRC Press New York, 1999).

73. Wise, J. A. *Liquid-in-Glass Thermometry*. *U.S. Department of Commerce, National Bureau of Standards* vol. 150 (US Department of Commerce, National Bureau of Standards, 1976).

74. Howard, E. Thermostatic Bimetal. *Eng. Sci.* **5**, 16–24 (1942).

75. Stephenson, R. J. Bimaterials Thermometers—The Measurement Instrumentation and Sensors Handbook. (1999).

76. Divita, R. V. Bimetal thermometer selection. *Meas. Control* 93–95 (1994).

77. Gao, Y. & Bando, Y. Carbon nanothermometer containing gallium. *Nature* **415**, 599 (2002).

78. Pollock, D. *Thermocouples: theory and properties*. (Routledge, 2018).

79. Kinzie, P. A. & Rubin, L. G. Thermocouple temperature measurement. *PhT* **26**, 52 (1973).

80. Riddle, J. L., Furukawa, G. T. & Plumb, H. H. *Platinum resistance thermometry*. vol. 126 (National Bureau of Standards, 1973).

81. Szmyrka-Grzebyk, A. & Lipiński, L. Linear diode thermometer in the 4–300 K temperature range. *Cryogenics (Guildf).* **35**, 281–284 (1995).

82. Grattan, K. T. V & Zhang, Z. Y. Fiber Optic Fluorescence Thermometry. in *Topics in Fluorescence Spectroscopy: Probe Design and Chemical Sensing* (ed. Lakowicz, J. R.) 335–376 (Springer US, 1994). doi:10.1007/0-306-47060-8_11.

83. Beheim, G. Fiber-optic temperature sensor using a thin-film Fabry-Perot interferometer. (1997).

84. Lawless, W. N., Clark, C. F. & Arenz, R. W. Method for measuring specific heats in intense magnetic fields at low temperatures using capacitance thermometry. *Rev. Sci. Instrum.* **53**, 1647–1652 (1982).

85. Walker, G. W., Sundar, V. C., Rudzinski, C. M., Wun, A. W., Bawendi, M. G. & Nocera, D. G. Quantum-dot optical temperature probes. *Appl. Phys. Lett.* **83**, 3555–3557 (2003).

86. Zhang, Y. & Chen, J. Thermometry based on Coulomb-coupled quantum dots. *Phys. E Low-Dimensional Syst. Nanostructures* **114**, 113635 (2019).

87. Ross, D., Gaitan, M. & Locascio, L. E. Temperature measurement in microfluidic systems using a temperature-dependent fluorescent dye. *Anal. Chem.* **73**, 4117–4123 (2001).

88. Wang, F., Tan, W. B., Zhang, Y., Fan, X. & Wang, M. Luminescent nanomaterials for biological labelling. *Nanotechnology* **17**, (2006).

89. Yang, G., Liu, X., Feng, J., Li, S. & Li, Y. Organic Dye Thermometry. (2015).

90. Bousseksou, A., Molnár, G., Salmon, L. & Nicolazzi, W. Molecular spin crossover phenomenon: Recent achievements and prospects. *Chem. Soc. Rev.* **40**, 3313–3335 (2011).

91. Cerruti, M. G., Sauthier, M., Leonard, D., Liu, D., Duscher, G., Feldheim, D. L. & Franzen, S. Gold and silica-coated gold nanoparticles as thermographic labels for DNA detection. *Anal. Chem.* **78**, 3282–3288 (2006).

92. Kolodner, P. & Tyson, J. A. Remote thermal imaging with 0.7-μm spatial resolution using temperature-dependent fluorescent thin flims. *Appl. Phys. Lett.* **42**, 117–119 (1983).

93. Assy, A., Lin, H. J., Schoenauer-Sebag, M., Gredin, P., Mortier, M., Billot, L., Chen, Z. & Aigouy, L. Nanoscale thermometry with fluorescent yttrium-based Er/Yb-doped fluoride nanocrystals. *Sensors Actuators, A Phys.* **250**, 71–77 (2016).

94. Aigouy, L., Sadi, E., Lalouat, L., Laḃguerie-Eǵa, J., Mortier, M., Löw, P. & Bergaud, C. AC thermal imaging of a microwire with a fluorescent nanocrystal: Influence of the near field on the thermal contrast. *J. Appl. Phys.* **106**, (2009).

95. Saïdi, E., Samson, B., Aigouy, L., Volz, S., Löw, P., Bergaud, C. & Mortier, M. Scanning thermal imaging by near-field fluorescence spectroscopy. *Nanotechnology* **20**, 115703 (2009).

96. Okabe, K., Inada, N., Gota, C., Harada, Y., Funatsu, T. & Uchiyama, S. Intracellular temperature mapping with a fluorescent polymeric thermometer and fluorescence lifetime imaging microscopy. *Nat. Commun.* **3**, (2012).

97. Stasiek, J., Stasiek, A., Jewartowski, M. & Collins, M. W. Liquid crystal thermography and true-colour digital image processing. *Opt. Laser Technol.* **38**, 243–256 (2006).

98. Srinath, V. E. & Je-Chin, H. A transient liquid crystal thermography technique for gas turbine heat transfer measurements. *Meas. Sci. Technol.* **11**, 957 (2000).

99. Wolfbeis, O. S. Sensor paints. *Adv. Mater.* **20**, 3759–3763 (2008).

100. Beckman, K. A., Graham, J. A., Examiner-thurman, P., Beckman, K. A. & Graham, J. A. Infrared thermometry system and method. (1990).

101. Fuchs, M. & Tanner, C. B. Infrared Thermometry of Vegetation. *Agron. J.* **58**, 597–601 (1966).

102. Ring, E. F. J. & Ammer, K. Infrared thermal imaging in medicine. *Physiol. Meas.* **33**, (2012).

103. Baffou, G., Bon, P., Savatier, J., Polleux, J., Zhu, M., Merlin, M., Rigneault, H. & Monneret, S. Thermal imaging of nanostructures by quantitative optical phase analysis. *ACS Nano* **6**, 2452–2458 (2012).

104. Berto, P., Ureña, E. B., Bon, P., Quidant, R., Rigneault, H. & Baffou, G. Quantitative absorption spectroscopy of nano-objects. *Phys. Rev. B - Condens. Matter Mater. Phys.* **86**, 1–5 (2012).

105. Hall, R. J. & Bonczyk, P. A. Sooting flame thermometry using emission/absorption tomography. *Appl. Opt.* **29**, 4590 (1990).

106. Shimizu, S., Sakai, S., Nomura, T. & Wakai, K. Measurement of Flame Temperature Distribution by Infrared-Rays Computed Tomography. *Trans. Japan Soc. Mech. Eng. Ser. B* **53**, 3803–3809 (1987).

107. Smith, J. D., Cappa, C. D., Drisdell, W. S., Cohen, R. C. & Saykally, R. J. Raman thermometry measurements of free evaporation from liquid water droplets. *J. Am. Chem. Soc.* **128**, 12892–12898 (2006).

108. LaPlant, F., Laurence, G. & Ben-Amotz, D. Theoretical and experimental uncertainty in temperature measurement of materials by Raman spectroscopy. *Appl. Spectrosc.* **50**, 1034–1038 (1996).

109. Barat, R. B., Longwell, J. P., Sarofim, A. F., Smith, S. P. & Bar-Ziv, E. Laser Rayleigh scattering for flame thermometry in a toroidal jet stirred combustor. *Appl. Opt.* **30**, 3003 (1991).

110. Murphy, A. B. & Farmer, A. J. D. Temperature measurement in thermal plasmas by rayleigh scattering. *J. Phys. D. Appl. Phys.* **25**, 634–643 (1992).

111. Hall, R. J. & Boedeker, L. R. CARS thermometry in fuel-rich combustion zones. *Appl. Opt.* **23**, 1340 (1984).

112. Herring, G. C., Roberts, W. L., Brown, M. S. & DeBarber, P. A. Temperature measurement by degenerate four-wave mixing with strong absorption of the excitation beams. *Appl. Opt.* **35**, 6544 (1996).

113. Goss, L. P., Smith, A. A. & Post, M. E. Surface thermometry by laser-induced fluorescence. *Rev. Sci. Instrum.* **60**, 3702–3706 (1989).

114. Owen, S. F., Liu, M. H. & Kreitzer, A. C. Thermal constraints on in vivo optogenetic manipulations. *Nat. Neurosci.* **22**, 1061–1065 (2019).

115. Arias-Gil, G., Ohl, F. W., Takagaki, K. & Lippert, M. T. Measurement, modeling, and prediction of temperature rise due to optogenetic brain stimulation. *Neurophotonics* **3**, 045007 (2016).

116. Zhou, J., del Rosal, B., Jaque, D., Uchiyama, S. & Jin, D. Advances and challenges for fluorescence nanothermometry. *Nat. Methods* **17**, 967–980 (2020).

117. del Rosal, B., Ximendes, E., Rocha, U. & Jaque, D. In Vivo Luminescence Nanothermometry: from Materials to Applications. *Adv. Opt. Mater.* **5**, (2017).

118. Van Herwaarden, a. W. W., Sarro, P. M. M. & Van Herwaarden, a. W. W. Thermal sensors based on the seebeck effect. *Sensors and Actuators* **10**, 321–346 (1986).

119. Podgorski, K. & Ranganathan, G. Brain heating induced by near-infrared lasers during multiphoton microscopy. *J. Neurophysiol.* **116**, 1012–1023 (2016).

120. Shin, Y., Yoo, M., Kim, H.-S., Nam, S.-K., Kim, H.-I., Lee, S.-K., Kim, S. & Kwon, H.-S. Characterization of fiber-optic light delivery and light-induced temperature changes in a rodent brain for precise optogenetic neuromodulation. *Biomed. Opt. Express* **7**, 4450 (2016).

121. AEROPAK®Mineral Insulated Thermocouple. *https://www.okazaki-mfg.com/en/BasicProducts/Aeropak.html*.

122. Rajagopal, M. C., Valavala, K. V., Gelda, D., Ma, J. & Sinha, S. Fabrication and characterization of thermocouple probe for use in intracellular thermometry. *Sensors Actuators, A Phys.* **272**, 253–258 (2018).

123. Balčytis, A., Ryu, M., Juodkazis, S. & Morikawa, J. Micro-thermocouple on nano-membrane: Thermometer for nanoscale measurements. *Sci. Rep.* **8**, 8–13 (2018).

124. Young, H. D. & Sears, F. W. *University physics.* (Addison-Wesley Pub. Co., 1992).

125. Usamentiaga, R., Venegas, P., Guerediaga, J., Vega, L., Molleda, J. & Bulnes, F. G.

Infrared thermography for temperature measurement and non-destructive testing. *Sensors (Switzerland)* **14**, 12305–12348 (2014).

126. Jaque, D. & Vetrone, F. Luminescence nanothermometry. *Nanoscale* **4**, 4301 (2012).

127. Donner, J. S., Thompson, S. A., Kreuzer, M. P., Baffou, G. & Quidant, R. Mapping intracellular temperature using green fluorescent protein. *Nano Lett.* **12**, 2107–2111 (2012).

128. Dramićanin, M. D. Trends in luminescence thermometry. *J. Appl. Phys.* **128**, (2020).

129. Samson, B., Aigouy, L., Latempa, R., Tessier, G., Aprili, M., Mortier, M., Lesueur, J. & Fournier, D. Scanning thermal imaging of an electrically excited aluminum microstripe. *J. Appl. Phys.* **102**, (2007).

130. Aigouy, L., Tessier, G., Mortier, M. & Charlot, B. Scanning thermal imaging of microelectronic circuits with a fluorescent nanoprobe. *Appl. Phys. Lett.* **87**, 184105 (2005).

131. Rivera, V. A. G., Ferri, F. A. & Marega, E. Localized Surface Plasmon Resonances: Noble Metal Nanoparticle Interaction with Rare-Earth Ions. *Plasmon. - Princ. Appl.* (2012) doi:10.5772/50753.

132. Aigouy, L., De Wilde, Y., Mortier, M., Giérak, J. & Bourhis, E. Fabrication and characterization of fluorescent rare-earth-doped glass-particle-based tips for near-field optical imaging applications. *Appl. Opt.* **43**, 3829–3837 (2004).

133. Vetrone, F., Naccache, R., Zamarrón, A., De La Fuente, A. J., Sanz-Rodríguez, F., Maestro, L. M., Rodriguez, E. M., Jaque, D., Sole, J. G., Capobianco, J. A., Zamarrón, A., Juarranz de la Fuente, A., Sanz-Rodríguez, F., Martinez Maestro, L., Martín Rodriguez, E., Jaque, D., García Solé, J. & Capobianco, J. A. Temperature sensing using fluorescent nanothermometers. *ACS Nano* **4**, 3254–3258 (2010).

134. Zhang, R., Zhang, J., Xie, M. & Chen, J. Optical characteristics of Agarose gel. *Hongwai yu Jiguang Gongcheng/Infrared Laser Eng.* **45**, 1–7 (2016).

135. Zhang, M., Che, Z., Chen, J., Zhao, H., Yang, L., Zhong, Z. & Lu, J. Experimental determination of thermal conductivity of water-agar gel at different concentrations and temperatures. *J. Chem. Eng. Data* **56**, 859–864 (2011).

136. Hernandez, O., Papagiakoumou, E., Tanesee, D., Felin, K., Wyart, C. & Emiliani, V. Three-dimensional spatiotemporal focusing of holographic patterns. *Nat. Commun.* **7**,

11928 (2016).

137. Yaroslavsky, A. N., Schulze, P. C., Yaroslavsky, I. V., Schober, R., Ulrich, F. & Schwarzmaier, H. J. Optical properties of selected native and coagulated human brain tissues in vitro in the visible and near infrared spectral range. *Phys. Med. Biol.* **47**, 2059–2073 (2002).

138. Blumm, J. & Lindemann, A. Characterization of the thermophysical properties of molten polymers and liquids using the flash technique. *High Temp. - High Press.* **35–36**, 627–632 (2003).

139. Yizhar, O., Fenno, L. E., Davidson, T. J., Mogri, M. & Deisseroth, K. Optogenetics in Neural Systems. *Neuron* **71**, 9–34 (2011).

140. Double-Clad Fiber. https://www.thorlabs.com/newgrouppage9.cfm?objectgroup_id=8950.

141. Li, A. H., Sun, Z. J. & Lü, Q. Laser heating effect on the power dependence of upconversion luminescence in Er3+-doped nanopowders. *J. Nanoparticle Res.* **15**, (2013).

142. Manzani, D., Petruci, J. F. D. S., Nigoghossian, K., Cardoso, A. A. & Ribeiro, S. J. L. A portable luminescent thermometer based on green up-conversion emission of Er3+/Yb3+ co-doped tellurite glass. *Sci. Rep.* **7**, 1–11 (2017).

143. Ronzitti, E., Conti, R., Zampini, V., Tanese, D., Foust, A. J., Klapoetke, N., Boyden, E. S., Papagiakoumou, E. & Emiliani, V. Sub-millisecond optogenetic control of neuronal firing with two-photon holographic photoactivation of Chronos. *J. Neurosci.* 1246–17 (2017) doi:10.1523/JNEUROSCI.1246-17.2017.

144. Jacques, S. L. Erratum: Optical properties of biological tissues: A review (Physics in Medicine and Biology (2013) 58). *Phys. Med. Biol.* **58**, 5007–5008 (2013).

145. Horton, N. G., Wang, K., Kobat, D., Clark, C. G., Wise, F. W., Schaffer, C. B. & Xu, C. In vivo three-photon microscopy of subcortical structures within an intact mouse brain. *Nat. Photonics* **7**, 205–209 (2013).

146. Bernstein, J. G., Garrity, P. A. & Boyden, E. S. Optogenetics and thermogenetics: Technologies for controlling the activity of targeted cells within intact neural circuits. *Curr. Opin. Neurobiol.* **22**, 61–71 (2012).

147. Bath, D. E., Stowers, J. R., Hörmann, D., Poehlmann, A., Dickson, B. J. & Straw, A.

D. FlyMAD: Rapid thermogenetic control of neuronal activity in freely walking Drosophila. *Nat. Methods* **11**, 756–762 (2014).

148. Ermakova, Y. G., Lanin, A. A., Fedotov, I. V., Roshchin, M., Kelmanson, I. V., Kulik, D., Bogdanova, Y. A., Shokhina, A. G., Bilan, D. S., Staroverov, D. B., Balaban, P. M., Fedotov, A. B., Sidorov-Biryukov, D. A., Nikitin, E. S., Zheltikov, A. M. & Belousov, V. V. Thermogenetic neurostimulation with single-cell resolution. *Nat. Commun.* **8**, 15362 (2017).

149. Connor, E. E., Mwamuka, J., Gole, A., Murphy, C. J. & Wyatt, M. D. Gold nanoparticles are taken up by human cells but do not cause acute cytotoxicity. *Small* **1**, 325–327 (2005).

150. Boisselier, E. & Astruc, D. Gold nanoparticles in nanomedicine: preparations, imaging, diagnostics, therapies and toxicity. *Chem. Soc. Rev.* **38**, 1759–1782 (2009).

151. Brayner, R. The toxicological impact of nanoparticles. *Nano Today* **3**, 48–55 (2008).

152. Stern, J. M., Stanfield, J., Kabbani, W., Hsieh, J.-T. & Cadeddu, J. A. Selective prostate cancer thermal ablation with laser activated gold nanoshells. *J. Urol.* **179**, 748–753 (2008).

153. Rastinehad, A. R., Anastos, H., Wajswol, E., Winoker, J. S., Sfakianos, J. P., Doppalapudi, S. K., Carrick, M. R., Knauer, C. J., Taouli, B., Lewis, S. C., Tewari, A. K., Schwartz, J. A., Canfield, S. E., George, A. K., West, J. L. & Halas, N. J. Gold nanoshell-localized photothermal ablation of prostate tumors in a clinical pilot device study. *Proc. Natl. Acad. Sci. U. S. A.* **116**, 18590–18596 (2019).

154. Carvalho-de-Souza, J. L., Treger, J. S., Dang, B., Kent, S. B. H., Pepperberg, D. R. & Bezanilla, F. Photosensitivity of neurons enabled by cell-targeted gold nanoparticles. *Neuron* **86**, 207–217 (2015).

155. Baffou, G., Ureña, E. B., Berto, P., Monneret, S., Quidant, R. & Rigneault, H. Deterministic temperature shaping using plasmonic nanoparticle assemblies. *Nanoscale* **6**, 8984–8989 (2014).

156. Baffou, G. & Quidant, R. Thermo-plasmonics: Using metallic nanostructures as nano-sources of heat. *Laser Photonics Rev.* **7**, 171–187 (2013).

157. Baffou, G., Quidant, R. & García De Abajo, F. J. Nanoscale control of optical heating in complex plasmonic systems. *ACS Nano* **4**, 709–716 (2010).

158. Myroshnychenko, V., Rodríguez-Fernández, J., Pastoriza-Santos, I., Funston, A. M., Novo, C., Mulvaney, P., Liz-Marzán, L. M. & García de Abajo, F. J. Modelling the optical response of gold nanoparticles. *Chem. Soc. Rev.* **37**, 1792–1805 (2008).

159. Baffou, G. & Rigneault, H. Femtosecond-pulsed optical heating of gold nanoparticles. *Phys. Rev. B - Condens. Matter Mater. Phys.* **84**, 1–13 (2011).

160. Khlebtsov, B., Zharov, V., Melnikov, A., Tuchin, V. & Khlebtsov, N. Optical amplification of photothermal therapy with gold nanoparticles and nanoclusters. *Nanotechnology* **17**, 5167–5179 (2006).

161. Chen, H., Shao, L., Ming, T., Sun, Z., Zhao, C., Yang, B. & Wang, J. Understanding the photothermal conversion efficiency of gold nanocrystals. *Small* **6**, 2272–2280 (2010).

162. Govorov, A. O., Zhang, W., Skeini, T., Richardson, H., Lee, J. & Kotov, N. A. Gold nanoparticle ensembles as heaters and actuators: Melting and collective plasmon resonances. *Nanoscale Res. Lett.* **1**, 84–90 (2006).

163. Baffou, G., Girard, C. & Quidant, R. Mapping heat origin in plasmonic structures. *Phys. Rev. Lett.* **104**, 1–4 (2010).

164. Baffou, G. Thermodynamics of Metal Nanoparticles. in *Thermoplasmonics* 36–80 (Cambridge University Press, 2017). doi:10.1017/9781108289801.004.

165. Polleux, J., Rasp, M., Louban, I., Plath, N., Feldhoff, A. & Spatz, J. P. Benzyl alcohol and block copolymer micellar lithography: A versatile route to assembling gold and in situ generated titania nanoparticles into uniform binary nanoarrays. *ACS Nano* **5**, 6355–6364 (2011).

166. Baffou, G., Berto, P., Bermúdez Ureña, E., Quidant, R., Monneret, S., Polleux, J. & Rigneault, H. Photoinduced heating of nanoparticle arrays. *ACS Nano* **7**, 6478–6488 (2013).

167. Calculateur javascript pour la diffusion de Mie. *https://saviot.cnrs.fr/mie/index.html*.

168. Thormählen, I., Straub, J. & Grigull, U. Refractive Index of Water and Its Dependence on Wavelength, Temperature, and Density. *J. Phys. Chem. Ref. Data* **14**, 933–945 (1985).

169. Cao, Z., Jiang, L., Wang, S., Wang, M., Liu, D., Wang, P., Zhang, F. & Lu, Y. All-glass extrinsic Fabry – Perot interferometer thermo-optic coefficient sensor based on a

capillary bridged two fiber ends. *Appl. Opt.* **54**, 2371–2375 (2015).

170. Ghosh, G. *Handbook of Thermo-Optic Coefficients of Optical Materials with Applications. Chemistry &* vol. 5 (1998).

171. Primot, J. & Sogno, L. Achromatic three-wave (or more) lateral shearing interferometer. *J. Opt. Soc. Am. A* **12**, 2679–2685 (1995).

172. Chanteloup, J.-C. Multiple-wave lateral shearing interferometry for wave-front sensing. *Appl. Opt.* **44**, 1559–1571 (2005).

173. Balderas-López, J. A., Mandelis, A. & Garcia, J. A. Thermal-wave resonator cavity design and measurements of the thermal diffusivity of liquids. *Rev. Sci. Instrum.* **71**, 2933–2937 (2000).

174. Berto, P., Mohamed, M. S. A., Rigneault, H. & Baffou, G. Time-harmonic optical heating of plasmonic nanoparticles. *Phys. Rev. B - Condens. Matter Mater. Phys.* **90**, 1–12 (2014).

175. Thalhammer, G., Bowman, R. W., Love, G. D., Padgett, M. J. & Ritsch-Marte, M. Speeding up liquid crystal SLMs using overdrive with phase change reduction. *Opt. Express* **21**, 1779–1797 (2013).

176. Bouchard, M. B., Voleti, V., Mendes, C. S., Lacefield, C., Grueber, W. B., Mann, R. S., Bruno, R. M. & Hillman, E. M. C. C. Swept confocally-aligned planar excitation (SCAPE) microscopy for high-speed volumetric imaging of behaving organisms. *Nat. Photonics* **9**, 113–119 (2015).

177. Ehrlicher, A., Betz, T., Stuhrmann, B., Koch, D., Milner, V., Raizen, M. G. & Kas, J. Guiding neuronal growth with light. *Proc. Natl. Acad. Sci.* **99**, 16024–16028 (2002).

178. Guillon, M., Forget, B. C., Foust, A. J., De Sars, V., Ritsch-Marte, M. & Emiliani, V. Vortex-free phase profiles for uniform patterning with computer-generated holography. *Opt. Express* **25**, 12640 (2017).

179. Jesacher, A., Maurer, C., Schwaighofer, A., Bernet, S. & Ritsch-Marte, M. Near-perfect hologram reconstruction with a spatial light modulator. *Opt Express* **16**, 2597–2603 (2008).

180. Curtis, A. S. G. THE MECHANISM OF ADHESION OF CELLS TO GLASS : A Study by Interference Reflection Microscopy . *J. Cell Biol.* **20**, 199–215 (1964).

181. Paris, L., Marc, I., Charlot, B., Dumas, M., Valmier, J. & Bardin, F. Millisecond

infrared laser pulses depolarize and elicit action potentials on in-vitro dorsal root ganglion neurons. *Biomed. Opt. Express* **8**, 4568 (2017).

182. Berto, P., Philippet, L., Osmond, J., Liu, C. F., Afridi, A., Montagut Marques, M., Molero Agudo, B., Tessier, G. & Quidant, R. Tunable and free-form planar optics. *Nat. Photonics* **13**, 649–656 (2019).

183. Lin, M. Z. & Schnitzer, M. J. Genetically encoded indicators of neuronal activity. *Nat. Neurosci.* **19**, 1142–1153 (2016).

184. Sequential dendritic voltage imaging and dendritic calcium imaging. *https://health.uconn.edu/antic-lab/image-gallery/*.

185. Göbel, W. & Helmchen, F. New angles on neuronal dendrites in vivo. *J. Neurophysiol.* **98**, 3770–3779 (2007).

186. Beaurepaire, E. & Mertz, J. Epifluorescence collection in two-photon microscopy. *Appl. Opt.* **41**, 5376 (2002).

187. Grewe, B. F., Voigt, F. F., van ’t Hoff, M. & Helmchen, F. Fast two-layer two-photon imaging of neuronal cell populations using an electrically tunable lens. *Biomed. Opt. Express* **2**, 2035 (2011).

188. Yang, W., Miller, J. eun K., Carrillo-Reid, L., Pnevmatikakis, E., Paninski, L., Yuste, R. & Peterka, D. S. Simultaneous Multi-plane Imaging of Neural Circuits. *Neuron* **89**, 269 (2016).

189. Kong, L., Tang, J., Little, J. P., Yu, Y., Lämmermann, T., Lin, C. P., Germain, R. N. & Cui, M. Continuous volumetric imaging via an optical phase-locked ultrasound lens. *Nat. Methods* **12**, 759–762 (2015).

190. Iyer, V., Hoogland, T. M. & Saggau, P. Fast functional imaging of single neurons using random-access multiphoton (RAMP) microscopy. *J. Neurophysiol.* **95**, 535–545 (2006).

191. Prevedel, R., Verhoef, A. J., Pernía-Andrade, A. J., Weisenburger, S., Huang, B. S., Nöbauer, T., Fernández, A., Delcour, J. E., Golshani, P., Baltuska, A. & Vaziri, A. Fast volumetric calcium imaging across multiple cortical layers using sculpted light. *Nat. Methods* **13**, 1021–1028 (2016).

192. Nadella, K. M. N. S., Roš, H., Baragli, C., Griffiths, V. A., Konstantinou, G., Koimtzis, T., Evans, G. J., Kirkby, P. A. & Silver, R. A. Random-access scanning microscopy for

3D imaging in awake behaving animals. *Nat. Methods* **13**, 1001–1004 (2016).

193. Tomer, R., Lovett-Barron, M., Kauvar, I., Andalman, A., Burns, V. M., Sankaran, S., Grosenick, L., Broxton, M., Yang, S. & Deisseroth, K. SPED Light Sheet Microscopy: Fast Mapping of Biological System Structure and Function. *Cell* **163**, 1796–1806 (2015).

194. Fahrbach, F. O., Voigt, F. F., Schmid, B., Helmchen, F. & Huisken, J. Rapid 3D light-sheet microscopy with a tunable lens. *Opt. Express* **21**, 21010 (2013).

195. Cheng, A., Gonçalves, J. T., Golshani, P., Arisaka, K. & Portera-Cailliau, C. Simultaneous two-photon calcium imaging at different depths with spatiotemporal multiplexing. *Nat. Methods* **8**, 139–142 (2011).

196. Kim, K. H., Buehler, C., Bahlmann, K., Ragan, T., Lee, W.-C. A., Nedivi, E., Heffer, E. L., Fantini, S. & So, P. T. C. Multifocal multiphoton microscopy based on multianode photomultiplier tubes. *Opt. Express* **15**, 11658 (2007).

197. Pnevmatikakis, E. A., Soudry, D., Gao, Y., Machado, T. A., Merel, J., Pfau, D., Reardon, T., Mu, Y., Lacefield, C., Yang, W., Ahrens, M., Bruno, R., Jessell, T. M., Peterka, D. S., Yuste, R. & Paninski, L. Simultaneous Denoising, Deconvolution, and Demixing of Calcium Imaging Data. *Neuron* **89**, 285–299 (2016).

198. Lu, R., Sun, W., Liang, Y., Kerlin, A., Bierfeld, J., Seelig, J. D., Wilson, D. E., Scholl, B., Mohar, B., Tanimoto, M., Koyama, M., Fitzpatrick, D., Orger, M. B. & Ji, N. Video-rate volumetric functional imaging of the brain at synaptic resolution. *Nat. Neurosci.* **20**, 620–628 (2017).

199. Ducros, M., Houssen, Y. G., Bradley, J., De Sars, V. & Charpak, S. Encoded multisite two-photon microscopy. *Proc. Natl. Acad. Sci. U. S. A.* **110**, 13138–13143 (2013).

200. Mahou, P., Zimmerley, M., Loulier, K., Matho, K. S., Labroille, G., Morin, X., Supatto, W., Livet, J., Débarre, D. & Beaurepaire, E. Multicolor two-photon tissue imaging by wavelength mixing. *Nat. Methods* **9**, 815–818 (2012).

201. Yang, S. J., Allen, W. E., Kauvar, I., Andalman, A. S., Young, N. P., Kim, C. K., Marshel, J. H., Wetzstein, G. & Deisseroth, K. Extended field-of-view and increased-signal 3D holographic illumination with time-division multiplexing. *Opt. Express* **23**, 32573 (2015).

202. Quirin, S., Peterka, D. S. & Yuste, R. Instantaneous three-dimensional sensing using

spatial light modulator illumination with extended depth of field imaging. *Opt. Express* **21**, 16007 (2013).

203. Quirin, S., Jackson, J., Peterka, D. S. & Yuste, R. Simultaneous imaging of neural activity in three dimensions. *Front. Neural Circuits* **8**, 1–11 (2014).

204. Broxton, M., Grosenick, L., Yang, S., Cohen, N., Andalman, A., Deisseroth, K. & Levoy, M. Wave optics theory and 3-D deconvolution for the light field microscope. *Opt. Express* **21**, 25418 (2013).

205. Prevedel, R., Yoon, Y.-G., Hoffmann, M., Pak, N., Wetzstein, G., Kato, S., Schrödel, T., Raskar, R., Zimmer, M., Boyden, E. S. & Vaziri, A. Simultaneous whole-animal 3D imaging of neuronal activity using light-field microscopy. *Nat. Methods* **11**, 727–730 (2014).

206. Maurer, C., Jesacher, A., Bernet, S. & Ritsch-Marte, M. What spatial light modulators can do for optical microscopy. *Laser Photonics Rev.* **5**, 81–101 (2011).

207. Collins, D. R., Sampsell, J. B., Hornbeck, L. J., Florence, J. M., Penz, P. A. & Gately, M. T. Deformable mirror device spatial light modulators and their applicability to optical neural networks. *Appl. Opt.* **28**, 4900 (1989).

208. Berge, B. & Peseux, J. Variable focal lens controlled by an external voltage: An application of electrowetting. *Eur. Phys. J. E* **3**, 159–163 (2000).

209. Kuiper, S. & Hendriks, B. H. W. Variable-focus liquid lens for miniature cameras. *Appl. Phys. Lett.* **85**, 1128–1130 (2004).

210. Klapoetke, N. C., Murata, Y., Kim, S. S., Pulver, S. R., Birdsey-Benson, A., Cho, Y. K., Morimoto, T. K., Chuong, A. S., Carpenter, E. J., Tian, Z., Wang, J., Xie, Y., Yan, Z., Zhang, Y., Chow, B. Y., Surek, B., Melkonian, M., Jayaraman, V., Constantine-Paton, M., *et al.* Independent optical excitation of distinct neural populations. *Nat. Methods* **11**, 338–346 (2014).

211. Zhang, D. Y., Lien, V., Berdichevsky, Y., Choi, J. & Lo, Y. H. Fluidic adaptive lens with high focal length tunability. *Appl. Phys. Lett.* **82**, 3171–3172 (2003).

212. Liebetraut, P., Petsch, S., Mönch, W. & Zappe, H. Tunable solid-body elastomer lenses with electromagnetic actuation. *Appl. Opt.* **50**, 3268 (2011).

213. Yu, H., Zhou, G., Chau, F. S. & Sinha, S. K. Tunable electromagnetically actuated liquid-filled lens. *Sensors Actuators, A Phys.* **167**, 602–607 (2011).

214. Xu, S., Ren, H., Lin, Y.-J., Moharam, M. G. J., Wu, S.-T. & Tabiryan, N. Adaptive liquid lens actuated by photo-polymer. *Opt. Express* **17**, 17590 (2009).

215. Glebov, A. L., Huang, L., Aoki, S., Lee, M. & Yokouchi, K. Planar hybrid polymer-silica microlenses with tunable beamwidth and focal length. *IEEE Photonics Technol. Lett.* **16**, 1107–1109 (2004).

216. Angelini, A., Pirani, F., Frascella, F. & Descrovi, E. Reconfigurable elastomeric graded-index optical elements controlled by light. *Light Sci. Appl.* **7**, 1–9 (2018).

217. Dong, L., Agarwal, A. K., Beebe, D. J. & Jiang, H. Adaptive liquid microlenses activated by stimuli-responsive hydrogels. *Nature* **442**, 551–554 (2006).

218. Radhakrishnan, T. S. Thermal degradation of poly(dimethylsilylene) and poly(tetramethyldisilylene-co-styrene). *J. Appl. Polym. Sci.* **99**, 2679–2686 (2006).

219. Markos, C., Vlachos, K. & Kakarantzas, G. Thermo-optic effect of an index guiding photonic crystal fiber with elastomer inclusions. *21st Int. Conf. Opt. Fiber Sensors* **7753**, 775340 (2011).

220. Xu, J. & Zhuang, S. Measurement of lens focal length with Hartmann-Shack wavefront sensor based on 4F system. *Optik (Stuttg).* **126**, 1303–1306 (2015).

221. Knöpfel, T. & Song, C. Optical voltage imaging in neurons: moving from technology development to practical tool. *Nature Reviews Neuroscience* vol. 20 719–727 (2019).

222. Lecoq, J., Orlova, N. & Grewe, B. F. Wide. Fast. Deep: Recent Advances in Multiphoton Microscopy of In Vivo Neuronal Activity. *J. Neurosci.* **39**, 9042–9052 (2019).